UNIVERSITÀ DEGLI STUDI DI PADOVA

Dipartimento di Fisica e Astronomia "Galileo Galilei"

Master Degree in Physics

Final Dissertation

Study of a novel free-space optical communication system with structured light beams

Relatore
Dr. Gianluca Ruffato
Controrelatore
Prof. Giulio Monaco

Studente
Dr. Marco Ferrari

Academic Year 2021/2022

Abstract

Since the advent of modern telecommunications, the necessity to exploit the same link to put in communication more users or to increase the amount of transmitted information has boosted the exploration of the different degrees of freedom of light, leading to the development of several division multiplexing techniques based on wavelength, time, polarization, phase/amplitude, and, more recently, space. Space division multiplexing (SDM) relies on structuring the intensity or phase distribution of electromagnetic waves over a set of non-interfering spatial configurations to be used as distinct information channels at the same frequency in combination with standard modulation formats, offering a way out to the impelling problem of networks saturation (optical crunch) and a wider alphabet of states for quantum protocols. That requires the choice of a suitable family of orthogonal beams and the design of specific devices, i.e., the multiplexer and the demultiplexer, realizing their superposition at the transmitter stage and separation at the receiver one.

In this thesis, a novel and innovative framework will be considered and investigated for SDM, based on the exploitation of a new type of beams characterized by multipole phases. The purpose of this work is the design and simulation of a free-space optical link based on multipole-phase division multiplexing. The generation (multiplexing), transmission, and sorting (demultiplexing) of multipole-phase beams will be analysed with both a theoretical and numerical approach, in order to engineer the design of efficient and compact all-optical devices for the manipulation and control of this new type of structured beams. This new spatial multiplexing technique provides an innovative and revolutionary solution in the scenario of free-space optical communication, from the optical up to the radio regimes, promising to solve the still-opened issues of previous techniques, as those based on orbital angular momentum, and offering an efficient and practical method for high-capacity transmission.

Contents

1 Introduction to the structured light application and the multipole-phase beams

In the last decades, the demand of data has increased exponentially, reaching peaks up to 90% in the annual growth rate [1], and the scenario of the saturation of the worldwide communication networks is becoming a reality. In addition, the energy consumption of the data centres and the network infrastructure is no longer sustainable, with a growth from the 1% to the 3% in the last 10 years, corresponding to the 3% of the greenhouse emission [2]. Moreover, the actual technology of the communication systems has a cost which forms an economic barrier for the developing countries. For example, the Africa continent takes into account for the 16% of the world's population but only 4% of Internet access [2]. These data clarify the urgent need for a redesign of our networks and the reason for which researchers and engineers are striving to design novel communication systems much cheaper and ecological, and that can carry more data, more efficiently than ever before. For instance, in many rural communities the access to electric power is not guaranteed, and the answer may be the integration of solar power, or other renewable resources, with the free-space optical communication systems (FSO), which do not request a solid medium in order to propagate the communication signals, as the deployment of the electric cables or the optical fibres, whose cost (about US$100,000 per km) will be prohibitive for these countries.

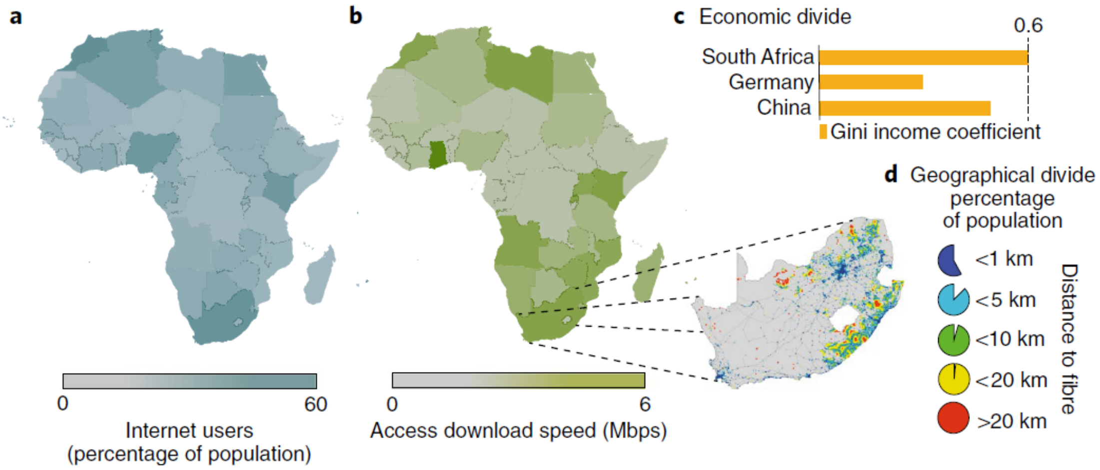

Figure 1: Internet users (frame a), and the relative download speeds (frame b), as a function of the population mapped across the Africa. The values are well below the averages for developed nation of 84% and >12 Mbps, respectively. Besides a 0.6 value of the Gini coefficient (frame c), which indicates that the richest 20% of the African continent earns 80% of all income generated by the country, these data indicate a country with a large social divide where only a few rich people have access to telecommunications [2].

An example in this direction was given by the Google X company, which has founded the Loon project in order to develop air balloons, powered with solar cells, in order to expand the internet connectivity to rural regions with the FSO technology. In the 2020, Loon has launched the first internet-via-balloon service in unserved areas of Kenya (see figure 2). This new type of networks can be also a solution in the regions where a natural calamity occurred, providing emergency connectivity.

Alongside these attempts aimed at creating new green and economic communication systems, five physical dimension, i.e., time, frequency, complex amplitude, polarization, and space, have been investigated, in these years, in order to increase the efficiency of the more widespread telecommunication systems. The easiest to understand is the *time dimension*, in the framework of which communication symbols are sent in temporal succession in the form of pulses, as the alphabet characters during the writing of a text. The shaping of these signals may be used to compress the pulse' spectrum, while multilevel modulations may be investigated in order to increase the information carried per pulse, associating different amplitudes to distinct channels of information [3]. Instead, exploiting the *frequency dimension*, multiple communications signals can be transmitted in parallel on distinct frequencies over the same medium, a technique called "wavelength-division multiplexing" (WDM).

Figure 2: The first balloon lunched by the team of the Loon project, in order to provide internet connectivity to rural areas of Kenya.

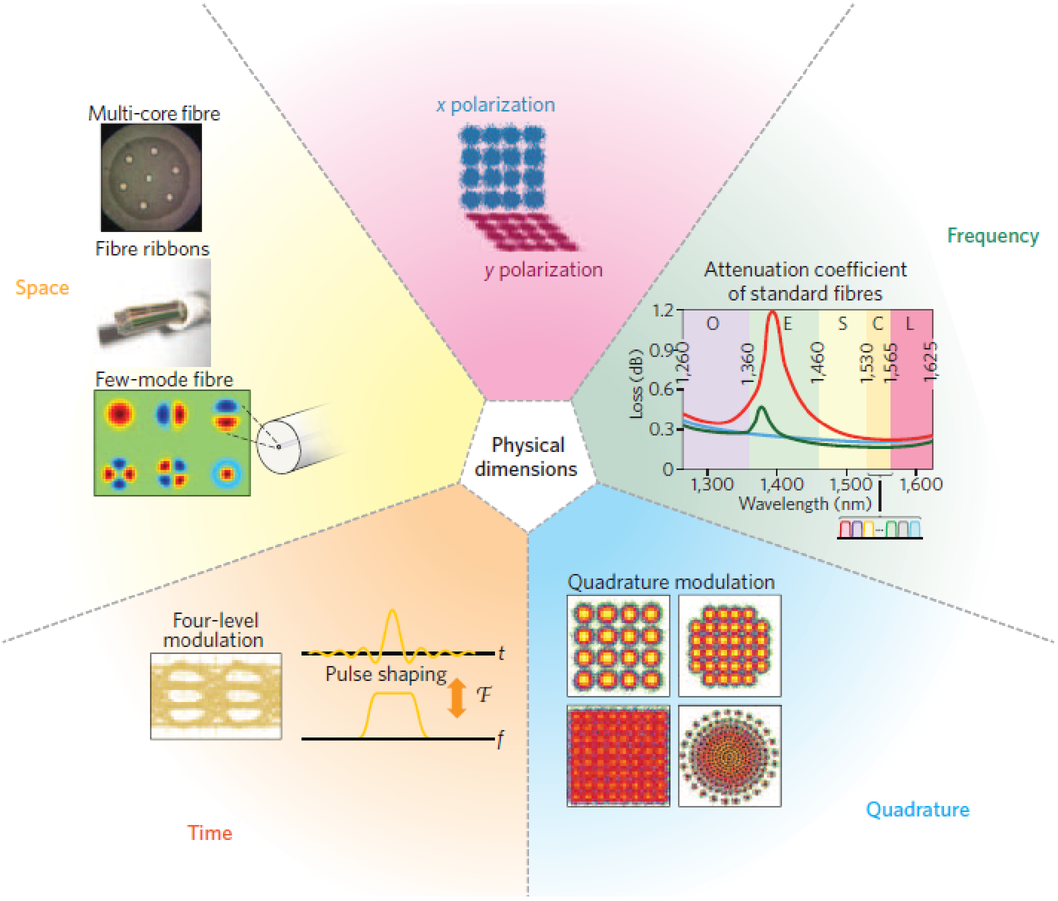

Figure 3: Five physic dimensions exploited in the communication technologies: time, frequency, polarization, quadrature, and space. Specific examples are reported for each dimension [1].

The limit of the WDMs systems is regulated by the bandwidth constraints on the shared mediums, as in the radio or mobile transmission, or due to physical and engineering limitations of the waveguides, for example in the optical fibres, where due to the absorption spectrum of the fibre's material, five frequency windows distributed in the range of $1300 \doteqdot 1600\,\mathrm{nm}$ are used (see figure 3). In the optical transmission, the further *polarization dimension* can be investigated, where the two different polarizations of the light can be adopted as an additional degree of freedom in the multiplexing process. Moreover, when the signals are modulated using both the sine and cosine components, of the carrier electromagnetic wave, a two-dimensional alphabet is obtained, and we refer to its components as two *quadrature dimensions*. Considering more values of phase and amplitude modulation, higher-dimensional quadrature protocols have been developed. Today, however, these division multiplexing techniques are almost saturated. Indeed, as shown in figure 4 for the transmission in optical fibres, in the past 40 years different technological breakthroughs have allowed an increasing of the capacity per fibre around tenfold every four years [4]. From an initial improvement of the optical fibres transmissivity and the development of the erbium-doped fibre amplifier (EDFA), for the amplification of the optical signals during the transmission into silica fibres, modulation techniques in the frequency domain have been reached in the 90s. Moreover, the improvement of the computers performances has unlocked high spectral efficiency coding in the signals' modulation.

However, the bandwidth of the optical fibres put a limit in the data transmission, where a single fibre can carry no more than about 100 Tbit s^{-1} of data [4]. Therefore, increases in the traffic demands will mean lighting more fibres, with the energy and environmental issues already introduced. For all these reasons, the most promising and recent candidate in the multiplexing technologies is the *spatial dimension*, which includes different strategies and modulation formats: from the multiple twisted wires used in Ethernet cables or in the fibre ribbons, up to the space division multiplexing (SDM) technique both for optical fibres and free-space propagation. The initial application of SDM consisted in exploiting a configuration of separated waveguides inside the same medium, as in multicore optical fibres [5]. Conversely, a more advanced approach, which is more effective for free-space applications, consists in using orthogonal spatial configurations of the electromagnetic fields which can be propagated along the same medium at the same frequency without any interference. This is the so-called mode-division multiplexing (MDM). In the MMD framework, an initial set of communication channels are multiplexed into a single electromagnetic field with a phase (or intensity) structure that is manipulated in order to transmit the information signals at the same time and frequency. Finally, at the receiver stage, the field is sorted into isolated light beams related to the initial set of channels. In this scenario, the SDM can not only increase the capacity per fibre, which is almost saturated (as reported in figure 4), with the possibility to transmit more light field at the same time and frequency, but it can also easily support WDM and others modulation formats in each spatial channel. In figure 3 all the physic dimensions described above are reported: time, frequency, quadrature, polarization and space are schematized, and specific practical examples are shown.

In particular, the work reported in this thesis finds its place in the scenario of the space division multiplexing, where it will be introduced and developed a new and unique framework for the free-space communication systems, based on the transmission of electromagnetic field with a wavefront characterized by a phase with a multipole structure, as can be seen in figure 5. These type of beams, in analogy with the fields produced by a magnetostatics multipole, will be called *multipole-phase beams* [6], and the purpose of this work is the exploration of new spatial modulation formats in the free-space communication systems in order to give an alternative to the traditional division multiplexing techniques.

In last years, some classes of beams have been investigated in the space division multiplexing: Hermite- and Laguerre-Gaussian [8], Bessel [9], and Elegant beams [10] are the most famous. However, the most promising candidates in the structured light applications were the beams carrying a twisted phase structure and, therefore, related to an orbital angular moment (OAM) of light as reported in figure 6. It is well known, indeed, that an electromagnetic wave can be interpreted quantum mechanically and thus can be imaged to carry both spin angular momentum (SAM) and OAM [8]. While the SAM is related to the vectorial nature of the electromagnetic field and can only assume two values, i.e., $\pm\hbar$ per photon, corresponding to right/left-handed circular polarization states, the OAM is related to the spatial configuration of the helical wavefronts and is an unbounded

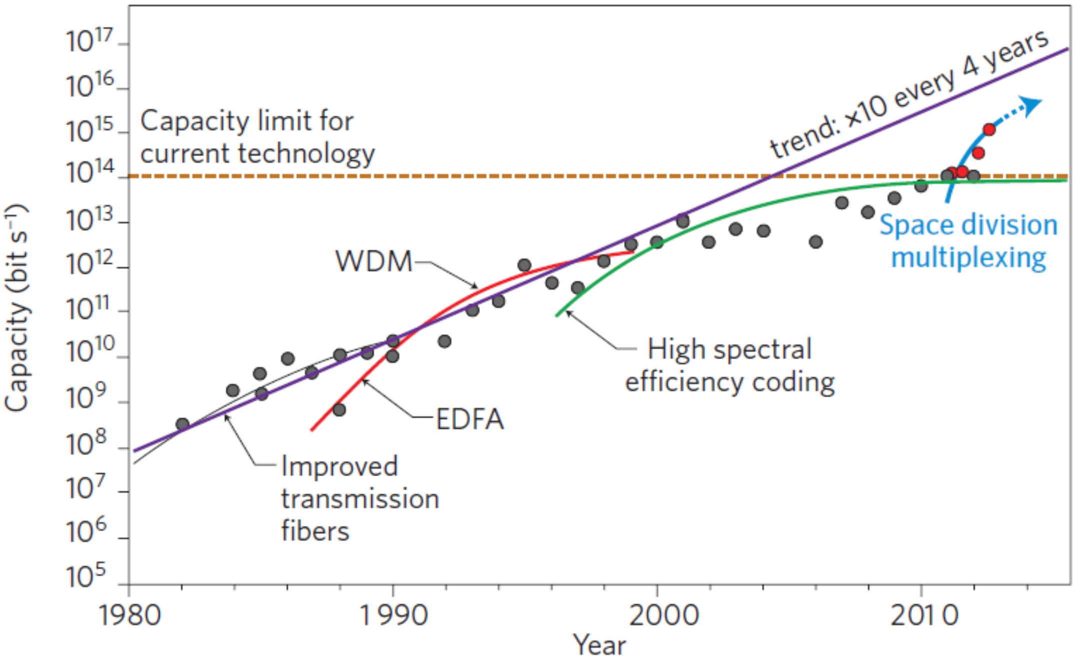

Figure 4: In the figure it is plotted the transmission capacity of the optical fibres as reported, from the 1982 to the present, by the annual Optical Fiber Communications Conference. The trend is approximately described by a ten-fold increment every four years [4]. However, due to fundamental physical limitations of the transmission via optical fibre, the data traffic is approaching the so-called ”optical crunch”, a saturation of the communication networks.

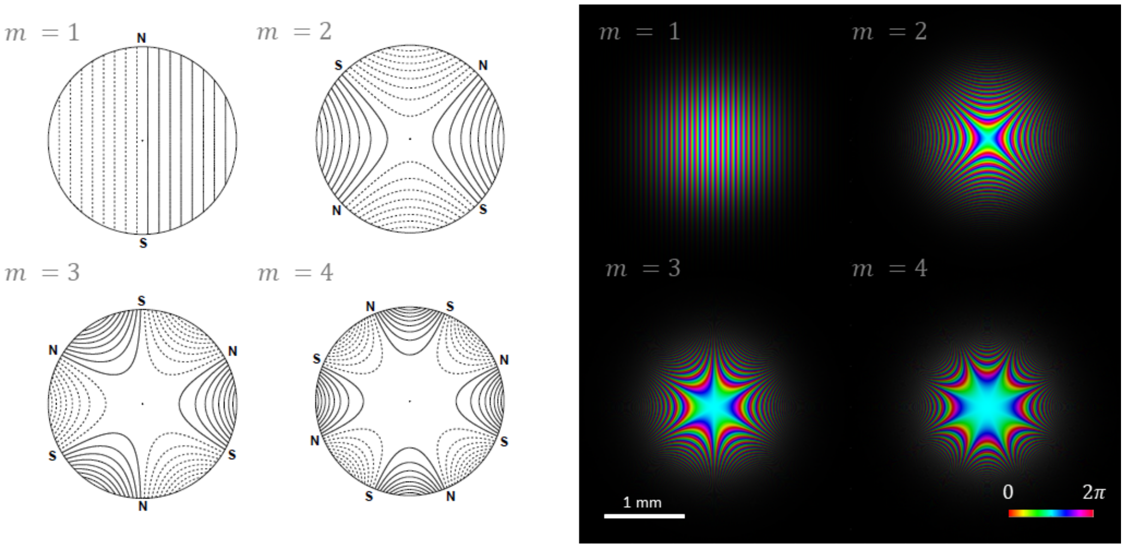

Figure 5: On the left, magnetic field lines for four cases of number of pole-pairs: $m = 1$, 2, 3 and 4, are reported. The solid and dotted lines are positive and negative values of the vector potential, respectively [7]. On the right, simulations of multipole-phase beams for the same values of the phase order $m = 1$, 2, 3 and 4, are shown. Brightness and colours refer to intensity and phase, respectively.

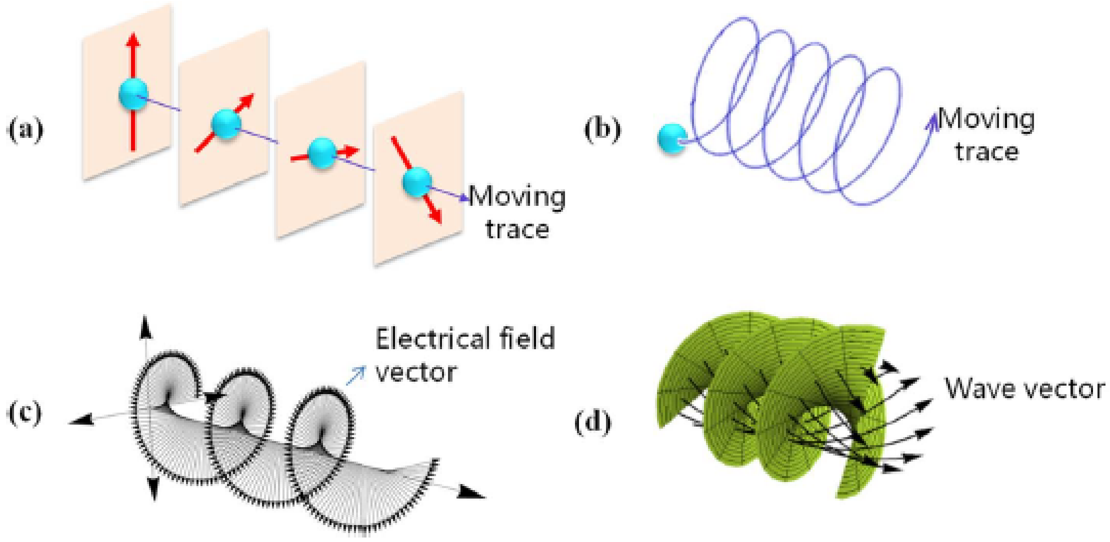

Figure 6: Two cases of angular momenta: (a) a spinning body carrying spin angular momentum (SAM), (b) an orbiting body carrying orbital angular momentum (OAM), (c) a circularly polarized light field carrying SAM, (d) and the phase structure of an OAM beam [31].

quantity. Therefore, the SAM beams add a two-dimensional degree of freedom to the space division multiplexing, as mentioned above (polarization division multiplexing). However, if the helical structure is generated by a precession of the wave vector, instead a rotation of the electric field, we obtain an OAM beam, which is characterized by a phase function, defined on the plane transversal to the propagation direction, which is $\exp\{il\theta\}$, where θ is the azimuthal coordinate and l is an integer referring to the number of intertwined helices (i.e., the 2π phase shifts along the circle around the propagation axes). Since l is an integer number, it can be a negative, positive, or even a zero value, corresponding to counterclockwise or clockwise phase helices or a Gaussian beam (i.e., no helix structure), respectively [8]. The advantage with respect to the SAM beams is that l, which represents the OAM in units of the reduced Plank's constant $\hbar$ [11, 12], can assume infinite values, providing an alphabet in the SDM limited only by technology constraints. Many important progresses have been achieved in the detection and generation [13–24], manipulation [25–27], and propagation [28–30], of the OAM-beams as astigmatic-mode conversion, spiral phase plates and q-plates, multiplane light conversion, integrated photonics, and conformal transformations. Among all, conformal transformations represent the most efficient, compact, and versatile way for the spatial manipulation of a wavefield. In a more general approach to conformal mappings, we demonstrate how a new framework can be developed where harmonic phases are used to encode, transmit, and process distinct spatial configurations of the electromagnetic field.
However, despite all that progress, OAM beams present a central phase singularity, as can be seen from the figure 7, which represents a still open issue since the relative dark zone will expand during a free space propagation, reducing the efficiency of OAM beams for long distance transmissions.

The multipole-phase beams, otherwise, are characterized by the absence of singularities in their phase structure, as can be seen from the simulations on the right of figure 5. Moreover, they provide two continuous degrees of freedom, which can be controlled and measured in an efficient and practical way via conformal transformations. For this reason, we expect that the new paradigm, encompassed in this work, will find widespread applications in the space division multiplexing of the electromagnetic fields. In this thesis, however, we focalized on the telecommunication field, in particular on the above-mentioned free-space optical communication systems (FSO) where the SDM [32] relies on the structuring of the phase distribution of electromagnetic fields over a set of non-interfering spatial configurations, each of them acting as a separated information channel with the same frequency as the others. As already anticipated, the SDM can be used in combination with the usual modulation formats [33, 34], offering a solution for different problems as the network saturation [35–37] or the necessity of wider alphabets in the quantum applications [38], as in the cryptography systems [39, 40]. Moreover, others important fields, in which the spatial division multiplexing is used, are the micromanipulation [41, 42], the

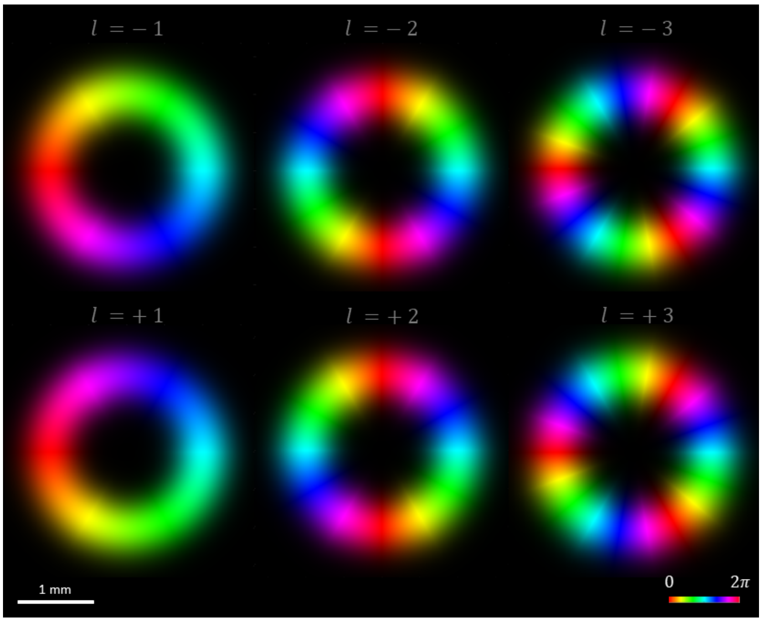

Figure 7: Simulations of six OAM beams, of wavelength $\lambda = 1310.0\,\mathrm{nm}$ and waist $w_0 = 0.5\,\mathrm{mm}$, carrying an orbital angular momentum $l = \{\pm1; \pm2; \pm3\}$. Brightness and colours refer to intensity and phase, respectively. Notice how, incrementing l, the number of completed 2π-phase periods increases (each colour corresponds to a different value of the phase). Moreover, changing the sign of l, the colours' sequence is reversed, due to a different rotation of the phase helices of the beam.

imaging and microscopy applications [43–45], besides the already anticipated communication systems [4, 46]. All these scenarios require the manipulation of beams which are orthogonal to each others and the design of two specific devices performing the superposition of such beams, at the transmitter stage, and the sorting of the received ones, as reported in figure 8. These two devices are called *multiplexer* and *demultiplexer*, respectively.

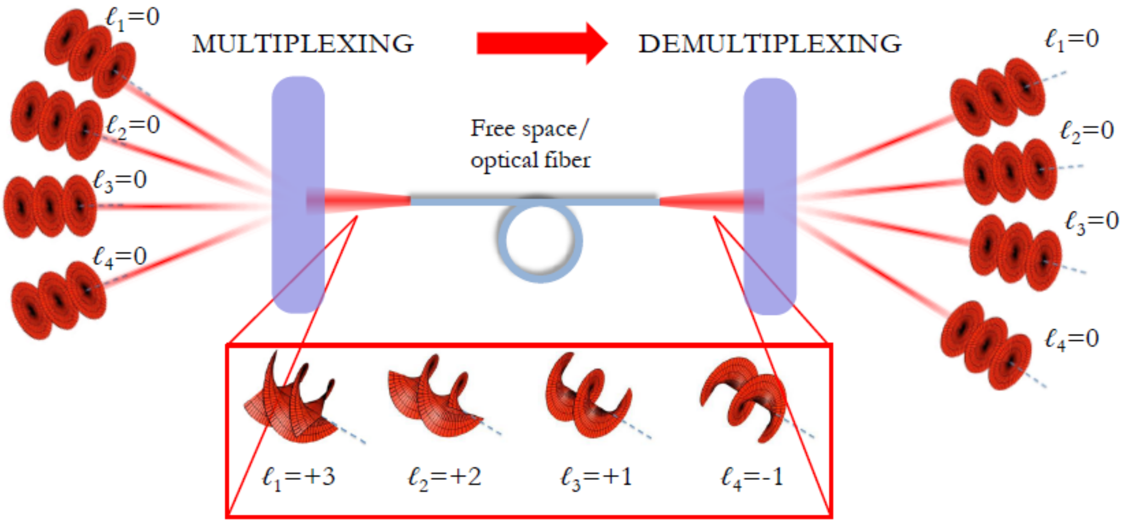

Figure 8: Four distinct Gaussian beams ($l_{1,2,3,4} = 0$) are multiplexed into a set of orthogonal OAM beams with different values of l. The superposition of these beams are, then, transmitted to the receiver stage, where they are sorted and transformed back to Gaussian light spots spatially separated.

As we will see, the free space propagation between the two stages can be mathematically described in terms of Fourier transformations [47], which guarantees a strategy in order to analyse the evolution of the phase and intensity patterns from the generation of the beam, up to its detection. Moreover, in a ray light picture, each point of the initial electromagnetic field, undergoes the coordinates' transformation which projects this initial point onto a specific position of the detected field. As will be shown, under reasonable assumptions of analyticity, the phase pattern of the wavefront will be found as a harmonic function. Indeed, in order to transmit correctly the information contained into the phase structure of the propagated beam, the angles of the phase pattern must be preserved. This means, as we will see, that the above-mentioned transformation of the coordinates is a conformal mapping, and the phase structure of the field will be given by a two-dimensional Laplace's equation [48]. Moreover, it will be found that the phase term of the OAM beams is a particular solution, independent of the radial coordinate, of the Laplace's equation. The OAM beams are, indeed, a particular case in the framework of the multipole-phase beams. However, as anticipated, their central phase singularity still represents a critical issue in the long-distance free-space propagation [24, 49–52]. For this reason, in the presented work it will be considered the general solution of the Laplace's equation for the phase of an electromagnetic field, discovering a new family of beams: the above-mentioned multipole-phase beams. In particular, these general phase solutions are able to implement the mapping of multipole-phase beams into linear momentum states (and vice versa), which can be easily sorted with a Fourier lens, showing an efficient method in order to multiplex and demultiplex this new family of beams with only two optical devices, the so-called *Transformer* and *Phase Corrector*. The first element, indeed, unwraps the multipole-phase structure into a linear phase gradient, corresponding to its related linear momentum state. The second optical element, instead, corrects the phase distortions introduced in the propagation between the two elements, and incorporates the Fourier lens, for the sorting of the beam into an isolated light spot, whose coordinates are related to the momentum state. In this way, an initial set of multipole-phase beam (each of them corresponding to a different communication channel) is easily demultiplexed into distinct light spots placed at different positions. In the reverse process, with the same two optical elements in the inverse order, an initial set of light beams can be multiplexed into a superposition of multipole-phase beams, and propagated as a unique electromagnetic field without the interference of the single channels. Therefore, it is easily to understand how, this work, considers a new more general approach to the SDM, called *multipole-phase division multiplexing* (MPDM), expected to be a starter point for promising applications in the free-space transmission in the whole range of wavelengths: from the optical, up to the radio and microwave fields. In particular, the work of this thesis will be structured as it follows.

1.1 A brief introduction to the contents of this work

After this initial introduction, in the **chapter 2**, we will see how the free space propagation of a general electromagnetic field can be simulated in a MatLab environment without the generation of artefacts and distortions. In particular, it will be shown how two regimes have to be introduced: the *short distance* and the *long distance* regimes. Indeed, the Fourier Transform that, as anticipated, allows us to mathematically describe the propagation in free space, has to be computed in two different ways, depending on the propagation distance considered. We will see that this corresponds to satisfy the *Nyquist-Shannon sampling theorem*. Taking into account these considerations, a MatLab macro for the free-space propagation of an electromagnetic field will be defined and discussed. In the next **chapter 3**, it will be given a theoretical description of the multipole-phase beams, showing in particular how their phase structure arises from the general solution of the two-dimensional Laplace's equation, and depends on two parameters, called *phase strength* and *phase orientation*, which represent the intensity and the orientation of the phase pattern of the wavefront, respectively. Moreover, we will see how the multipole-phase beams can be divided into different families depending on the *phase order*, m, which is related to the number of poles of the phase structure of these beams (see figure 5). In the same chapter, the evolution of multipole-phase beams during a free space propagation will be described, and it will be reported a criterion that must be adopted to avoid phase distortions during the propagation. Moreover, it will be introduced how we can act on the phase, thanks to conformal mappings of the coordinates on the propagation planes, in order to unlock new strategies in the SDM. With these notions, in the **chapter 4**, we will finally be able to understand how to simulate the sorting of a superposition of multipole-phase beams into different and isolated light spots, acting as independent channels of information. It will be shown that the demultiplexing of multipole-phase beams can be achieved with an anti-holomorphic conformal mapping described by a *circular-*

sector transformation, which converts a multipole-phase structure into a linear phase gradient, that can be sorted by a Fourier lens. As anticipated, this transformation can be performed with two optical elements: the Transformer and the Phase Corrector. Moreover, in the **chapter 5**, will be described how, inverting the two previous optical elements, we can produce the reverse process, i.e., as an initial configuration of light beams can be manipulated in order to generate a set of multipole-phase beams, which can be transmitted as a unique electromagnetic field without loss of information.

Then, in the **chapter 6** it will be introduced the concept of the *Cross-Talk* as an estimation of the ability of a telecommunication system to distinguish different channels at the receiver stage. It will be analysed, in particular, how we can integrate the Cross-Talk computation in a MatLab simulation and how to interpret the relative results. In this way, in the **chapter 7**, a demultiplexing device will be design in order to maximize the number of distinct channels that can be transmitted without an excessive interference between them, showing a way to increase the capacity and the efficiency of the free-space communication system. In this way, as described in the **chapter 8**, it will be analysed the whole multiplexing, transmission and demultiplexing process for multipole-phase beams in an optimized device. Thanks to that, it will be possible to describe the evolution of wavefields along an entire communication link using this new type of structured light. The analysis will turn out the potentialities of the beams with a multipole-phase structure, showing, in particular, their versatility and the ease of implementation in the telecommunication field. Moreover, in the **chapter 9**, it will be described as the demultiplexer stage of a such device can be adapted to an experimental setup and tested in an optical laboratory, putting the focus on the limitation due to the sizes of the experimental tools. The scheme of an optical bench for optical tests will be outlined and described for future experimental analyses in the laboratory. Then, in the chapter 10, a possible strategy in the fabrication of the optical elements, necessary in order to work with the multipole-phase beams, will be introduced. In particular, the recent developed *metasurfaces* with anisotropic *metaelements* will be considered. Finally, a conclusion on the role of the multipole-phase beams in the scenario of the free-space optical communication systems is given in the last chapter.

2 Free space propagation

Before considering the demultiplexing and the multiplexing of a set of multipole-phase beams, we need to know the theory necessary to simulate the free space propagation of an electromagnetic field. In particular, two different, but complementary methods will be discussed: the Fresnel Transfer Function (TF) propagation method and the Fresnel Impulse Response (IR) method.
Moreover, at the end of the chapter, it will be shown how a converging lens can be used in order to practically perform the Fourier Transform of an electromagnetic field. This will be necessary in the multiplexing and demultiplexing techniques described in the following chapters, and it will be reported here as a natural consequence of the theory of the free space propagation of electromagnetic fields.

2.1 The Fresnel-Kirchhoff integral

We know that an electromagnetic field is described by two vector fields related to each other: the electric field $\boldsymbol{E}(\boldsymbol{r},t)$ and the magnetic field $\boldsymbol{H}(\boldsymbol{r},t)$, which are functions of position and time and satisfy the Maxwell's equations. In the vacuum, in the absence of charges and currents, the Maxwell's equations are the following:

$$\boldsymbol{\nabla}\times\boldsymbol{H}=\epsilon_0\tfrac{\partial\boldsymbol{E}}{\partial t} \tag{1}$$
$$\boldsymbol{\nabla}\times\boldsymbol{E}=-\mu_0\tfrac{\partial\boldsymbol{H}}{\partial t} \tag{2}$$
$$\boldsymbol{\nabla}\cdot\boldsymbol{H}=0 \tag{3}$$
$$\boldsymbol{\nabla}\cdot\boldsymbol{E}=0 \tag{4}$$

where $\epsilon_0 = 8.85\times10^{-12}\frac{\mathrm{C}^2}{\mathrm{m}^2\mathrm{N}}$ and $\mu_0 = 4\,\pi\,\times10^{-7}\frac{N}{A^2}$ are the *electric permittivity* and the *magnetic permeability* of vacuum, respectively.
Applying the curl to the second equation, we get

$$\boldsymbol{\nabla}\times\boldsymbol{\nabla}\times\boldsymbol{E}=-\mu_0\boldsymbol{\nabla}\times\frac{\partial\boldsymbol{H}}{\partial t} \tag{5}$$

Now, remembering that $\boldsymbol{\nabla}\times\boldsymbol{\nabla}\times\boldsymbol{E}=\nabla(\boldsymbol{\nabla}\cdot\boldsymbol{E})-\nabla^2\boldsymbol{E}$, and using the fourth and first equation, we obtain

$$\nabla^2\boldsymbol{E}-\frac{1}{c_0^2}\frac{\partial^2 E}{\partial t^2}=0 \tag{6}$$

where $c_0=\frac{1}{\sqrt{\epsilon_0\mu_0}}=3\times10^8\mathrm{ms}^{-1}$, is the *speed of light in vacuum.* The equation 6 is called *wave equation*, and its simplest solution is the monochromatic wave

$$u(\boldsymbol{r},t)=a(\boldsymbol{r})\cos\left[\phi(\boldsymbol{r})-\omega t\right] \tag{7}$$

where $a(\boldsymbol{r})$ is the amplitude of the wave, $\phi(\boldsymbol{r})$ its initial phase, and $w=2\pi f$ where f is the frequency of the wave. For simplicity, we can rewrite this field as the real part of the complex amplitude $U(\boldsymbol{r},t)$:

$$u(\boldsymbol{r},t)=\mathrm{Re}\{U(\boldsymbol{r},t)\} \tag{8}$$

where $U(\boldsymbol{r},t)$ is defined as

$$U(\boldsymbol{r},t)=a(\boldsymbol{r})e^{i(\phi(\boldsymbol{r})-\omega t)} \tag{9}$$

Now, substituting the equation 9 in the wave equation 6, we obtain the so-called *Helmholtz equation*

$$\nabla^2U+k^2U=0 \tag{10}$$

where $k:=\frac{\omega}{c}=\frac{2\pi}{c}=\frac{2\pi}{\lambda}$ is the *wave number*, i.e. the modulus of the wave vector $\boldsymbol{k}$, whose direction is the

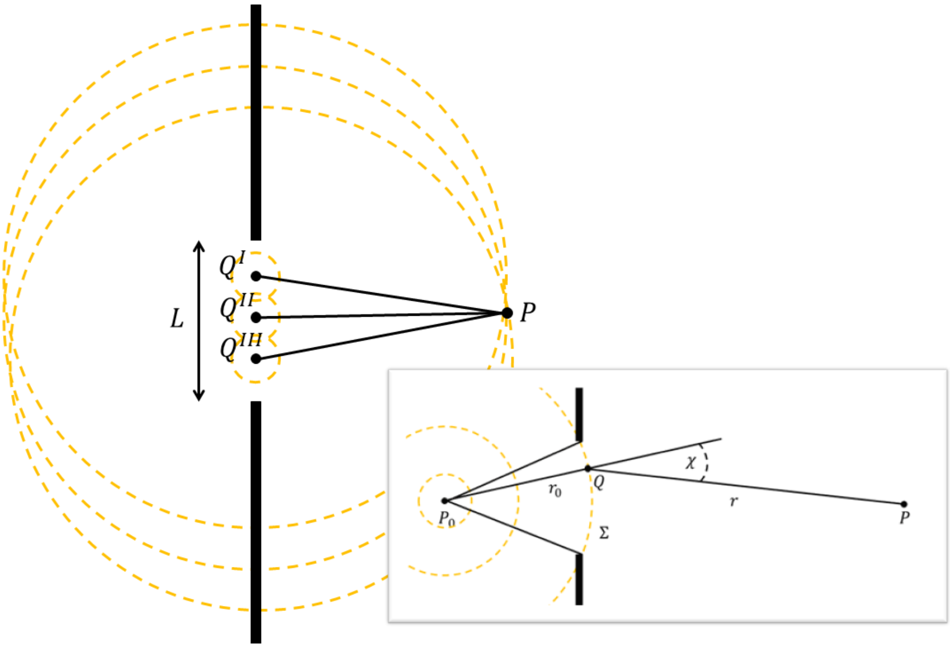

Figure 9: Schematization of the Fresnel-Huygens principle for an aperture of size L and area Σ. An initial spherical wave (plotted in yellow, in the figure) is generated in the point P_0, at the distance r_0 from the screen. Reaching the aperture, a series of secondary spherical wave are generated (points $Q^{I,II,III}$ of the wavefront of the source field) and propagated for a distance $r \gg L$. The final field is evaluated in the point P.

propagation one.

A simple solution, in spherical coordinates, of the Helmholtz equation 10, is the *spherical wave*, characterized by a complex amplitude that depends only on the modulus of the radial coordinate

$$U(r) = \frac{U_0}{r} e^{ikr} \tag{11}$$

where r is the distance from the source of the wave, and U_0 a constant defining the total energy carried by the wave. The spherical waves hold an important role in the propagation and diffraction of the electromagnetic fields. Indeed, according to the *Huygens principle*, every point which a luminous disturbance reaches becomes a source of a spherical wave itself; the superposition of these secondary wavelets determines the wavefront at any subsequent time. Moreover, Fresnel showed that this principle, together with his own principle about the light interferences, could explain both the rectilinear propagation and the diffraction of the light. From a mathematical point of view, the *Huygens-Fresnel's principle* states that the electromagnetic field, $U(P)$, at a point P is given by the integration over the spherical waves (given by the equation 11) propagating from a surface Σ and reaching that point P

$$U(P) = U_0 \iint_{\Sigma} \frac{e^{ikr}}{r} K(\chi)\, d\Sigma \tag{12}$$

where $K(\chi)$, reported in equation 13, is a mathematical correction of the diffraction integral 12 in order to explain the experimental results, and it is called *obliquity factor* [53]

$$K(\chi) = \frac{1}{2i\lambda}\,(1 + \cos\chi) \tag{13}$$

As reported in figure 9, we can imagine the situation as a spherical wave, with its source in P_0, impinging an aperture whose linear size L is very small compared with the distance r from a general point Q, of the wavefront at the screen, to the point P. In this scenario, Σ is the area of the wavefront at the aperture.

In our hypothesis of $L \ll r$, $K(\chi)$ will not vary appreciably over the aperture, and the following approximation can be assumed:

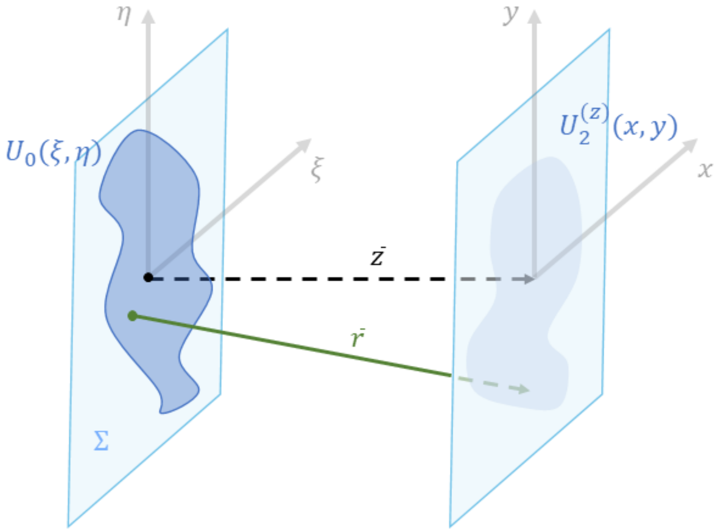

Figure 10: Free space propagation along z-axis of an initial electromagnetic field reaching the aperture of area Σ on the plane (ξ, η). The final field is detected on the plane (x, y) at the distance z.

$$\cos(\chi) \approx 1 \tag{14}$$

and the integral 12 becomes

$$U(P) = \frac{U_0}{i\lambda} \iint_{\Sigma} \frac{e^{ikr}}{r} \, d\Sigma \tag{15}$$

At this point, we can generalize the integral 15, taking the screen with an arbitrary aperture of transmission function $A(\xi, \eta)$, and assuming the generating electromagnetic field

$$U_1(\xi, \eta) = \frac{U_0(\xi, \eta)}{r} e^{ikr} \tag{16}$$

characterized by the generic amplitude $U_0(\xi, \eta)$ impinging on the screen.
In this way, in agreement with the equation 15, the transmitted field $U_2^{(z)}(x, y)$, at the distance z along the propagation direction, will be

$$U_2^{(z)}(x, y) = \frac{1}{i\lambda} \iint_{\Sigma} U_0(\xi, \eta) A(\xi, \eta) \frac{e^{ikr}}{r} \, d\xi d\eta \tag{17}$$

where r is the distance between two points of the wavefront, before and after the field propagation of a length z, i.e., the distance between two points on the initial and final planes, where (ξ, η) and (x, y) are the respectively Cartesian coordinates systems (see figure 10).

$$r = \sqrt{z^2 + (x - \xi)^2 + (y - \eta)^2} \tag{18}$$

The equation 17 is called *Fresnel-Kirchhoff integral*, and it is the starting point of our strategy in order to simulate the free-space propagation of an electromagnetic field.

2.2 Fresnel Transfer Function (TF) propagation

In equation 18 we can collect z, obtaining

$$r = z\sqrt{1 + \left(\frac{x - \xi}{z}\right)^2 + \left(\frac{y - \eta}{z}\right)^2} \tag{19}$$

It is important to notice that the square root of this equation makes the calculation of the Fresnel integral 17 very laborious. For this reason, a more convenient scalar diffraction form is obtained expanding in series the square root and taking the first terms

$$r \approx z + \frac{(x-\xi)^2}{2z} + \frac{(y-\eta)^2}{2z} \tag{20}$$

We remember, indeed, that we have chosen the aperture with a linear size very small compared with the propagation distance z, justifying the previous expansion, called *paraxial approximation.*
Now, assuming $r \approx z$ in the denominator of the equation 17, and performing the powers in equation 20, we obtain the following expression of the Fresnel integral

$$U_2^{(z)}(x,y) = \frac{e^{ikz}}{i\lambda z} e^{i\frac{k}{2z}(x^2+y^2)} \iint_\Sigma A^*(\xi,\eta) e^{i\frac{k}{2z}(\xi^2+\eta^2)} e^{-i\frac{k}{z}(x\xi+y\eta)}\, d\xi d\eta \tag{21}$$

That we can rewrite as

$$U_2^{(z)}(x,y) = \iint_\Sigma A^*(\xi,\eta) h(x-\xi, y-\eta)\, d\xi d\eta \tag{22}$$

where we have made the position

$$A^*(\xi,\eta) := A(\xi,\eta) U_0(\xi,\eta) \tag{23}$$

and introduced the *impulse response function* of the free-space

$$h(x,y) := \frac{e^{ikz}}{i\lambda z} e^{i\frac{k}{2z}(x^2+y^2)} \tag{24}$$

From the equation 22, it is easy to see that the Fresnel integral has a convolution nature and can be rewritten as

$$U_2^{(z)} = A^* * h \tag{25}$$

Taking the Fourier Transform of both sides of the Fresnel integral 25, we have

$$\mathcal{F}\{U_2^{(z)}(x,y)\} = \mathcal{F}\{A^* * h(x,y)\} = \mathcal{F}\{A^*(\xi,\eta)\} \cdot H(f_x, f_y) \tag{26}$$

where we used the convolution property of the Fourier Transform, and denoting with $H(f_x, f_y)$ the transfer function, which is the Fourier Transform of the impulse response function: $H(f_x, f_y) = \mathcal{F}\{h(x,y)\}$. Taking now the Fourier Antitransform, we finally obtain the detected field

$$U_2^{(z)}(x,y) = \mathcal{F}^{-1}\{\mathcal{F}\{A^*(\xi,\eta)\} \cdot H(f_x, f_y)\} \tag{27}$$

Notice now, that in our case of a free-space propagation, we don't have an aperture and A^* is simply the amplitude of our initial field $U_0(\xi,\eta)$. Therefore, in order to obtain the final field $U_2^{(z)}(x,y)$, we only need to know the amplitude structure of the initial field, U_0, and the transfer function $H(x,y)$. Considering now the equation 24 and remembering that

$$\mathcal{F}\left\{exp\left[-i\pi\left(\frac{x^2}{a^2}+\frac{y^2}{b^2}\right)\right]\right\} = i|ab| \exp\left[-i\pi(a^2 f_x^2 + b^2 f_y^2)\right] \tag{28}$$

where in this case $a = b = \sqrt{-\lambda z}$, we obtain the following transfer function:

$$H(f_x, f_y) = e^{ikz} \exp\left[-i\pi\lambda z(f_x^2 + f_x^2)\right] \tag{29}$$

At this point, we have the all information necessary, and it is possible to determine U_2.

Far field approximation It is worth noting from the Fresnel integral 21, that in a far field approximation, where the two exponential terms are negligible $exp\left[i\frac{k}{2z}(\xi^2+\eta^2)\right] \approx exp\left[i\frac{k}{2z}(x^2+y^2)\right] \approx 1$, the Fresnel integral 21 becomes:

$$U_2^{(z)}(x,y) = \frac{e^{ikz}}{i\lambda z}\iint_\Sigma A^*(\xi,\eta)e^{-i\frac{k}{z}(x\xi+y\eta)}\,d\xi d\eta \tag{30}$$

Therefore, remembering that the Fourier Transform of a function of two variables is

$$\mathcal{F}\{g(x,y)\} = \iint g(x,y)e^{-i2\pi(xf_x+yf_y)}\,dxdy \tag{31}$$

where, in this case, $f_x = \frac{\xi}{\lambda z}$ and $f_y = \frac{\eta}{\lambda z}$ (which are actually spatial frequencies since λ, ξ, η and z are distances), the integral 30, except for the phase term, $\exp[ikz]$, is the Fourier Transform of the two-variables function $A^*(\xi,\eta)$.

2.2.1 Space discretization

As the first thing, we have to discretize (as represented in figure 11) the two-variables analytic function which describes the source field

$$U_1(x,y) \rightarrow U_1(m\Delta_x, n\Delta_y) \tag{32}$$

where Δ_x, Δ_y are the sampling intervals along the x-axis and y-axis respectively, while m, n are two integer indexes such that

$$m = -\frac{M}{2},\ldots,\frac{M}{2}-1 \qquad n = -\frac{N}{2},\ldots,\frac{N}{2}-1 \tag{33}$$

with M, N integer numbers. In this way the source plane is composed of $M \times N$ samples which fill it completely

$$L_x = M\Delta_x \qquad L_y = N\Delta_y \tag{34}$$

For simplicity, we assume $L_x = L_y := L$ and the same sampling interval $\Delta_x = \Delta_y$. In this way the coordinates along the x-axis (analogue along y-axis) are:

$$x \rightarrow \left[-\frac{L}{2} : \Delta_x : \frac{L}{2} - \Delta_x\right] \tag{35}$$

With this discretization we are finally enabled to create a mesh grid $[X,Y]$ of the source plane and define the initial field $U_1(X,Y)$. In the following, for example, it is reported the MatLab code of a Gaussian beam of waist $w_0 = 2\,\text{mm}$ defined on a plane of side $L = 10\,\text{mm}$ sampled with $M = 2000$.

Listing 2.2.1: space discretization

```
L            = 10;                   % plane side [mm]
M            = 2000;                 % plane num. of samples
dx           = L/M;                  % sample interval
x            = -L/2 : dx : L/2-dx;   % x coords
y            = x;                    % y coords
[X,Y]        = meshgrid(x,y);        % cartesian coords
[theta, r]   = cart2pol(X,Y);        % polar coords
w0           = 2.0;                  % beam waist [mm]
U1           = exp(-(r/w0).^2);      % gaussian beam
```

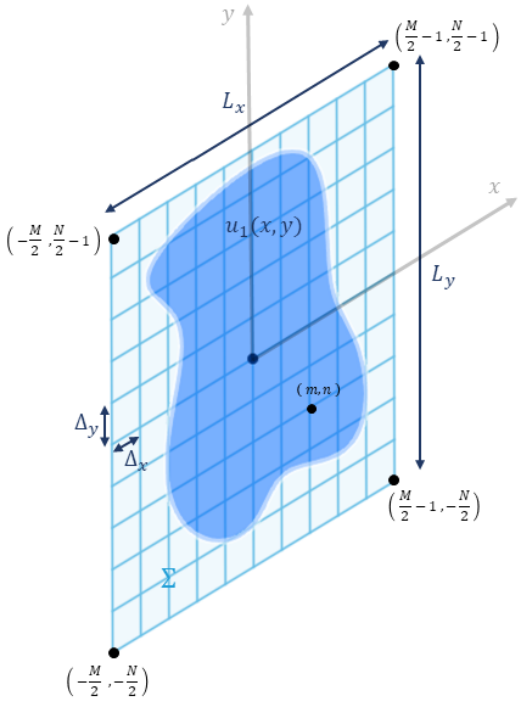

Figure 11: Space discretization of the wavefront of an electromagnetic field, $u_1(x,y)$ (dark blue region), into M and N samples along the x-axis, and y-axis, respectively. The sampling intervals are $\Delta_x = \frac{L_x}{M}$ and $\Delta_y = \frac{L_y}{N}$, where L_x and L_y are the sides of the propagation plane along the two axes.

2.2.2 Frequency discretization

Now, before to perform the Fourier Transform, we have to define the domain of the frequencies. Conventionally, the continuous space of the frequencies is sampled in the same $M \times N$ samples of the real space:

$$\begin{aligned} f_x \to p\Delta_{f_x} &= \frac{p}{M\Delta_x} = \frac{p}{L_x} \qquad p = -\frac{M}{2}, \dots, \frac{M}{2} - 1 \\ f_y \to q\Delta_{f_y} &= \frac{q}{N\Delta_y} = \frac{q}{L_y} \qquad q = -\frac{N}{2}, \dots, \frac{N}{2} - 1 \end{aligned} \tag{36}$$

And under the same hypothesis of $M = N$ and $L_x = L_y := L$, we get the following discretization (analogue for f_y):

$$f_x \to \left[-\frac{1}{2\Delta_x} : \frac{1}{L} : \frac{1}{2\Delta_x} - \frac{1}{L} \right] \tag{37}$$

In the following it is reported the MatLab code for this discretization of the frequencies and the generation of a mesh grid, as we have seen in the spatial case. We assumed $f_x = f_y$ as a consequence of the above positions.

Listing 2.2.2: frequency discretization

```
    fx       = -1/(2*dx) : 1/L : 1/(2*dx)-1/L;    % frequation coords
    [FX,FY]  = meshgrid(fx,fx);                   % frequation space mesh
```

2.2.3 Computing of the transfer function

At this point, after the generation of the mesh in the frequency space, $[F_X, F_Y]$, we can determine the transfer function for each point thanks to the equation 29:

$$H = \exp\left\{-j\pi\lambda z \left(F_X^2 + F_Y^2\right)\right\} \tag{38}$$

where we have ignored the factor, e^{jkz}, since it doesn't change the structure of the wavefront in the x-y plane. The MatLab instructions of this step are reported in the code below.

Listing 2.2.3: transfer function

```
    H = exp(-1i*pi*lambda*z*(FX.^2+FY.^2));      % transf. function
```

2.2.4 Fourier Transform

Now we are able to compute the final field, $U_2(X,Y)$, after a free space propagation of a distance z, thanks to the equation 27, just multiplying the Fourier Transform of $U_1(X,Y)$ with the transfer function $H(F_X,F_Y)$ and anti-transforming the result.

$$U_2(X,Y) = \mathcal{F}^{-1}\{\mathcal{F}\{U_1(X,Y)\}H\left(F_X,F_Y\right)\} \tag{39}$$

However, the indexes m,n are both positive and negative values, while in a MatLab vector the indexes are only positive. For this reason a shift has been made, as reported in figure 12, and only then the Fourier Transform of $U_1(X,Y)$ has been done. In the same way, $H(F_X,F_Y)$ is shifted and, after the product and the anti-transformation, the result is re-shifted to the initial coordinates as reported in the following listing

Listing 2.2.4: TF propagation

```
    H   = fftshift(H);                % shift of H
    FU1 = fft2(fftshift(U1));         % Fourier transf. of shifted u1
    FU2 = H.*FU1;                     % final field in frequation domain
    U2 = ifftshift(ifft2(FU2));       % anti-transf. of re-shifted U2
```

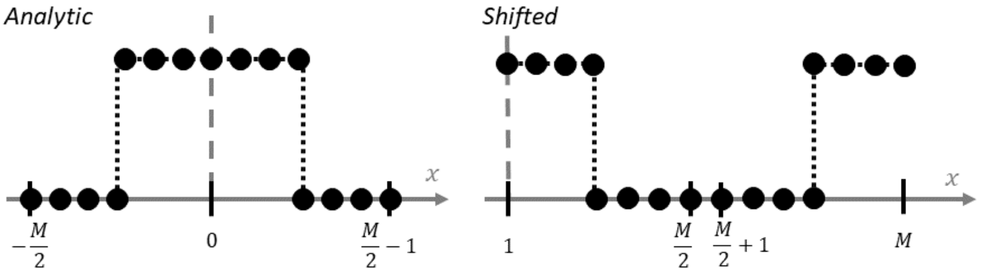

Figure 12: Shift of the sampling along the x-axis necessary in order to have a range of only positive values as the index of a MatLab vector, in order to perform the Fourier Transform. The same shift is performed also for the y-axis.

2.3 Fresnel Impulse Response (IR) propagation

It is easy to see that the equation 27 is analytically equivalent to the following one:

$$U_2(x,y) = \mathcal{F}^{-1}\{\mathcal{F}\{U_1(x,y)\}\mathcal{F}\{h\left(x,y\right)\}\} \tag{40}$$

where we didn't use directly the equation 29 of the transfer function $H(F_X,F_Y)$ but, this is computed as the Fourier Transform of the impulse response function $h(x,y)$ expressed in equation 24, using the discretization (equation 35) as seen in the TF propagation method.
The following steps are the same of the previous method, and the corresponding MatLab code is reported in the following.

Listing 2.3.1: IR propagation

```
x         = -L/2  :  dx  :  L/2-dx;
[X,Y]     = meshgrid(x,x);
h         = 1/(1i*lambda*z)*exp(1i*k/(2*z)*(X.^2+Y.^2));
H         = fft2(fftshift(h))*dx^2;
FU1         = fft2(fftshift(U1));
FU2        = H.*FU1;
U2        = ifftshift(ifft2(FU2));
```

2.4 TF or IR criteria of propagation

The two methods seen, TF and IR, are analytically equivalent, but they can give different results if applied to discretized fields. Indeed, we will see that, in order to avoid artefacts, the two approaches work in different limits of the propagation distance for a fix sampling of the simulated field. In particular, the TF method will be used in the *short distance regime*, while the IR method works better in the *long distance regime*.

2.4.1 Propagation limit for the Transfer Function method

The transfer function (equation 29) has the phase that is a function of the square of the frequencies

$$\phi_H(f_x, f_y) = -\pi\lambda z \left(f_x^2 + f_y^2\right) \tag{41}$$

This expression is called *chirp* function, whose absolute value increases with the square of the frequency variables, and its propagation simulation can be problematic due to the increasing slope of the phase with frequency [54]. Now, due to the orthogonality of the two frequency variables f_x and f_y, we can analyse the chirp function only in one direction (the x-axis for instance). For a constant sampling interval, Δ_{f_x}, along this axis, the phase is described uniquely only in a range of 2π, therefore the variation of its module must be less than π

$$\Delta_{f_x} \left|\frac{\partial \phi_H}{\partial f_x}\right|_{max} \leq \pi \tag{42}$$

and resolving the derivative we get

$$\Delta_{f_x} \leq \frac{1}{2\lambda z\,|f_x|_{max}} \tag{43}$$

Remembering now the frequency discretization (equation 37) we have

$$|f_x|_{max} = \left|-\frac{1}{2\Delta_x}\right| \qquad \Delta_{f_x} = \frac{1}{L} \tag{44}$$

Substituting in the previous equation, we finally have the working condition of the TF propagation method:

$$z \leq \frac{\Delta_x L}{\lambda} \tag{45}$$

Now we want to show that the equation 45 it is nothing but the *Shannon–Nyquist sampling theorem*, which tell us that: when the spectral content of a signal is limited to a finite range of frequencies, a continuous function can be recovered correctly from the samples if the sample interval is smaller than

$$\Delta_x \leq \frac{1}{2B_X} \tag{46}$$

where B_X is the bandwidth of the spectrum of the continuous function along the x-axis [55]. Rearranging this expression, and taking the limit condition, we get the *Nyquist frequency*

$$f_{NX} = \frac{1}{2\Delta_x} \tag{47}$$

which is, precisely, the maximum frequency expressed in the equation 44, telling us that we are using the correct bandwidth for our samplings.

2.4.2 Propagation limit for the Impulse Response method

In this case, from the impulse response function (equation 24) we have a phase pattern in the propagation plane expressed by the following equation:

$$\phi_h(x,y) = \frac{k}{2z}\left(x^2 + y^2\right) \tag{48}$$

Similarly to before, the variation of the phase module must be

$$\Delta_x \left|\frac{\partial \phi_h}{\partial x}\right|_{max} \leq \pi \tag{49}$$

and performing the derivative, we obtain

$$\Delta_x \frac{k}{z} |x|_{max} \leq \pi \tag{50}$$

where $k = \frac{2\pi}{\lambda}$ and, from the space discretization (equation 35), $|x|_{max} = \frac{L}{2}$. Substituting in the previous equation, we have the working condition of the IR propagation method:

$$z \geq \frac{\Delta_x L}{\lambda} \tag{51}$$

As we can see, the two regimes (equation 45 and equation 51) are complementary, and it will be used one method rather than the other in function of the distance, z, of the observation plane from the source one (both of side L and sampling interval Δ_x) for a certain field of wavelength λ.
In the code below, it is reported the complete MatLab function used for the free space propagation.

Listing 2.4.1: free space propagation MatLab macro

```
function[u2] = FreeSpaceProp(u1, L, lambda, z);

    [M,N]     = size(u1);
    dx        = L/M;
    k         = 2*pi/lambda;

    % prop. TF (short distance regime)
    if z <= dx*L/lambda
        fx        = -1/(2*dx) : 1/L : 1/(2*dx)-1/L;
        [FX,FY]   = meshgrid(fx,fx);
        H         = exp(-1i*pi*lambda*z*(FX.^2+FY.^2));
        H         = fftshift(H);
        FU1         = fft2(fftshift(U1));
        FU2         = H.*FU1;
        U2        = ifftshift(ifft2(FU2));
    end

    % prop. IR (long distance regime)
    if z > dx*L/lambda
        x         = -L/2 : dx : L/2-dx;
```

```
        [X,Y]     = meshgrid(x,x);
        h         = 1/(1i*lambda*z)*exp(1i*k/(2*z)*(X.^2+Y.^2));
        H         = fft2(fftshift(h))*dx^2;
        FU1        = fft2(fftshift(U1));
        FU2        = H.*FU1;
        U2        = ifftshift(ifft2(FU2));
    end
end
```

2.5 Fourier Transform of electromagnetic fields

Consider now a converging lens characterized by the following quadratic phase term Ω_f, as reported on the left of figure 13:

$$\Omega_f = -\frac{k}{2f}\rho^2 \tag{52}$$

where f is the focal length and ρ is the position on the wavefront defined in the (ξ, η)-plane:

$$\rho = \sqrt{\xi^2 + \eta^2} \tag{53}$$

If we imagine, at this point, an initial field U_1 (as expressed in equation 11) impinging our lens, the propagated field, after a distance z, will be given by the Fresnel integral 21, where, instead of the transmission function of an aperture, we have now the transmission function related to the lens, which is the following

$$A(\xi, \eta) = e^{i\Omega_f(\xi,\eta)} \tag{54}$$

Therefore, the Fresnel integral 21 becomes:

$$U_2^{(z)}(x, y) = \frac{e^{ikz}}{i\lambda z} e^{ik\frac{x^2+y^2}{2z}} \iint_\Sigma U_0(\xi, \eta) e^{ik\frac{\xi^2+\eta^2}{2}\left(\frac{1}{z}-\frac{1}{f}\right)} e^{-i\frac{k}{z}(x\xi+y\eta)}\, d\xi d\eta \tag{55}$$

In the particular case that the propagation distance is equal to the focal length, $z = f$, the previous integral will be reduced to

$$U_2^{(f)}(x, y) = \frac{e^{ikf}}{i\lambda f} e^{ik\frac{x^2+y^2}{2f}} \iint_\Sigma U_0(\xi, \eta) e^{-i\frac{k}{f}(x\xi+y\eta)}\, d\xi d\eta \tag{56}$$

Therefore, remembering the equation 31, the integral 56, except for the phase term, $\exp\left[ik\frac{x^2+y^2}{2z}\right]$, is the Fourier Transform of the two-variables function $U_0(\xi, \eta)$:

$$U_2^{(f)}(x, y) = \frac{e^{ikf}}{i\lambda f} e^{ik\frac{x^2+y^2}{2f}} \mathcal{F}\left\{U_0(\xi, \eta)\right\} \tag{57}$$

Therefore, we finally found that placing a converging lens in front of the object, the image formed on the focal plane is proportional to the Fourier Transform of the object, apart from a curvature phase term. This situation is reported on the right of figure 13. It is important to notice that the same result can be obtained also in a $f - f$ configuration (consisted in placing the lens at the distance f from the object), as we'll see in a moment.

2.5.1 The $f - f$ configuration

We consider now the case with the lens placed at a distance d from the object, as reported in figure 14. Defining with $U^{(d)}(u, v)$ the beam impinging the lens, using the result expressed in equation 57, the field on the focal plane will be

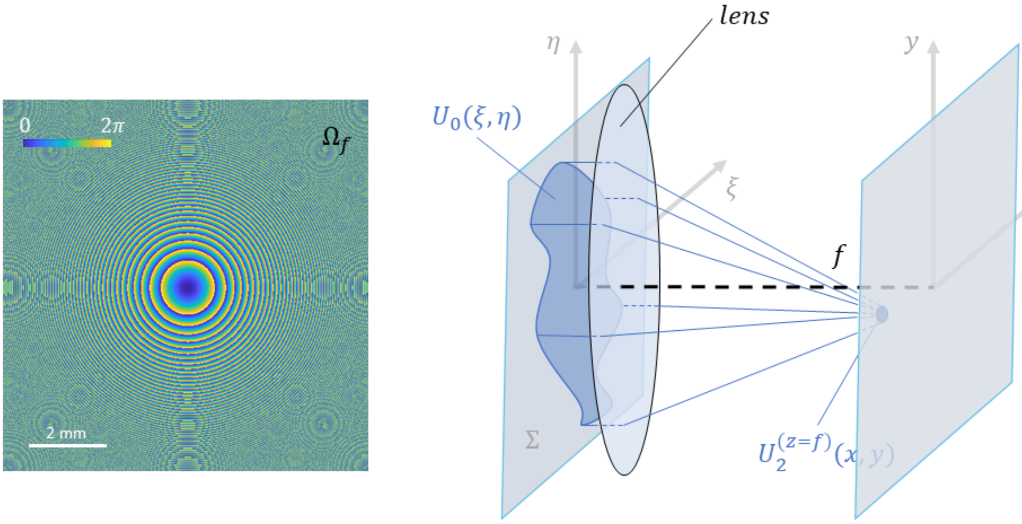

Figure 13: On the left, it is reported the phase pattern Ω_f, modulo 2π, of a lens with focal length of $f = 400\,\text{mm}$ designed for an impinging beam of wavelength $\lambda = 632.8\,\text{nm}$. On the right, the optical configuration, with the lens placed in front of the initial field, defined by a structure $U_0(\xi,\eta)$, which is focused on the final field, $U_2^{(z=f)}(x,y)$, on the focal plane (x,y).

$$U^{(f)}(x,y) = \frac{e^{ikf}}{i\lambda f} e^{ik\frac{x^2+y^2}{2f}} \mathcal{F}\left\{U^{(d)}(u,v)\right\} \tag{58}$$

where $U^{(d)}$ is the free-space propagation of the initial field U_0 for a distance d. Therefore, using the result 26, we have that the Fourier Transform of $U^{(d)}$ will be the following

$$\mathcal{F}\{U^{(d)}(u,v)\} = \mathcal{F}\{U_0(\xi,\eta)\} \cdot H(f_u, f_v) \tag{59}$$

where the transfer function $H(f_u, f_v)$ is given by the equation 29 evaluated in $z \equiv d$

$$H(f_u, f_v) = e^{ikd} e^{-i\pi\lambda d(f_u^2+f_v^2)} \tag{60}$$

where $f_u = \frac{u}{\lambda d}$ and $f_v = \frac{v}{\lambda d}$. Making the variables changing $u, v \longleftrightarrow x, y$ in equation 60 and substituting the result into equation 59, the expression of the final field 58 becomes

$$U^{(f)}(x,y) = \frac{e^{ik(f+d)}}{i\lambda f} e^{ik\frac{x^2+y^2}{2d}\left(1-\frac{f}{d}\right)} \mathcal{F}\{U_0(\xi,\eta)\} \tag{61}$$

Therefore, in the particular case of a $f-f$ configuration, where $d \equiv f$, we finally found

$$U^{(f)}(x,y) = \frac{e^{ik2f}}{i\lambda f} \mathcal{F}\{U_0(\xi,\eta)\} \tag{62}$$

telling us that we have, as in the case of a converging lens placed in front of the object, an image on the focal plane which is proportional to the Fourier Transform of the object. For this reason, in the following chapters, we will use the first or the second configuration, as needed, whenever it will be necessary to perform the Fourier Transform of our beams.

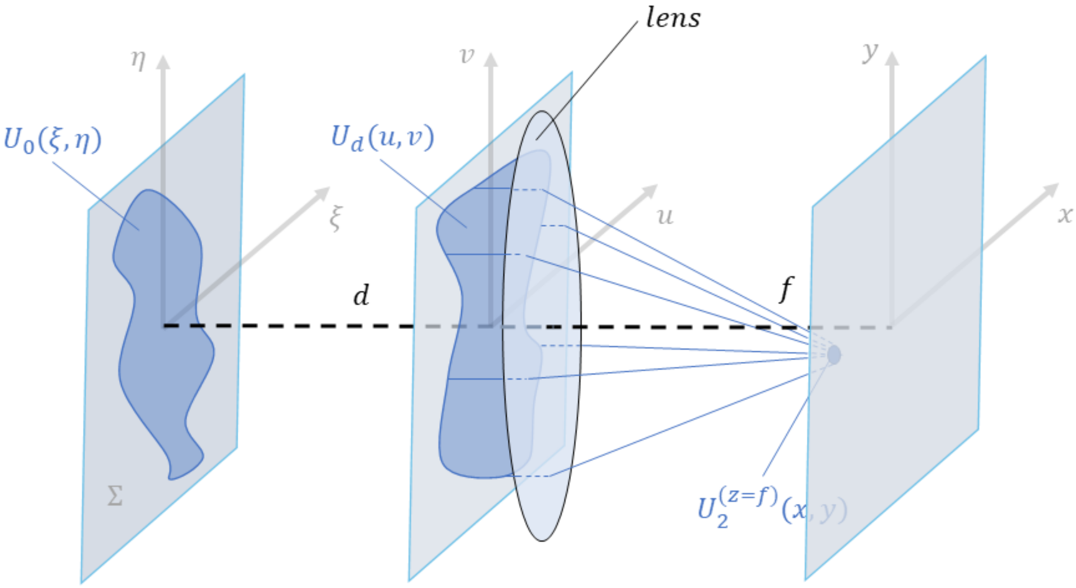

Figure 14: A $d - f$ configuration, where a converging lens, characterized a focal length f, is placed at the distance d from the object. In the particular case of $d \equiv f$, the relative image, formed on the focal plane, is proportional to the Fourier Transform of the object, as expressed by the equation 62.

3 Theory of the multipole-phase beams

In this chapter it will be described in detail the theory of the multipole-phase beams. In particular, it will be demonstrated the quasi-orthogonality of multipole-phase beams characterized by different values of their parameters, and how these distinct phase patterns can be transformed into different linear phase gradients, which can be separated into isolated light spots using a Fourier lens. However, in order to preserve the information content during the conversion of the multipole-phase beams into linear phase gradients, a conformal mapping is needed. For this reason, in the first section 3.1, it will be demonstrated that such a type of transformation satisfies the Laplace's equation, whose solutions are actually expressed in terms of multipole phases. Then, in the section 3.2, it will be shown that this conformal mapping consists in a circular-sector transformation which can be performed by the cascade of two phase plates, that will be called *Transformer* and *Phase Corrector*. At this point, knowing how to generate a multipole-phase beam and how to transform it into a linear phase gradient, an introduction to the demultiplexing of the multipole-phase beams thanks to these circular-sector transformations will be given in the section 3.3. Then, in section 3.4, the free-space propagation of the multipole-phase beams for long distances will be studied, and eventually phase distortions are considered in section 3.5. In this way, exploiting the demonstration, in section 3.6, of the actual orthogonality of multipole-phase beams with different parameters, we are finally able to guarantee that this new type of structured light can be actually used in the communication system.

3.1 Laplace's equation in structured phase transmission

Consider an initial structured electromagnetic field, $u^{(i)}(r,\theta)$, defined by an amplitude $U^{(i)}(r,\theta)$ and a phase $\Omega(r,\theta)$:

$$u^{(i)}(r,\theta) = U^{(i)}(r,\theta)e^{i\Omega(r,\theta)} \tag{63}$$

where (r,θ) are the polar coordinates of the initial plane, orthogonal to the propagation directions.
In the previous chapter, we have seen that, in the paraxial approximation, the propagation (along the z-axis) of a field $U^{(i)}(x,y)$, is described by the following diffraction integral

$$U^{(z)}(u,v) \propto \frac{1}{i\lambda z}\iint U^{(i)}(r,\theta)e^{i\Omega(r,\theta)}e^{-ik\frac{xu+yv}{z}}\,dxdy \tag{64}$$

where we can make a change of coordinates passing to the polar coordinates $\boldsymbol{\rho} = \rho(\cos\phi,\sin\phi) \equiv (u,v)$ and $\boldsymbol{r} = r(\cos\theta,\sin\theta) \equiv (x,y)$, for the final and the initial planes, respectively, both orthogonal to the propagation direction.

$$U^{(z)}(\rho,\phi) \propto \frac{1}{i\lambda z}\iint U^{(i)}(r,\theta)e^{i\Omega(r,\theta)}e^{-ik\frac{r\rho}{z}\cos(\theta-\phi)}r\,dr\,d\theta \tag{65}$$

According to the stationary phase approximation [56], this integral can be evaluated as the contribution, around the saddle points, of the total phase function, $\Phi(r,\theta)$, of its argument

$$\Phi(r,\theta) = \Omega(r,\theta) - k\frac{r\rho}{z}\cos(\theta-\phi) \tag{66}$$

and the equation 65 can be rewritten as

$$U^{(z)}(\rho,\phi) \cong \frac{2\pi\sigma}{\lambda z}\frac{U^{(i)}(r^*\theta^*)}{\sqrt{|H|}}e^{i\Phi(r^*\theta^*)} \tag{67}$$

where $(r^*\theta^*)$ is the saddle point, H is the Hessian determinant of Φ and

$$\sigma = \begin{cases} \mathrm{sgn}\left(\frac{\partial^2\Phi}{\partial x^2}\right) & \text{if } H > 0 \\ -i & \text{otherwise} \end{cases} \tag{68}$$

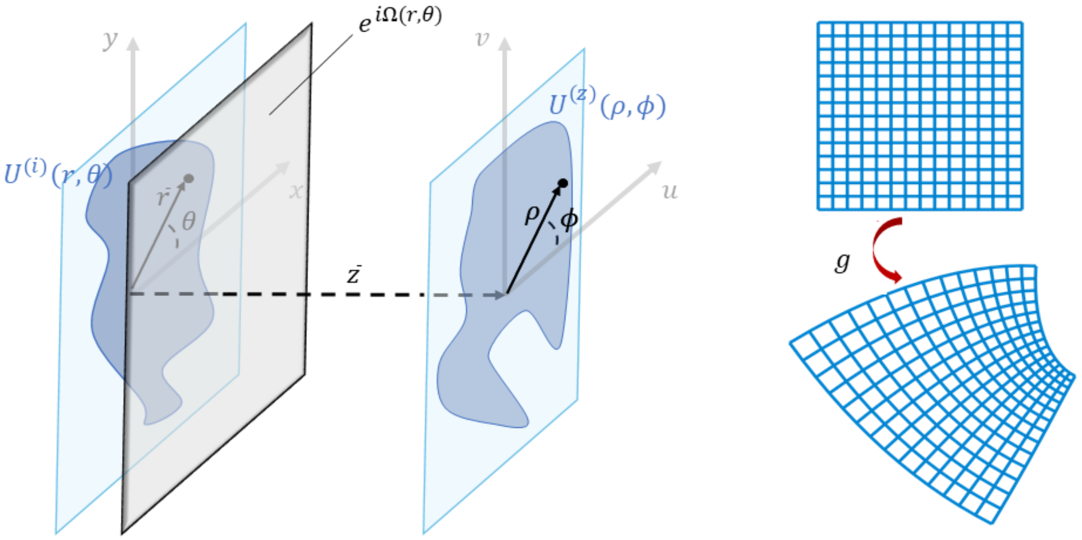

Figure 15: A conformal mapping g imparted by a phase pattern Ω on an electromagnetic field $U^{(i)}$.

Considering the equation 66, from the condition $\nabla\Phi = 0$ of a saddle point, we obtain the following identity

$$\nabla\Omega = \frac{k}{z}\boldsymbol{\rho} \tag{69}$$

Now, rearranging the previous equation and applying the curl (remember that the curl of the gradient is null), we get

$$\boldsymbol{\nabla} \times \rho = \frac{z}{k}\boldsymbol{\nabla} \times \nabla\Omega = 0 \tag{70}$$

This means that $\boldsymbol{\rho}$ is irrotational and admits the following relation on the partial derivatives

$$\frac{\partial u}{\partial y} = \frac{\partial v}{\partial x} \tag{71}$$

It is important to notice that the equation 69 establishes a connection between a point, $\boldsymbol{r} \equiv (x, y)$, of the input wavefront and a point, $\boldsymbol{\rho} \equiv (u, v)$, on the same wavefront at the distance z. This connection can be thought of as an optical transformation of the input intensity pattern $U^{(i)}(r, \theta)$ imparted by the phase term $\Omega(r, \theta)$. This implies that, controlling the phase Ω, one can use the transformation in order to transfer or manipulate information. However, in order to avoid the distortion of the data contained in the phase structure of the wavefront, it is needed to assume that this transformation locally conserves the angles, i.e., it is conformal.

In the complex formalism, a conformal mapping of the point $\zeta = x + iy$ which satisfies the equation 71, is described by an anti-holomorphic function as the following

$$g\left(\bar{\zeta}\right) = u(x, y) + iv(x, y) \tag{72}$$

where $\bar{\zeta} = x - iy$ is the complex coniugate of ζ [25]. We recall that a function is anti-holomorphic if it satisfies the following identity of the Wirtinger operator $\frac{\partial}{\partial\bar{\zeta}}$:

$$\frac{\partial g(\bar{\zeta})}{\partial\zeta} \equiv \frac{1}{2}\left(\frac{\partial}{\partial x} - i\frac{\partial}{\partial y}\right) g(\bar{\zeta}) = 0 \tag{73}$$

Substituting the expression 72 into this equation and rearranging, we get

$$\left(\frac{\partial u}{\partial x} + \frac{\partial v}{\partial y}\right) + i\left(\frac{\partial v}{\partial x} - \frac{\partial u}{\partial y}\right) = 0 \tag{74}$$

From the equation 71, however, the second term is null and, therefore, we obtain the following second Cauchy-Rieman condition

$$\frac{\partial u}{\partial x} = -\frac{\partial v}{\partial y} \tag{75}$$

Now, taking the two-dimensional divergence of the equation 69

$$\boldsymbol{\nabla} \cdot \nabla \Omega = \frac{k}{z} \boldsymbol{\nabla} \cdot \boldsymbol{\rho} \tag{76}$$

we obtain

$$\nabla^2 \Omega = \frac{k}{z} \left[\frac{\partial \rho_x}{\partial x} + \frac{\partial \rho_y}{\partial y} \right] = \frac{k}{z} \left[\frac{\partial u}{\partial x} + \frac{\partial v}{\partial y} \right] \overset{(75)}{=} 0 \tag{77}$$

where the relation 75 was used. We have, therefore, obtained the following Laplace's equation

$$\nabla^2 \Omega = 0 \tag{78}$$

which tells us that a conformal anti-holomorphic mapping imparts a phase term Ω which is a harmonic function. The explicit form of the Laplace's equation in polar coordinates is the following

$$\left(\frac{1}{r} \frac{\partial}{\partial r} r \frac{\partial}{\partial r} + \frac{1}{r^2} \frac{\partial^2}{\partial \theta^2} \right) \Omega(r, \theta) = 0 \tag{79}$$

Rearranging, we obtain

$$\frac{\partial^2 \Omega(r, \theta)}{\partial r^2} + \frac{1}{r} \frac{\partial \Omega(r, \theta)}{\partial r} + \frac{1}{r^2} \frac{\partial^2 \Omega(r, \theta)}{\partial \theta^2} = 0 \tag{80}$$

At this point, we look for solution with separated variables

$$\Omega(r, \theta) = R(r) T(\theta) \tag{81}$$

and substituting in the equation 80, we get

$$T(\theta) R''(r) + \frac{T(\theta)}{r} R'(r) + \frac{R(r)}{r^2} T''(\theta) = 0 \tag{82}$$

Dividing for $T(\theta)R(r)$, and rearranging, we obtain

$$r^2 \frac{R''(r)}{R(r)} + r \frac{R'(r)}{R(r)} = -\frac{T''(\theta)}{T(\theta)} \tag{83}$$

where the left term is a function of the only radial coordinate r, and the right term depends only on the azimuthal angle θ. Therefore, the expression is true if, and only if, the two terms are constants, that we can call C, and the equation 83 can be rewritten as the following system:

$$\begin{cases} T''(\theta) + C T(\theta) = 0 \\ r^2 R''(r) + r R'(r) - C R(r) = 0 \end{cases} \tag{84}$$

Now, for continuity of the derivatives, a periodic boundary condition (PBC) has to be introduced for the angular function:

$$T(0) = T(2\pi) \tag{85}$$

With this assumption, the only values of the constant C corresponding to non-identically null solutions are $C > 0$, and, in this case, the first equation of the system 84 returns

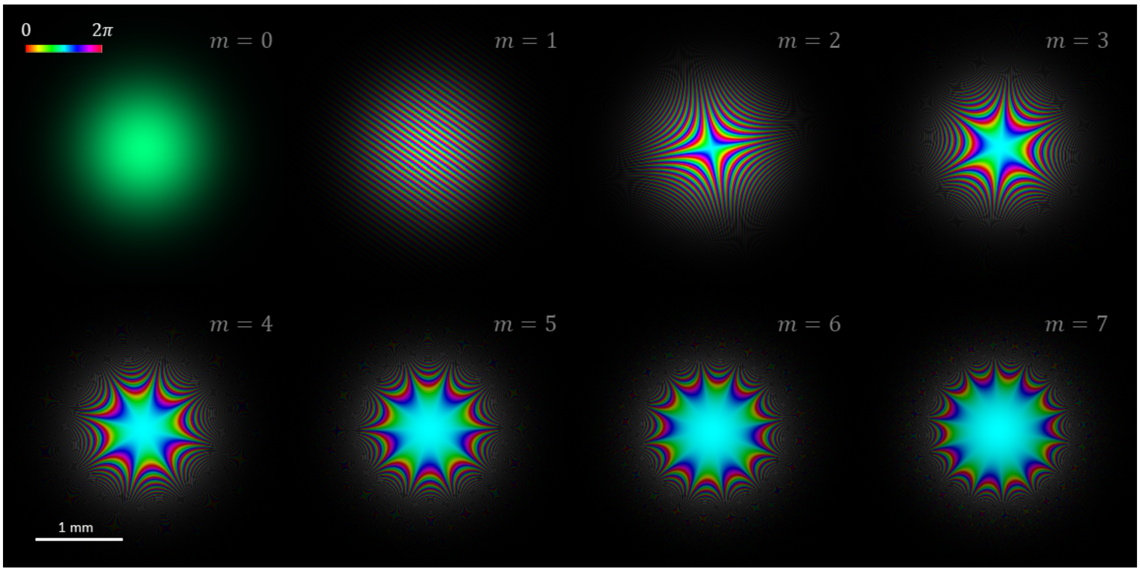

Figure 16: Multipole-phase beams with the same phase strength and orientations but different phase orders m. Brightness and colours refer to intensity and phase, respectively.

$$T(\theta) = \alpha \cos\left(\theta\sqrt{C}\right) + \beta \sin\left(\theta\sqrt{C}\right) \tag{86}$$

where, α and β, are two real constants. This equation satisfies the periodic boundary conditions 85, if $C = m^2$ with $m \in \mathbf{N}$, obtaining

$$T(\theta) = \alpha \cos(m\theta) \tag{87}$$

With this choice of C, the second equation of the system 84 becomes

$$r^2 R''(r) + rR'(r) - m^2 R(r) = 0 \tag{88}$$

which has solutions of the type

$$R(r) = r^m \tag{89}$$

Using the two results 87 and 89, the equation 81 becomes:

$$\Omega(r, \theta) = \alpha r^m \cos[m(\theta - \theta_0)] \tag{90}$$

where θ_0 is an initial angle, introduced in order to generalize the result, taking into account different possible orientations of the phase pattern $\Omega(r, \theta)$. Notice that the sine solution can be equally chosen.
Due to the analogy with the fields produced by an electrostatic or magnetostatic multipole, we will refer to an electromagnetic field, with a phase patterns described by the previous equation, as a "multipole-phase beam". Indeed, as can be seen from the figure 16, incrementing the parameter m, the number of poles of the phase structure increases, similarly to a magnetostatic multipole. For this reason, m is called "phase order".

We call the two continuous parameters, α and θ_0, as "phase strength" and "phase orientation", respectively. Indeed, as we will see in detail in the following chapters, the phase strength is associated to the phase gradient in the radial direction. Referring to the figure 17, where it is reported a simulation of this pattern as described in the equation 90, the various colours are related to different phase values. In this way, in a 2π-phase period, each colour is present only once. Consequently, incrementing α, the density of the coloured stripes rises and a "stronger" multipole-phase beam is obtained. The θ_0, instead, is the orientation of the phase pattern in the plane transversal to the propagation direction (i.e., the plane represented in the figure). Finally, the parameter m describes the multiplicity order of the phase and identifies the beam's family. After the assumption of periodic

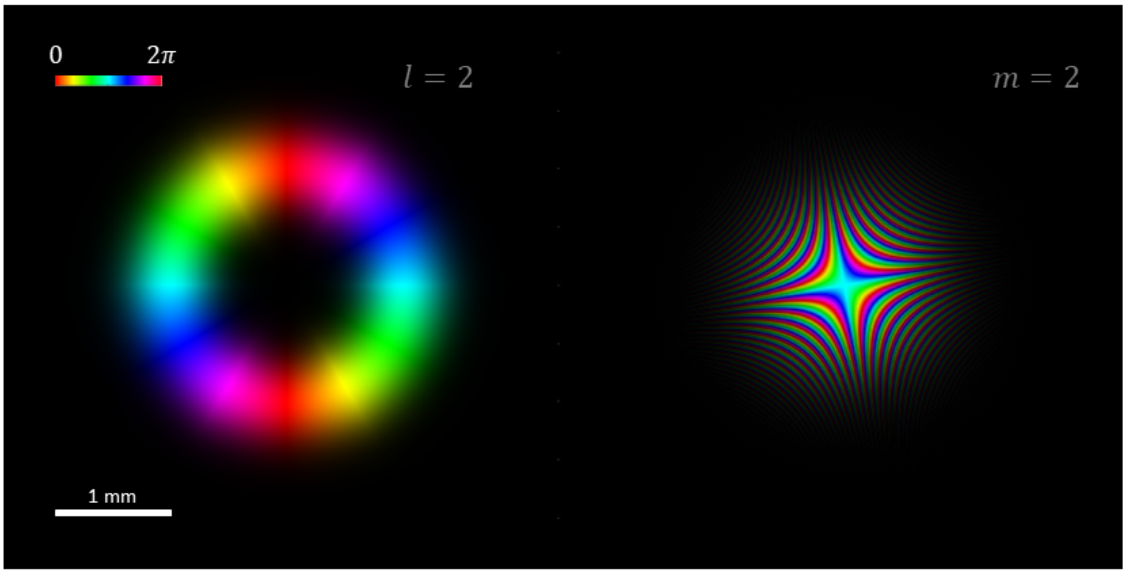

Figure 17: On the left, an OAM beam with angular momentum $l = 2$ and beam waist $w_0 = 1.0\,\text{mm}$. On the right, a multipole-phase beam of order $m = 2$ with phase strength $\alpha = 60\,\text{mm}^{-2}$ and phase orientation $\theta_0 = \frac{\pi}{3}$. Brightness and colours refer to intensity and phase, respectively.

boundary conditions in $\theta = 0$, the phase order m can be assumed integer, as demonstrated above. Observe that, for $m > 0$, the phase pattern is defined over the whole plane (r, θ). This is an evident consequence of the Laplace's equation 78, and it is an important distinction with respect to the orbital angular moment beams (OAM), a family of beams widely used in the structured light applications. Indeed, the OAM beams, described by an azimuthal phase term $\Omega(\theta) = m\theta$ which is a trivial solution of equation 78, are characterized by a phase pattern with a central phase singularity, as can be seen from the OAM simulated beam on the left of figure 17. This singularity can be a problem in communication systems, since the relative central dark zone will expand during a free space propagation, reducing the detection efficiency of OAM beams for long distances, and it is, certainly, a waste of the detection area of the detectors. We want to further focus the attention on the fact that we had rediscovered the OAM beams as a particular solution, of the Laplace's equation, which is independent of the radial coordinate: $\Omega(r, \theta) \equiv \Omega(\theta) = m\theta$.

3.2 Circular-sector transformation in the stationary phase approximation

The purpose of this work is the study of multipole-phase beams in structured light applications. For this reason, it is important to discover, for each order m, an effective method to sort and generate multipole-phase beams on the basis of their parameters α and θ_0. A way out is the mapping of these multipole phases onto linear phase gradients, which can be easily separated into isolated light spot thanks to a Fourier lens. Therefore, these spots can be used as single channels of information, showing the possibility to propagate, simultaneously, more signals at the same frequency without any interference and loss of information. The mapping just introduced can be achieved implementing an n-fold circular-sector transformation with $n = -\frac{1}{m}$. This transformation maps, conformally, a point (r, θ) into the new coordinates (ρ, ϕ) as it follows:

$$\begin{cases} \rho = a\left(\frac{r}{b}\right)^{-\frac{1}{n}} = a\left(\frac{r}{b}\right)^{m} \\ \phi = \frac{\theta}{n} = -m\theta \end{cases} \tag{91}$$

where a and b are arbitrary scaling factors. Substantially, this change of coordinates is a scaling of the azimuthal coordinate θ and a power scaling of the radial coordinate r, where the last one is dictated by the Cauchy-Riemann conditions 71 and 75. Substituting the relations 91 in the expression 90, we found that, after the application of the circular-sector transformation, the phase of the beam is converted into the following linear gradient:

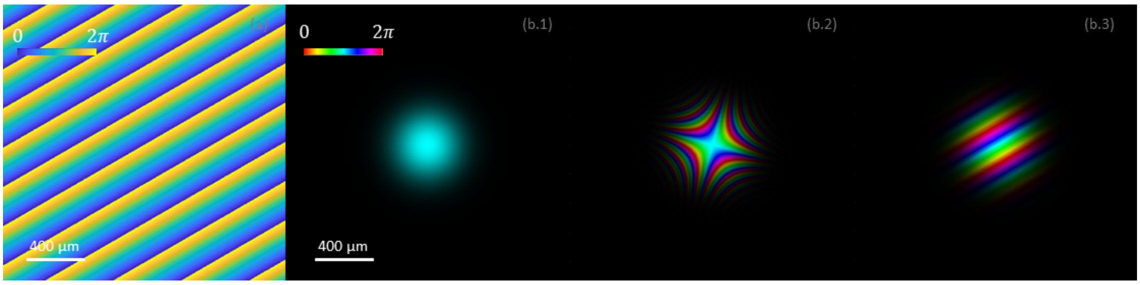

Figure 18: In the frame (a) it is reported an example of the phase pattern, modulo 2π, of a linear phase gradient as expressed by the equation 92. In the frame (b.1), instead, it is show the initial Gaussian beam ($\lambda = 632.8\,\mathrm{nm}$ and $w_0 = 312\,\mu\mathrm{m}$) used in order to generate the multipole-phase beam, shown in the frame (b.2), characterized by a phase strength $\alpha = 16\,\mathrm{mm}^{-2}$ and a phase orientation $\theta_0 = 120°$. In the last frame, we found the linear phase gradient obtained after a circular-sector transformation of the previous multipole-phase beam, where the period and orientation of the linear phase gradient are related to the parameters of the multipole-phase beam as expressed by the system 91. Brightness and colours refer to intensity and phase, respectively.

$$\Phi^{out}(\rho,\phi) = \beta\rho\cos(\phi - \phi_0) \tag{92}$$

where $\phi_0 = -m\theta_0$ and $\beta = \frac{\alpha b^m}{a}$. In figure 18, for instance, it is reported a multipole-phase beam with $\alpha = 16\,\mathrm{mm}^{-2}$ and $\theta_0 = 120°$, and the relative field after the circular-sector transformation (frame b.2 and b.3, respectively). Notice the coloured stripes in the output beam, indication of a linear gradient in its phase structure, which is rotated due to the choice of a phase orientation θ_0 different from zero.

In order to demonstrate as a n-fold circular-sector transformation can produce the gradient as in equation 92, we recall, as seen in the chapter 2, that the diffraction integral 65 can be obtained, in the paraxial approximation, illuminating with a field $U^{(i)}(r,\theta)$ an optical element with a transmission function $A(r,\theta) = \exp\{i\Omega(r,\theta)\}$, as reported in figure 15). The exact expression of the integral 65 is the following:

$$U^{(z)}(\rho,\phi) = \frac{e^{ik\frac{\rho^2}{2z}}}{i\lambda z}\iint U^{(i)}(r,\theta)e^{i\Omega(r,\theta)}e^{ik\frac{r^2}{2z}}e^{-ik\frac{r\rho}{z}\cos(\theta-\phi)}r\,dr\,d\theta \tag{93}$$

This integral, according to the stationary phase approximation already introduced, can be approximated with the contributions of the phase function around the saddle points. We can express the phase of the integrand in the previous equation, as the sum of the phase term, Ω_n, imparted by the n-fold circular-sector transformation, and a quadratic focusing term

$$\Omega(r,\theta) = \Omega_n(r,\theta) - k\frac{r^2}{2f} \tag{94}$$

where, in this case, $f \equiv z$.
Now, from the saddle point condition $\nabla\Phi = 0$ we obtain the following expression

$$\nabla\Omega_n = \frac{k}{z}\left[\boldsymbol{\rho} - \left(1 - \frac{z}{f}\right)\boldsymbol{r}\right] \tag{95}$$

where we remember that $\boldsymbol{r} = r(\cos\theta, \sin\theta)$ and $\boldsymbol{\rho} = \rho(\cos\phi, \sin\phi)$. Considering, then, the coordinate change expressed by the relation 91

$$(\rho,\phi) = \left(a\left(\frac{r}{b}\right)^{-\frac{1}{n}}, \frac{\theta}{n}\right) \tag{96}$$

we perform a mapping between the frame (r,θ), on the input plane ($z = 0$) transversal to the propagation direction, and the new frame (ρ,ϕ) on the destination plane ($z = f$). As said before, this mapping is a n-fold circular-sector transformation consisting in a rescaling of the azimuthal angle θ by a factor n and in a power scaling of the radial coordinate, $\left(\frac{r}{b}\right)^{-\frac{1}{n}}$, dictated by the Cauchy-Riemann conditions 71 and 75. Substituting the change of coordinates 96 into the equation 95 and solving for $z = f$, one get:

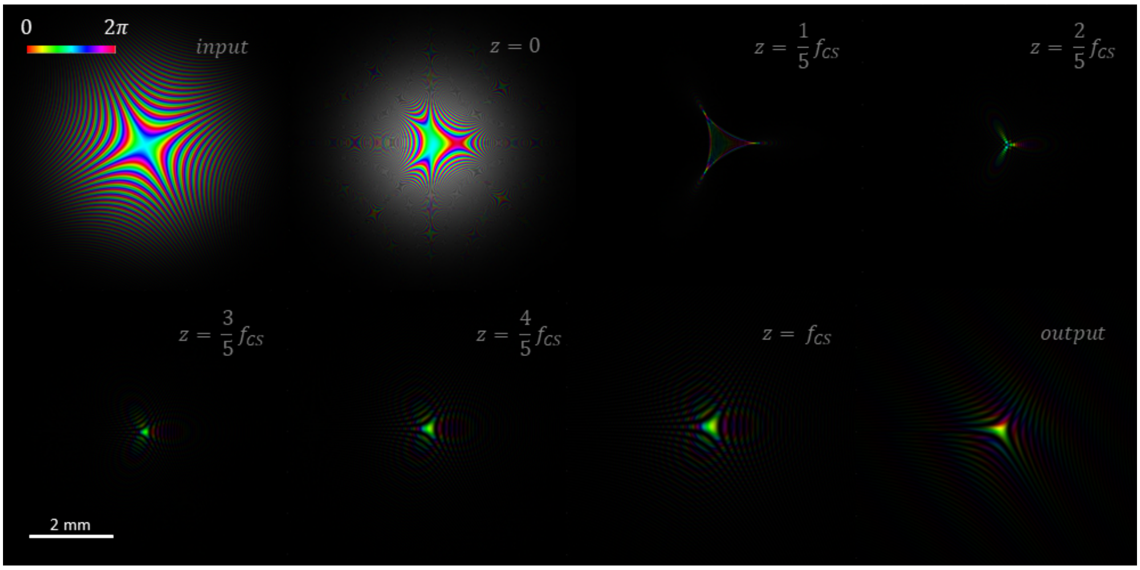

Figure 19: Simulation of the evolution of a multipole-phase beam, of order $m = 2$, during a n-fold circular-sector transformation where $n = -1/m$. The initial multipole-phase beam, reported in the first frame, is characterized by wavelength $\lambda = 632.8\,\mathrm{nm}$, phase strength $\alpha = 16\,\mathrm{mm}^{-2}$ and phase orientation $\theta_0 = 72°$. In the second frame ($z = 0$), we found the field after the Transformer, i.e., the input beam after the application of the phase term $\Omega_n^{(CS)}$ with the additional focusing term $-k\frac{r^2}{2f_{CS}}$ (see equation 101). In the following frames, it is reported the field at different distances between the Transformer and the Phase Corrector. Finally, in the last frame ($z = f_{CS}$), we have the output beam, i.e., the field after the application of the phase term $\Omega_n^{(PC)}$ with the additional correction term $-k\frac{r^2}{2f_{CS}}$ (see equation 103). Notice the characteristic coloured stripes of a linear phase gradient. The parameters of the circular-sector transformation are: $a = 2.0\,\mathrm{mm}$, $b = 0.85\,\mathrm{mm}$ and $f_{CS} = 250\,\mathrm{mm}$. Brightness and colours refer to intensity and phase, respectively.

$$\nabla\Omega_n = \frac{k}{f}a\left(\frac{r}{b}\right)^{-\frac{1}{n}}\left(\cos\left(\frac{\theta}{n}\right), \sin\left(\frac{\theta}{n}\right)\right) \tag{97}$$

In order to obtain Ω_n, we can integrate this expression, remembering the definition

$$\nabla\Omega_n \cdot \hat{r} = \frac{\partial\Omega_n}{\partial r} \tag{98}$$

where $\hat{r}$ is the versor in the radial direction. We obtain:

$$\begin{align} \frac{\partial\Omega_n}{\partial r} &= \frac{k}{f}a\left(\frac{r}{b}\right)^{-\frac{1}{n}}\left[\cos\left(\frac{\theta}{n}\right)\cos(\theta) + \sin\left(\frac{\theta}{n}\right)\sin(\theta)\right] \tag{99} \\ &= \frac{k}{f}a\left(\frac{r}{b}\right)^{-\frac{1}{n}}\cos\left(\theta - \frac{\theta}{n}\right) \tag{100} \end{align}$$

A straightforward integration returns the following result

$$\Omega_n^{(CS)}(r,\theta) = k\frac{ab}{f}\left(\frac{r}{b}\right)^{1-\frac{1}{n}}\frac{\cos\left(\left(1-\frac{1}{n}\right)\theta\right)}{1-\frac{1}{n}} \tag{101}$$

The equation 101 defines the phase pattern of the optical element that perform the circular-sector transformation required to produce a linear phase gradient starting from a multipole-phase beam. For this reason, we will refer to such a type of phase plate as "Transformer" or "Circular-Sector plate" (CS). However, a second element, placed at $z = f$, is needed in order to take into account the phase distortions due to the propagation. This element is called "Phase-Corrector" (PC). In figure 19, for example, a simulation is reported showing the wavefront of a multipole-phase beam during the CS-transformation. It is worth noting that the phase structure of the field at $z = f_{CS}$ does not present a linear phase gradient as expected. Indeed, a further step is necessary in order to get an output characterized by a sequence of coloured stripes typical of a linear phase gradient (the last frame in the figure). This step is performed by the Phase Corrector.

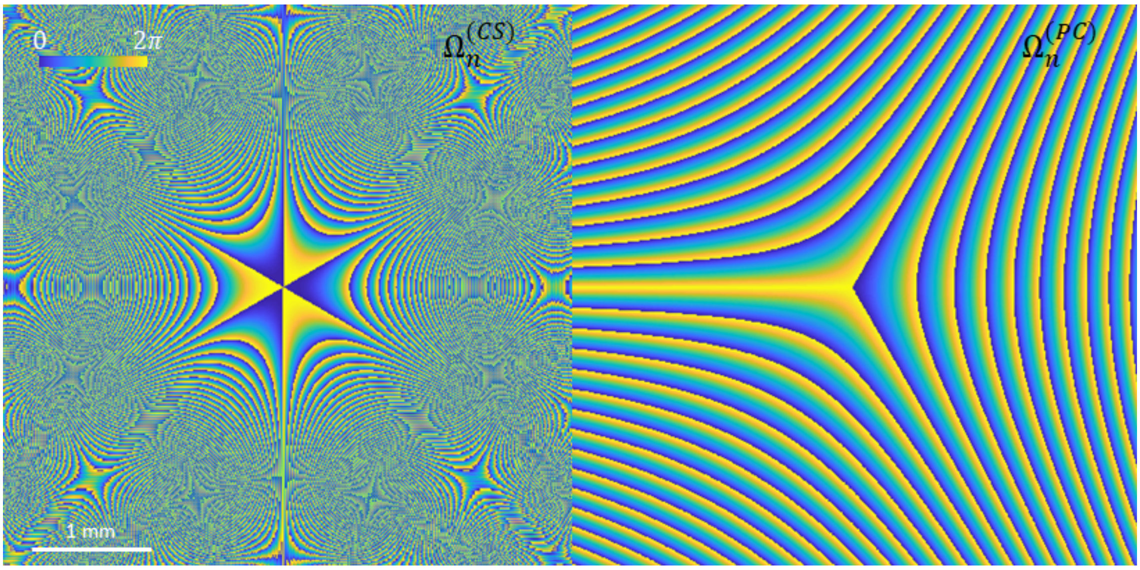

Figure 20: On the left, the phase pattern, modulo 2π, $\Omega_n^{(CS)}$ of the Transformer used in the simulation of figure 19. On the right, the phase pattern $\Omega_n^{(PC)}$ of the Phase Corrector. We remember the parameters of the circular-sector transformation: $a = 2.0\,\text{mm}$, $b = 0.85\,\text{mm}$ and $f_{CS} = 250\,\text{mm}$.

In order to obtain the phase $\Omega_n^{(PC)}$ of the phase plate, we have to consider the reverse process, i.e., the transformation of a linear phase gradient into a multipole-phase beam. Thinking in this way, this second optical element has to be another circular-sector transformation but characterized by an order $\frac{1}{n}$. Therefore, the phase corrector is the mapping defined by the following change of coordinate

$$(r, \theta) = \left(b \left(\frac{\rho}{a} \right)^{-n}, n\phi \right) \tag{102}$$

Performing the same calculation for the previous case, we obtain

$$\Omega_n^{(PC)}(\rho, \phi) = k \frac{ab}{f} \left(\frac{\rho}{a} \right)^{1-n} \frac{\cos((1-n)\,\phi)}{1-n} \tag{103}$$

which is, substantially, the same expression as in equation 101, under the substitutions $b \longleftrightarrow a$, $n \longleftrightarrow 1/n$ and $(r, \theta) \longleftrightarrow (\rho, \phi)$.

In figure 20 the two phase patterns, $\Omega_n^{(CS)}$ and $\Omega_n^{(PC)}$, used in the simulations of the figure 19, are shown. The parameters of these two optical elements are: $a = 2.0\,\text{mm}$, $b = 0.85\,\text{mm}$ and $f = 250\,\text{mm}$. Notice how the phase pattern of the Phase Corrector is rediscovered in the intensity structure of the simulated output beam reported in the last frame of figure 19, where the brightness variations define such structure.

3.3 A brief introduction to the demultiplexing of multipole-phase beams

From equation 92 one can observe that, incrementing the absolute value of the phase strength $|\alpha|$, the intensity of the linear phase gradient Φ^{out} increases and, therefore, the density of 2π-periods in the phase pattern of the wavefront is higher in the radial direction. With the colour notation already introduced, this mean that each colour appears a major number of times, as can be seen from the figure 21. Indeed, observing the first two columns of the figure, one can see that reducing $|\alpha|$, the phase structure of the output beam looks more "spread", i.e., the coloured stripes, appearing a less number of times, have to be larger in order to cover the whole wavefront. Furthermore, looking at the last column of figure 21, we can see that changing the phase orientation θ_0 of the initial multipole-phase beam, the output beam will be characterized by a rotated linear phase gradient.

This relation between the phase gradient and the density of 2π-periods is related to the linear momentum of the photons composing the radiation. Indeed, it is well-known that a plane wave $u(\boldsymbol{r}) = U_0(\boldsymbol{r})e^{i\Phi(\boldsymbol{r})}$ of phase function

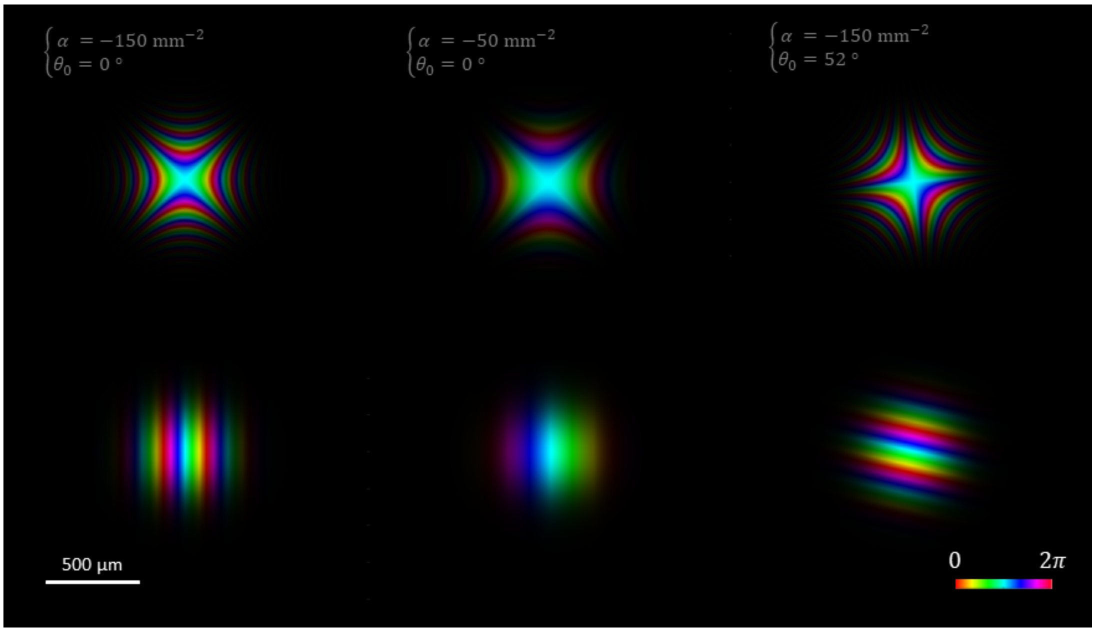

Figure 21: On the top, three different multipole-phase beams for various values of phase strength α and orientation θ_0. On the bottom, the relative demultiplexed fields with the characteristic linear phase gradient, whose period and orientation depend on the parameters of the initial multipole-phase beam. It is worth noting that, even if α was defined as a positive quantity, negative values are also acceptable, and they correspond to a further $\frac{\pi}{2}$-rotation of the phase structure. As usual, brightness and colours refer to intensity and phase, respectively.

$$\Phi(\boldsymbol{r}) = \boldsymbol{k} \cdot \boldsymbol{r} \tag{104}$$

is composed by photons of linear momentum $\boldsymbol{p} = \hbar \boldsymbol{k}$. For a plane wave with a phase pattern as expressed in equation 92, we obtain

$$\Phi(\rho, \phi) = \beta \rho \cos \phi \tag{105}$$

where we have made the position $\beta := \frac{b^m}{a} \alpha$ with α denoting the phase strength. In analogy with the equation 92, β is the modulus, in units of $\hbar$, of the components of the linear momentum on a plane perpendicular to the propagation direction (i.e., the intensity of the phase gradient in the point of coordinates (ρ, ϕ)).
This density variation of the linear phase gradient according to the phase strength value, suggests a way in order to sort a superposition of multipole-phase beams. Indeed, different linear phase gradients can be separated, by a Fourier lens, into a set of light spots whose positions depend on the properties of the phase gradients, as we will see in a moment. This process is called *demultiplexing*.

3.3.1 Tilted plane wave in a $f - f$ configuration

In the previous chapter, we have seen that, in the paraxial approximation, both a Fourier lens (of focal length f) placed in front of an initial electromagnetic field U_0 and a $f - f$ configuration, produced on the focal plane a field which is proportional to the Fourier Transform of the initial one. In particular, for a $f - f$ configuration, we have found the equation 62:

$$U^{(f)}(x, y) = \frac{e^{ik2f}}{i\lambda f} \mathcal{F}\{U^{(i)}(\xi, \eta)\} \tag{106}$$

where, in this case, we supposed $U^{(i)}(\xi, \eta) = U_0 e^{i\Phi(\xi,\eta)}$ characterized by a linear phase gradient as expressed in equation 92. Therefore, the previous integral becomes

$$U^{(f)}(x, y) = \frac{U_0 e^{ik2f}}{i\lambda f} \int d\xi \int d\eta e^{i\Phi(\xi,\eta)} e^{-i2\pi(xf_x + yf_y)} \tag{107}$$

where we have already seen that the two frequencies are $f_x = \frac{\xi}{\lambda z}$, and $f_y = \frac{\eta}{\lambda z}$, with $z \equiv f$ in this case. Rewriting the linear phase gradient 92 in Cartesian coordinates,

$$\Phi(\xi, \eta) = \beta\rho\cos(\phi - \phi_0) = i\beta\xi\cos\phi_0 + i\beta\eta\sin\phi_0 \tag{108}$$

the integral 107 becomes the following:

$$U^{(f)}(x, y) = \frac{U_0 e^{ik2f}}{i\lambda f} \int e^{-i(\beta\sin\phi_0 - \frac{2\pi}{\lambda f}y)\eta} d\eta \int e^{-i\left(\beta\cos\phi_0 - \frac{2\pi}{\lambda f}x\right)\xi} d\xi \tag{109}$$

Remembering that

$$\delta(x - u) = \frac{1}{2\pi} \int e^{i\xi(x-u)} d\xi \tag{110}$$

we finally obtain

$$U^{(f)}(x, y) = \frac{U_0 e^{ik2f}}{i\lambda f} 2\pi\delta\left(x - \frac{\lambda f}{2\pi}\beta\cos\phi_0\right) 2\pi\delta\left(y - \frac{\lambda f}{2\pi}\beta\sin\phi_0\right) \tag{111}$$

which tell us that the final field, on the focal plane, is a light spot of coordinates

$$\begin{cases} x = \frac{\lambda f}{2\pi}\beta\cos\phi_0 \\ y = \frac{\lambda f}{2\pi}\beta\sin\phi_0 \end{cases} \tag{112}$$

Therefore, in the case of a set of light fields characterized by linear phase gradients with different β values but without any initial rotational angle ($\phi_0 = 0$), the light spots produced by a Fourier lens in a $f - f$ configuration, will be displaced along the x-axis, as reported in the simulations of the figure 22.

Instead, in the case of a non-null initial rotational angle, the final light spots will be focused onto circular concentric distributions with radius R given by the previous system

$$R = f\frac{\lambda}{2\pi}\frac{\alpha b^m}{a} \tag{113}$$

where we have made explicit the β parameter. For instance, in figure 23, the sorting of five linear phase gradients with the same β value, but different orientations ϕ_0, is shown.

It should be clear now, how changing the phase strength and orientation into a set of multipole-phase beams, final distinct light spots can be obtained. Associating to each different multipole-phase beam a distinct channel of information, a new space division multiplexing format can be exploited. Indeed, the remaining properties requested are: the possibility to propagate more multipole-phase beams at the same frequency without interferences between them, i.e., the demonstration that they are orthogonal fields for different phase strength and/or phase orientation values, and the characteristic of keeping unaltered the information content during the transmission. These two properties are analysed in the following.

3.4 Free-space propagation of a multipole-phase beam

Until now, we have discussed the theory of multipole-phase beams and briefly introduced their demultiplexing/multiplexing in order to use them in communication applications. In particular, we have implicitly assumed $m = 2$ for our considerations. However, the only restriction made, about the phase order, is that it is an integer number and higher values of m could be adopted. As we will see in detail, since the phase structure 101 depends on m, changing the phase order, new families of beams with different phase patterns will be obtained. For this reason, m can be a further degree of freedom in the design of communication system working with multipole-phase beams. This will be analysed in detail from a theoretical and practical point of view in the next chapters. Here, however, we want to show that the beams characterized by a phase order $m = 2$, assume a peculiar role in the free space propagation. Indeed, this family of beams is the only one (except for the trivial case $m = 0$) which conserves the same multipole-phase order during the whole propagation and, therefore, they

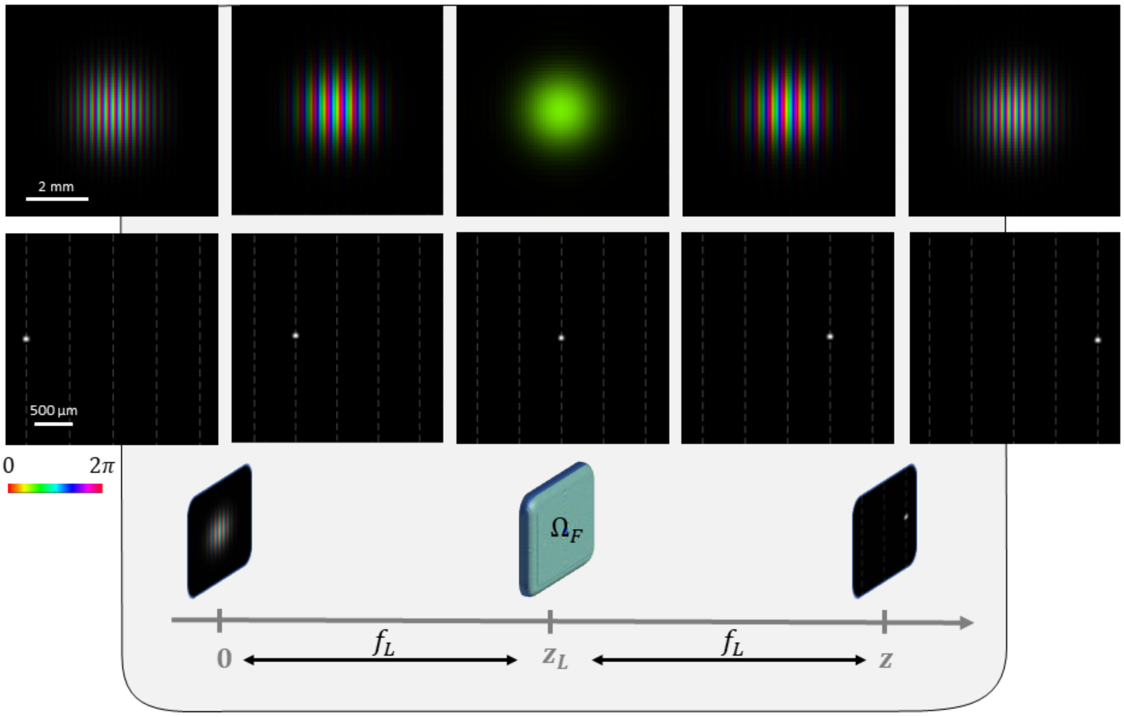

Figure 22: Demultiplexing of Gaussian beams characterized by a wavelength $\lambda = 632.8\,\mathrm{nm}$, and a linear phase gradient (as expressed by the equation 92) for different values of $\beta(\rho, \phi)$. The Fourier transforms are performed by a lens of focal length $f_L = 400\,\mathrm{mm}$ in a $f_L - f_L$ configuration. Brightness and colours refer to intensity and phase, respectively.

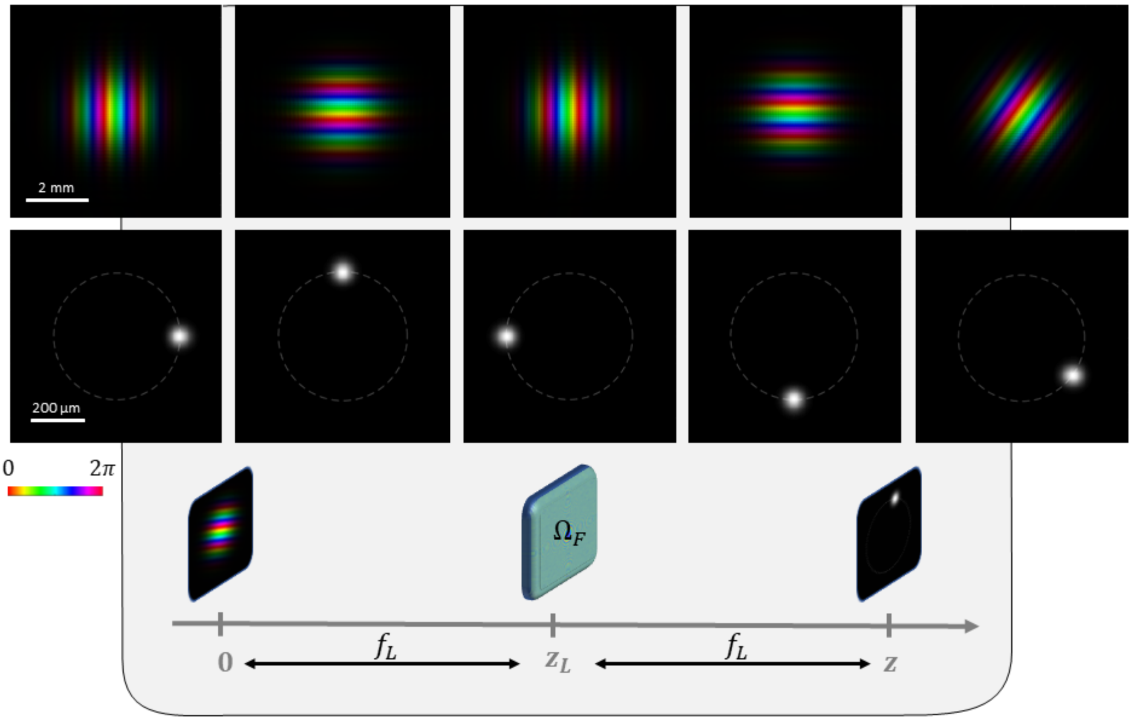

Figure 23: Demultiplexing of Gaussian beams characterized by a wavelength $\lambda = 632.8\,\mathrm{nm}$, and a linear phase gradient (as expressed by the equation 92) for different values of ϕ_0. The Fourier transforms are performed by a lens of focal length $f_L = 400\,\mathrm{mm}$ in a $f_L - f_L$ configuration. Brightness and colours refer to intensity and phase, respectively.

conserve the phase structure and the information contained in it. It can be proved as it follows. Considering again an initial structured light field, $u^{(i)}(r,\theta)$, described as in the equation 63

$$u^{(i)}(r,\theta) = U^{(i)}(r)e^{i\alpha_0 r^m \cos(m(\theta-\theta_0))} \tag{114}$$

where, in this case: $U^{(i)}(r)$ is an axially symmetric field distribution, for example a Gaussian beam (as the one produce by a common laser source, for instance). Moreover, (α_0, θ_0) are the initial phase strength and the phase orientations of the multipole-phase beam $u^{(i)}(r,\theta)$. With the aim of transmitting this field for a distance f, we impart, to the beam, a focusing term $\exp\{i\Omega_f\}$ with a phase

$$\Omega_f(r) = -\frac{k}{2f}r^2 \tag{115}$$

Therefore, the electromagnetic field, at a distance $z = f$, is described by the following diffraction integral

$$U^{(f)}(\rho,\phi) = \frac{e^{ik\frac{\rho^2}{2f}}}{i\lambda f}\iint U^{(i)}(r)e^{i\alpha_0 r^m \cos(m(\theta-\theta_0))}e^{-ik\frac{r\rho}{f}\cos(\theta-\phi)}r\,dr\,d\theta \tag{116}$$

Applying the stationary phase approximation, as done in the relation 67, we obtain

$$U^{(f)}(\rho,\phi) \propto \frac{e^{ik\frac{\rho^2}{2f}}}{i\lambda f}\frac{U^{(i)}(r^*)}{\sqrt{|H|}}e^{i\Phi(r^*\theta^*)} \tag{117}$$

where, again, $(r^*\theta^*)$ is the saddle point and H is the Hessian determinant of the phase term, Φ, of the argument, that is

$$\Phi(r,\theta) = \alpha_0 r^m \cos(m(\theta-\theta_0)) - k\frac{r\rho}{f}\cos(\theta-\phi) \tag{118}$$

In polar coordinates, the saddle point condition $\nabla\Phi = 0$ is equivalent to the following system

$$\begin{cases} \frac{\partial\Phi}{\partial r} = m\alpha_0 r^{m-1}\cos(m(\theta-\theta_0)) - k\frac{\rho}{f}\cos(\theta-\phi) = 0 \\ \frac{\partial\Phi}{\partial\theta} = -m\alpha_0 r^m \sin(m(\theta-\theta_0)) + k\frac{r\rho}{f}\sin(\theta-\phi) = 0 \end{cases} \tag{119}$$

whose solutions are

$$\begin{cases} \rho = \frac{mf\alpha_0}{k}r^{m-1} \\ \phi = (1-m)\theta + m\theta_0 \end{cases} \tag{120}$$

After inverting these equations and substituting in the relation 117, we obtain the phase term, of the beam in the diffraction integral 116, after the propagation for a distance f.

$$\begin{aligned} \Omega^{(f)}(\rho,\phi) &= \Phi(r^*,\theta^*) \\ &= \alpha_0\left(\frac{k\rho}{mf\alpha_0}\right)^{\frac{m}{m-1}}\cos\left(m\left[\frac{\phi}{1-m} - \frac{m}{1-m}\theta_0 - \theta_0\right]\right) - \\ &\frac{k\rho}{f}\left(\frac{k\rho}{mf\alpha_0}\right)^{\frac{1}{m-1}}\cos\left(\frac{\phi}{1-m} - \frac{m}{1-m}\theta_0 - \phi\right) \end{aligned} \tag{121}$$

Rearranging, we finally get the following expression for $\Omega^{(f)}$

$$\Omega^{(f)}(\rho,\phi) = \alpha_0(1-m)\left(\frac{k\rho}{mf\alpha_0}\right)^{\frac{m}{m-1}}\cos\left(\frac{m}{m-1}(\phi-\theta_0)\right) \tag{122}$$

Notice, from the cosine factor and the radial power

$$\cos\left(\frac{m}{m-1}(\phi-\theta_0)\right) \tag{123}$$

that the transmitted beam is still endowed with a multipole-phase term 90 but with a new phase order, m', expressed by the following relation

$$m' := \frac{m}{m-1} \tag{124}$$

As anticipated, since the phase structure of a multipole-phase beam depends on m, this beam can be propagated without the alteration of the information contained in its phase structure, only if $m' \equiv m$. This is satisfied, apart from the trivial case $m = 0$, only by the family of multipole-phase beams of order $m = 2$. For these fields, the equation 122 becomes

$$\Omega^{(f)}(\rho,\phi) = -\frac{1}{\alpha_0}\frac{k^2}{4f^2}\rho^2\cos\left(2(\phi-\theta_0)\right) \tag{125}$$

which can be rewritten in the usual form 90 of a multipole phase term

$$\Omega^{(f)}(\rho,\phi) = \alpha_1\rho^2\cos(2(\phi-\theta_1)) \tag{126}$$

where, now, the phase strength and the phase orientation are transformed into the following

$$\begin{cases} \alpha_1 = \frac{k^2}{4f^2}\frac{1}{\alpha_0} \\ \theta_1 = \theta_0 + \frac{\pi}{2} \end{cases} \tag{127}$$

where the $\pi/2$ term, arises from the factor $(1-m) \overset{m=2}{\equiv} -1$ in the equation 122. Remember, indeed, that $-\cos(\beta) \overset{(1)}{=} \cos(\pi-\beta)$ and, therefore:

$$\begin{aligned} \Omega^{(f)}(\rho,\phi) &\propto -\cos\left(2[\phi-\theta_0]\right) \\ &\overset{(1)}{=} \cos\left(2[\phi-\theta_0]-\pi\right) \\ &= \cos\left(2\left[\phi-\theta_0-\frac{\pi}{2}\right]\right) \end{aligned} \tag{128}$$

At this point, another phase factor $-\frac{k}{2f}\rho^2$, has to be applied in order to compensate the Fresnel's term present in the equation 117. Then, the transmitted beam is obtained. However, the transformation of the beam's parameters, accordingly to the equations 127, implies that the detected beam will be slightly different from the original one. Indeed, the phase structure will be rotated of $\pi/2$ and the phase strength will be changed as a function of the propagation distance f. From the figure 24 it is possible to see, easily, how the transmitted beam has a phase orientation rotated of $\pi/2$.

3.5 Distortion of circular-sector transformation for multipole-phase beams

In the theoretical framework introduced in this chapter, we have used the stationary phase approximation assuming an input field which was a planar wave. However, physically, no electromagnetic field has a wavefront which is exactly planar.

In the paraxial ray approximation, a ray that impinges, on the position $\boldsymbol{r_0} := (x_0, y_0)$, on a phase plate with a pattern Ω, placed in the plane $z = 0$, is deflected to the position [57]

$$\boldsymbol{r}(z) = \boldsymbol{r_0} + \frac{z}{k}\boldsymbol{\nabla}\Omega|_{\boldsymbol{r_0}} \tag{129}$$

In our case, we want to perform a circular-sector transformation of a multipole-phase beam. Therefore, Ω, will be the sum

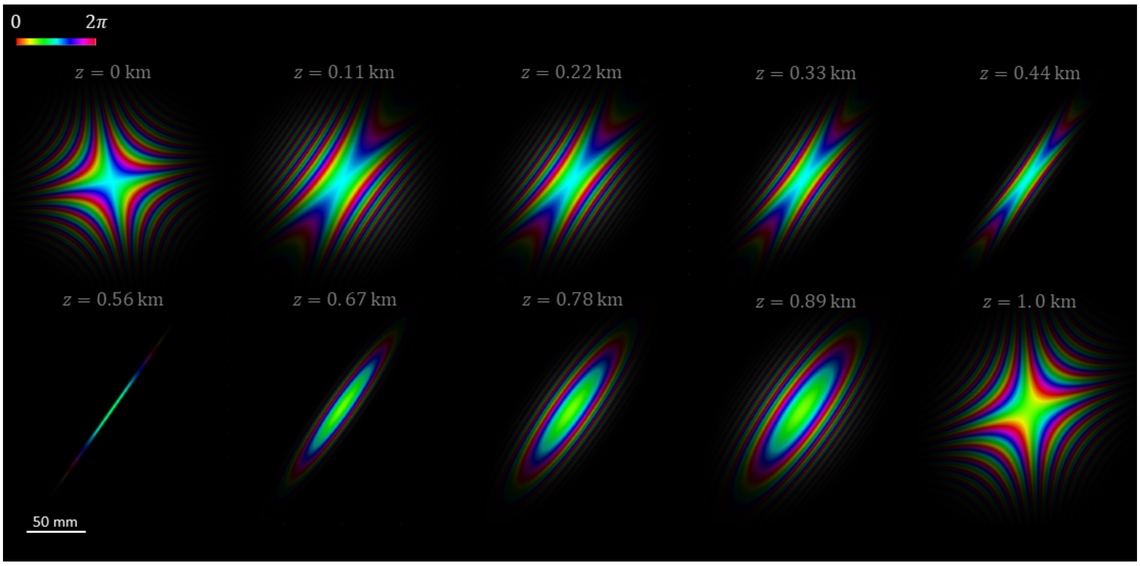

Figure 24: The evolution of a multipole-phase beam in a free space propagation of 1 km. The beam has the following characteristics: wavelength $\lambda = 632.8\,\mathrm{nm}$, waist $w_0 = 60\,\mathrm{mm}$, phase strength $\alpha = 6 \times 10^{-3}\mathrm{mm}^{-2}$ and phase orientation $\theta_0 = \pi/3$. Brightness and colours refer to intensity and phase, respectively.

$$\Omega := \Phi^{(in)} + \Omega_n \tag{130}$$

of the phase of the impinging multipole-phase beam $\Phi^{(in)}$ (given by the equation 90), and the phase pattern, Ω_n, of the Transformer of the n-fold circular-sector transformation (given by the equation 101). Indeed, in order to generate and sort a multipole-phase beam, we need to impart to an initial light field (for example the output beam of a laser) a phase function $\Phi^{(in)}$ and, then, the phase term Ω_n. Substituting these two phase terms in the equation 129 and performing the derivation, we obtain

$$\begin{cases} x(z) = r\cos\theta\left(1 - \frac{z}{f}\right) + \frac{az}{f}\left(\frac{r}{b}\right)^{-\frac{1}{n}}\cos\left(\frac{\theta}{n}\right) + \frac{z}{k}\alpha m r^{m-1}\cos((m-1)\theta - m\theta_0)) \\ y(z) = r\sin\theta\left(1 - \frac{z}{f}\right) + \frac{az}{f}\left(\frac{r}{b}\right)^{-\frac{1}{n}}\sin\left(\frac{\theta}{n}\right) - \frac{z}{k}\alpha m r^{m-1}\sin((m-1)\theta - m\theta_0)) \end{cases} \tag{131}$$

where $(x_0, y_0) = (r\cos\theta, r\sin\theta)$. At the focal plane, these equations become

$$\begin{cases} x(f) = a\left(\frac{r}{b}\right)^{-\frac{1}{n}}\cos\left(\frac{\theta}{n}\right) + \frac{f}{k}\alpha m r^{m-1}\cos((m-1)\theta - m\theta_0)) \\ y(z) = a\left(\frac{r}{b}\right)^{-\frac{1}{n}}\sin\left(\frac{\theta}{n}\right) - \frac{f}{k}\alpha m r^{m-1}\sin((m-1)\theta - m\theta_0)) \end{cases} \tag{132}$$

At this point, considering the radial distance $R := \sqrt{x^2 + y^2}$ as function of the angle ϕ, defined as $\phi := \theta/n$, we get

$$R(r,\phi)|_{z\equiv f} = \sqrt{a^2\left(\frac{r}{b}\right)^{-\frac{2}{n}} + \left(\frac{f}{k}\alpha m r^{m-1}\right)^2 + 2\frac{af\alpha m}{kb^{-1/n}}r^{m-\frac{1}{n}-1}\cos\left[n(m-1)\phi - m\theta_0 + \phi\right]} \tag{133}$$

Then, remembering that between the order, n, of the n-fold circular-sector transformation, and the phase order, m, of the multipole-phase beam sorted by that transformation, there is the relation $n = -1/m$, the previous equation becomes

$$R(r,\phi)|_{z\equiv f} = \sqrt{a^2\left(\frac{r}{b}\right)^{2m} + \left(\frac{f}{k}\alpha m r^{m-1}\right)^2 + 2\frac{af\alpha m}{kb^m}r^{2m-1}\cos\left[\frac{\phi}{m} - m\theta_0\right]} \tag{134}$$

which is, due to the cosine term, an oscillating function with period of $2\pi|m|$. However, notice that the factor, before the cosine function, can be rewritten as

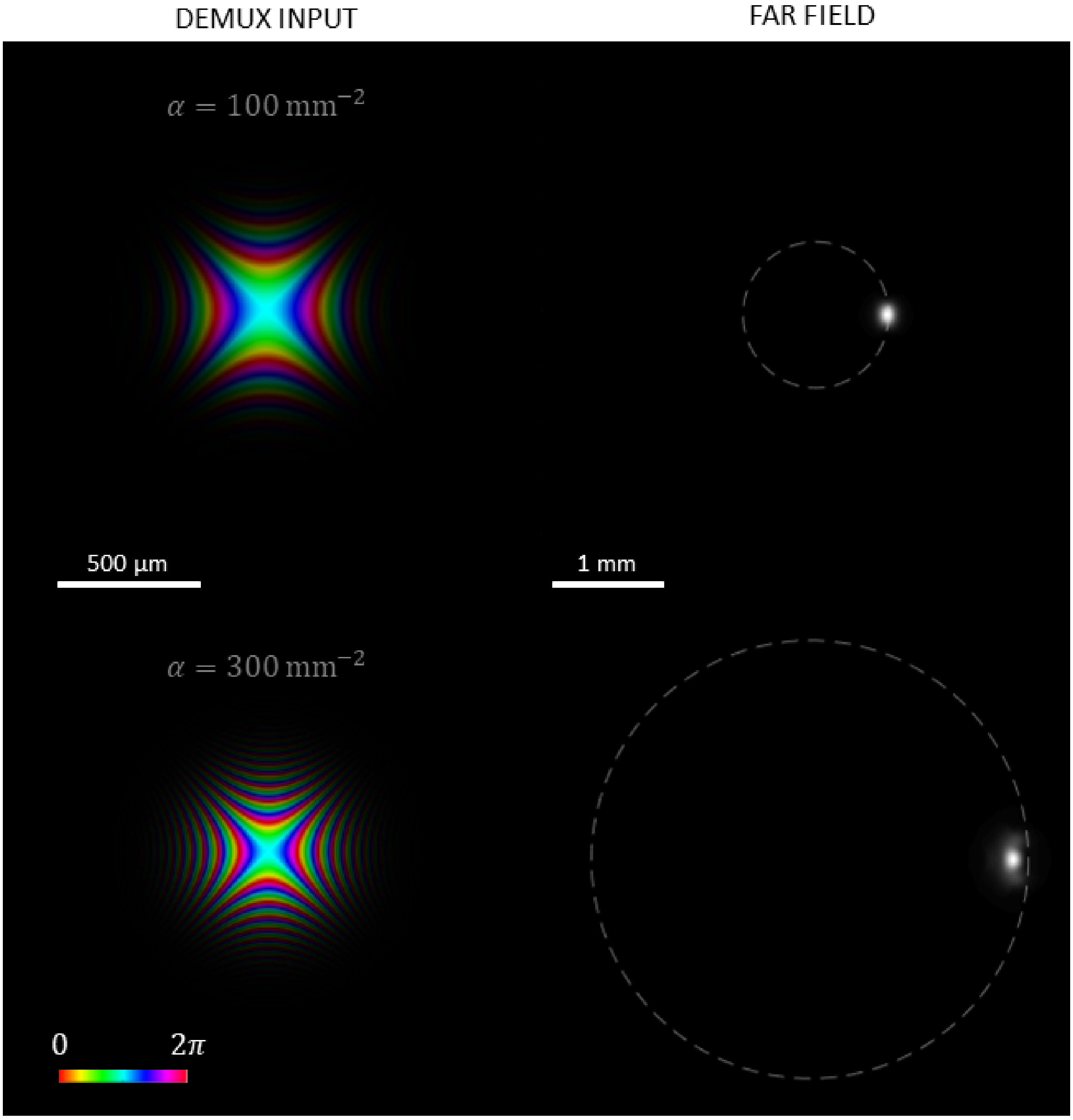

Figure 25: Effects of a phase distortion in the sorting of two multipole-phase beams of phase strengths $\alpha^{(1)} = 100\,\mathrm{mm}^{-2}$ and $\alpha^{(2)} = 300\,\mathrm{mm}^{-2}$, for the same parameters of circular-sector transformation: $a = 1.0\,\mathrm{mm}$, $b = 0.4\,\mathrm{mm}$, $f = 10.0\,\mathrm{mm}$ and for the same beam waist $w_0 = 312\,\mu\mathrm{m}$. On the left, the input multipole-phase beams are reported, while the demultiplexed light spots are show on the right. The dashed lines indicate the theoretical radial coordinate of the sorted beams, as expressed in equation 113. Brightness and colours refer to intensity and phase, respectively.

$$2\left(\frac{f}{k}\alpha m r^{m-1}\right) a\left(\frac{r}{b}\right)^m \tag{135}$$

Therefore, in the following condition

$$\frac{f}{k}\alpha m r^{m-1} \ll a\left(\frac{r}{b}\right)^m \tag{136}$$

the oscillating term is negligible. Notice that this condition corresponds to

$$\left|\boldsymbol{\nabla}\Phi^{(in)}\right| \ll \left|\boldsymbol{\nabla}\Omega_n\right| \tag{137}$$

which is the request that the changing of the phase structure, $\Phi^{(in)}$, of the impinging beam, has to be much smaller than the scale of variation of the phase pattern of the Transformer. In this way, the CS-phase plate "sees" a wavefront which has a very smaller gradient and, therefore, the assumption of plane wave in the stationary phase approximation is satisfied. Moreover, the previous relation suggests a limit condition for the phase strength α of the input multipole-phase beam, which is

$$\alpha \ll \frac{kaw_0}{fmb^m} \tag{138}$$

where we have assumed, as an estimation of the average radius, r, of the input beam, its waist w_0.
For instance, in figure 25, it is reported the demultiplexing of two multipole-phase beams of phase strength $\alpha^{(1)} = 100\,\mathrm{mm}^{-2}$ and $\alpha^{(2)} = 300\,\mathrm{mm}^{-2}$, for the same parameters of circular-sector transformation: $a = 1.0\,\mathrm{mm}$, $b = 0.4\,\mathrm{mm}$, $f = 10.0\,\mathrm{mm}$ and for the same beam waist $w_0 = 312\,\mu\mathrm{m}$ of the input beam. Notice how, due to the high value of $\alpha^{(2)}$, the demultiplexing of this multipole-phase beam produces an output light spot which is more distorted, with respect to the one obtained with the phase strength $\alpha^{(1)}$. Indeed, from the equation 138, with the parameters adopted, the limit of the phase strength is $\alpha \approx 970\,\mathrm{mm}^{-2}$, which is not so far from $\alpha^{(2)}$.

3.6 Quasi-orthogonality of the multipole-phase beams

Until now, we have supposed a perfect orthogonality of a set of multipole-phase beams with different values of the phase strength $\{\alpha_i\}$ and/or phase orientation $\{\theta_{0,i}\}$. In order to verify this, we have considered a double configuration of multipole-phase beams. The first set is made up of three multipole-phase beams with the same phase strength value $\alpha_1 = 120\,\mathrm{mm}^{-2}$ but different orientations in the range of 2π (beams 1, 2 and 3). Then, a second set is considered, where the beams have, now, the same three orientations of the first configuration, but different phase strength value $\alpha_2 = 60\,\mathrm{mm}^{-2}$ (beams 4, 5 and 6). In this way, the orthogonality of multipole-phase beams with same orientation but different phase strengths, and beams with same phase strength, but different phase orientations, are both investigated. The double configuration is reported in figure 26, where, on the left, we can see the multipole-phase beams, obtained from Gaussian spots of wavelength $\lambda = 632.8\,\mathrm{nm}$ and waist $w_0 = 0.312\,\mathrm{mm}$, after the application of a phase term as expressed in equation 90. Notice, from the colours of the simulated beams, how the first three fields have a higher 2π-phase density due to a higher phase strength with respect to the others three beams. Therefore, in according to the equation 113, the two set of beams will be demultiplexed onto two concentric distributions of light spots: the internal one, related to the lower phase strength $\alpha_2 = 60\,\mathrm{mm}^{-2}$, and the external one corresponding to the phase strength $\alpha_1 = 120\,\mathrm{mm}^{-2}$. On the right of the figure, these two output distributions are shown.
Now, the orthogonality of these beams has to be investigated. Imposing with $\psi_{\alpha_i,\theta_{0,i}}$ the multipole-phase beam of phase strength α_i and phase orientation $\theta_{0,i}$, the overlap between them are expressed by the following normalized integral:

$$w_{i,j} = \frac{|\langle\psi_{\alpha_i,\theta_{0,i}}|\psi_{\alpha_j,\theta_{0,j}}\rangle|^2}{\langle\psi_{\alpha_i,\theta_{0,i}}|\psi_{\alpha_i,\theta_{0,i}}\rangle\langle\psi_{\alpha_j,\theta_{0,j}}|\psi_{\alpha_j,\theta_{0,j}}\rangle} = \frac{|\langle\psi_{\alpha_i,\theta_{0,i}}|\psi_{\alpha_j,\theta_{0,j}}\rangle|^2}{|\psi_{\alpha_i,\theta_{0,i}}|^2|\psi_{\alpha_j,\theta_{0,j}}|^2} \tag{139}$$

The results of this computation are reported on the left of the figure 27. Notice how the integrals $w_{i,j}$ are

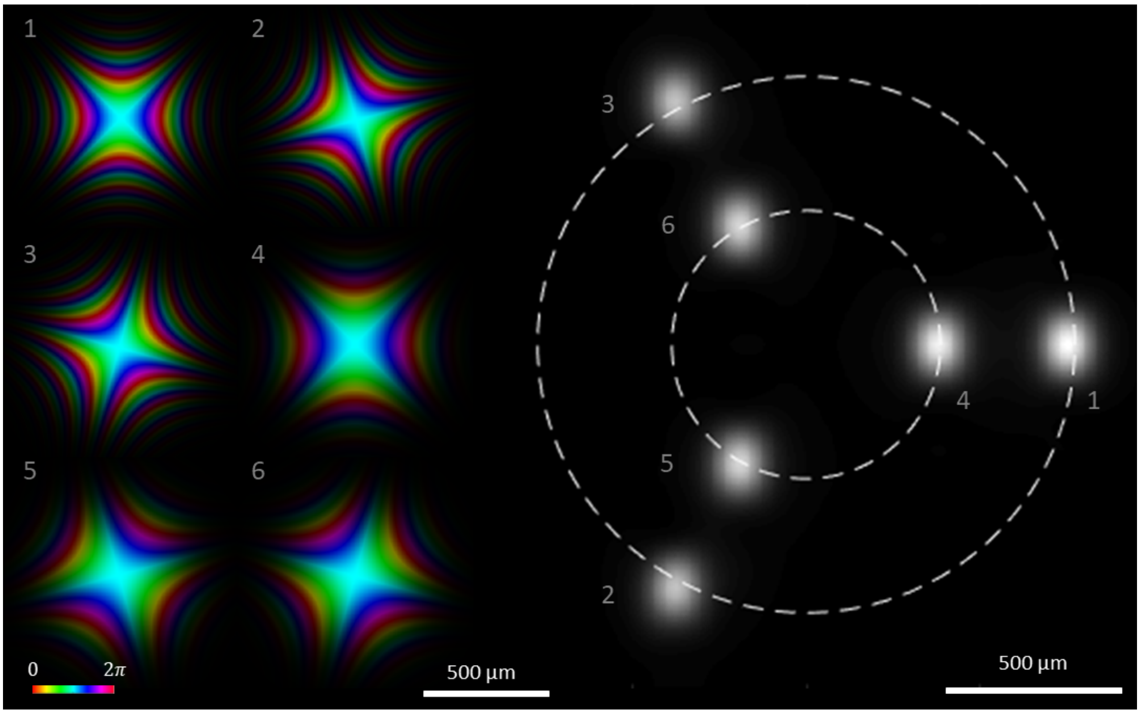

Figure 26: A configuration of six multipole-phase beams $\{\psi_{\alpha_i,\theta_{0,i}}\}$ with different phase strengths and orientations, for the same phase order $m = 2$, and obtained from an initial set of Gaussian beams, with wavelength $\lambda = 632.8\,\mathrm{nm}$ and waist $w_0 = 0.312\,\mathrm{mm}$, using a circular-sector transformation of parameters: $a = 1.0\,\mathrm{mm}$, $b = 0.4\,\mathrm{mm}$, and $f_{CS} = 10\,\mathrm{mm}$. The output configuration of the light spots (on the right, in figure), is obtained thanks to a Fourier lens with focal length $f_L = 400\,\mathrm{mm}$, and it is composed by two concentric distribution of spots. The external one, is made up of $N_1 = 3$ beams related to multipole-phase beams of phase strength $\alpha_1 = 120\,\mathrm{mm}^{-2}$ and orientations $\theta_0 \in [0; \frac{2\pi}{m}]$ with steps of $\frac{1}{m}\frac{2\pi}{N_1}$. The internal one, instead, corresponds to multipole-phase beams with the same orientations but with a phase strength $\alpha_2 = \alpha_1 * 0.5$. The dashed white circles on the right indicate the theoretical radial coordinates of the sorted beams, related to the phase strength values as expressed in equation 113 Brightness and colours refer to intensity and phase, respectively.

plotted as a $M \times M$ matrix, where $M = 6$ is the number of distinct multipole-phase beams analysed, $\{\psi_{\alpha_i,\theta_{0,i}}\}$ with $i = 1, ..., M$. As expected, the off-diagonal elements are negligible, only the overlaps between a multipole-phase beam and itself are significant, and the beams can be assumed orthogonal, at least in a telecommunication meaning. Indeed, as it will be described in detail in the chapter 6, in the telecommunication system, in order to quantify the independence of communication channels transmitted together, it was introduced the Cross-Talk XT quantity.

3.6.1 Cross-Talk in the overlap analysis

Considering the i-channel, whose information content is transmitted by a field $\psi_{\alpha_i,\theta_{0,i}}$, the relative Cross-Talk value, XT_i, is defined as the amount of signals, $\sum_{j\neq i} w_{i,j}$, collected into this channel, but due to the others fields $\{\psi_{\alpha_j,\theta_{0,j}}\}_{j\neq i}$, normalized for the total information collected by that channel:

$$XT_i = 10\log_{10}\frac{\sum_{j\neq i} w_{i,j}}{\sum_j w_{i,j}} \tag{140}$$

Using this equation, the Cross-Talk values for the configuration of multipole-phase beams analysed, are computed and plotted on the right of the figure 27. In the telecommunication, XT-values lower than -15dB are considered acceptable.

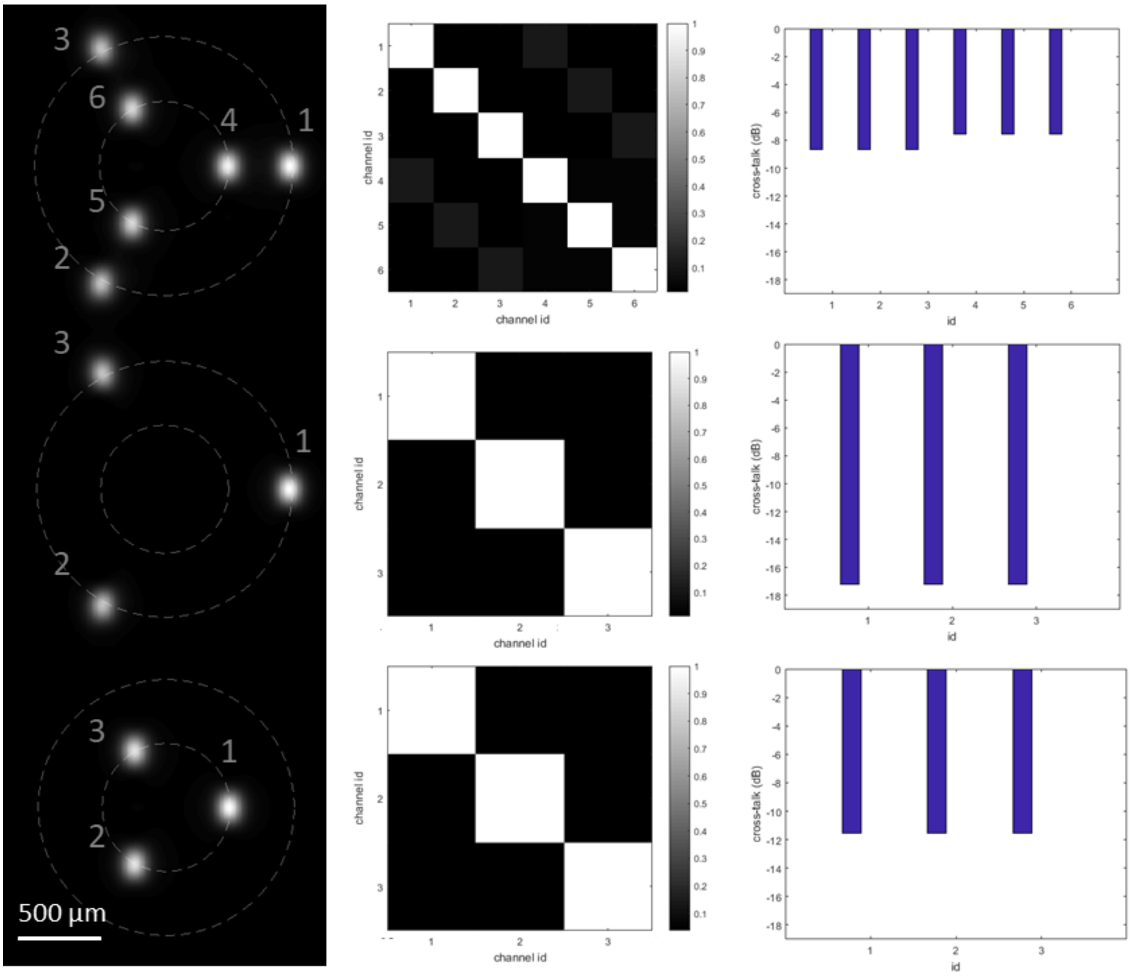

Figure 27: The overlapping maps of the configuration of multipole-phase beams reported in figure 26, computed with the integral 139, and the relative XT values. The two concentric distribution were analysed separately (last two rows) and together (first row).

4 Demultiplexing of a multipole phase beam

In chapter 3 we have seen that applying an n-fold circular-sector transformation with $n = -1/m$, a multipole-phase beam of order m is mapped onto a linear phase gradient. The importance of this phenomenon is that, applying a Fourier transformation in sequence, we can produce a light spot whose position depends on the intensity and the orientation of this linear gradient. However, according to the equation 92, these characteristics of the phase pattern are related to the two parameters of the initial multipole-phase beam: the phase strength, α, and the phase orientation, θ_0. For this reason, a superposition of multipole-phase beams, characterized by different values of α and/or θ_0, can be sorted onto a set of isolated light spots which can act as independent channels of information. As introduced in chapter 3, and as it can be seen in figure 28, this demultiplexing process is performed by three optical elements. The first one, the circular-sector plate (CS), transforms the phase of the wavefront onto a linear phase gradient. The second element, the phase-corrector (PC), corrects the phase distortion introduced by the propagation after the (CS) plate. Finally, a lens transforms the linear phase gradient into a single light spot, where its position depends on the (α, θ_0) values of the original multipole phase beam.

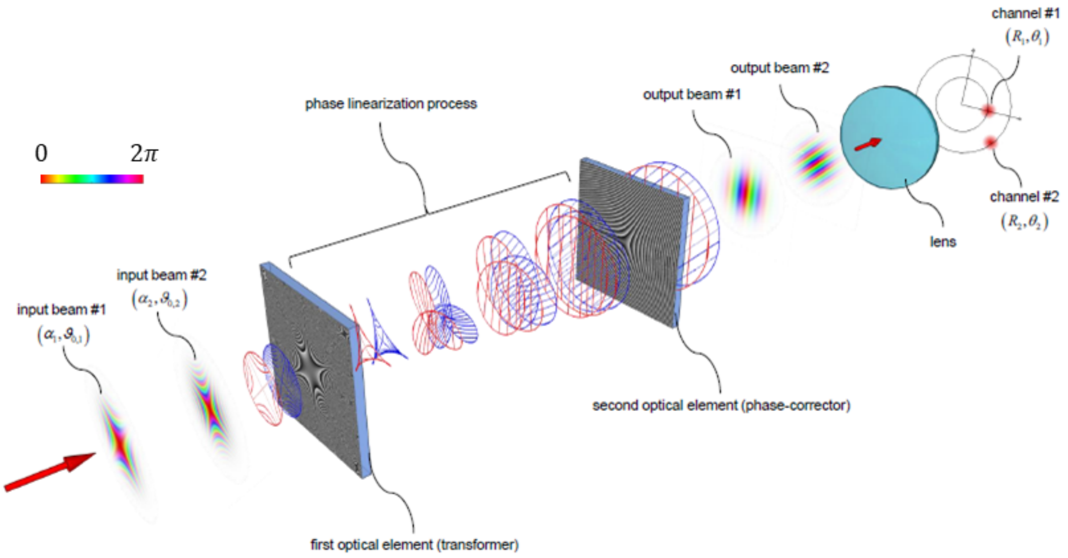

Figure 28: Demultiplexing of two multipole-phase beams with different phase strength and orientation. A first phase plate (the Transformer) is used in order to transform the initial superposition of multipole-phase patterns into a sum of linear phase gradients, while a second plate (the Phase Corrector) compensates the phase distortion introduced by the propagation after the Transformer. Finally, a Fourier lens focalizes the demultiplexer output into two distinct light spots related to the two different initial multipole-phase beams.

4.0.1 Dependence on θ_0

We know that changing the value of θ_0, the circular-sector transformation produces linear phase gradients with different orientations on the plane orthogonal to the propagation direction. For example, a multipole-phase beam with four different values of θ_0 is reported in figure 29 (first row). The corresponding fields after the Phase Corrector, with the expected linear phase gradients, are also reported (second row). It is possible to notice the orientation variations of the coloured stripes, as a function of the θ_0 value (remember that the colour represents the phase value in a range of 2π).

At this point, however, we recall that applying a Fourier transform to a generic linear phase gradient that rotates on the transversal plane, for example using a lens (of focal length f_L and characterized by a phase term $\Omega_F = -k\frac{r^2}{2f}$) in a $f_L - f_L$ setup (as the one reported in figure 30), one gets a configuration of single spots distributed on a circle, as reported in the third row of figure 29. In a system of polar coordinates (r, θ), each spot is, therefore, identified by its angle $\theta = -m\theta_0$ (see equation 91), which is related to the orientation of the linear phase gradient and, therefore, by the θ_0 value of the initial multipole-phase beam of order m.

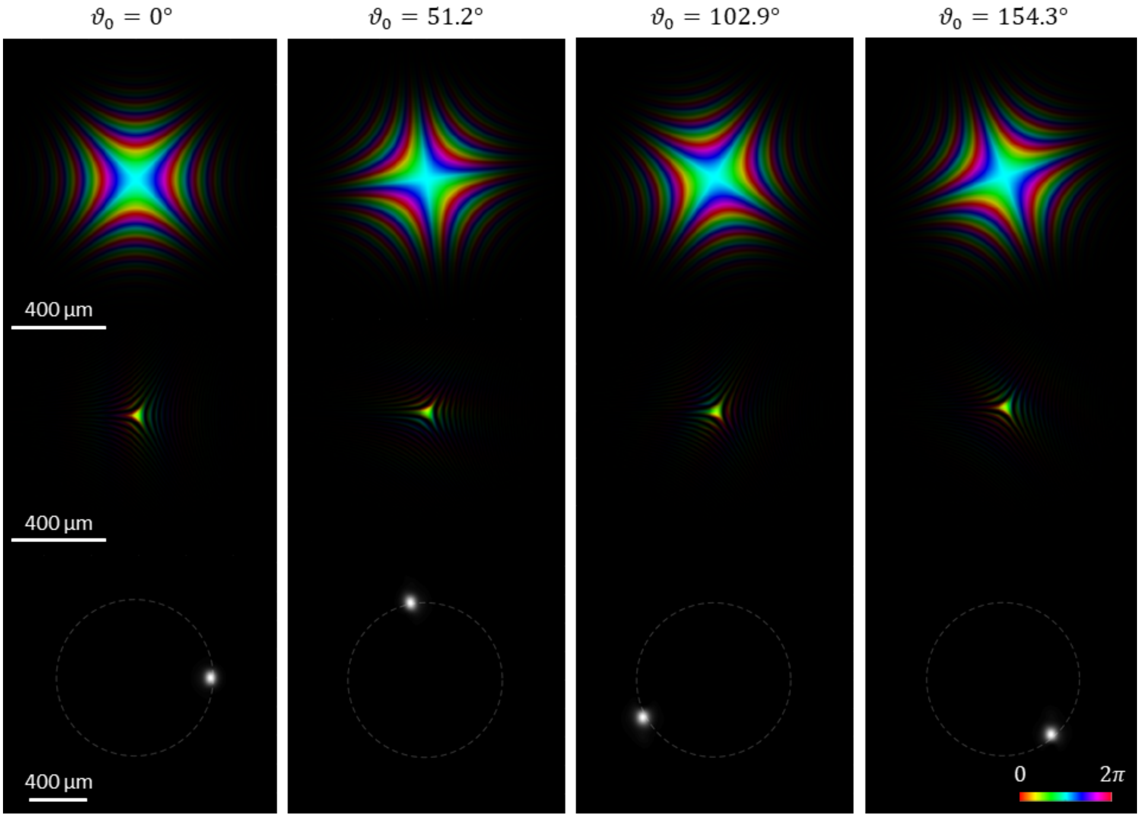

Figure 29: Four multipole-phase beams with the same phase strength, $\alpha = 1.5 \times 10^2 \mathrm{mm}^{-2}$, but different orientations $\theta_0 \in [0; \pi]$, are reported in the first row of the figure. The linear phase gradients obtained by the circular-sector transformation of these initial multipole-phase beams are shown in the second row. The parameters of the transformation are: $f_{CS} = 10\,\mathrm{mm}$, $a = 0.5\,\mathrm{mm}$ and $b = 0.3\,\mathrm{mm}$. Finally, these linear phase gradients are sorted in the final light spots reported in the last row of the figure. As usual, brightness and colours refer to intensity and phase, respectively.

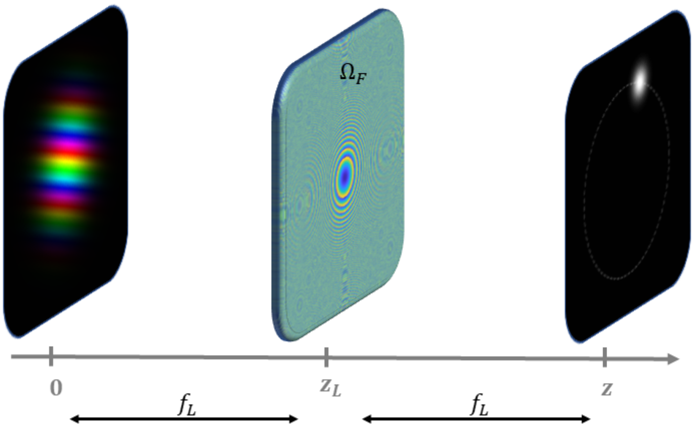

Figure 30: The $f_L - f_L$ configuration used, in the simulation of the figure 29, for the transformation of the linear phase gradients into isolated light spots at the distance z. The Fourier lens has a focal length of $f_L = 200\,\mathrm{mm}$ and is placed in z_L corresponding to the position of the Phase Corrector. Alternatively, in our simulation, the phase correction of the beam and the focusing of the spots are performed by the same plate, whose phase pattern is the sum of the focusing term Ω_F and the phase term Ω_{PC} of the Phase Corrector.

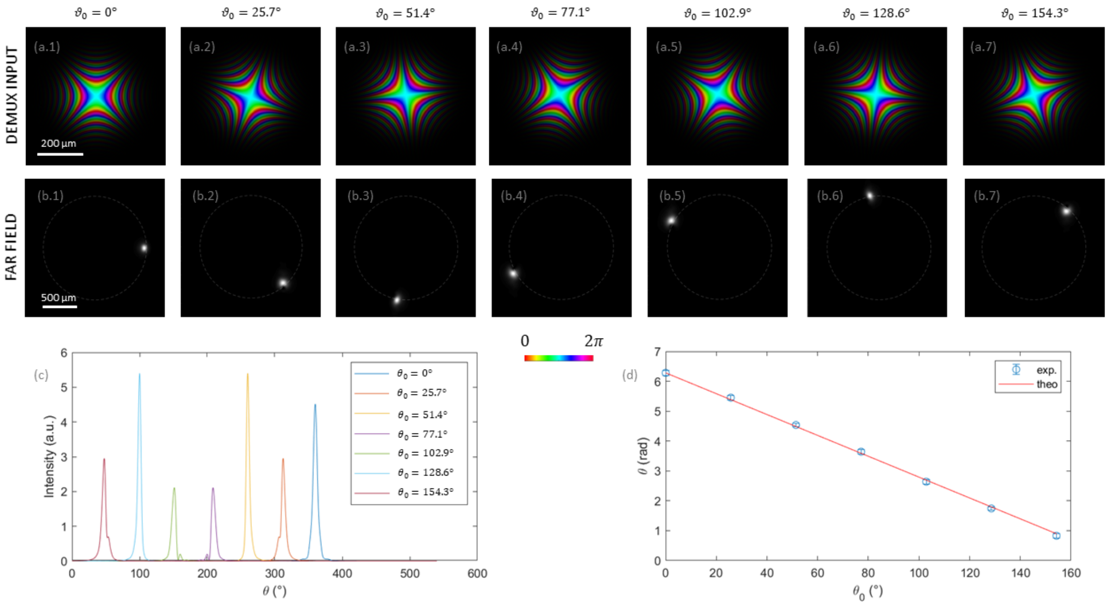

Figure 31: On the top, seven multipole-phase beams characterized by the same phase strength $\alpha = 100\,\text{mm}^{-2}$ but different orientations $\theta_0 \in [0, \frac{2\pi}{m}]$ (a.1, ..., a.7). Brightness and colours refer to intensity and phase, respectively. In the second row (b.1, ..., b.7), we found the fields after the demultiplexing of the input multipole-phase beams with the following parameters of the circular-sector transformation: $f_{CS} = 10\,\text{mm}$, $a = 0.5\,\text{mm}$, $b = 0.3\,\text{mm}$, while the focal length, used in the sorting of the light spots, is $f_L = 200\,\text{mm}$. On the bottom, instead, we have the cross-sections of the intensity of the output light spots as a function of the polar coordinate (c) and the plot of the spots positions obtained from the fit with a Gaussian profile (d).

These observations tell us that the phase orientation, θ_0, is a first degree of freedom regarding the propagation of independents channels in a communication system. Indeed, we can propagate a bundle of multipole-phase beams with the same phase strength but different orientations, and then, sort them into a circular configuration of isolated spots. That is, choosing a proper set of phase orientations $\{\theta_{0,1}, ..., \theta_{0,N}\}$ in a range of $[0, \frac{2\pi}{m}]^1$, we are able to produce light spots sufficiently far from each other in order to detect them unambiguously. In figure 31, for example, are reported the input multipole-phase beams of order $m = 2$ (a) and the output spots (b) for seven different values of θ_0 (and the same $\alpha = 100\,\text{mm}^{-2}$). In order to evaluate the simulated spots angular positions as a function of θ_0 (d), a Gaussian fit of the intensity of the electromagnetic field, along the circle of the expected positions of the spots, is performed (c). The correct *slope* = -2, correspondent to $\theta = -m\theta_0$ with $m = 2$, is found (red line in (d)).

4.0.2 Dependence on α

The other degree of freedom we can play with is the phase strength α. Indeed, as reported in figure 32, multipole-phase beams with different α-values, after the circular-sector transformation, produce spots with a linear phase gradient that complete its 2π-phase period a number of times that increases with $|\alpha|$. However, as it can be seen from the last row of the figure, inserting a lens in the same $f_L - f_L$ configuration as seen before, the higher ”dense” linear phase gradients produce the most external light spots. Therefore, controlling the phase strength, one can set the displacement of the spots from the centred one, corresponded to α null.

In this way it is possible to create, this time, a linear configuration of isolated channels keeping θ_0 fix and changing α. For example, in figure 33, a simulation of an input multipole-phase beams of order $m = 2$ (a), and the output spots (b), for seven different values of $\alpha \in [-200, 200]\text{mm}^{-2}$ (and the same $\theta_0 = 0°$) is reported. In order to evaluate the spots positions as a function of α (d), a Gaussian fit of the intensity of the electromagnetic field, along the line of the expected arrangement of the spots, is performed (c). It is worth noting, from the fit results, that the position of each simulated output beam intersects correctly the theoretical line (red in figure). This means that the spots are actually arranged in a row, i.e., no variation of their azimuthal coordinate is

---

[1] The factor $\frac{1}{m}$ is necessary in order to have the final spots arranged on the entire circumference. Indeed, we remember that mapping a multipole phase beam into a linear phase gradient, the angular coordinate undergoes the transformation: $\theta_0 \to -m\theta_0$

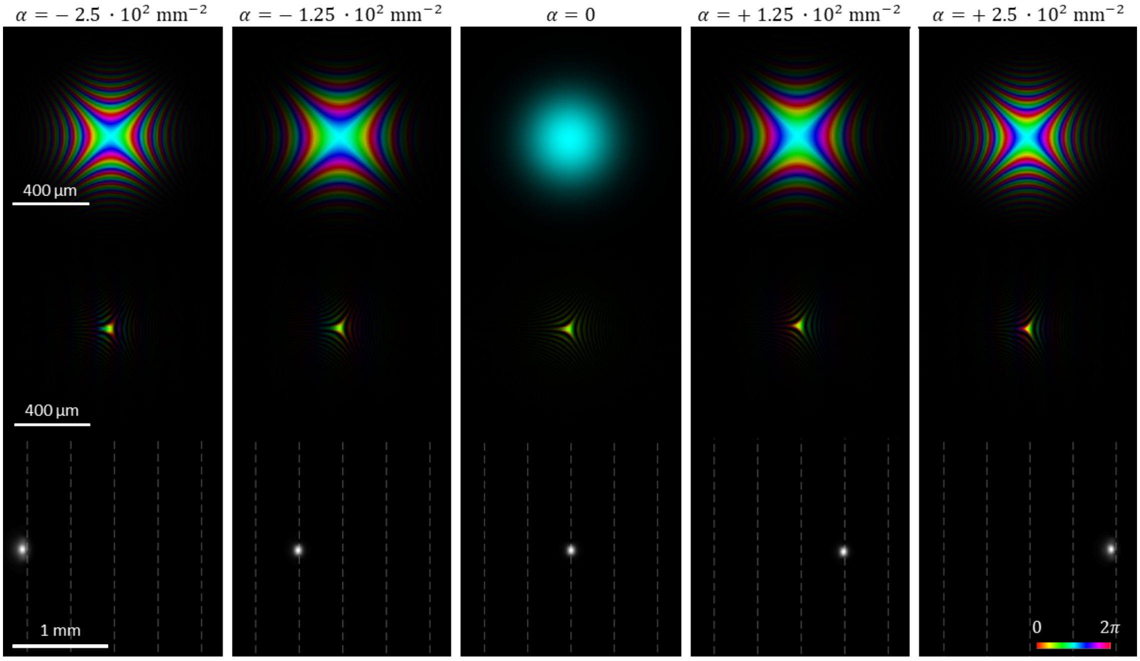

Figure 32: Five multipole-phase beams with the same phase orientation, $\theta_0 = 0$, but different phase strength $\alpha \in [-2.5; +2.5] \times 10^2 \mathrm{mm}^{-2}$, are reported in the first row of the figure. The linear phase gradients obtained by the circular-sector transformation of these initial multipole-phase beams are shown in the second row. The parameters of the transformation are: $f_{CS} = 10\,\mathrm{mm}$, $a = 0.5\,\mathrm{mm}$ and $b = 0.3\,\mathrm{mm}$. Finally, these linear phase gradients are sorted in the final light spots reported in the last row of the figure. As usual, brightness and colours refer to intensity and phase, respectively.

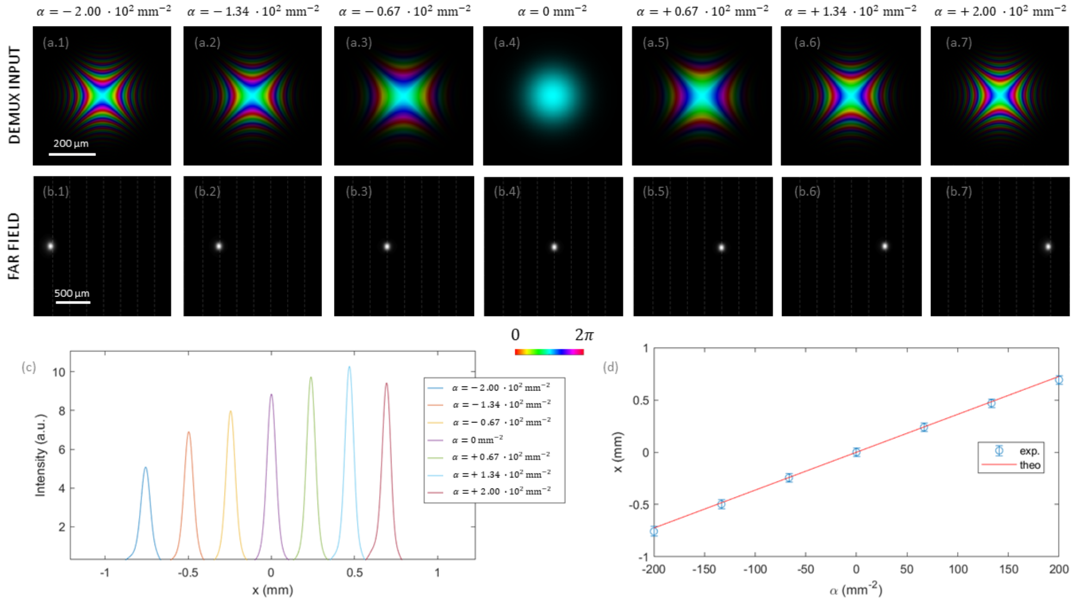

Figure 33: On the top, seven multipole-phase beams characterized by the same phase orientation $\theta_0 = 0°$ but different phase strength in the range $\alpha \in [-2.0, +2.0] \times 10^2 \mathrm{mm}^{-2}$ (a.1, ..., a.7). Brightness and colours refer to intensity and phase, respectively. In the second row (b.1, ..., b.7), we found the fields after the demultiplexing of the input multipole-phase beams with the following parameters of the circular-sector transformation: $f_{CS} = 10\,\mathrm{mm}$, $a = 0.5\,\mathrm{mm}$, $b = 0.3\,\mathrm{mm}$, while the focal length, used in the sorting of the light spots, is $f_L = 200\,\mathrm{mm}$. On the bottom, the cross-sections of the intensity of the output light spots as a function of the position (c) and the plot of the spots positions obtained from the fit with a Gaussian profile (d).

induced if θ_0 is kept constant. Similarly, in the previous case, we had seen that the final spots were correctly placed onto the expected circle (the dashed line in b.1, ..., b.7 of the figure 31); i.e., there is no variation of the radial coordinate if α is kept constant. These two results show that the phase strength and the phase orientation are, actually, independent degrees of freedom for the final arrangement of the light spots.

4.1 Demultiplexing simulation of a set of multipole-phase beams

Now, we want to analyse in detail the simulation steps, with the relative MatLab code, necessary to perform the demultiplexing of a set of multipole-phase beams as seen, from a theoretical point of view, until now. In particular, referring to the example configuration of final light spots shown in the figure 34, will be considered the evolution of the multipole-phase beam corresponding to the second spot (in anticlockwise order starting from $\theta_0 = 0$) along the whole multiplexing chain.

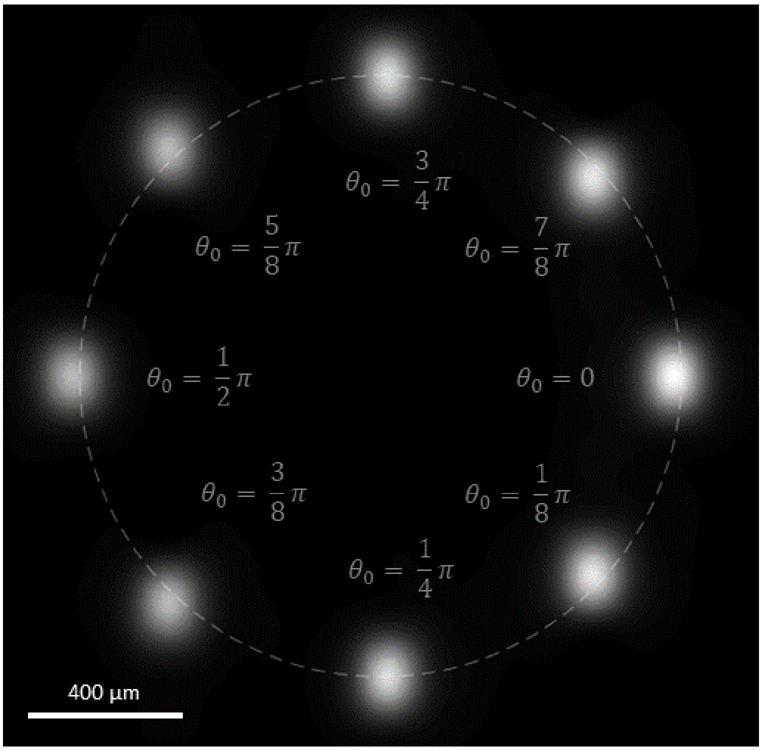

Figure 34: The output of the simulation considered in this section. Starting from eight initial multipole-phase beams of order $m = 2$ and characterized by a phase strength $\alpha^{(1)} = 120\,\text{mm}^{-2}$ and $\theta_0 \in [0, \frac{2\pi}{m}]$, we have obtained the shown result thanks to a circular-sector transformation of parameters: $f_{CS} = 10\,\text{mm}$, $a = 1.0\,\text{mm}$ and $b = 0.4\,\text{mm}$. Brightness refers to intensity.

4.1.1 Definition of the observation plane

The first step is the definition of the coordinates of the plane on which we will simulate and sample the wavefront of our light beams. Indicating with L the linear size and with M the number of samples along each axis, the discretization of the observation plane is the following

$$x \rightarrow \left[-\frac{L}{2} : \Delta_x : \frac{L}{2} - \Delta_x\right] \tag{141}$$

where $\Delta_x = \frac{L}{M}$ as already described in the section 2.2.1. In the following is reported the MatLab code of this discretization.

Listing 4.1.1: space discretization

```
    dx          = L/M;                      % sample interval
    x           = -L/2 : dx : L/2-dx;       % x coords
    y           = x;                        % y coords
```

```
    [X,Y]         = meshgrid(x,y);         % cartesian coords
    [theta, r]    = cart2pol(X,Y);         % polar coords
```

In figure 35 it is represented the observation plane and the polar coordinates used in the field propagation. Notice that the sampling is the same on both x and y-axis.

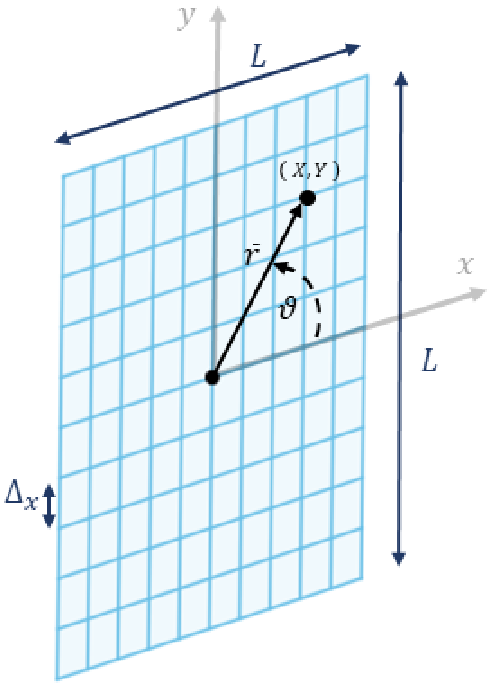

Figure 35: A representation of the squared observation plane of side L used in order to compute the simulated wavefronts reported in this section. It is also shown the mesh grid with the same sampling interval $\Delta_x = L/M$ for both axes. Notice how, each pixel of the mesh, is defined by the coordinates (X, Y) of one of its vertexes. The relative polar coordinates are also reported.

4.1.2 The initial light beam

Once defined the observation plane, in order to generate a multipole-phase beam, an initial Gaussian beam, $u_0(r, \theta)$, is produced:

$$u_0(r,\theta) = \exp\left\{ -\left(\frac{r}{w_0}\right)^2 \right\} \tag{142}$$

where w_0 is the beam waist. The simulated wavefront of this initial field is reported in figure 36, while the MatLab code of its generation is the following:

Listing 4.1.2: initial gaussian beam

```
    u0 = exp(-(r/w0).^2);
```

4.1.3 Definition of the multipole-phase beam

After the creation of the initial Gaussian beam, each i-th multipole-phase beam, $u_1^{(i)}$, of our configuration, is generated individually[2]. In figure 36, for example, is reported the wavefront of the multipole-phase beam related to the spot corresponding to $\theta_0 = \frac{\pi}{8}$ of the configuration in figure 34. As usual, the colours represent the phase values in a range of 2π and brightness refers to intensity.

---

[2] Thanks to the orthogonality of multipole phase beams with different α and/or θ_0 and to the linearity of the optical system this is irrelevant on the final result

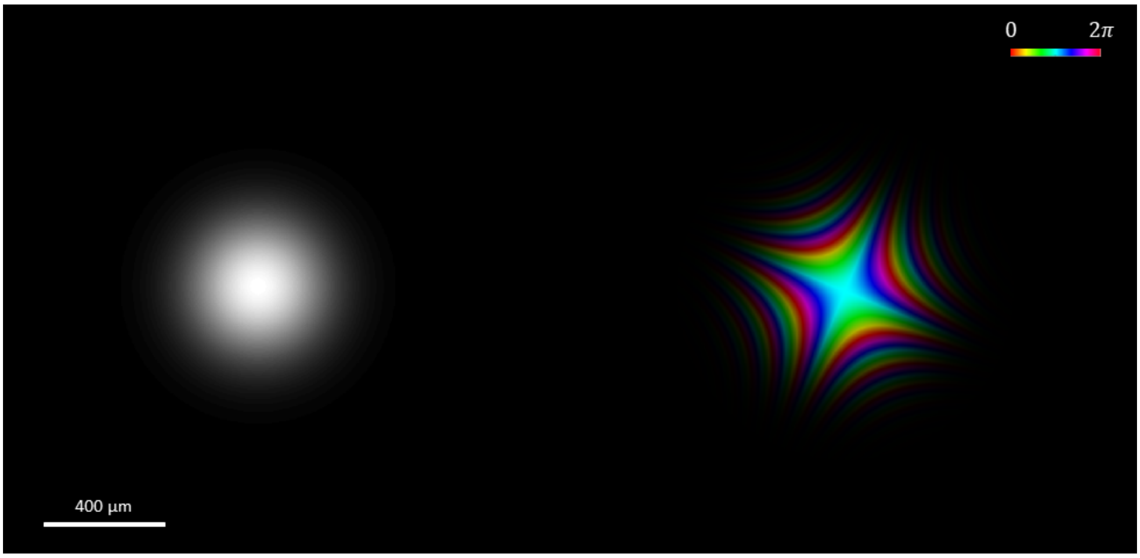

Figure 36: On the left, a simulated Gaussian beam with wavelength $\lambda = 632.8\,\mathrm{nm}$ and waist $w_0 = 312\,\mu\mathrm{m}$. On the right, the relative multipole-phase beam, characterized by a phase strength $\alpha^{(1)} = 120\,\mathrm{mm}^{-2}$ and orientation $\theta_0 = \frac{\pi}{8}$, corresponding to the second light spot in clockwise order of the configuration reported in figure 34. Brightness and colours refer to intensity and phase, respectively.

The MatLab code is reported in the following where we have applied, to each points (r, θ) of the wavefront of the initial field, u_0, the multipole-phase term expressed by the equation 90:

$$\Omega(r, \theta) = \alpha r^m \cos[m(\theta - \theta_0)] \tag{143}$$

Listing 4.1.3: i-th multipole phase beam

```
    u1(:,:,i) = u0.*exp(1i*alpha(i)*(r.^m).*cos(m*(theta-theta0(i))));
```

4.1.4 Circular-sector transformation

At this point, the multipole-phase beams of order m generated, have to be sorted in the final isolated light spots. For this reason, the n-fold circular-sector transformation with $n = -1/m$, is implemented by the first optical element: the Transformer (CS). This phase plate produces the unwrapping of the multipole phase beam (first line of the MatLab code 4.1.4) and its transformation into a linear phase gradient at the distance f_{CS}, where is placed the second element: the Phase Corrector (PC). For this reason, the beam is free space propagated for a such distance f_{CS} (second line of the code) using the macro described in the chapter 2. Finally, the beam arrives at the Phase Corrector (PC), which compensates the phase distortion introduced during the free space propagation between these two phase plates (third line of the code). We call $\Omega^D_{m,1}$ the phase function of the Transformer ("Phase1" in the MatLab code) and $\Omega^D_{m,2}$ the one of the Phase Corrector ("Phase2 in the code).

Listing 4.1.4: Circular-sector transformation

```
1      u1(:,:,i) = u1(:,:,i).*exp(1i*Phase_1);                  % CS transform
2      u1(:,:,i) = FreeSpaceProp(u1(:,:,i),L,lambda,f_CS);      % prop. CS - PC
3      u1(:,:,i) = u1(:,:,i).*exp(1i*Phase_2);                  % Phase Correction
```

Remembering the equations 101, 103 and using the substituting $n \longleftrightarrow -1/m$, we obtain the following expressions for $\Omega^D_{m,1}$ and $\Omega^D_{m,2}$:

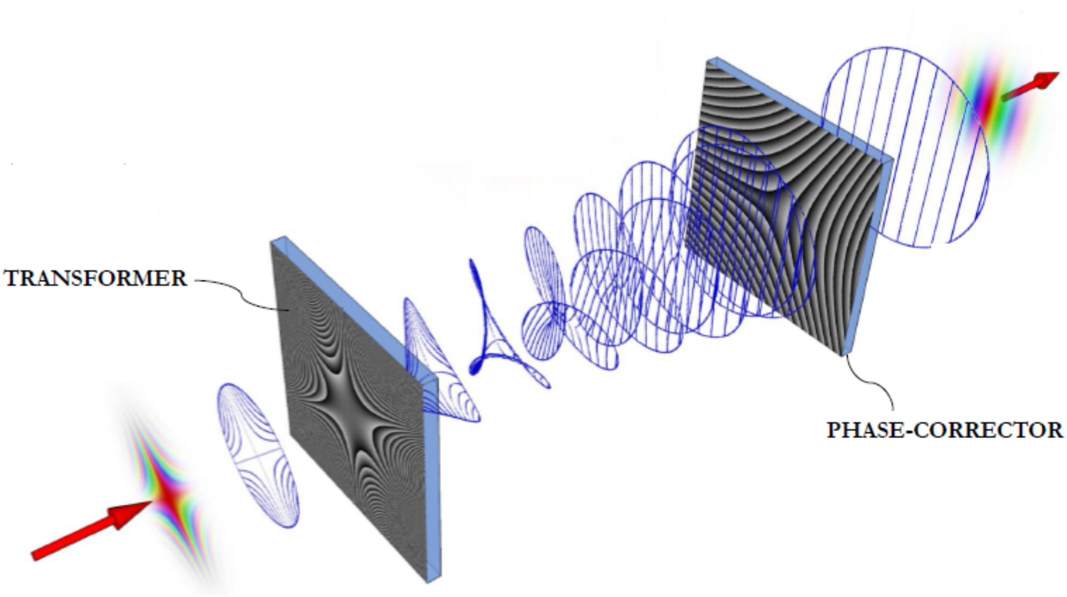

Figure 37: A detailed representation of a circular-sector transformation of a multipole-phase beam into a linear phase gradient.

$$\Omega^D_{m,1} = \Omega_{CS} - k\frac{r^2}{2f_{CS}} \tag{144}$$

$$\Omega^D_{m,2} = \Omega_{PC} - k\frac{r^2}{2f_{CS}} \tag{145}$$

where Ω_{CS} and Ω_{PC} are defined as:

$$\Omega_{CS} = k\frac{ab}{f_{CS}}\left(\frac{r}{b}\right)^{1+m}\frac{\cos[(1+m)\theta]}{1+m} \tag{146}$$

$$\Omega_{PC} = k\frac{ab}{f_{CS}}\left(\frac{r}{a}\right)^{1+\frac{1}{m}}\frac{\cos[(1+\frac{1}{m})\theta]}{1+\frac{1}{m}} \tag{147}$$

with $k = \frac{2\pi}{\lambda}$, which is the wave vector. Notice in the equation 144, the addition of the focusing term $k\frac{r^2}{2f_{CS}}$ and, in equation 145, the addition of the same term which acts as a Fresnel correction. All the phase patterns are plotted, in period of 2π, in figure 38, where the parameters of the transformation are: $f_{CS} = 10\,\text{mm}$, $a = 1.0\,\text{mm}$ and $b = 0.4\,\text{mm}$.

The whole circular-sector transformation is schematized in figure 37, while, in figure 39 we can see a simulation of it. In the first frame we have the multipole phase beam at the input of the Transformer, then it is reported the wavefront of the field at different distances of the travel between the (CS) and (PC) phase plates. Finally, we have the field after the phase correction, where it is possible to see the coloured stripes of the linear phase gradient. Notice also, from figure 39, how the phase pattern Ω_{PC} is found on the wavefront structure of the output electromagnetic field. Similarly, for the phase pattern Ω_{CS} in the wavefront of the field in z null.

4.1.5 Focusing of the final spots

Finally, the demultiplexer output beams, whose wavefronts are characterized by linear phase gradients, are focalized into isolated light spots thanks to a Fourier lens of focal length f_L and phase function

$$\Omega_F(r,\theta) = -\frac{k}{2f_L}r^2 \tag{148}$$

After the application of the previous phase term (first line of the MatLab code 4.1.5), and a free-space

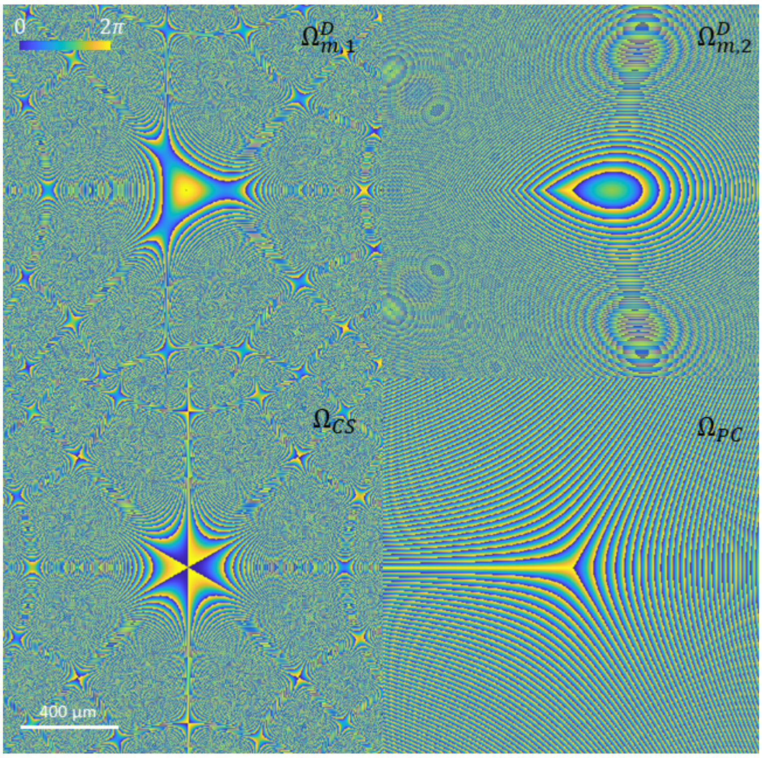

Figure 38: The phase patterns, $\left\|\frac{\Omega}{2\pi}\right\|$, of the plates performing the circular-sector transformation of the simulation analysed in this chapter. From the top left, in clockwise order: the phase pattern, $\Omega^D_{m,1}$, of the Transformer completed of the focusing term $-k\frac{r^2}{2f_{CS}}$ (equation 144), the pattern of the Phase Corrector, $\Omega^D_{m,1}$, including the same focusing term (equation 145) and, finally, the same two patterns, Ω_{CS} and Ω_{PC}, without the focusing terms (equations 146 and 147, respectively). The parameters used in order to generate these patterns are: $f_{CS} = 10\,\text{mm}$, $a = 1.0\,\text{mm}$ and $b = 0.4\,\text{mm}$.

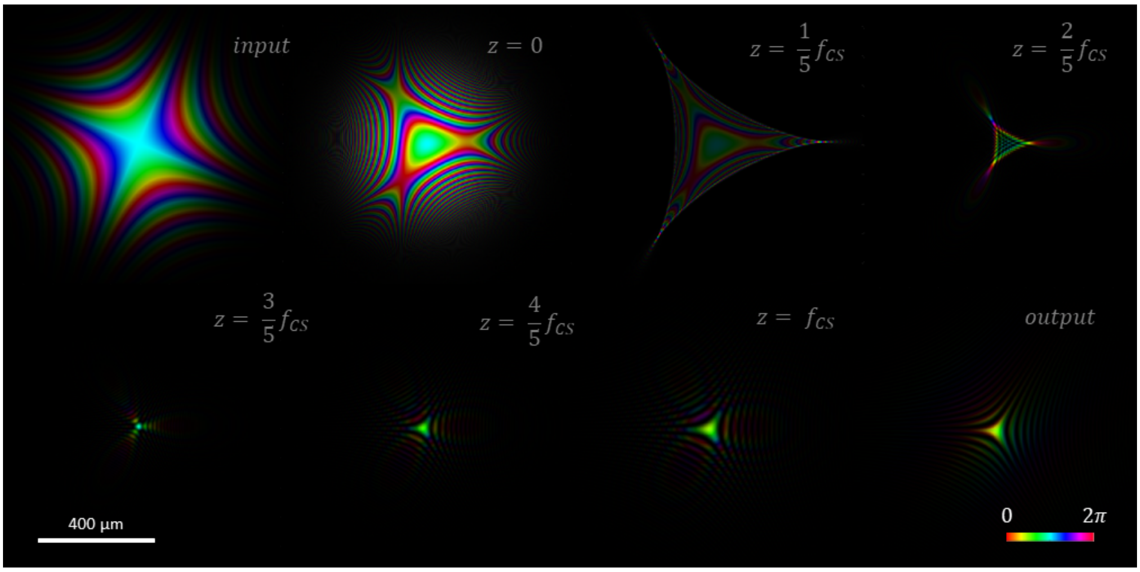

Figure 39: The circular sector transformation of the multipole-phase beam, reported in figure 36, of phase strength $\alpha^{(1)} = 120\,\text{mm}^{-2}$ and $\theta_0 = \frac{\pi}{8}$. The parameters of the circular-sector transformation are: $f_{CS} = 10\,\text{mm}$, $a = 1.0\,\text{mm}$ and $b = 0.4\,\text{mm}$. In the first and second frames, respectively, it is reported the multipole-phase beam before and after the application of the phase term $\Omega^D_{m,1}$. In the following frames we have the evolution of the field between the Transformer and the Phase Corrector placed in $z = f_{CS}$. Finally, the output beam with the linear phase gradient is shown in the last frame. As usual, brightness and colours refer to intensity and phase, respectively.

propagation for a distance equal to f_L (second line of the code), the spots appear.

Listing 4.1.5: Fourier transformation

```
    u1(:,:,i) = u1(:,:,i).*exp(1i*Phase_F);              % lens
    u2(:,:,i) = FreeSpaceProp(u1(:,:,i),L,lambda,f_L);   % final light spot
```

In figure 40 it is reported the intensity of the final field $u_2(r, \theta)$ for $f_L = 400\,\text{mm}$. It is possible to see that the multipole phase beam was converted into a single spot, placed at the angular coordinate $\theta = -m\theta_0$ and radial coordinate given by the equation 113.

$$R = f_L \frac{\lambda}{2\pi} \frac{\alpha b^m}{a} \tag{149}$$

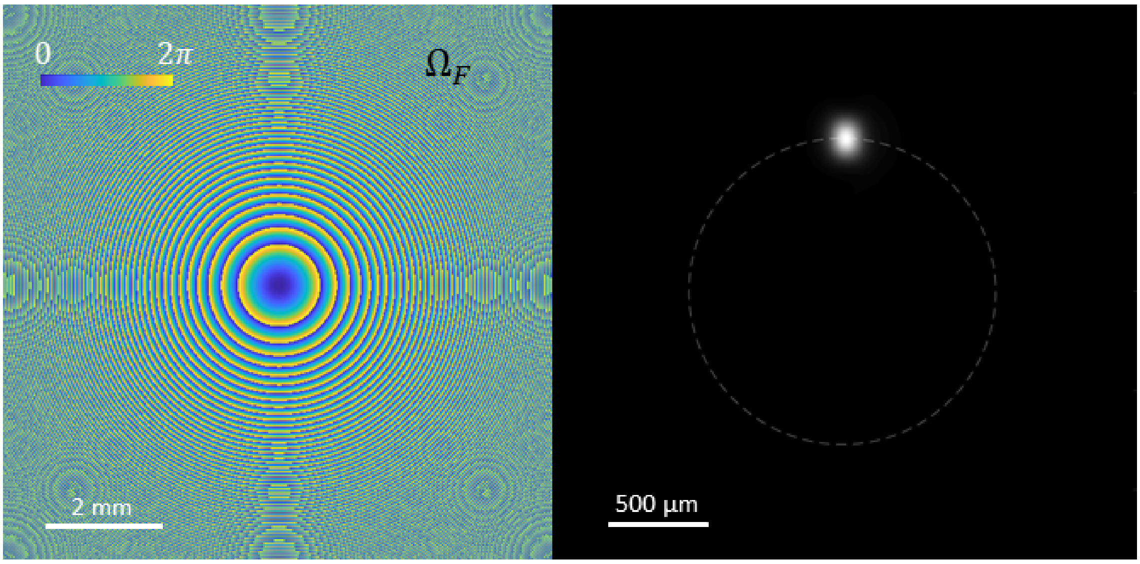

Figure 40: On the left, the Fourier phase term Ω_F, for a focal length $f_L = 400\,\text{mm}$, used in order to transform the linear phase gradient reported in the last frame of the figure 39 into the final light spot shown on the right of this figure.

4.2 Multipole-phase beam of higher orders

Until now, in order to get orthogonal multipole phase beams, which propagate independently, we have considered only the two parameters α and θ_0. However, even multipole-phase beams with the same (α, θ_0) couple of values, but different order parameter m, can be orthogonal. Therefore, m, is a further degree of freedom. On the top of the figure 41, for instance, it is shown three multipole-phase beams of order $m = 2$, 3 and 4 for the same phase strength, $\alpha = 100\,\text{mm}^{-2}$, and phase orientation, $\theta_0 = \frac{\pi}{3}$. These beams reported, tell us that changing the order m, new real families of multipole-phase beams with different phase structure are generated. This is quite obvious if one notice that the phase patterns, equations 146 and 147, of the two optical elements of the circular-sector transformation depend on m. For all these reasons, higher values of the phase order were investigated, in particular it was considered the demultiplexing of multipole-phase beams with $m = 3$ and $m = 4$. As shown on the bottom of the figure 41, multipole-phase beams, characterized by the same (α, θ_0) couple of values, but for different order, m, are demultiplexed into a set of light spots placed at different positions. Indeed, we remember that demultiplexing a multipole-phase beams, one obtain a light spot of polar coordinates

$$\begin{cases} r = f_L \frac{\lambda}{2\pi} \frac{\alpha b^m}{a} \\ \theta = -m\theta_0 \end{cases} \tag{150}$$

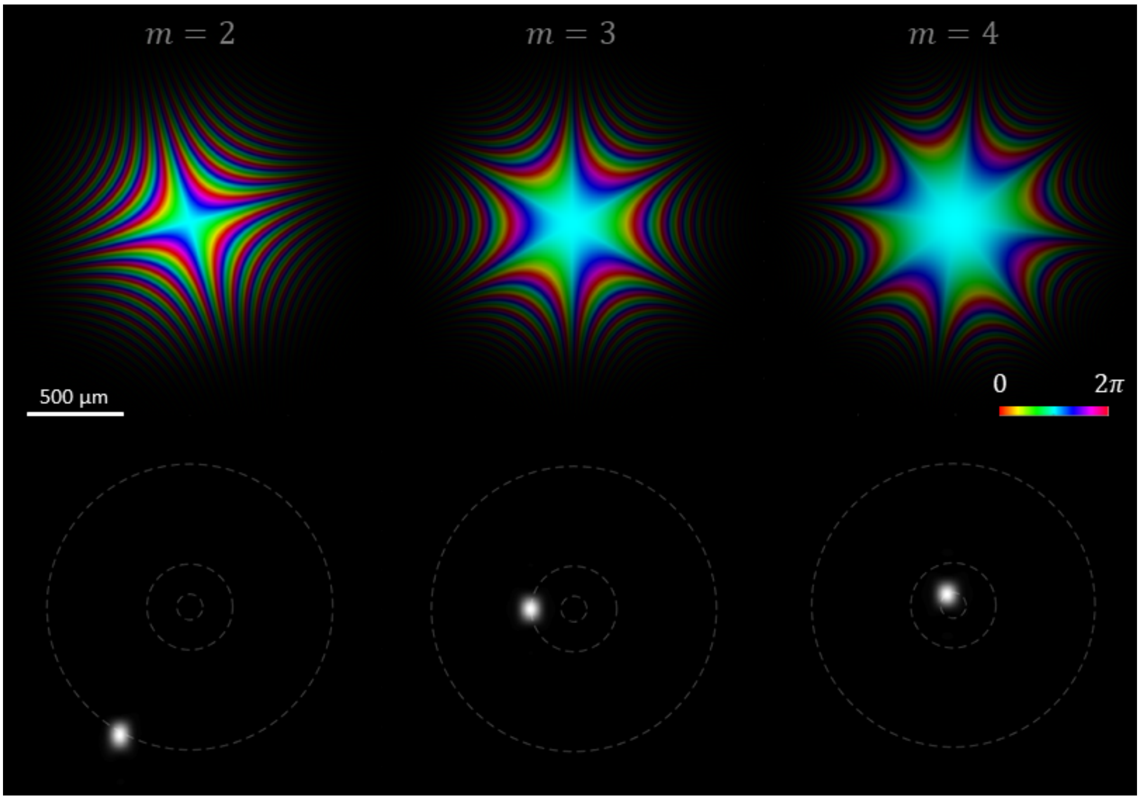

Figure 41: On the top, the wavefront of multipole-phase beams of order $m = 2$, 3 and 4 for the same modulus $\alpha = 100$ (but different units) of the phase strength and the same phase orientation $\theta_0 = \frac{\pi}{3}$. On the bottom, the relative sorted light spots after a demultiplexing characterized by the following parameters: $f_{CS} = 10\,\text{mm}$, $a = 0.5\,\text{mm}$, $b = 0.3\,\text{mm}$ and $f_L = 400\,\text{mm}$. Notice how the different phase order m implies different positions of the light spots. Brightness and colours refer to intensity and phase, respectively.

where the radial coordinate depends on the phase order thanks to the factor b^m while the azimuthal angle is proportional to m. For instance, the light spots shown in figure 41, are produced by the same setup with the following parameters: $a = 0.5\,\text{mm}$, $b = 0.3\,\text{mm}$ and $f_L = 400\,\text{mm}$. Since $b < 1$, the spots occupy a circle whose radius decreases to increasing m, while, the angle that define their position on these circle, increases with m (in the counterclockwise direction, due to the minus sign in the second equation of the system 150). For this reason, in the following chapters, in order to optimize the design of a demultiplexer for multipole-phase beams of different phase orders, the channels configuration will be defined by phase orientations $\{\theta_0\}$ in the range

$$\theta_0 \in \left[0, \frac{2\pi}{m}\right] \tag{151}$$

In this way, defining the θ_0 in units of m, the final light spots will be arranged on the whole circle.

In order to understand the differences in the phase structure of the multipole-phase beams of order $m = 2$, $m = 3$ and $m = 4$, in figure 42 it was reported the phase patterns, Ω_{CS} and Ω_{PC}, of the Transformer and of the Phase Corrector, respectively, of the circular-sector transformation used for the generation of the multipole-phase beams shown in figure 41. It is worth noting that it is shown the phase patterns without the usual focusing term, $-\frac{r^2}{2f_{CS}}$, in Ω_{CS} and without the same Fresnel's correction term in Ω_{PC}. From the phase structure of the CS-plates, for the different phase orders, it is possible to understand the analogy of the multipole-phase beams with the magnetostatic multipole field [58]. Indeed, incrementing m, more two-dimensional "lobes" are generated on the plane transversal to the propagation direction. Instead, as usual, the phase structure of the PC-phase plate is found in the output beam of the demultiplexer, as can be seen in figure 43 for the case $m = 2$. In the others two cases, the same pattern is less recognizable but still presents.

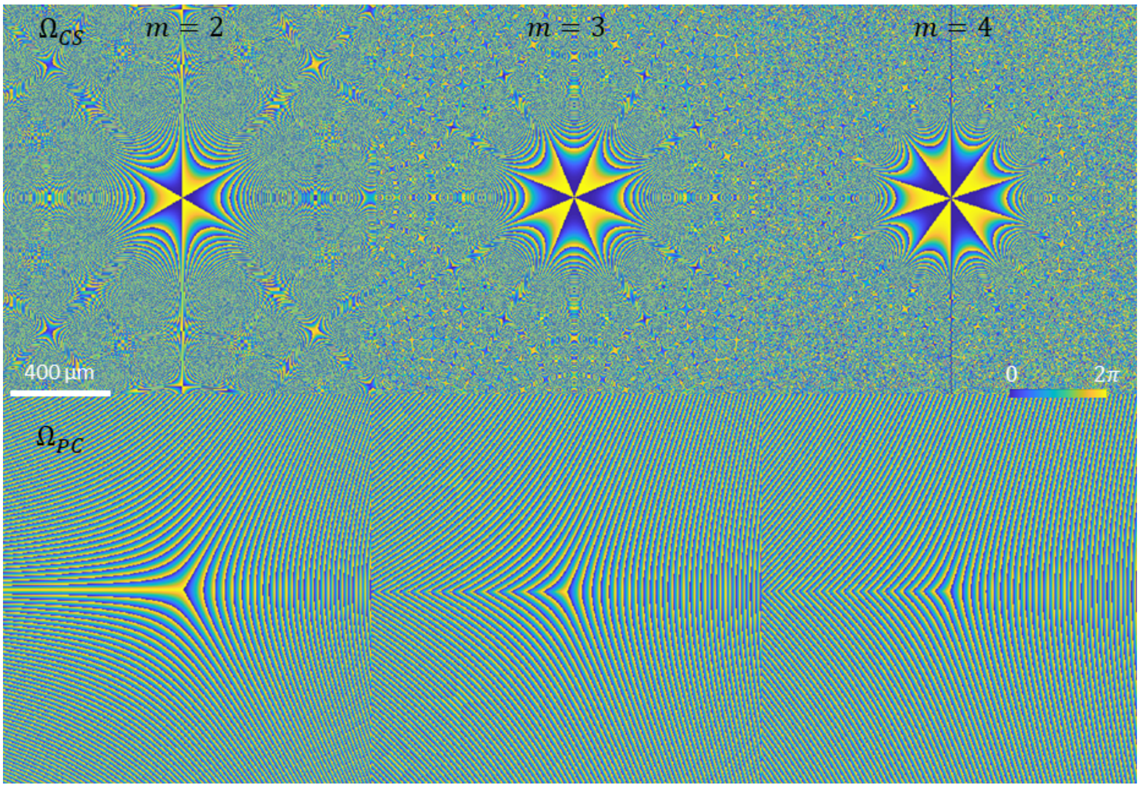

Figure 42: The phase patterns of the Transformer (Ω_{CS}) and the Phase Corrector (Ω_{PC}), without the focusing terms $-k\frac{r^2}{2f_{CS}}$, used for the circular-sector transformation of the multipole-phase beams reported in figure 41. The parameters of the circular-sector transformation are the same: $f_{CS} = 10\,\mathrm{mm}$, $a = 0.5\,\mathrm{mm}$ and $b = 0.3\,\mathrm{mm}$.

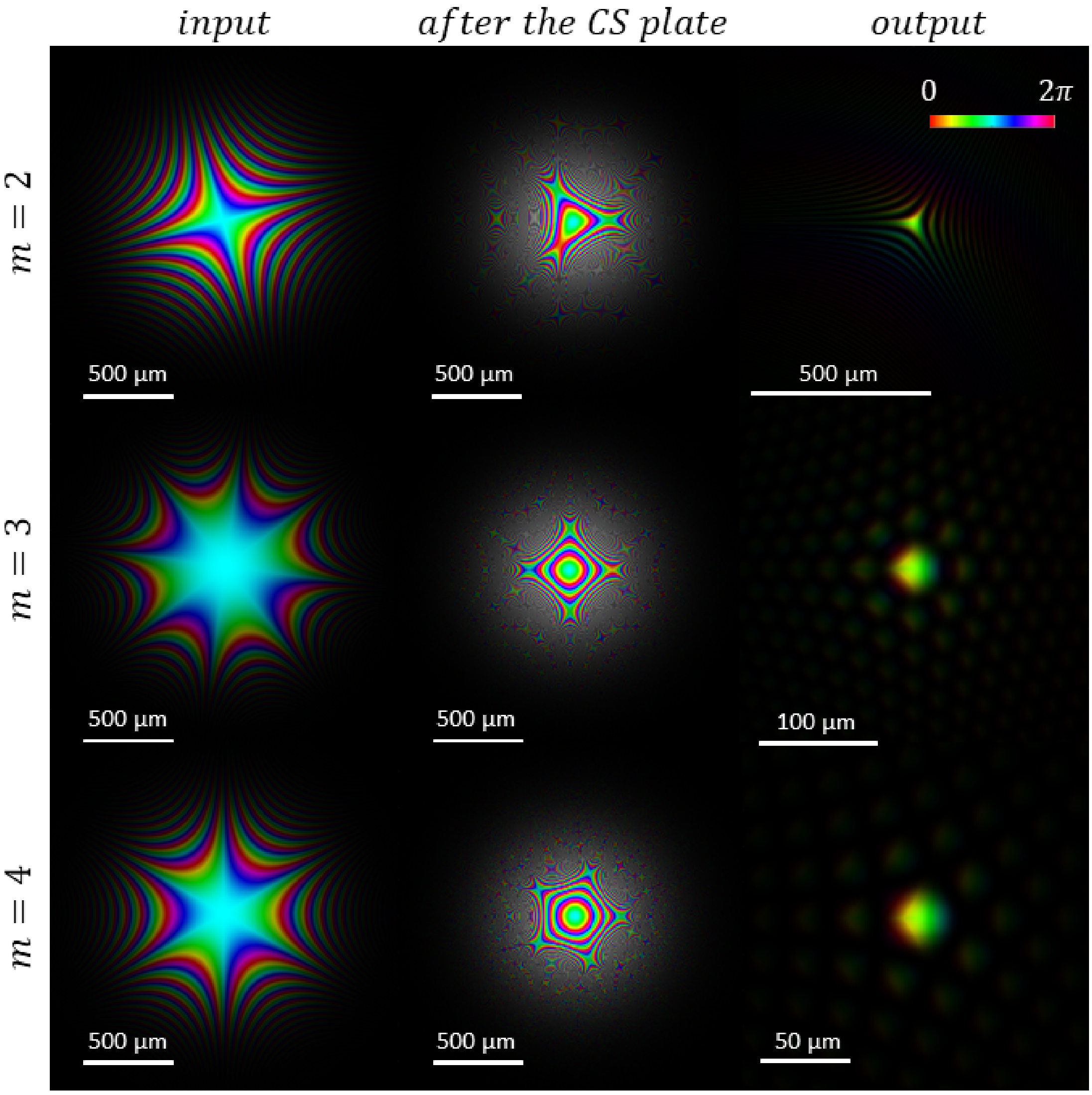

Figure 43: In analogy with the figure 37, here it is reported the simulations of the circular-sector transformation performed with the phase plates shown in figure 42 for the three multipole-phase beams of order $m = 2$, 3 and 4 analysed in this section. In particular, the input beams, the beams after the Transformer and the Phase Corrector, are shown. Brightness and colours refer to intensity and phase, respectively.

5 Multiplexing of a multipole-phase beam

In the previous chapter, we have seen the demultiplexing of multipole-phase beams into isolated light spots. Here we want to simulate the inverse process, i.e., the multiplexing of several input beams into a collimated bunch of multipole-phase beams with the same order m but differing in phase strength α and rotation angle θ_0. Indeed, each spot can be labelled by the polar coordinates of its centre (r_c, θ_c), which are related to the two parameters (α, θ_0) of the final multipole-phase beam by the following transformation:

$$\begin{cases} \theta_0 = -\frac{1}{m}\theta_c \\ \alpha = \frac{2\pi}{\lambda}\frac{a}{f_L b^m} r_c \end{cases} \tag{152}$$

where α is simply give by the inverse of the equation 113. As it will be demonstrated from the simulation results, the optical setup needed for a multiplexing process is the same[3], but in reverse order, as the demultiplexing case, and it is reported in the figure 44. Starting from a set of isolated light spots, thanks to a Fourier phase term (produced by a lens of focal length f_L), each beam is converted into an electromagnetic field with a wavefront characterized by a linear phase gradient. Then, the field is propagated through the same two optical elements of the circular-sector transformation seen for the demultiplexing, but in the reverse order. In this way, at the end, we obtain the superposition of the multipole-phase beams related to the starting light spots configuration.

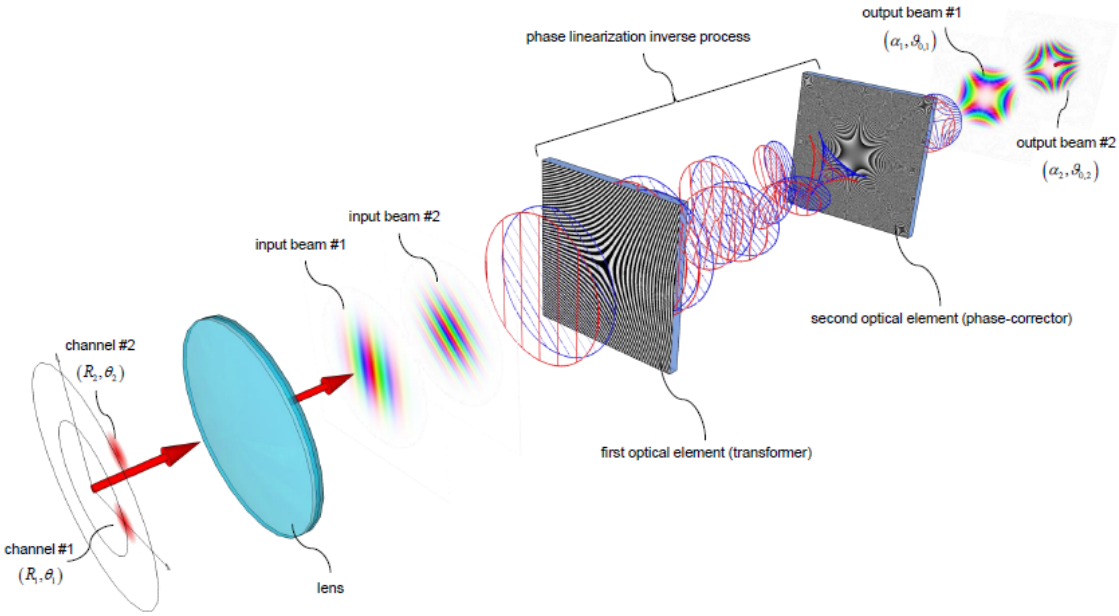

Figure 44: Multiplexing of two multipole-phase beams of the same order $m = 2$ but different phase strength and orientation. In particular, it is shown how two initial light spots are converted, by a Fourier lens, into a superposition of linear phase gradients, which undergoes the "reverse" circular-sector transformation performed by the two phase plates: the Transformer and the Phase Corrector. At the end, the superposition of the two multipole-phase beams, related to the initial light spots, is obtained.

In the demultiplexing case, indeed, we have already seen that when a plane wave, with a wavefront characterized by a linear phase gradient, is Fourier transformed, for instance using a lens in a $f_L - f_L$ configuration, a light spot is generated. The radial coordinate of the spot, r_C, is related to the 2π-phase period enclosed in this phase gradient, i.e., related to the component on the plane perpendicular to the propagation direction of the linear momentum of the photons (see section 3.3). Instead, its angular coordinate, θ_C, depends on the orientation of the gradient, i.e., on the direction of the linear momentum component on the plane. The setup can also work in the reverse configuration, where a light spot is transformed into an electromagnetic field characterized by that linear phase gradient whose orientation, and the 2π-phase period density, are related to the spot position.

---

[3] Actually, as we will see in a while, the first element is not exactly the same as the second element of the demultiplexer.

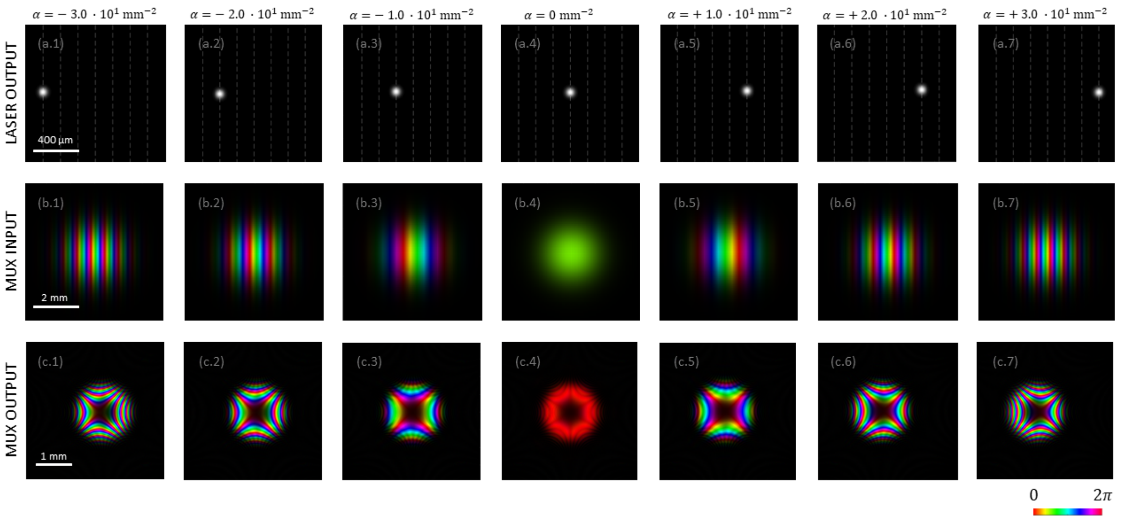

Figure 45: Multiplexing of multipole-phase beams of order $m = 2$ with the same orientation $\theta_0 = 0°$ but seven different phase strengths in the range $[-30; 30]\,\mathrm{mm}^{-2}$ (c.1, ..., c.7). The parameters of the circular-sector transformation used are: $f_{CS} = 250\,\mathrm{mm}$, $a = 2.0\,\mathrm{mm}$ and $b = 0.85\,\mathrm{mm}$. While the focal length, of the Fourier lens used in order to transform the initial light spots (a.1, ..., a.7) into the linear phase gradients (b.1, ..., b.7), is $f_L = 400\,\mathrm{mm}$. The initial light spots have a wavelength of $\lambda = 632.8\,\mathrm{nm}$ and waist $w_0 = 50\,\mu\mathrm{m}$. As usual, brightness and colours refer to intensity and phase, respectively.

As anticipated, these phase gradients can be used to generate a multipole-phase beam with a phase strength, α, related to the 2π-phase period density of the linear phase gradient and, so, thanks to equation 152, depending on the radial coordinate of the spot, r_C. Similarly, for the phase orientation, θ_0, that will be related to the rotation of this gradient and, so, on the θ_C value.

5.0.1 Dependence on α

To better understand this "reverse" circular-sector transformation in figure 45 it is reported a simulation of seven initial laser spots (a.1, ..., a.7) characterized by the same $\theta_C = 0°$ but different radial coordinates. The corresponding multipole-phase beams (c.1, ..., c.7) have a phase strength α that varies in the range $[-30, 30]\mathrm{mm}^{-2}$ and the same phase orientation $\theta_0 = 0°$. The intermediate beams, with their linear phase gradient, are also reported (b.1, ..., b.7). Notice how the number of the coloured stripes, an indicator of the modulus of this phase gradient, increases with the displacement of the initial light spot. Indeed, we remember that each colour corresponds to a different phase value and, in a complete phase period of 2π, each colour is repeated only once. This increment does not regard only the input spots of the multiplexer but also the output multipole-phase beams where, to a more dense colour profile, corresponding a higher value of the phase strength α. In the particular case of α null, i.e., the initial light spot is centred in the origin of the system, the Fourier transformation of the spot returns a beam without any phase gradient, i.e., a planar wavefront. Therefore, the final multipole-phase beam will be characterized by a wavefront with a uniform phase. Indeed, if we set $\alpha = 0$ in the equation 90, of the phase pattern of a generic multipole-phase beam, $\Omega(r, \theta)$ will be zero.

5.0.2 Dependence on θ_0

In figure 46, instead, it is reported the case of laser spots with different angular coordinate θ_C but the same radial coordinate. The spots, therefore, will be placed along a circle, the dashed line in the frames a.1, ..., a.7 of the figure. The radius of this circle is related, thanks to equation 152, to the α value of the final multipole-phase beams, which will be, therefore, the same for all the fields. Indeed, from the multiplexer outputs reported in figures (c.1, ..., c.7), one can see how the phase pattern is identically for each beam but simply rotated by an angle θ_0, which is half of θ_C and it goes in the opposite direction (clockwise in figure). This is quite obvious if one notices the minus sign in the first equation of the system 152 and remembers that we are considering a phase order $m = 2$.

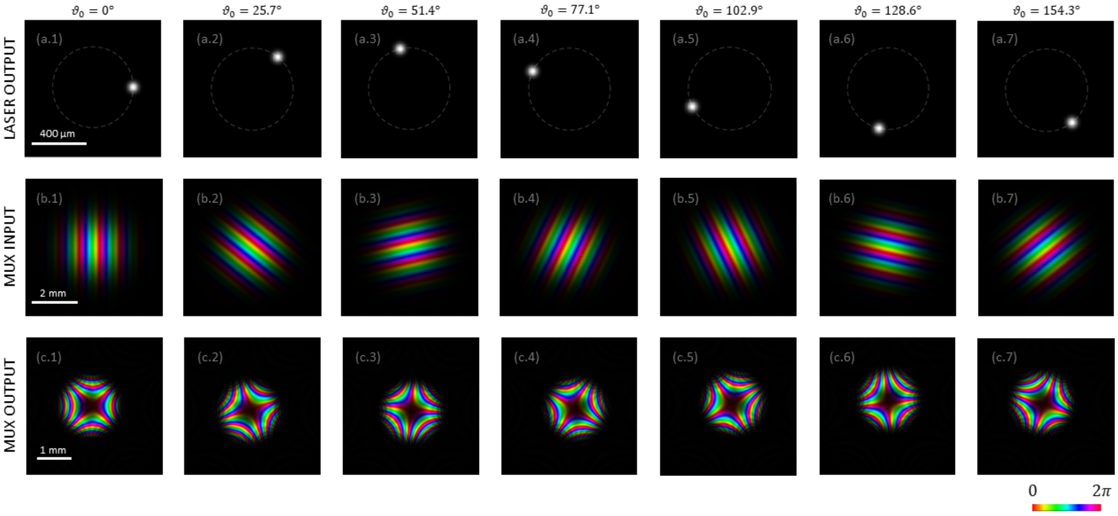

Figure 46: Multiplexing of seven multipole-phase beams of order $m = 2$ with the same phase strength $\alpha = 20\,\text{mm}^{-2}$ but different phase orientation in the range $\left[0; \frac{2\pi}{m}\right]$ (c.1, ..., c.7). The initial light spots (a.1, ..., a.7), of wavelength $\lambda = 632.8\,\text{nm}$ and waist $w_0 = 50\,\mu\text{m}$, are transformed into linear phase gradients (b.1, ..., b.7) by the same Fourier lens of the figure 45 with $f_L = 400\,\text{mm}$. The parameters of the circular-sector transformation are also the same: $f_{CS} = 250\,\text{mm}$, $a = 2.0\,\text{mm}$ and $b = 0.85\,\text{mm}$. Brightness and colours refer to intensity and phase, respectively.

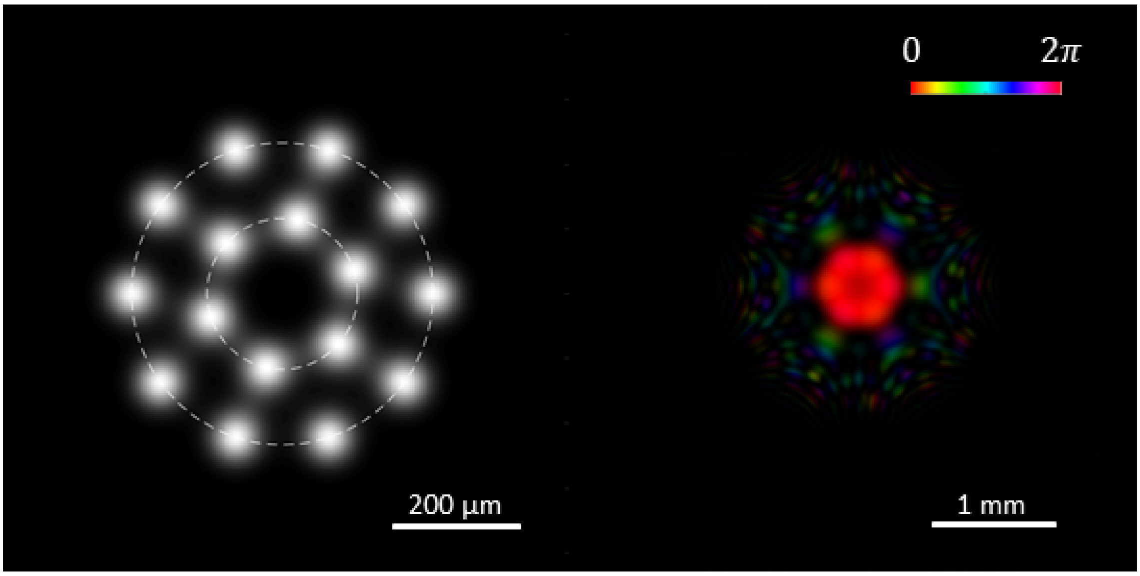

Figure 47: The starting Gaussian spots configuration analysed in this section (on the left) and its multiplexing into a superposition of multipole-phase beams of order $m = 2$ (on the right). In particular, the initial configuration is composed by $N_1 = 10$ external spots, related to multipole-phase beams of phase strength $\alpha^{(1)} = 16\,\text{mm}^{-2}$ and phase orientations in the range $[0; \pi]$, and $N_2 = 6$ internal spots related to multipole-phase beams of phase strength $\alpha^{(2)} = 8\,\text{mm}^{-2}$ and the same θ_0 range. These initial light spots have a wavelength of $\lambda = 632.8\,\text{nm}$ and a waist of $w_0 = 50\,\mu\text{m}$, while the parameters of the circular-sector transformation are: $f_{CS} = 250\,\text{mm}$, $a = 2.0\,\text{mm}$ and $b = 0.85\,\text{mm}$. As usual, brightness and colours refer to intensity and phase, respectively.

5.1 Multiplexing simulation

In the following, we want to analyse in detail each simulation step of the transformation of a single light spot into the corresponding multipole-phase beam. In particular, it will be considered the third external spot (in anticlockwise order starting from $\theta = 0°$) of the configuration reported on the left of the figure 47. This configuration is composed by $N_1 = 10$ external spots, distributed on a circle characterized by the value $\alpha^{(1)}$ and radius given by the equation 113, and $N_2 = 6$ internal spots defined by $\alpha^{(2)} = g\alpha^{(1)}$ with $g = 0.5$. The angular coordinates of the spots are arranged over a range of $[0, 2\pi]$, and correspond to $-m$ times the phase orientation θ_0 of the final multipole-phase beams of order $m = 2$. On the right of the figure, instead, it is reported the superposition of the multipole-phase beams generated in the multiplexing process by this spots configuration.
The algorithm of the simulation is the following one. After the definition of the initial Gaussian beams, they are propagated for a distance equal to the focal length, f_L, of the lens used in order to produce the Fourier transform (which is characterized by the phase term reported in equation 148). The field is so propagated for a further distance f_L, obtaining the usual $f_L - f_L$ configuration. Then, it is performed the reversed circular-sector transformation, where the first element is not exactly as the second one in a demultiplexer. Indeed, since the multiplexing transformation is a mapping of the phase pattern onto a circular sector (characterized by an amplitude of $\frac{2\pi}{|m|}$), in order to obtain an output beam defined over the whole range of 2π, a first $|m|$-fold multiplication is needed. This is performed by the first optical element called, for this reason, "multiplier". Recalling the equation 101 of a circular-sector transformation of order n:

$$\Omega_{CS} = k\frac{ab}{f_{CS}}\left(\frac{r}{b}\right)^{1-\frac{1}{n}}\frac{\cos[(1-\frac{1}{n})\theta]}{1-\frac{1}{n}} \tag{153}$$

it is easy to visualize that, in order to have an $|m|$-fold multiplication of the phase of the input beam, the required expression of the first term, $\Omega^M_{m,1}$, must be the combination of two phase patterns ($|m|$ patterns in the general case) performing an n-fold circular-sector transformations with $n = -m$ and rotated with respect to each other of a $\frac{2\pi}{|m|}$ term. Therefore, taking in account also the focusing factor $-k\frac{r^2}{2f_{CS}}$, we obtain

$$\Omega^M_{m,1}(r,\theta) = arg\left\{\sum_{p=1}^{|m|} e^{i\Omega^{D,(p)}_{m,2}}\right\} \tag{154}$$

which is a combination of terms as:

$$\Omega^{D,(p)}_{m,2}(r,\theta) = k\frac{ab}{f_{CS}}\left(\frac{r}{a}\right)^{1+\frac{1}{m}}\frac{\cos\left[\theta\left(1+\frac{1}{m}\right)+(p-1)\frac{2\pi}{|m|}\right]}{1+\frac{1}{m}} - k\frac{r^2}{2f_{CS}} \tag{155}$$

Notice that this expression is, actually, equal to the equation 103 of the second element, $\Omega^D_{m,2}$, of a demultiplexer but with the correction factor $(p-1)\frac{2\pi}{|m|}$ which performs the above-mentioned rotation (equal to π in this $m = 2$ case). Then the second element, in order to generate the final multipole-phase beam, has to perform a simply $|m|$-fold circular-sector transformation and, so, has a phase expression identical to the first element of the demultiplexer:

$$\Omega^M_{m,2} = \Omega^D_{m,1} = k\frac{ab}{f}\left(\frac{\rho}{a}\right)^{1+m}\frac{\cos((1+m)\,\phi)}{1+m} - k\frac{r^2}{2f_{CS}} \tag{156}$$

These two phase patterns, $\Omega^M_{m,1}$ and $\Omega^M_{m,2}$, are reported, modulo 2π, in figure 48.

In figure 49 it is shown a simulation of the whole transformation. The multiplexer input beam, with its characteristic linear phase gradient (first frame of the figure), undergoes to a 2-fold wrapping during the propagation for the distance, f_{CS}, between the two phase plates $\Omega^M_{m,1}$ and $\Omega^M_{m,2}$. Notice how the phase pattern of the multiplier (on the left of figure 48), is found in the phase structure of the wavefront of the electromagnetic field after the application of this optical element (at $z = 0$ in figure 49). Finally, at the output of the multiplexer, after the application of the second phase term $\Omega^M_{m,2}$, we find the multipole-phase beam.

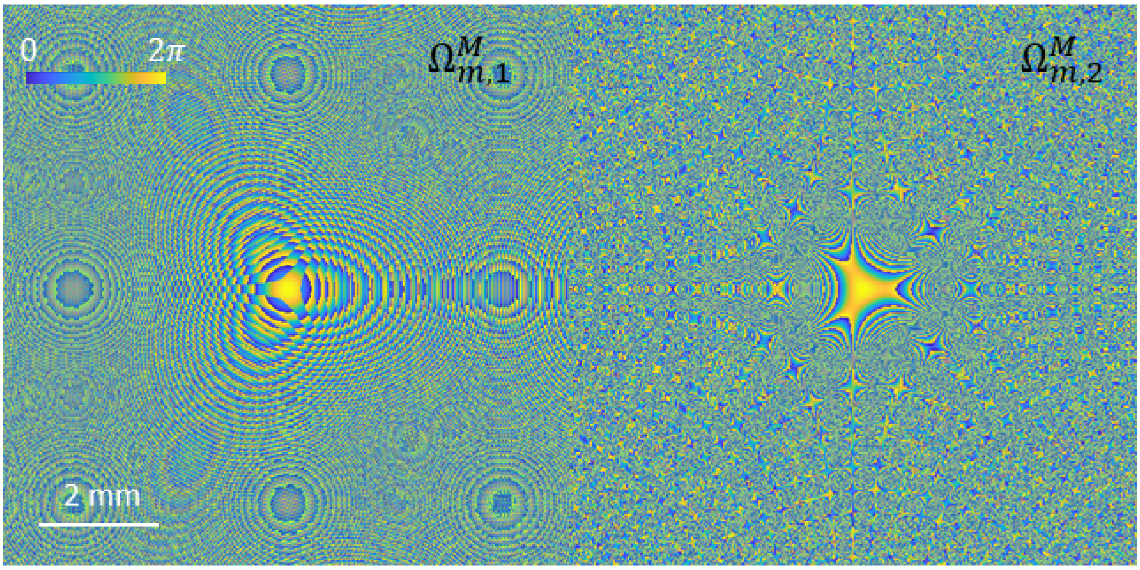

Figure 48: The phase patterns, modulo 2π, of the two phase plates used for the circular-sector transformation (whose output is reported on the right of figure 47). In particular, on the left, it is reported $\Omega^M_{m,1}$ (equation 154), while, on the right, it is reported $\Omega^M_{m,2}$ (equation 156). The parameters of the phase patterns are: $f_{CS} = 250\,\text{mm}$, $a = 2.0\,\text{mm}$ and $b = 0.85\,\text{mm}$.

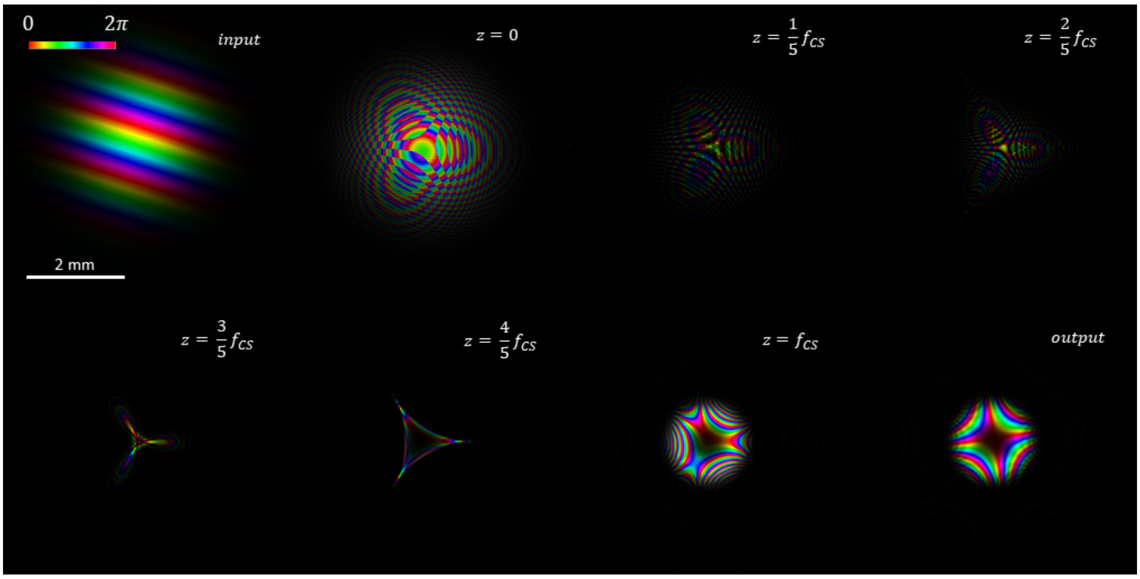

Figure 49: The circular-sector transformation of the third spot (in anticlockwise order starting from $\theta = 0°$) of the external circle spots configuration reported on the left of figure 47. In the first frame, we have the linear phase gradient, obtained by the Fourier Transform of the initial light spot, impinging the $\Omega^M_{m,1}$ phase plate (i.e., the Transformer). Then it is reported the field after this phase plate ($z = 0\,\text{mm}$) and its evolution between the Transformer and the Phase Corrector, $\Omega^M_{m,2}$, placed in $z = f_{CS}$. Finally, the output multipole-phase beam is shown in the last frame. As usual, brightness and colours refer to intensity and phase, respectively, while the patterns of the two phase plates used in the circular-sector transformation are shown in figure 48.

5.2 MatLab code

In the following, it will be described the MatLab code used in order to simulate the multiplexing process.

5.2.1 The observation plane

The first step is the definition of the observation plane, where it will be defined the wavefront of our electromagnetic field for the various propagation steps. The observation plane has already been described in the section 4.1.1 but, for simplicity, we report again the spatial discretization 35:

$$x \to \left[-\frac{L}{2} : \Delta_x : \frac{L}{2} - \Delta_x \right] \tag{157}$$

where $\Delta_x = \frac{L}{M}$ is the sampling interval along both x and y-axis, L is the side of the observation plane (supposed squared) and M the number of samples. The MatLab code is the following, where the mesh of the Cartesian coordinates [X,Y] is converted to the more convenient polar coordinates [theta,r] (line 5).

Listing 5.2.1: space discretization

```
1    dx          = L/M;                  % sample interval
2    x           = -L/2 : dx : L/2-dx;   % x coords
3    y           = x;                    % y coords
4    [X,Y]       = meshgrid(x,y);        % cartesian coords
5    [theta, r]  = cart2pol(X,Y);        % polar coords
```

5.2.2 The initial light spot configuration

After that, we can define the initial isolated light spots, $u_0^{(i)}(r, \theta)$, one for each i-th different channel of communication and identified by the coordinates of their centres $(r_C, \theta_C)^{(i)}$. A Gaussian shape is assumed

$$u_0^{(i)}(r,\theta) = \exp\left\{ -\left[\left(\frac{X - x_C^{(i)}}{w_0} \right)^2 + \left(\frac{Y - y_C^{(i)}}{w_0} \right)^2 \right] \right\} \tag{158}$$

where w_0 is the beam waist of these light spots and $(x_C, y_C)^{(i)}$ are the Cartesian coordinates of the centre of the i-th spot:

$$\begin{cases} x_C^{(i)} = r_C^{(i)} \cos\theta_C^{(i)} \\ y_C^{(i)} = r_C^{(i)} \sin\theta_C^{(i)} \end{cases} \tag{159}$$

The corresponding MatLab code is the following one, where the for-loop is repeated for all the values of the vector "alpha", which contains the phase strength $\alpha^{(i)}$ of each i-th multipole-phase beam associated to the relative light spot. By introducing an amplitude factor for the Gaussian profile, it is possible to further control the weight of each generated multipole-phase contribution.

Listing 5.2.2: Gaussian beams definition

```
for i = 1 : length(alpha)
    xC(i) = rC(i)*cos(thetaC(i));
    yC(i) = rC(i)*sin(thetaC(i));
    u0(:,:,i) = exp(-(((X - xC(i))/w0).^2 + ((Y - yC(i))/w0).^2));
end
```

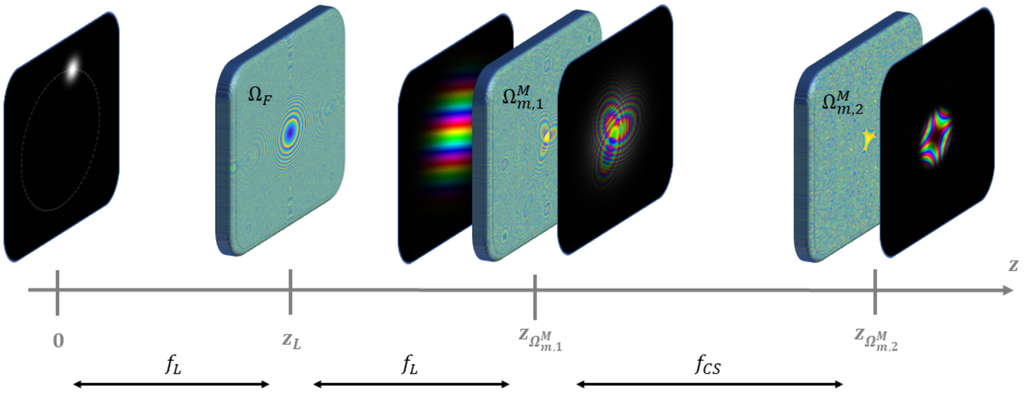

Figure 50: The optical path of the multipole-phase beam multiplexer simulated in this section. From the left, the initial light spots are transformed into linear phase gradients by a Fourier lens in a $f_L - f_L$ configuration. Then, we have the two phase plates (i.e., the Transformer and the Phase Corrector) which perform the circular-sector transformation of these linear phase gradients, producing the final multipole-phase beams.

5.2.3 The phase patterns of the circular-sector transformations

Now, before propagating the input beams, $u_0^{(i)}$, as reported in the figure 50, we have to define the phase patterns, $\Omega^M_{m,1}$ and $\Omega^M_{m,2}$, of the two elements of the multiplexer.

- The first one, $\Omega^M_{m,1}$, which performs the $|m|$-fold multiplication is called "Phase1" in the MatLab code reported in the following (lines 6-12). This phase plate is described by the equation 154 which is a combination of $|m|$ terms that we rewrite in a more compact notation as:

$$\Omega^{D,(p)}_{m,2}(r,\theta) = A\left(\frac{r}{a}\right)^B \frac{\cos\left[\theta B + (p-1)\frac{2\pi}{|m|}\right]}{B} - C \tag{160}$$

  where we have defined the two constants A, B and the focusing term C as:

$$\begin{cases} A := k\frac{ab}{f_{CS}} \\ B := 1 + \frac{1}{m} \\ C := k\frac{r^2}{2f_{CS}} \end{cases} \tag{161}$$

- The second phase plate, $\Omega^M_{m,2}$, which performs the circular-sector transformation in order to obtain the multipole-phase beams associated to the initial light spots, is described by the equation 156. We rewrite this equation in the same notation as before

$$\Omega^M_{m,2}(r,\theta) = A\left(\frac{r}{b}\right)^{1+m} \frac{\cos[(1+m)\theta]}{1+m} - C \tag{162}$$

  In the code (line 15) is called "Phase2".

Listing 5.2.3: the phase patterns

```
1       A = k*(a*b/f_CS);
2       B = 1+1/m;
3       C = k*(r.^2)/(2*f_CS);
4
5       % phase pattern of the 1st mux element
6       Phase1   = zeros(length(x),length(y));
7       for p = 1 : abs(m)
```

```
        Omega    = A*((r/a).^B).*cos(theta*B+(p-1)*2*pi/abs(m))/B - C;
        Phase1i  = exp(1i*Omega);
        Phase1   = Phase1 + Phase1i;
    end
    Phase1 = angle(Phase1);

    % phase pattern of the 2nd mux element
    Phase2 = A*((r/b).^(1+m)).*cos(theta*(1+m))/(1+m) - C;
```

5.2.4 Multiplexing of the initial light spots

At this point, we have to multiplex the initial Gaussian spots into a superposition of multipole-phase beams of order m. We know that this procedure consists, initially, in the transformation of the light spot into an electromagnetic field characterized by a wavefront with a linear phase gradient. This transformation is performed by a lens in a $f_L - f_L$ configuration (lines 2-4 of the MatLab code reported below), characterized by a phase term

$$\Omega_F(r,\theta) = -\frac{k}{2f_L}r^2 \tag{163}$$

Then, we have the multiplier which, as already said, performs the $|m|$-fold multiplication in order to have an output multipole-phase beam defined in the whole range of 2π (line 5). Finally, after a further free-space propagation for the distance that separates the two phase elements $\Omega^M_{m,1}$ and $\Omega^M_{m,2}$ (line 6 of the code), we have the circular-sector transformation (line 7). This procedure is so repeated for each i-th beam.

Listing 5.2.4: multiplexing of the spots into a multipole-phase beams

```
1     for i = 1 : length(alpha)
2         u1(:,:,i) = FreeSpaceProp(u0(:,:,i),L,lambda,f_L);
3         u1(:,:,i) = u1(:,:,i).*exp(-1i*(k/(2*f_L))*r.^2);
4         u1(:,:,i) = FreeSpaceProp(u1(:,:,i),L,lambda,f_L);
5         u1(:,:,i) = u1(:,:,i).*exp(1i*Phase1);
6         u1(:,:,i) = FreeSpaceProp(u1(:,:,i),L,lambda,f_CS);
7         u2(:,:,i) = u1(:,:,i).*exp(1i*Phase2);
8     end
```

6 Cross-talk in the communication system

In the previous chapter we have seen that, thanks to their orthogonality, a set of multipole-phase beams of the same order m, characterized by different parameters (α, θ_0), can be propagated simultaneously at the same frequency and, then, separated into isolated light spots. In this way, each spot acts as an independent channel of communication. It appears clearly that, in order to realize a good telecommunication system, the level of this independence is a crucial design parameter. To better understand this aspect, we can consider the following example. Image a two-level digital communication link where each bit of information is carried by a pulse of light, which is on, if the bit is value is 1, off otherwise. Then, in order to reduce the time necessary to propagate the total information, we want to propagate more bits simultaneously. We could use a bunch of optical fibres, where each fibre is a different communication channel. We suppose now that the propagation, from the emitter to the receiver of our link, cannot be performed via optical fibre but only in free space. It is quite obvious that propagating this set of channels as parallel light beams for a long distance, without any interference, is very difficult due to the divergence of a collimated beam in a free space propagation. Therefore, we can multiplex them into a single superposition of multipole-phase beams (we have seen the multiplexing process in the previous chapter 5), propagate this single field and, finally, demultiplex the beam into the original set of light spots (as seen in the chapter 4). Then a set of detectors, placed in correspondence to each spot, detects the values of the bits from the light intensities collected on their detection areas. However, if these spots are too close to each other, it could happen that, for example, the l-th bit, whose value is 0 (and the relative light beam is off), can be confused, due to the luminosity of the neighbouring channels, as a 1. This example tell us that we need to introduce a new parameter that quantifies the independence level of the channels of our communication system. For this reason, it was introduced the Cross-Talk (XT). Considering the channel l^*, the relative Cross-Talk, $XT_{l=l^*}$, is defined as the ratio of the intensity, $I_{l^*,ALL/l^*}$, detected in correspondence to the spot of the channel l^* when the channel l^* is off, and all the others are on, and the same intensity, $I_{l^*,ALL}$, when all channels are on, included l^*. The lower is this ratio, the lower is the light intensity, collected in the detection area of l^*, due to the others channels:

$$XT_{l=l^*} = 10 \log_{10} \frac{I_{l^*,ALL/l^*}}{I_{l^*,ALL}} \tag{164}$$

Typically, in a telecommunication system, the cross-talk has to be lower than $-15\,\mathrm{dB}$. For this reason, the final step of our simulation is the computation of the Cross-Talk defined by equation 164.

6.1 Cross-Talk implementation in a MatLab simulation

First of all, we have to compute the intensity of the final field, $u_2(r, \theta)$, of each single multipole-phase beam as

$$I(r, \theta) = |u_2(r, \theta)|^2 \tag{165}$$

The MatLab code is simply the following, where I will be a vector, of length equal to the number of channels of our link, of X×X square matrices (remember that the observation plane is sampled with a mesh [X,Y] with the same number of samples for both x and y-axis).

Listing 6.1.1: Intensity definition

```
    I = abs(u2.^2);
```

6.1.1 Mask generation for the communication channels

Now, for each i-th light spot, we have to obtain the coordinates of the detection areas which are disks of radius R_I placed in correspondence to the theoretical centre of the spot (X_C, Y_C):

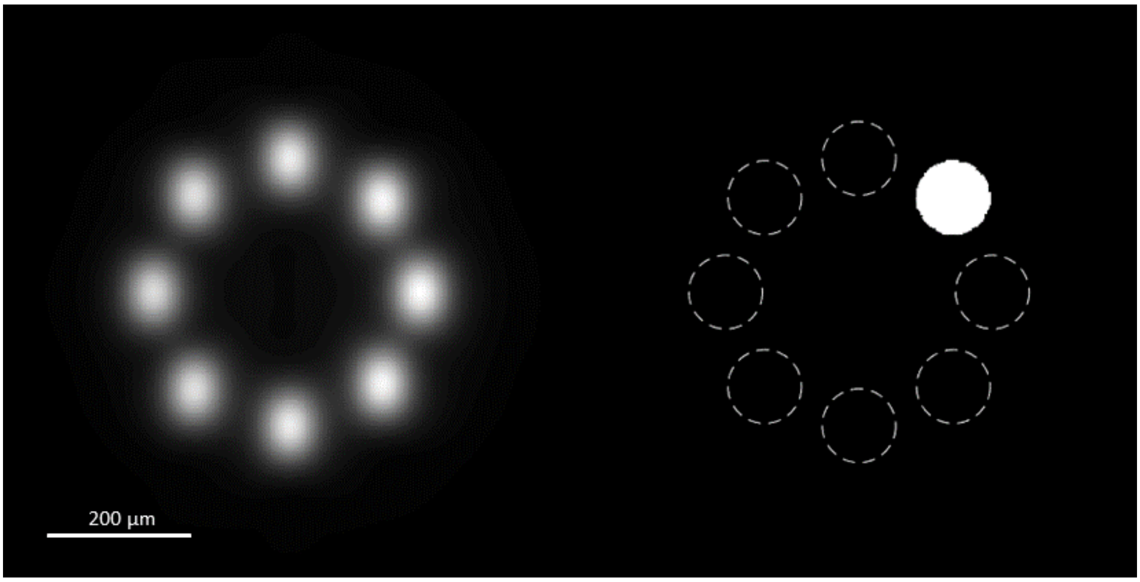

Figure 51: On the left, the light spot, corresponding to the demultiplexer output, for a superposition of eight multipole-phase beams. On the right, the mask of the second spot (i.e., the detection area of that channel), used for the computation of the Cross-Talk. The mask is a two-levels digital mesh (where the white and the black colour correspond to the values 1 and 0, respectively), defined in order to obtain the portion of the observation plane where the light intensity has to be integrated. The boundaries of the others detection areas are plotted with a dashed line.

$$\begin{cases} X_C^{(i)} = R^{(i)} \cos\left(-m\theta_0^{(i)}\right) \\ Y_C^{(i)} = R^{(i)} \sin\left(-m\theta_0^{(i)}\right) \end{cases} \tag{166}$$

where R is given by the equation 113. Once created the two arrays, X_C and Y_C, it was defined, for each spot, a logical mask for the mesh [X,Y] of the observation plane. The values of the mask are equal to 1, if the point (X, Y) is inside the i-th spot detection area, 0 otherwise.

$$\begin{cases} 1 & \text{if } \sqrt{(X - X_C)^2 + (Y - Y_C)^2} \leq R_I \\ 0 & \text{otherwise} \end{cases} \tag{167}$$

For example, in figure 51, it is reported the demultiplexer output beams, for a configuration of eight channels, and the relative mask corresponding to the second light spot. Notice that the mask is, actually, a two-levels digital mesh where the white colour corresponds to the value 1 and the black colour to the value 0, as described in the equation 167. Superimposed to this mask are plotted the boundaries of the others (dashed line). In figure 52, instead, a representation of the mask relative to the same spot of the figure 51 is reported.

In the following, it is reported the MatLab code for the generation of the masks, which is simply the application of the equation 167 to each i-th spot.

Listing 6.1.2: mask of the detection area

```
    mask = false(length(X), length(Y), length(Xc));
    for i = 1 : length(Xc)
        mask(:,:,i) = mask(:,:,i) | hypot(X - Xc(i), Y - Yc(i)) <= RI;
    end
```

6.1.2 Computation of the Cross-Talk

With the so-defined masks, we are able to measure the total intensity detected for each channel, simply integrating the intensity on the whole observation plane after the application of the mask. Indeed, since outside the i-th detection area the i-th mask values are all null, after the application of the mask, the field is different

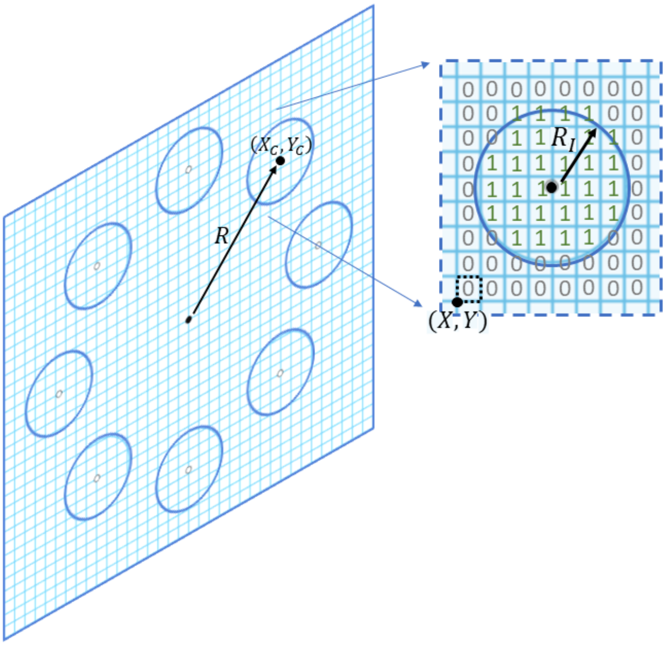

Figure 52: A representation of the mask of the second spot reported in figure 51. The value of each pixel (related to the white and black colours of that figure) is also shown. According to the conditions 167, these values are equal to 1 if the (X, Y) coordinate, of the left-bottom corner of the pixel considered, is inside the detection area of radius R_I and centred in the expected position (X_C, Y_C) of that light spot.

from zero only in that detection area of radius R_I. In this way, the equation 164 is easy to compute, as reported in the MatLab code below. We define, with q_on(j), the integral of the intensity detected by the j-th channel when all the multipole phase beams are on, included the j-th beam (i.e., the denominator of the equation 164). Then, we define, with q_off(j), the same integral when all the multipole-phase beams, except for the j-th, are on (i.e., the numerator of the equation 164). The algorithm is the following. We apply the i-th mask to the intensity, I(:,:,j), of j-th multipole-phase beam, obtaining the intensity, I_XT(:,:,j,i), of the j-th beam detected on the i-th channel (line 11). This I_XT(:,:,j,i) is then integrated on the all observation plane (line 14). The result of this integration, q(i,j), is then summed up to q_on(j) (line 17) and the procedure is repeated for each i-th mask, obtaining the final value of q_on(j). Then the index j changes and the algorithm is repeated. In order to get q_off(j), inside the i-th loop, we check if j is different from i and, if it is true, we sum q(i,j) to q_off(j) (lines 20-22). Finally, the j-th cross-talk, XT(j), is computed as the ratio, expressed in decibel, of q_off(j) over q_on(j).

Listing 6.1.3: Cross-talk computing

```
1     q     = zeros(length(Xc),length(Xc));
2     q_on  = zeros(length(Xc));
3     q_off = zeros(length(Xc));
4     I_XT  = zeros(length(X),length(Y),length(Xc),length(Xc));
5     XT    = zeros(length(Xc));
6
7     for j = 1 : length(Xc)
8         for i = 1 : length(Xc)
9
10            % Intensity of j-spot detected by i-mask
11            I_XT(:,:,j,i) = I(:,:,j).*mask(:,:,i);
12
13            % Integral of j-spot detected by i-mask I_XT(j,i)
```

```
            q(j,i) = sum(trapz(I_XT(:,:,j,i)), 'all');

            % Integral of j-spot with all mask on
            q_on(j) = q_on(j) + q(j,i);

            % Integral of j-spot with all\j mask on
            if i ~= j
                q_off(j) = q_off(j) + q(j,i);
            end

        end

        % Cross-talk of j-spot
        XT(j) = 10*log10(q_off(j)/q_on(j));
    end
```

From the integral q(i,j) of the *j*-th spot detected by the *i*-th channel, we are able to produce a map like the two reported in the central column of figure 53. Notice that the gray level of the cell is the value of q(i,j) in arbitrary unit, while the "channel id" indicates the *i*-th channel activated to the detection of the field (i.e., the *i*-th mask), and "id" indicates the *j*-th multipole-phase beam turned on. In a good configuration, with low Cross-Talk between the channels (as the bottom one in the figure), the off-diagonal elements are very small while the diagonal elements have very high values. On the right of the figure, it is reported the corresponding Cross-Talk values of each channel of the simulated configuration reported on the left.

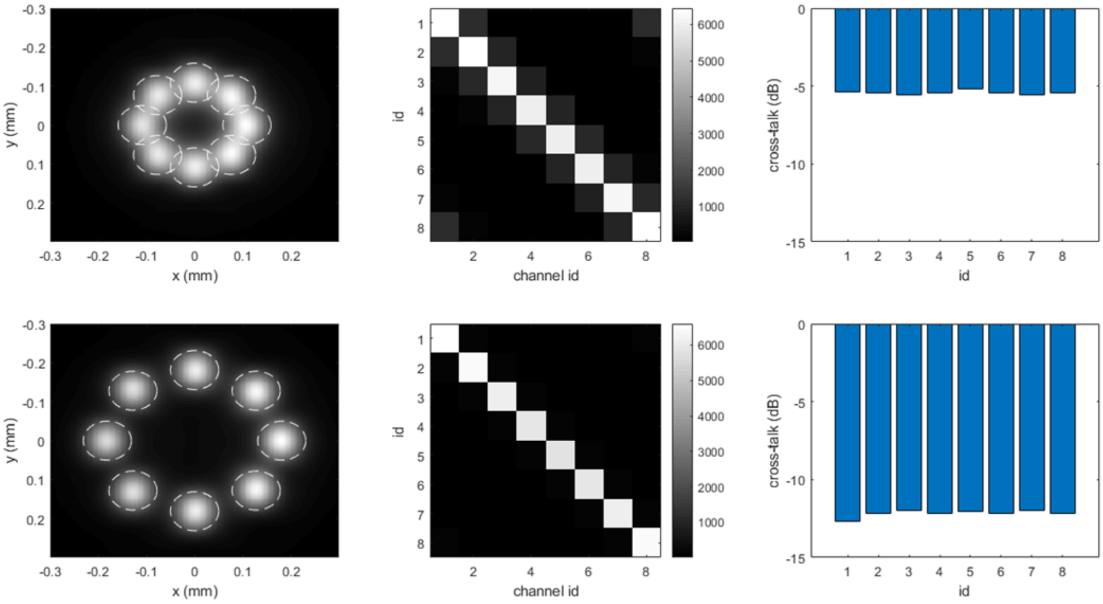

Figure 53: The Cross-Talk computation for two example configurations of demultiplexed multipole-phase beams. In the first frame, it is shown the final light spots and their detection areas (dashed line). In the second and the last frames, we have the intermodal overlapping map of the channels and the corresponding Cross-Talk values, respectively. In the first case (on the top), an excessive proximity of the spots produces interference between the channels, as can be seen from the not negligible values of the off-diagonal elements in the intermodal map. Consequently, the Cross-Talk values are very low with respect to the second case, where the spots are well separated.

7 Optimization of a multipole-phase beams demultiplexer

In the previous chapters, we have seen the theory of the multipole-phase beams and how this new type of structured light can be handled in order to multiplex and demultiplex a set of several independent signals in a communication system. In order to estimate the transmission quality of this system, we have also introduced the Cross-Talk (XT) and the procedure for its computation. Typically, in the telecommunication technologies, an acceptable XT value is lower than $-15\,\mathrm{dB}$. For this reason, the purpose of this section is the design of an apparatus able to perform the demultiplexing of a set of multipole-phase beams, keeping the Cross-Talk of each channel around this $-15\,\mathrm{dB}$ limit. In order to do this, we have to start from the choice of a channel's configuration in which the light spots are well isolated from each other. We recall that for a family of multipole-phase beams of order m, there are two degrees of freedom: the phase orientation, θ_0, and the phase strength, α. We remember also that changing the first one, the output beams will be characterized by different azimuthal angles, i.e, the light spots will be distributed onto a circular configuration. Conversely, changing only the phase strength, one gets a linear spot configuration. In order to maximize the number of separated channels, but keeping the Cross-Talk around the $-15\,\mathrm{dB}$, it was chosen to work with both α and θ_0, generating a double circular distribution of the output light spots.

7.1 Demultiplexer for $m = 2$

As anticipated, it was chosen a set of $\{\alpha, \theta_0\}$ in such a way that the final spots were arranged over two concentric circles. The internal one, characterized by a lower radius (i.e., a lower phase strength), contains $N_2 = 6$ light spots. In the external one, instead, $N_1 = 14$ beams are distributed, for a total of twenty channels. These two configurations are described in the following.

External spots distribution For the external circle, characterized by a phase strength $\alpha^{(1)}$ (which determines the radius of the distribution), the orientation values $\theta^{(1)}_{0,i=1,\ldots,N_1}$ are assumed in the range $[0; \frac{2\pi}{m}]$ and they are separated by an angle of

$$\Delta\theta_0^{(1)} = \frac{1}{m}\frac{2\pi}{N_1} \tag{168}$$

Internal spots distribution For the internal circle, characterized by a strength of $\alpha^{(2)} = g\alpha^{(1)}$ with $g \in [0; 1]$, we have a similar distribution $\theta^{(2)}_{0,i=1,\ldots,N_2} \in [0; \frac{2\pi}{m}]$ with steps of

$$\Delta\theta_0^{(2)} = \frac{1}{m}\frac{2\pi}{N_2} \tag{169}$$

but, in this case, each $\theta_0^{(2)}$ is shifted of $\frac{\Delta\theta_0^{(1)}}{2}$. This shifting factor was adopted to avoid excessive Cross-Talk between the spots of the two circles that are close to each other.

These two distributions are shown in figure 54, where it is reported the simulation output of our demultiplexer working with multipole-phase beams of order $m = 2$ with phase strength $\alpha^{(1)} = 100\,\mathrm{mm}^{-2}$, $g = 0.5$ and wavelength $\lambda = 632.8\,\mathrm{nm}$. The radius of the two circular distributions is related to the phase strength by the equation 113:

$$R = f_L\frac{\lambda}{2\pi}\frac{\alpha b^m}{a} \tag{170}$$

where, in our design, $a = 1.0\,\mathrm{mm}$, $b = 0.4\,\mathrm{mm}$ and $f_{CS} = 10\,\mathrm{mm}$ are the parameters of the circular-sector transformation and $f_L = 400\,\mathrm{mm}$ is the focal length of the Fourier lens.

In order to evaluate the performance of this demultiplexer, the Cross-Talk computation was performed with a detection area, of each channel, characterized by a radius of $100\,\mu\mathrm{m}$. These detection areas and the results of this XT computation are shown in the figure 55. In the left frame, it is reported the simulated demultiplexer output, with the boundaries of the detection areas (dashed lined) and the channel's index wrote in white. In the central frame, it is shown the overlapping map of the light intensities collected by each spot's detection

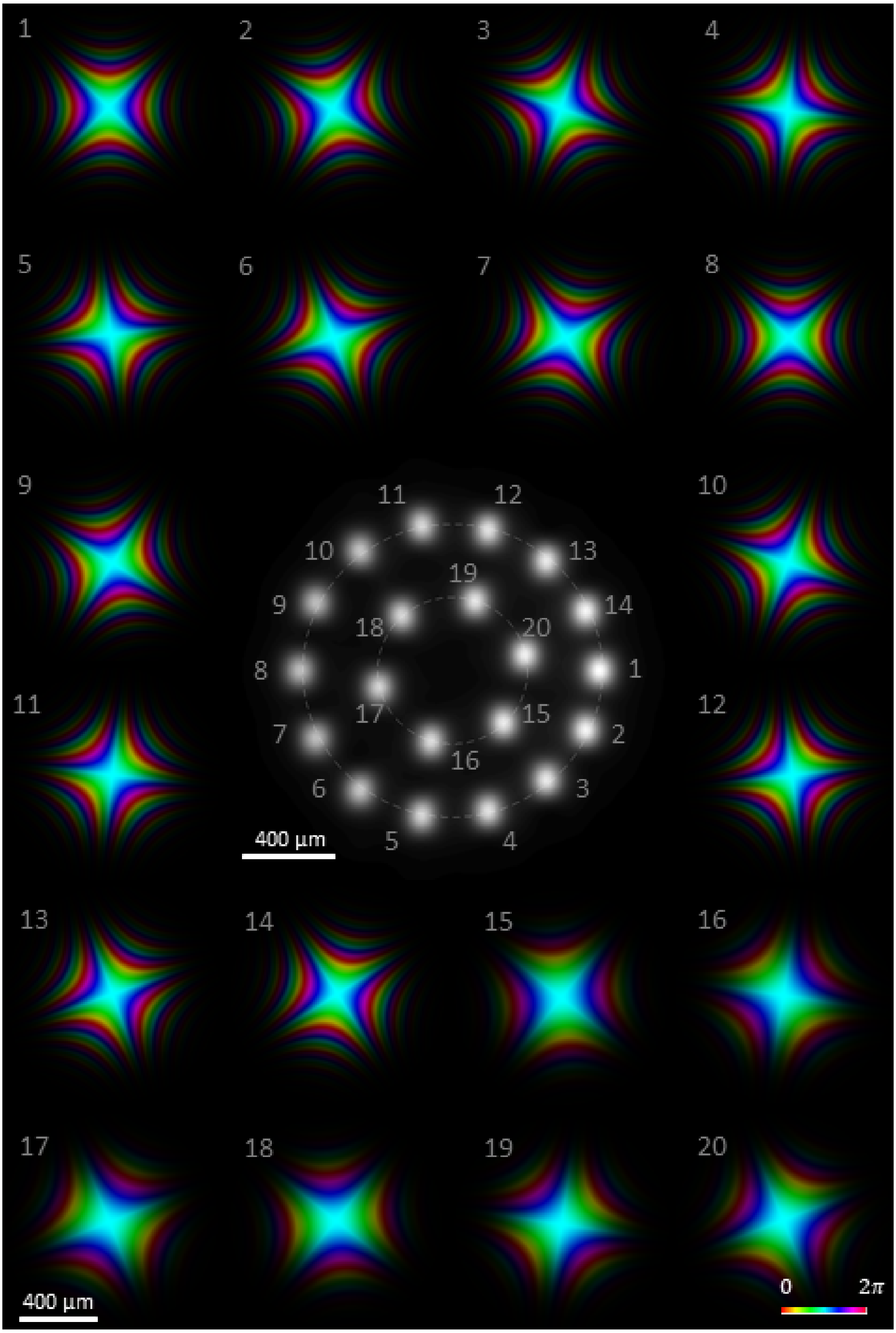

Figure 54: In the figure, it is shown the set of multipole-phase beams at the input of the demultiplexer (whose simulation is described in this chapter), and their relative sorted beams. The output configuration, reported in the centre, is composed by twenty light spots arranged over two concentric circles. The external one has $N_1 = 14$ beams, which are related to multipole-phase beams of order $m = 2$, phase strength $\alpha^{(1)} = 100\,\mathrm{mm}^{-2}$ and phase orientation $\theta_0 \in [0; \frac{2\pi}{m}]$ with steps of $\Delta\theta_0^{(1)} = \frac{1}{m}\frac{2\pi}{N_1}$. The internal distribution, instead, is composed by $N_2 = 6$ light spots corresponded to multipole-phase beams of the same order, and range of θ_0, but characterized by a phase strength $\alpha^{(2)} = 50\,\mathrm{mm}^{-2}$ and a shift of the orientations equal to $\frac{\Delta\theta_0^{(1)}}{2}$. The parameters of the circular-sector transformation, used in the demultiplexing process, are: $a = 1.0\,\mathrm{mm}$, $b = 0.4\,\mathrm{mm}$ and $f_{CS} = 10\,\mathrm{mm}$, while the focal length, of the Fourier lens used for the final sorting of the beams, is $f_L = 400\,\mathrm{mm}$. As usual, brightness and colours refer to intensity and phase, respectively.

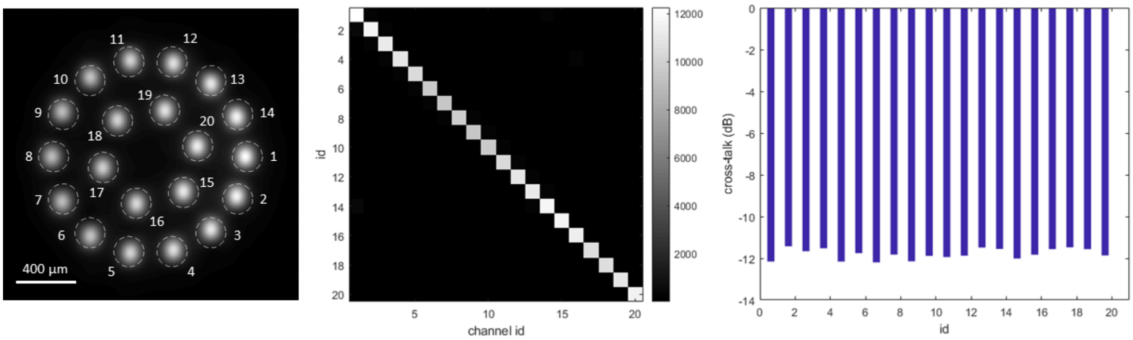

Figure 55: In the first frame, it is reported the demultiplexer output, as shown in the centre of figure 54, with the channel's index, related to each light beam, wrote in white. The detection areas used for the Cross-Talk computation are plotted with a dashed line. In the second frame, the intermodal overlapping map, with the intensities in arbitrary unit, is reported. Finally, in the last frame, the XT values of each channel are plotted. Case $m = 2$

area. Notice the absence of significant values of the off-diagonal elements. This means that, for each channel, the detected field, produced by the other channels, is very low. Indeed, the XT values reported in the right frame, are all around the $-12\,\text{dB}$, which is a remarkable result considering the high number of channels.

7.2 Demultiplexer for $m = 3$

The same design, with the final light spots distributed over a double circular configuration, was used also for a set of multipole-phase beams of order $m = 3$, as reported in figure 56. The external circle, composed by $N_1 = 11$ light spots, is related to multipole-phase beams with a phase strength $\alpha^{(1)} = 550\,\text{mm}^{-3}$ and phase orientation in the range $\theta_0^{(1)} \in [0; \frac{2\pi}{m}]$ with regular steps of $\frac{2\pi}{mN_1}$. On the internal distribution, instead, $N_2 = 6$ beams are placed, related to an initial set of multipole-phase beams characterized by a phase strength $\alpha^{(2)} = g\alpha^{(1)}$ with $g = 0.5$ and phase orientation, again, in the range $[0; \frac{2\pi}{m}]$ with steps of $\frac{2\pi}{mN_2}$ but, now, with an additional shift of $\frac{\pi}{mN_2}$. Due to the dependence of m on the phase functions of the circular-sector transformation, equations 101 and 103, the simulation's parameters have to be different. In particular, it was adopted the following values for the two phase plates: $a = 2.0\,\text{mm}$, $b = 0.4\,\text{mm}$ and $f_{CS} = 10\,\text{mm}$. The increment of the parameter a produces an important consequence, as can be seen from the equation 170. Indeed, in order to have a radius of the two circular spot distributions sufficiently high, which permits to have the spots well separated, the increment of a has to be followed by an increment of α too.

However, higher phase strengths can produce phase distortions, as described in section 3.5, providing a misalignment of the spots with respect to their expected coordinates, which can produce a worsening of the Cross-Talk. For this reason, a manual correction of the positions of the detection areas was adopted during the computation. Then, the Cross-Talk is obtained as usual and the results are reported in the figure 57. The XT-values are similar to the $m = 2$ case, but with a total number of channels reduced.

7.3 Demultiplexer for $m = 4$

Similarly to before, also the demultiplexing of multipole-phase beams of order $m = 4$ has been investigated. In this case, the output configuration is composed by thirteen light spots arranged over two concentric circles. The external one has $N_1 = 9$ beams, which are related to a phase strength $\alpha^{(1)} = 2000\,\text{mm}^{-4}$ and phase orientation $\theta_0 \in [0; \frac{2\pi}{m}]$ with steps of $\Delta\theta_0^{(1)} = \frac{1}{m}\frac{2\pi}{N_1}$. The internal distribution, instead, is composed by $N_2 = 4$ light spots corresponded to a phase strength $\alpha^{(2)} = 1100\,\text{mm}^{-4}$, and the same range of θ_0 but shifted of $\frac{\Delta\theta_0^{(1)}}{2}$. 58.

The parameters of the circular-sector transformation used are: $a = 2.0\,\text{mm}$, $b = 0.4\,\text{mm}$ and $f_{CS} = 5\,\text{mm}$. Notice that in this case, a and b are kept the same of the demultiplexer for beams of order $m = 3$, but it was reduced f_{CS}. At the same time, even g was changed ($g = 0.55$ in this case) in order to keep the spots, of the internal circle, sufficiently far from each other. Indeed, due to the phase distortions produced by a higher

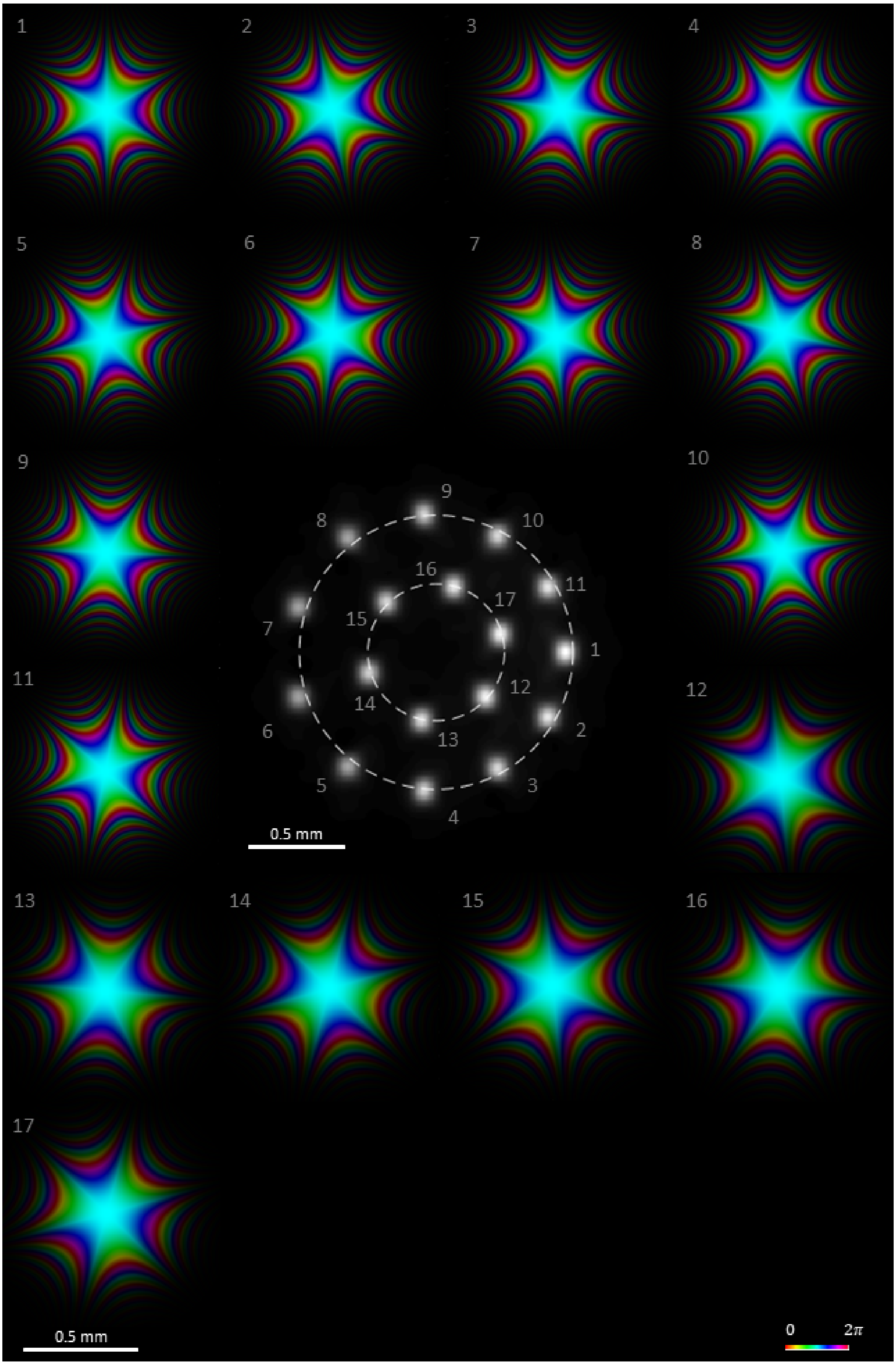

Figure 56: In the figure, the input and the output of a demultiplexer for multipole-phase beams of order $m = 3$ are reported. The output configuration, shown in the centre, is composed by seventeen light spots arranged over two concentric circles. The external one has $N_1 = 11$ beams, which are related to multipole-phase beams with phase strength $\alpha^{(1)} = 550\,\mathrm{mm}^{-3}$ and phase orientation $\theta_0 \in [0; \frac{2\pi}{m}]$ with steps of $\Delta\theta_0^{(1)} = \frac{1}{m}\frac{2\pi}{N_1}$. The internal distribution, instead, is composed by $N_2 = 6$ light spots corresponded to multipole-phase beams of the same order, and range of θ_0, but characterized by a phase strength $\alpha^{(2)} = 275\,\mathrm{mm}^{-3}$ and a shift of the orientations equal to $\frac{\Delta\theta_0^{(1)}}{2}$. The parameters of the circular-sector transformation used are: $a = 2.0\,\mathrm{mm}$, $b = 0.4\,\mathrm{mm}$ and $f_{CS} = 10\,\mathrm{mm}$, while the Fourier lens, used for the final sorting of the beams, has a focal length $f_L = 400\,\mathrm{mm}$. Brightness and colours refer to intensity and phase, respectively.

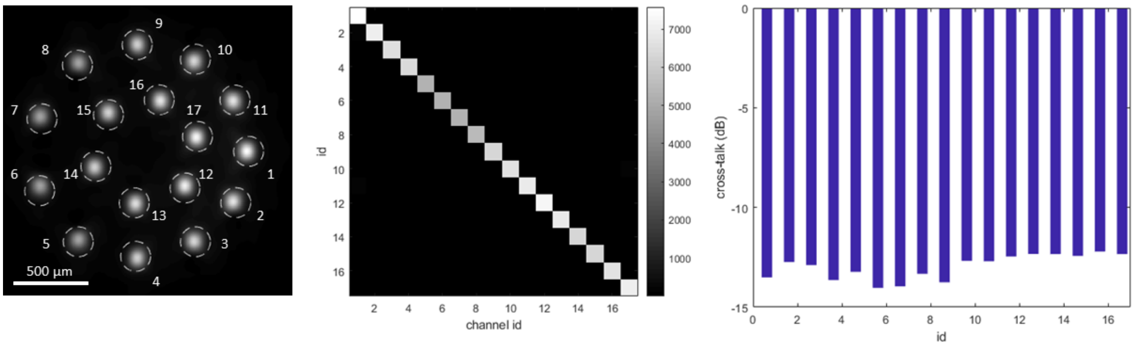

Figure 57: In the first frame, the demultiplexer output, of the multipole-phase beams reported in figure 56, is shown. The channel's index, related to each light beam, is also reported, while the detection areas (of radius $R_I = 100\,\mu m$) used for the Cross-Talk computation are plotted with a dashed line. In the second frame, the intermodal overlapping map, with the intensities in arbitrary unit, is reported. Finally, in the last frame, the XT values of each channel are plotted.

value of the phase strength ($\alpha = 2000\,\text{mm}^{-4}$), the spots are more spread, causing a higher interference in the neighbouring beams. For the same reason, it was also incremented the radius of the detection areas: from $100\,\mu m$ to $150\,\mu m$. After a manual correction of the external spots, as in the previous case, we have obtained the results reported in the figure 59. Also in this setup we were able to get a Cross-Talk level around the $-12\,\text{dB}$ but for a further reduction of the number of total channels.

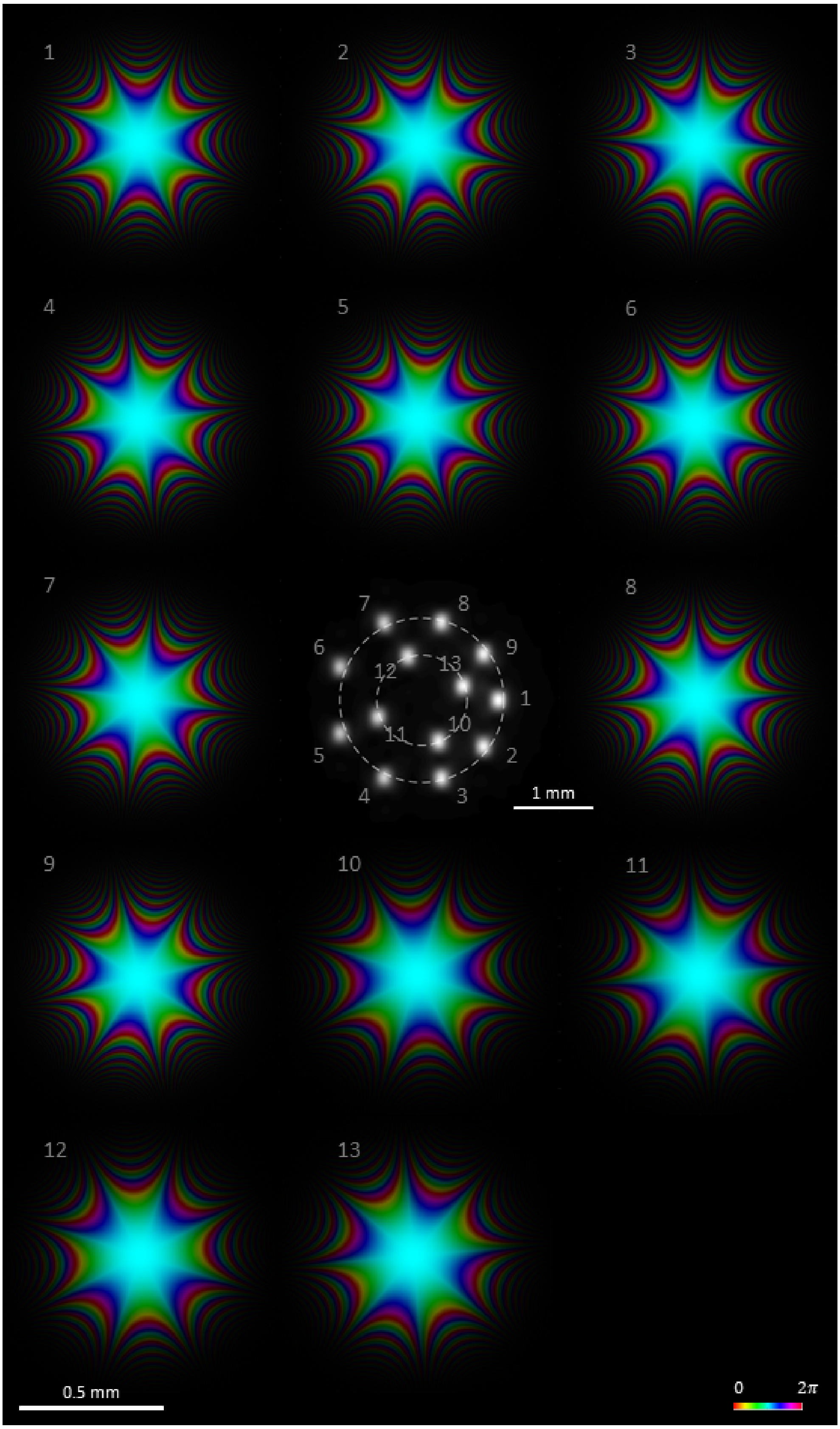

Figure 58: In the figure, it is shown a set of multipole-phase beams at the input of a demultiplexer, and their relative sorted beams. The output configuration, reported in the centre, is composed by thirteen light spots arranged over two concentric circles. The external one has $N_1 = 9$ beams, which are related to multipole-phase beams of order $m = 4$, phase strength $\alpha^{(1)} = 2000\,\mathrm{mm}^{-4}$ and phase orientation $\theta_0 \in [0; \frac{2\pi}{m}]$ with steps of $\Delta\theta_0^{(1)} = \frac{1}{m}\frac{2\pi}{N_1}$. The internal distribution, instead, is composed by $N_2 = 4$ light spots corresponded to multipole-phase beams of the same order, and range of θ_0, but characterized by a phase strength $\alpha^{(2)} = 1100\,\mathrm{mm}^{-4}$ and a shift of the orientations equal to $\frac{\Delta\theta_0^{(1)}}{2}$. The parameters of the circular-sector transformation, used in the demultiplexing process, are: $a = 2.0\,\mathrm{mm}$, $b = 0.4\,\mathrm{mm}$ and $f_{CS} = 5\,\mathrm{mm}$, while the focal length, of the Fourier lens used for the final sorting of the beams, is $f_L = 400\,\mathrm{mm}$. As usual, brightness and colours refer to intensity and phase, respectively.

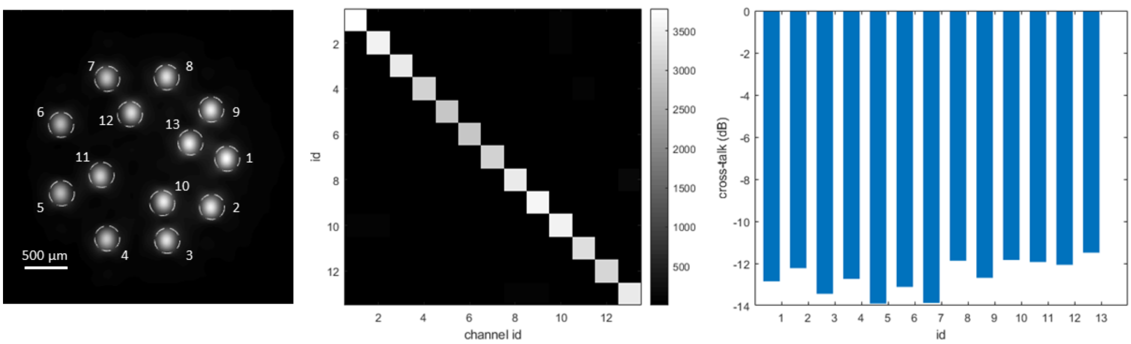

Figure 59: In the first frame, it is reported the demultiplexer output, as shown in the centre of figure 58, with the channel's index, related to each light beam, wrote in white. The detection areas used for the Cross-Talk computation are plotted with a dashed line. In the second frame, the intermodal overlapping map, with the intensities in arbitrary unit, is reported. Finally, in the last frame, the XT values of each channel are plotted. Case $m = 4$

8 Communication links in the multipole-phase beams framework

In the recent years, there has been more and more interest regarding the optical communication technologies that use the light propagation in free space in order to perform wireless transmission of data. These free-space optical communication systems (FSO) differ from the transmission via optical fibres for the absence of a solid medium supporting the electromagnetic field. This implies the possibility to create communication links where a cable connection is prohibitive, for example when there is the necessity to connect two or more buildings in a city, or between a building and a satellite or between vehicles in movement like cars, aeroplanes, and ships. These and more examples are well represented in figure 60. Also, the FSO can be a cheaper solution, with respect to the installation of long underground optical fibre cables, and this is particularly useful in the developing world. For instance, the Africa continent takes into account for the 16% of the world's population but only 4% of Internet access, due to the prohibitive capital costs of US$100,000 per km of optical fibres, which creates an impenetrable economic barrier for many countries [2].

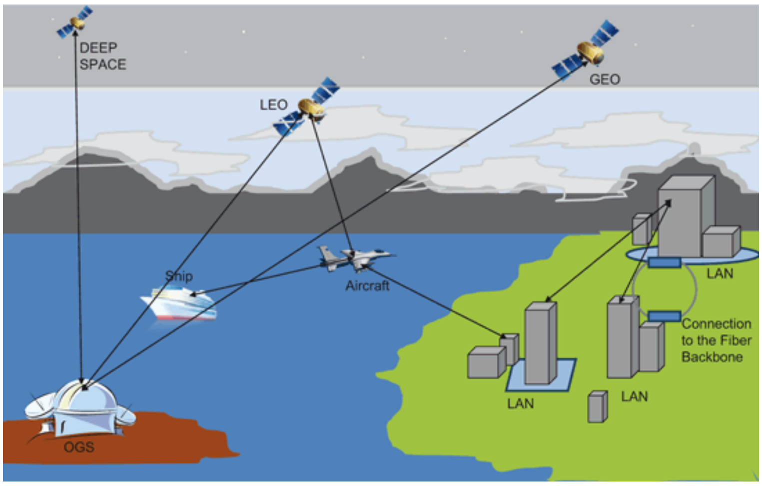

Figure 60: Different types of FSO communications. Arun K. Majumdar - "Optical Wireless Communications for Broadband Global Internet Connectivity".

Consequentially, the possibility to increment the efficiency of these FSO communication systems, propagating more information channels in the same electromagnetic frequency thanks to the properties of the multipole-phase beams, is very interesting. For this reason, we want now to analyse an entire link of communication, where an initial set of laser spots is, at first, transformed into a superposition of multipole-phase beams, which are so propagated in free space for a long distance and, finally, the electromagnetic field is converted into a bright spot constellation correlated to the input configuration of laser beams. Each beam corresponds to a single channel of information, the set of which, thanks to the orthogonality properties of the multipole-phase beams, can be multiplexed into one electromagnetic field without thus losing the information content. Therefore, this single light beam so obtained can be easily propagated in the free space between the transmitter and the receiver of the link. Finally, thanks to a demultiplexer, the single channels are again separated in the form of isolated bright spots. For these light beams, which we can imagine as generic Gaussian beams carrying a structured phase, the waist w_0, and the divergence Θ_0, are inversely proportional ($w_0\Theta_0 = \frac{\lambda}{\pi}$) [53]. Therefore, beams excessively collimated, diverge a lot during the propagation. For this reason, in order to propagate the light beam for a distance of several kilometres, the size of the intensity pattern of the multiplexer output field must be in the order of the centimetres. However, keeping in mind possible future practical applications, it is convenient to keep the size of the optical setup, which performs the multiplexing/demultiplexing of the light spots, miniaturized. In this way, it is possible to have a better coupling with the integrated electronic circuits used to control the communication link. Accordingly, the electromagnetic field obtained after the multiplexing must be magnified before the propagation. Similarly, the received light beam must be demagnified before the demultiplexing. These two operations can be performed by a simple telescope system. Finally, the sorting

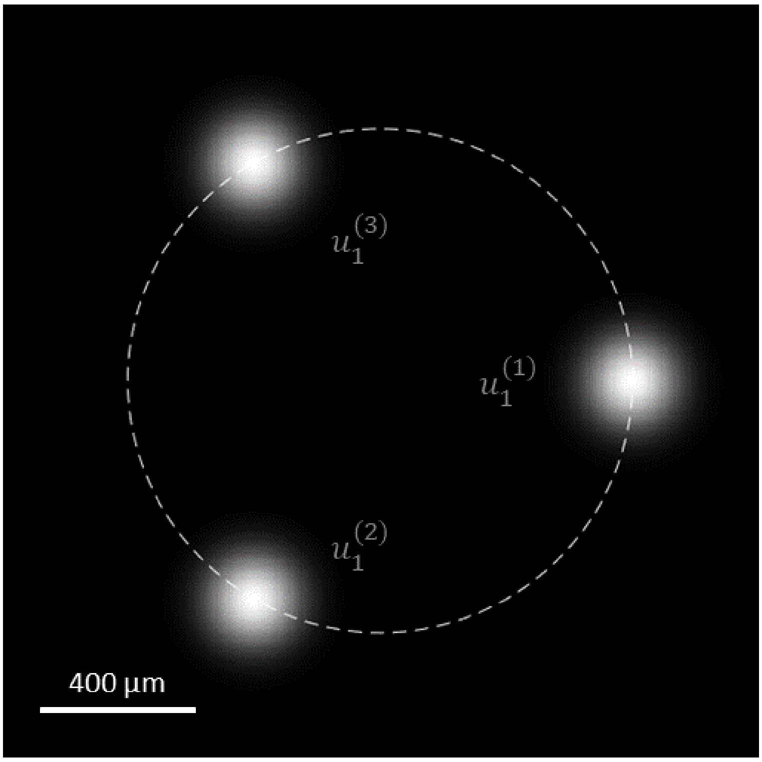

Figure 61: The initial light spots of a link with three different channels of communication. The spots are obtained by a back forward propagation starting from linear phase gradients of wavelength $\lambda = 632.8\,\text{nm}$ and waist $w_0 = 1\,\text{mm}$, using a Fourier lens with a focal length $f_L = 400\,\text{mm}$ in a $f_L - f_L$ configuration.

process can be performed, obtained the final detected light beams.

8.1 Simulation of a communication link

In the theory chapter 3, we have seen that during the transmission of a multipole-phase beam of phase order m, the transmitted beam is still endowed with a multipole-phase but characterized, now, by an order m' given by the relation 124

$$m' = \frac{m}{m-1} \tag{171}$$

This expression tell us that the only family of multipole-phase beams which can be transmitted for a long distance conserving successfully the phase structure is the one characterized by a phase order $m = 2$[4]. For this reason, in this section, we want to analyse in detail the evolution of a set of multipole-phase beams, of order $m = 2$, along an entire communication link. In particular, will be considered the example configuration of three channels reported in figure 61. In particular, for the case $m = 2$ the multiplexer and the demultiplexer are based on the same architecture, in reverse, which is not true for different values of m. However, as shown in previous chapters, a communication link can be established also using different values of m, taking into account the above-mentioned implications.

8.1.1 Multiplexing of the initial laser inputs

The starting point of our simulation are the linear phase gradients associated to the initial light spots of the three different channels characterized by a wavelength $\lambda = 632.8\,\text{nm}$. Indeed, we already know that a light spot can be Fourier transformed into an electromagnetic field with a wavefront characterized by a linear phase gradient. This implies that the initial information content, of each communication channel, is totally enclosed in the linear phase gradient of the beam related to that particular channel. For this reason, we want to maximize

---

[4] The trivial solution for $m = 0$ (i.e., a Gaussian beam) is ignored in this description

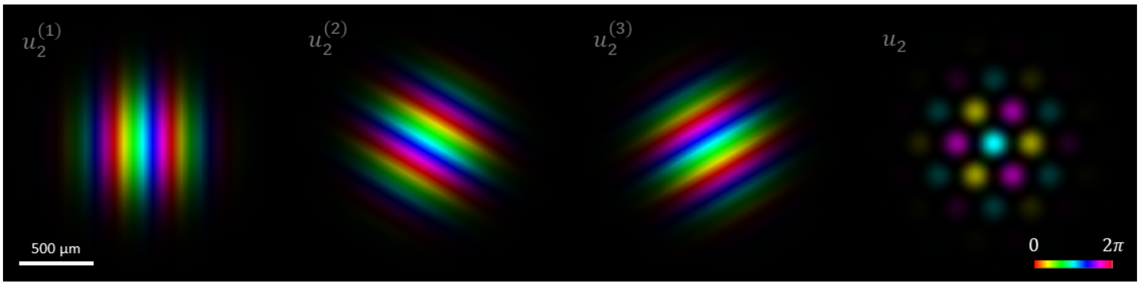

Figure 62: The three linear phase gradients related to the spot configuration of figure 61, and their superposition. Brightness and colours refer to intensity and phase, respectively.

the resolution of these gradients, starting the simulation from the definition of them rather than from the initial light spots, which can be obtained, afterwards, from a back-forward propagation. Therefore, if $(\alpha, \theta_0)^{(i)}$ are the phase strength and orientation of the (i)-th multipole-phase beam, related to the spots of the configuration in figure 61, we can define a first Gaussian beam

$$u_0(r, \theta) = \exp\left\{ -\left(\frac{r}{w_0} \right)^2 \right\} \tag{172}$$

and, then, applying to $u_0(r, \theta)$ the phase term 92

$$\Phi^{(i)}(r, \theta) = \beta^{(i)} r \cos\left(\theta - \phi_0^{(i)} \right) \tag{173}$$

we get the (i)-th beam, $u_2^{(i)}(r, \theta)$, characterized by the linear phase gradient described by the equation 173, where $\beta^{(i)}$ is the component of the wave vector $\boldsymbol{k}$ on the simulation plane, and it is related to the period of the linear phase. Indeed, we remember that this phase gradient will be characterized by an orientation, given by the angular coordinate of the initial light spot, and a modulus, which depends, instead, on the radial coordinate of the spot and defined by the on-plane component of the linear momentum. Since the channels, of the configuration in figure 61, have the same radial coordinates, the three linear phase gradients obtained, will differ only for the orientation. Indeed, as can be seen from the figure 62, the coloured stripes of the gradients simulated change their direction but not their period (remember that each colour is a different phase value in the 2π-phase period).

At this point, thanks to the orthogonality of linear phase gradients with different orientation, we can multiplex these three beams together

$$u_2(r, \theta) = \sum_i u_2^{(i)}(r, \theta) \tag{174}$$

This superposition, $u_2(r, \theta)$, is shown in the last frame of the figure 62, where the three single beams, characterized by the orientations $\phi_0^{(1)} = 0°$, $\phi_0^{(2)} = 120°$ and $\phi_0^{(3)} = 240°$, are also reported.

We remember now that a linear phase gradient can be transformed, thanks to a circular-sector transformation, into a multipole-phase beam with phase orientation θ_0 and phase strength α, given by the following conditions

$$\begin{cases} \theta_0 = -\phi_0/m \\ \alpha^{(i)} = ab^{-m}\beta^{(i)} \end{cases} \tag{175}$$

where $a = 1.0\,\text{mm}$ and $b = 0.4\,\text{mm}$ are the parameters of the circular-sector transformation, $m = 2$ is the order of the multipole-phase beams obtained and $\alpha = 100\,\text{mm}^{-2}$.

MatLab code The relative source code, used for the generation of each $u_2^{(i)}$ beam, is reported in the following. The (i)-th phase gradient $\Phi^{(i)}$ is called "Phi", the relative beam is defined as "u2i" and the multiplexed field is named "u2" as in the equation 174. As usual, "x" and "y" are the coordinates of the observation plane

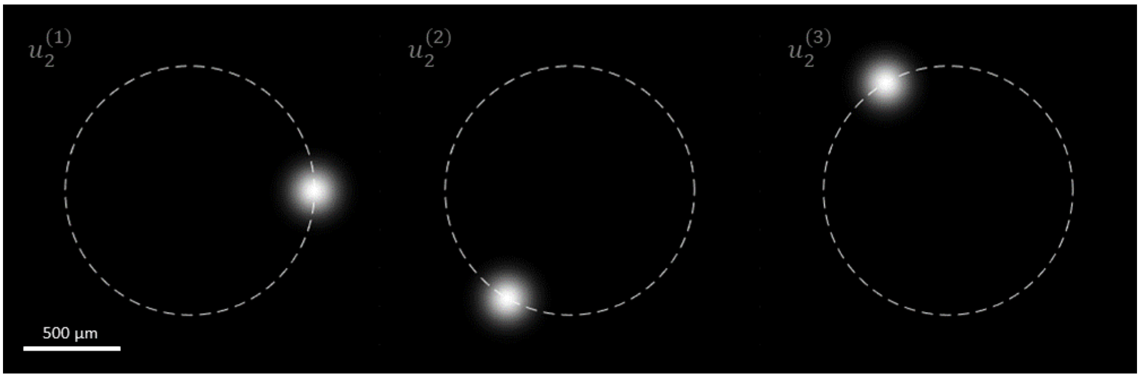

Figure 63: The initial electromagnetic fields (i.e., the input beams of our communication link) of the configuration reported in figure 61, obtained by a back forward propagation in a $f_L - f_L$ system with a Fourier phase term Ω_F as described in equation 176.

along the two axis and "alpha" is the array of the phase strengths of the multipole-phase beams related to the channel's configuration to simulate.

Listing 8.1.1: linear phase gradients defintion

```
 % Gaussian beam
 u0 = exp(-(r/w0).^2);

 % linear phase gradients
 u2  = zeros(length(x),length(y));
 u2i = zeros(length(x),length(y), length(alpha));
 for i = 1 : length(alpha)
     Phi(i)       = alpha(i)*b^m*r.*cos(theta + m*theta0(i));
     u2i(:,:,i)   = u0.*exp(1i*Phi(i));
     u2           = u2 + u2i(:,:,i);
 end
```

8.1.2 The initial light beams

Now we can get the initial light spots, $u_1(r,\theta)$, thanks to a back-forward propagation of $u_2(r,\theta)$ through a Fourier lens with the usual phase function

$$\Omega_F(r,\theta) = -\frac{k}{2f_L}r^2 \tag{176}$$

and a further free-space propagation for a distance $f_L = 400\,\mathrm{mm}$, which is the focal length of the lens. In figure 63 it is reported the light spots so obtained, while the MatLab code is the following:

Listing 8.1.2: initial light spots

```
 OmegaF  = -(k/(2*f_L))*r.^2;                 % lens phase
 u1      = u2.*exp(1i*OmegaF);                % Fourier transf.
 u1      = FreeSpaceProp(u1,L,lambda,f_L);    % prop. after lens
```

8.1.3 The multipole-phase beams

At this point, we have to generate the superposition, $u_3(r,\theta)$, of multipole-phase beams of order m associated to the initial set of beams, $\{u_2^{(i)}\}$, with the linear phase gradients. We know, from chapter 5, that this procedure consists in the mapping of the pattern of the linear phase gradient onto a circular sector. This transformation is performed by two optical elements and, for the definition of the first one, we remember that the final circular

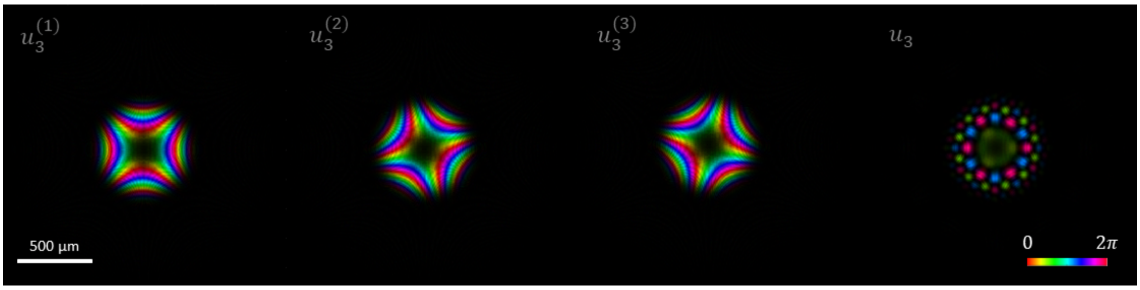

Figure 64: In the first three frames we have the multipole-phase beams of order $m = 2$, phase strength $\alpha = 100\,\text{mm}^{-2}$ and phase orientations $\theta_0^{(1)} = 0°$, $\theta_0^{(2)} = 60°$ and $\theta_0^{(3)} = 120°$, obtained after the multiplexing stage for the three linear phase gradients shown in the figure 62. In the last frame, their superposition (u_3 in the MatLab code) is reported. The parameters of the circular-sector transformation used are: $f_{CS} = 10\,\text{mm}$, $a = 1.0\,\text{mm}$ and $b = 0.4\,\text{mm}$. Brightness and colours refer to intensity and phase, respectively.

sectors generated are characterized by an amplitude of $\frac{2\pi}{|m|}$. Accordingly, in order to obtain an output beam defined over the whole phase range of 2π, an initial $|m|$-fold multiplication is needed. This multiplication can be performed by a combination of $p = 1, ..., m$ phase terms, where each of them is a n-fold circular-sector transformation with $n = -m$ and rotated with respect to the others by a factor $(p-1)\frac{2\pi}{|m|}$, as in the equation 154. Equation that, for simplicity, we report in the following:

$$\Omega_{m,I}^{M}(r,\theta) = arg\left\{\sum_{p=1}^{|m|} e^{i\Omega_{m,II}^{D,(p)}}\right\} \tag{177}$$

where $\Omega_{m,I}^{M}$ is, therefore, the phase pattern of the first optical element, i.e., the multiplier, which is a combination of $|m|$ terms:

$$\Omega_{m,II}^{D,(p)}(r,\theta) = A\left(\frac{r}{a}\right)^{B}\frac{\cos\left[\theta B + (p-1)\frac{2\pi}{|m|}\right]}{B} - C \tag{178}$$

where we have defined the usual constants A, B and C as:

$$\begin{cases} A := k\frac{ab}{f_{CS}} \\ B := 1 + \frac{1}{m} \\ C := k\frac{r^2}{2f_{CS}} \end{cases} \tag{179}$$

Now, the second optical element, placed at a distance equal to f_{CS}, has to perform a circular-sector transformation of order m, characterized by the following phase pattern

$$\Omega_{m,II}^{M}(r,\theta) = A\left(\frac{r}{b}\right)^{1+m}\frac{\cos[(1+m)\theta]}{1+m} - C \tag{180}$$

In our simulation, we have adopted the following values of the design parameters: $f_{CS} = 10\,\text{mm}$, $a = 1.0\,\text{mm}$ and $b = 0.4\,\text{mm}$.
At this point, the multiplexing procedure is completed. We have obtained an electromagnetic field, $u_3(r,\theta)$, as reported in figure 64, which is the superposition of the multipole-phase beams, $\{u_3^{(i)}(r,\theta)\}$, associated to the initial light spots. In the same figure, we show, also, these single multipole-phase beams related to the linear phase gradients that can be seen in figure 62. Notice how the phase pattern of the beams is the same but rotated. Indeed, the initial light spots have the same radial coordinate and, therefore, the multipole-phase beams will have the same phase strength.

MatLab code Here it is reported the source code used in order to define the phase term of the phase plates necessary for the circular-sector transformation. In particular, we have defined $\Omega_{m,I}^{M}$ as "Phase_I" and called $\Omega_{m,II}^{M}$ as "Phase_II".

Listing 8.1.3: multiplexer phase plates

```
A = k*(a*b/f_CS);
B = 1+1/m;
C = k*(r.^2)/(2*f_CS);

% 1st phase plate
Phase_I = zeros(length(x),length(y));
for p = 1 : abs(m)
    Omega    = A*((r/a).^B).*cos(theta*(B)+(p-1)*2*pi/abs(m))/B - C;
    Phase_Ip = exp(1i*Omega);
    Phase_I  = Phase_I + Phase_Ip;
end
Phase_I = angle(Phase_I);

% 2nd phase plate
Phase_II = A*((r/b).^(1+m)).*cos(theta*(1+m))/(1+m) - C;
```

Below, instead, it is reported the code used in order to generate the superposition, $u_3(r,\theta)$, of the multipole-phase beams, thanks to these two phase plates. Notice that, to the field $u_2(r,\theta)$ is, before, applied the phase term $\Omega^M_{m,I}$ (first line of the code), obtaining $u_3^{(I)}(r,\theta)$. Then, the beam is free space propagated for the focal length, f_{CS}, of the focusing term C (second line). In this way, we get the field $u_3^{(II)}(r,\theta)$ and, finally, also the second phase term, $\Omega^M_{m,II}$, is applied (last line of the code).

Listing 8.1.4: multipole-phase beams generation

```
u3_I  = u2.*exp(1i*Phase_I);                % 1st phase plate
u3_II = FreeSpaceProp(u3_I,L,lambda,f_CS);  % prop. between the plates
u3    = u3_II.*exp(1i*Phase_II);            % 2nd phase plate
```

8.1.4 Magnification and propagation of the multiplexed beam

As initially said, before propagating the electromagnetic field from the transmitter to the receiver, this light beam has to be magnified in the order of the centimetres, to avoid an excessive divergence of the field over long distances. Remember, indeed, that we want to transmit the signals along a link of the order of the kilometres. This magnification can be achieved thanks to a $4f$ configuration, i.e., a telescope. The two more simple possibilities are the Galilean telescope, where a diverging lens, L_1, is followed by a converging lens, L_2, and the Keplerian telescope, composed by two converging lenses. Each lens produces a phase term like the one described in the equation 176 with the substitution $f_L \longleftrightarrow f_1, f_2$, where $f_{1,2}$ are the two focal lengths of the lenses of the telescope. Remembering that the magnification power, M_P, of a telescope is the ratio of the two focal lengths

$$M_P = \frac{f_2}{f_1} \tag{181}$$

choosing properly these two values, f_1 and f_2, one can set the size of the beam to transmit.
Then the beam can be correctly propagated in the free space between the transmitter and the receiver. However, in order to focus, properly, the transmitter output beam into the receiver, a further phase term Ω_{F_z} has to be introduced, where, now, f is the transmission distance

$$\Omega_{F_z}(r,\theta) = -\frac{k}{2f^2}r^2 \tag{182}$$

In an experimental setup this can be achieved introducing a further lens after the telescope with a focal length f. Moreover, in order to compensate the Fresnel term, Ω_{F_z}, another identically lens has to placed before the detector. Now, the detected beam could be sorted in a spots configuration which is correlated to the input one. However, we recall from the theory that, a multipole-phase beam of order $m = 2$ characterized, in the original plane (r, θ), by a phase structure

$$\Omega^{(i)}(r, \theta) = \alpha_0 r^2 \cos(2(\theta - \theta_0)) \tag{183}$$

after the propagation for the distance f_1, the phase pattern of its wavefront becomes

$$\Omega^{(1)}(\rho, \phi) = \alpha_1 \rho^2 \cos(2(\phi - \theta_1)) \tag{184}$$

where $\theta_1 = \theta_0 + \frac{\pi}{2}$ and the phase strength is given by the equation 127

$$\alpha_1 = \frac{k^2}{4f_1^2}\frac{1}{\alpha_0} = \frac{k^2}{4f_2^2}\frac{M_p^2}{\alpha_0} \tag{185}$$

where we have substituted f_1 with the equation 181. At this point, supposing we are using a Keplerian telescope, where the distance between the two lenses is the sum of their focal lengths $(f_1 + f_2)$, the beam has to be propagated for a further distance f_2, and the same relation gives the new phase strength:

$$\alpha_2 = \frac{k^2}{4f_2^2}\frac{1}{\alpha_1} = \frac{\alpha_0}{M_p^2} \tag{186}$$

where we have substituted α_1 with the equation 185. Now the rescaled beam is propagated for the distance f between the transmitter and the receiver stage. Therefore, we have:

$$\alpha_3 = \frac{k^2}{4f^2}\frac{1}{\alpha_2} = \frac{k^2}{4f^2}\frac{M_p^2}{\alpha_0} \tag{187}$$

Now, since in this case the beam waist has to be magnified from the order of the hundreds of micrometers to the centimetres, the magnification factor is very high: $M_p \sim 10^2$. Therefore, $\alpha_3 << \alpha_0$. However, we remember that the centres, of the demultiplexed final light spots, have a radial coordinate, r_C, which is related to the phase strength by the following relation

$$r_C = f_L \frac{\lambda}{2\pi}\frac{\alpha b^m}{a} \propto \alpha \tag{188}$$

This means that, reducing α, also the spot positions change. For this reason, a modification of α_3 is needed in order to obtain the same light spot configuration of the initial one. Therefore, a further rescaling of the beam is necessary and can be performed with a second telescope. This telescope will be identical to the previous one, but with the two lenses in the inverted order, producing a resize of the beam by the factor M_P^{-1}. In this way, after the further propagation between the two lenses of this second telescope, the final phase strength becomes

$$\alpha_f = \frac{k^2}{4f^2}\frac{M_p^4}{\alpha_0} \tag{189}$$

Setting M_p properly, the multipole-phase beam transmitted can be correctly reduced to the original size and the demultiplexing can be performed, producing a final configuration of light spots similar to the initial one. Actually, the final spots will have a different angular coordinate, θ_C, with respect to the original light beams. Indeed, from the equation 184, the phase orientation of the transmitted multipole-phase beam, is shifted of $\pi/2$ in respect to θ_0 in each step: the first telescope, the link propagation and the final telescope. Therefore, in the case of beams with phase order $m = 2$, the azimuthal coordinate of the final spot will be shifted of an angle of $2 \cdot 3\pi/2 = 3\pi$. This angle deviation, and the changing of the phase strength 189, have been correctly observed in the simulation described in this chapter.

From a simulation point of view, in order to reduce the computational time, the rescaling of the beam is

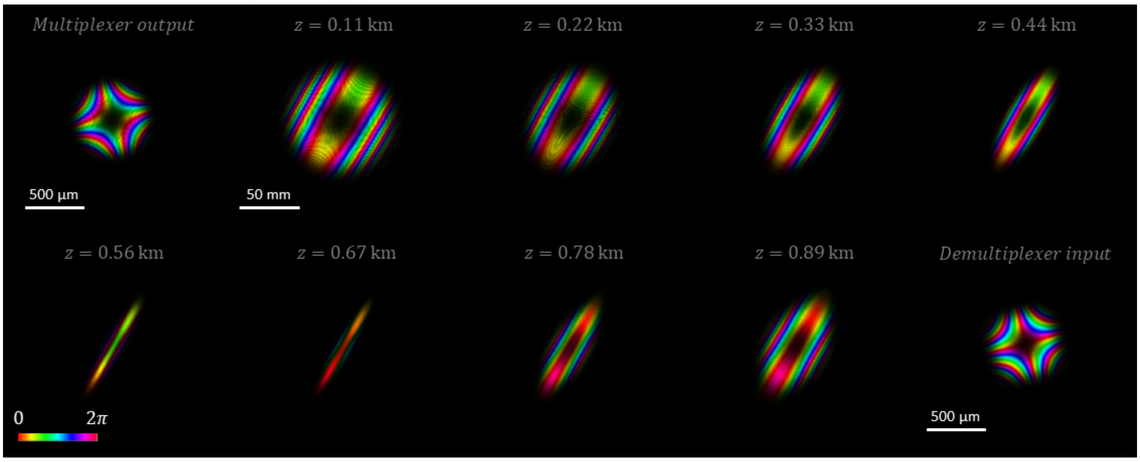

Figure 65: The transmission field at various intermediate distances between the transmission and the receiver stage of the communication link simulated in this section. In the first frame, the multiplexer output (i.e., the field $u_3^{(2)}$ of figure 64) is reported. In the following frames, it is shown the evolution of the rescaled wavefronts during the free space propagation along the communication link. Finally, in the last frame, it is reported the multipole-phase beam after the descaling (i.e., the impinging field to the Transformer phase plate, $\Omega^D_{m,1}$, of the demultiplexing receiver stage). Brightness and colours refer to intensity and phase, respectively.

performed by simply resizing each pixel of the observation plane where the wavefront of our beams is simulated. Indeed, we recall that the coordinates of this plane are defined by a mesh [X,Y], where each axis is sampled with the usual spatial discretization

$$x \longleftrightarrow \left[-\frac{L}{2} : \Delta_x : \frac{L}{2} - \Delta_x\right] \tag{190}$$

where L is the side of the squared observation plane and M the number of samples. This means that the initial size, of the single pixel of the mesh, is $\Delta_x = L/M$. In order to perform a rescaling of the beams, we can multiply this size for the scaling factor M_p

$$\frac{L}{M} \longleftrightarrow \frac{L}{M} \cdot M_p \tag{191}$$

In this way, the matrix, $X \times Y$, of the mesh of the rescaled beam, will have the same number of pixels as in the original field, but with the wavefront magnified. Notice that even the coordinates, of the both axes of the observation plane, have to be rescaled for the same M_p factor, in order to obtain, finally, images with the proper axis values. Remember, indeed, that in a MatLab image, the values of the matrix elements (which make up the image) and the arrays of the axis coordinates, are independent objects.

In order to perform this resizing, we can apply, directly, the phase term Ω_{F_z} to the multiplexer output beam, $u_3(r, \theta)$, remembering, however, to make the substitution $r^2 \longrightarrow (M_p r)^2$ in the equation 182. In this way we have implemented the above-mentioned rescaling, avoiding the use of a telescope (from a computational point of view. The telescope is indeed necessary in practical implementations). After that, the field can be propagated, keeping in mind that the observation plane has to be resized for the same factor M_p. In figure 65, for instance, it is reported the wavefront of the simulated electromagnetic field, $u_3^{(2)}(r, \theta)$, at various distances. Notice, from the second frame of the figure, how the multiplexer output of the first frame has been correctly magnified to the order of the centimetres. Notice moreover that, due to the Fresnel's correction term with the same expression 182, also the receiver beam is rescaled, but by a factor M_p^{-1}, as it can be seen from the last frame of the figure.

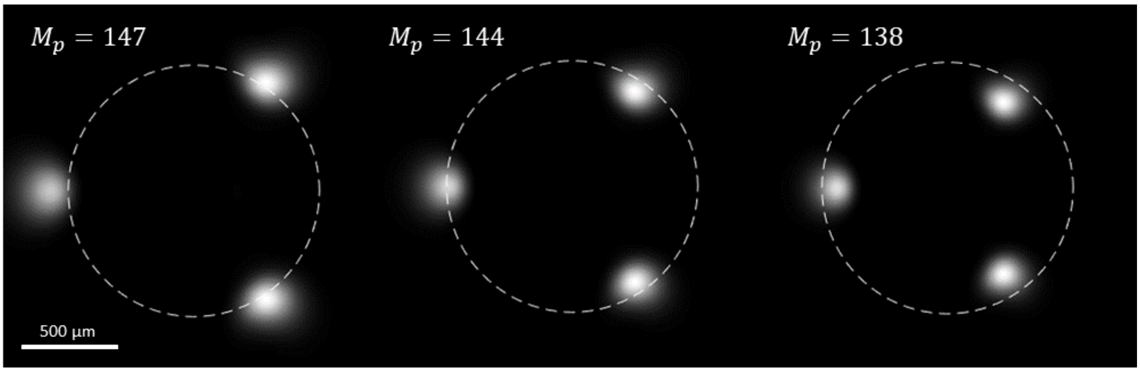

Figure 66: Effect of the scaling factor M_p on the final light spots disposition

The scaling factor It is important to open a parenthesis about the scaling factor, M_p, due to its close relationship with the phase strength of a transmitted beam, as previously seen. Indeed, even if the magnification of the transmitter beam, and the rescaling of the received one, are executed with the same scaling factor, after a free space propagation for a long distance, the detected beam can be different in size with respect to the original one. This is due to the natural divergence of an electromagnetic field during a free space propagation. However, we have seen that, a magnification of the wavefront is connected to a variation of the phase strength. Consequentially, the final light spots can be displaced differently, in the radial direction, in respect to the initial ones. In figure 66, for instance, the simulation outputs of the same communication link, for three different scaling factors, are reported. It is easy to see that, incrementing the scaling factor, the radial coordinate of the light spots increases. Conversely, the angular coordinates of the spots, remain the same. For this reason, in our simulation, M_p is chosen in order to produce an output as close as possible to the original channel configuration, whose radial coordinate are represented by the circle plotted with a dashed line in the figure 66.

MatLab code In the following it is shown the MatLab code used for the magnification of the beam, $u_3(r, \theta)$, and its propagation between the transmitter and the receiver. In the first line of the code it is defined the phase term Ω_{F_z}, which is called "OmegaFz". Notice that this phase function contains the power M_p^2 as anticipated. Indeed, since the beam has to be rescaled, also the radial coordinate r, has to be magnified by the same M_p factor. Then, this focusing phase term Ω_{F_z} is applied to the multiplexer output beam $u_3(r, \theta)$ (second line of the code below). At this point, the field can be free space propagated for the distance z_{max} (third line). Notice that, due to the necessary resizing of the beam, the side of the observation plane is multiplied by the same factor M_p. Finally, at the received beam, the compensation of the Fresnel's term $-\frac{k}{2z_{max}}r^2$ is applied (last line of the code).

Listing 8.1.5: rescaling and propagation of the field

```
OmegaFz = -(k/(2*z_max))*(r.^2)*(Mp^2);        % lens phase
u3      = u3.*exp(1i*OmegaFz);                 % focusing
u3      = FreeSpaceProp(u3,L*Mp,lambda,z_max); % free space prop.
u3      = u3.*exp(1i*OmegaFz);                 % Fresnel correction
```

8.1.5 Demagnification and sorting of the received beam

After the propagation, the following simulation step is the reconversion of the received field, $u_3(r, \theta)$, into the initial configuration, where the single channels of information are identified by a set of isolated light spots. This operation, described in detail in the chapter 4, is performed by a first optical element which transforms each multipole-phase beam into a linear phase gradient thanks to a circular-sector transformation. This transformation is described by a phase term, $\Omega^D_{m,I}$, that is identical to the second element of the multiplexer, $\Omega^M_{m,II}$. After a phase correction, produced by the (PC)-phase plate, characterized by the following phase pattern

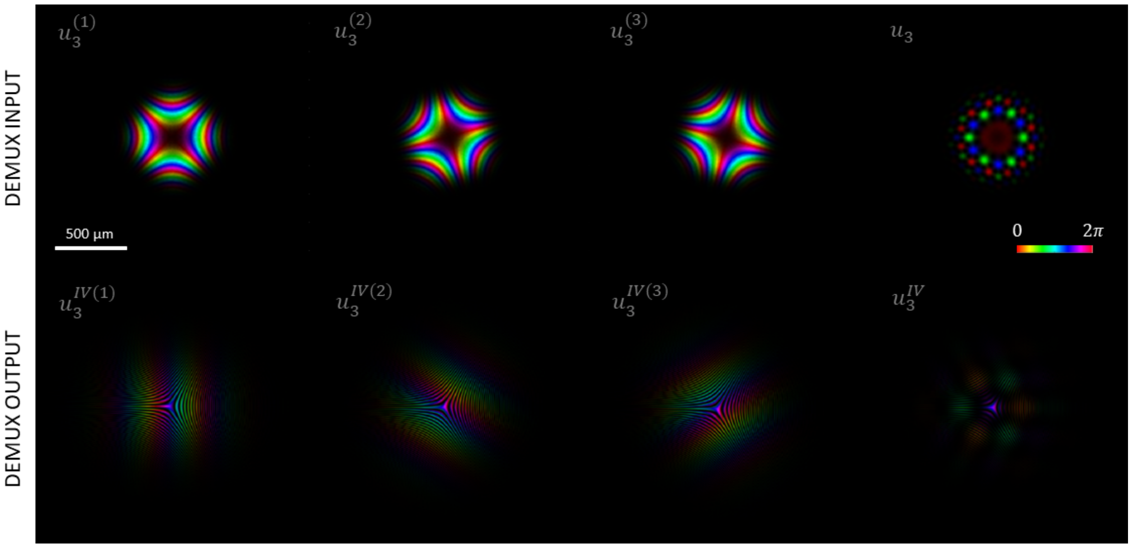

Figure 67: On the top, the demultiplexer input beams (and their superposition), i.e., the multipole-phase beams of figure 64 after the free space propagation between the transmitter and the receiver stages of the link, as reporting in figure 65 for the field $u_3^{(2)}$. On the bottom, instead, we have the demultiplexer output beams (and their superposition), i.e., the linear phase gradients used in order to obtain the final light spots after the application of the phase term Ω_F. Brightness and colours refer to intensity and phase, respectively.

$$\Omega^D_{m,II}(r,\theta) = A\left(\frac{r}{a}\right)^B \frac{\cos\left[\theta B\right]}{B} - C, \tag{192}$$

where we remember that

$$\begin{cases} A := k\frac{ab}{f_{CS}} \\ B := 1 + \frac{1}{m} \\ C := k\frac{r^2}{2f_{CS}} \end{cases} \tag{193}$$

we obtain the demultiplexer output beams reported in the figure 67, where it is possible to see the coloured stripes of the linear phase gradients of their wavefronts. In the top of the same figure, the demultiplexer input fields $\{u_3^{(i)}\}$ and their superposition, i.e., the rescaled multipole-phase beams detected at the receiver, are also shown. Finally, after the application of the same phase term 176, these linear phase gradients are Fourier transformed into the original light spots configuration, as reported in the bottom of the figure 68. Actually, the spots are shifted of a π-angle, with respect to the initial positions (shown in the top of the figure).

MatLab code In the MatLab code below, it is reported the demultiplexing procedure used in the simulation. The phase terms, $\Omega^D_{m,I}$ and $\Omega^D_{m,II}$, called "Phase_III" and "Phase_IV" respectively, are reported in the line two and three.

Listing 8.1.6: rescaling and propagation of the field

```
1     % phase plates functions
2      Phase_III = Phase_II;                        % 3rd phase plate (CS)
3      Phase_IV  = A*((r/a).^B).*cos(theta*B)/B - C; % 4th phase plate (PC)
4
5     % propagation
6      u3_III  = u3.*exp(1i*Phase3);                % 3rd phase plate
7      u3_IV   = FreeSpaceProp(u3_III,L,lambda,f_CS); % prop. between the two plates
8      u3_IV   = u3_IV.*exp(1i*Phase_IV);           % 4th phase plate
9      u3_IV   = u3_IV.*exp(-1i*(k/(2*f_L))*r.^2);  % Fourier transf. (lens)
10     u4      = FreeSpaceProp(u3_IV,L,lambda,f_L); % final prop.
```

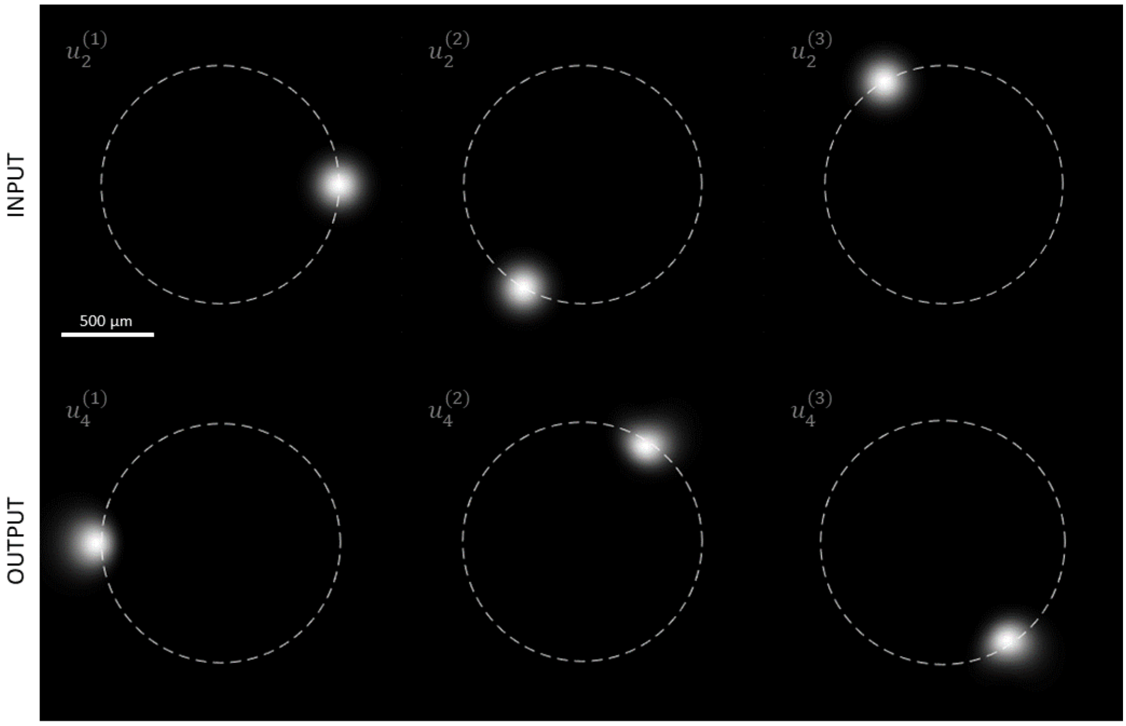

Figure 68: On the top, the initial light spot configuration as reported in figure 63 (i.e., the input signals of the communication link analysed). On the bottom, the detected fields after the demultiplexing receiver stage (i.e., the output signals of the link).

8.2 Link optimization

The link described previously is, then, optimized in order to carry an higher number of channels but keeping their Cross-Talk values under the just mentioned limit of $-15\,\mathrm{dB}$. In the simulation, it was adopted an initial set of linear phase gradients characterized by a beam waist of $w_0 = 1.0\,\mathrm{mm}$ for an electromagnetic field with the usual wavelength of $\lambda = 632.8\,\mu\mathrm{m}$. The orientations of the linear phase gradients, and their 2π-phase period densities, are chosen correspondingly to the input configuration of light beams reported on the left of the figure 69. These input beams, corresponding to thirty different communication channels, are arranged over two circular distributions. The internal one, characterized by a radius related to a phase strength of $\alpha_1 = 100\,\mathrm{mm}^{-2}$, is made up of sixteen beams. The external distribution, instead, is composed by fourteen light spots with a radial coordinate corresponded to an α_2 value of $150\,\mathrm{mm}^{-2}$. The parameters for the generation of superposition of multipole-phase beams of order $m = 2$, used for the transmission of these thirty channels, are again: $f_{CS} = 10\,\mathrm{mm}$, $a = 1.0\,\mathrm{mm}$ and $b = 0.4\,\mathrm{mm}$. The focusing of the initial and the final light spots are, instead, performed thanks to a Fourier lens with a focal length of $f_L = 400\,\mathrm{mm}$. Finally, before the propagation, the beam is magnified by a factor $M_p = 140$ and, after the propagation, the field is reduced by the same factor.

In the figure 69 are, also, reported the two constellations of spots after the propagation on the whole link, long $1\,\mathrm{km}$. Notice how the fourteen external beams, after the transmission, have become the internal ones. Indeed, from the equation 189, it can be seen that, the higher is the initial phase strength α_0, the lower is the final phase strength α_f. Consequentially, from the equation 188, the lower is the radial coordinate of the spots.

In order to evaluate the performance of this link, the Cross-Talk of each channel was computed. The results of this computation are shown in figure 70. In the first frame (from the left), it is possible to see the output beams with the detection areas (dashed line) used in order to compute the XT values. These areas have a radius of $50\,\mu\mathrm{m}$ for both the internal and external configuration. In the second frame, instead, it is plotted the intermodal map of the collected light intensity on each channel's detection area for each output light beam. It is worth noting the negligible values of the off-diagonal elements, denoting the lower interference between the channels, as it can be confirmed by the low values of the Cross-Talk reported in the last image.

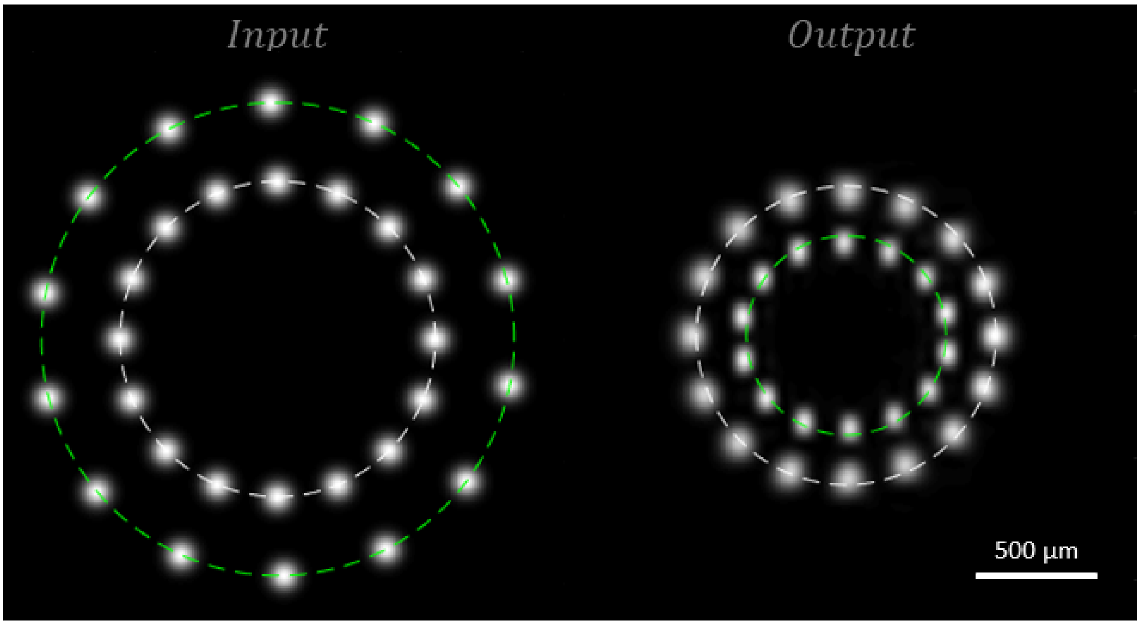

Figure 69: On the left, the initial configuration of the transmission channels of a 1 km communication link composed by N_1 = 16 internal light spots, and N_2 = 14 external spots, related to multipole-phase beams of order $m = 2$ and phase strength $\alpha_1 = 100\,\text{mm}^{-2}$ and $\alpha_2 = 150\,\text{mm}^{-2}$, respectively. These light spots are obtained by a back forward propagation in a $f_L - f_L$ configuration with $f_L = 400\,\text{mm}$, starting from a set of linear phase gradients of wavelength $\lambda = 632.8\,\mu\text{m}$ and waist $w_0 = 1.0\,\text{mm}$. On the right, instead, the transmitted beams (i.e., the output signals of the link) are reported. Notice how the internal spots are now the internal ones. The parameters of the circular-sector transformation of the transmission multiplexing stage, and the receiving demultiplexing stage, are: $f_{CS} = 10\,\text{mm}$, $a = 1.0\,\text{mm}$ and $b = 0.4\,\text{mm}$, while the focal length of the focusing of the final spots is, again, $f_L = 400\,\text{mm}$, and the rescaling factor of the multipole-phase beams during the free space propagation is M_p = 140.

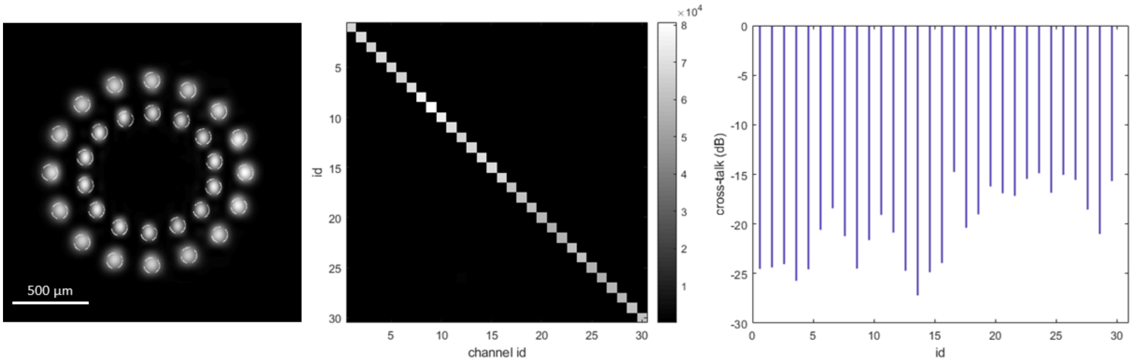

Figure 70: The Cross-Talk analysis of the detected beams of the figure 69. From the left: the output of the link with the detection areas (dashed line) used for the XT computation, the intermodal map and the final XT values.

9 Design of an experimental free-space optical communication system

In the chapter 7 we have seen three different possible designs of a demultiplexer working with the multipole-phase beams of order $m = 2$, $m = 3$ and $m = 4$. Now we want to adapt these designs to an experimental apparatus, in order to perform demultiplexing tests on the multipole-phase beams. However, due to some experimental limits, the design parameters have to be changed, and further simulations are necessary. These limitations are mainly related to the size and resolution of the optical elements available in the laboratory, which dictates an increment of the focal length, f_{CS}, of the focusing terms of the Transformer and the Corrector phase plates. Actually, since these two elements are supposed to be implemented using a spatial light modulator (SLM) with a resolution of 8 µm, the laser beam of the optical setup has to be magnified, from the scale of the micrometers to the scale of the millimetres. This magnification is necessary to transfer properly the phase functions of these phase plates to the light beam. Consequentially, the parameters of the circular-sector transformation, used in the demultiplexing process are forced to be in a range where phase distortions can appear. Therefore, the obtained final configuration of light spots, in terms of quality, is far away from the results seen in the previous chapters, but they are still remarkable. In particular, the number of channels has to be reduced in order to keep the Cross-Talk level around the −15 dB limit requested in the telecommunication technologies. Moreover, due to these phase distortions, the manually positioning of the detection areas of the light spots was used also for the multipole-phase beams of order $m = 2$ and not only for the higher phase orders. However, despite all the these limitations, we are still able to increase the channels number of at least one order of magnitude using spatial division multiplexing based on multipole-phase beams.

9.1 The light spot configuration

In the case of multipole-phase beams of order $m = 2$ it was adopted the same double circular configuration seen in the chapter 7. This light spot disposition is composed by an external circle of $N_1 = 10$ spots, whose related multipole-phase beams are characterized by a phase strength $\alpha^{(1)} = 16\,\mathrm{mm}^{-2}$ and phase orientations, $\theta^{(1)}_{0,i=1,\ldots,N_1}$, assumed in the range $[0; \frac{2\pi}{m}]$. Therefore, these θ_0 values are separated by an angular interval of

$$\Delta\theta_0^{(1)} = \frac{1}{m}\frac{2\pi}{N_1} \tag{194}$$

The relative MatLab code, used for the generation of the array, "theta0_1", of these $\theta_0^{(1)}$ values, is reported below. Notice that, to avoid the superposition of the 0 and 2π spots, the last element of the array (corresponding to 2π) was deleted, as done above. Then, in the last line, an array of the same length of "theta0_1" and filled with the $\alpha^{(1)}$ values are defined. In this way, we have the two parameters $(\alpha, \theta_0)^{(1)}$ for each multipole-phase beam of the (1)-configuration of light spots.

Listing 9.1.1: external configuration definition

```
    dtheta0_1        = 2*pi/(m*N1);              % spots separation
    theta0_1         = 0 : dtheta0_1 : 2*pi/m;   % theta0_1 array
    theta0_1(end)    = [];                       % avoid 0-2pi superposition

    alpha_1 = ones(1,length(theta0_1)) * alpha1;
```

At this point, a further set of six channels are defined by multipole-phase beams with a phase strength $\alpha^{(2)} = g\alpha^{(1)}$ with $g = 0.5$ and orientations $\theta^{(2)}_{0,i=1,\ldots,N_2}$ distributed in the same range $[0; \frac{2\pi}{m}]$. However, as just seen in the chapter 7, an additional angle of $\Delta\theta_0^{(1)}/2$ is summed up to these values in order to avoid excessive interference from the spots of the two distributions. The relative MatLab code is reported in the following. Notice that the code is identically to the previous one, except for the addition of the shift term $\frac{\Delta\theta_0^{(1)}}{2}$ to the array ”theta0_2” of the $\theta_0^{(2)}$ values (fourth line). Notice also that the phase strength array is filled with $g\alpha^{(1)}$ in order to obtain the two parameters $(\alpha, \theta_0)^{(2)}$ for each beam of the (2)-configuration of spots. Then, in the last two line of the code, the arrays of the two distributions are unified, obtaining the complete set of the initial multipole-phase beam parameters.

Listing 9.1.2: internal configuration and the total one

```
1     dtheta0_2        = 2*pi/(m*N2);                % spots separation
2     theta0_2         = 0 : dtheta0_2 : 2*pi/m;     % theta0_2 vector
3     theta0_2(end)    = [];                         % avoid 0-2pi superposition
4     theta0_2         = theta0_2 + dtheta0_1/2;     % shift
5
6     alpha_2 = ones(1,length(theta0_1))* g*alpha1;
7
8     % final total configurations
9     theta0 = [theta0_1 theta0_2];
10    alpha  = [alpha_1  alpha_2];
```

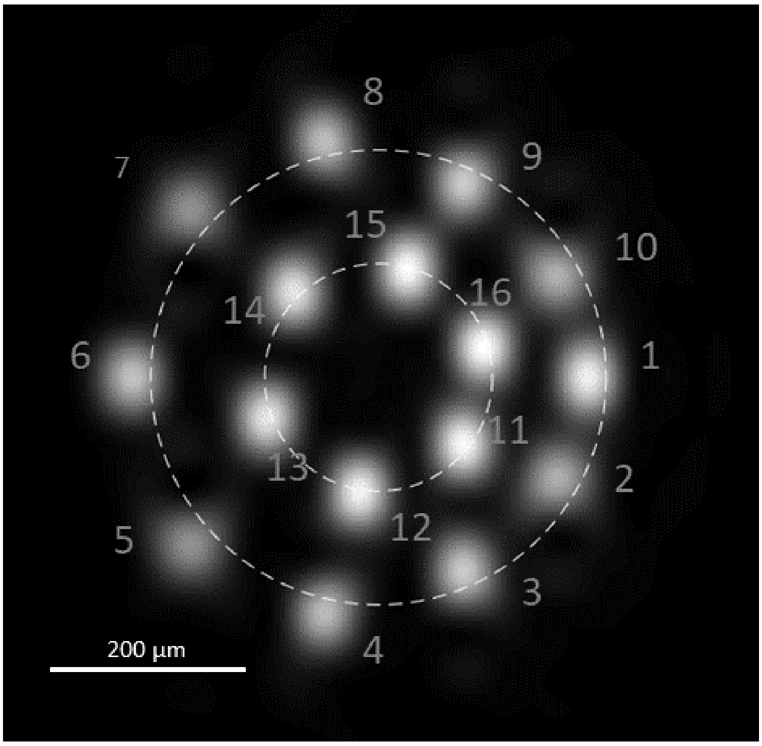

Figure 71: The output light spots of the superposition of sixteen multipole-phase beams of order $m = 2$ demultiplexed in the simulation analysed in this section. In particular, this output configuration is composed by $N_1 = 10$ external spots, related to multipole-phase beams of phase strength $\alpha^{(1)} = 16\,\mathrm{mm}^{-2}$ and phase orientations in the range $[0;\pi]$, and $N_2 = 6$ internal spots related to multipole-phase beams of phase strength $\alpha^{(2)} = 8\,\mathrm{mm}^{-2}$ and the same θ_0 range. The parameters of the circular-sector transformation are: $f_{CS} = 250\,\mathrm{mm}$, $a = 2.0\,\mathrm{mm}$ and $b = 0.85\,\mathrm{mm}$.

In figure 71 it is reported the simulated demultiplexer output, where it is possible to see the configurations of the $N_1 + N_2 = 16$ final light spots. Notice that the spot numeration is in the counterclockwise direction, while the $\theta_{0,i=1,\ldots}$ values increase from 0 to 2π, as can be seen from the previous MatLab codes (line two). This is not surprising if one remembers that a multipole-phase beam, of phase orientation θ_0, is demultiplexed into a spot of azimuthal angle $\theta = -m\theta_0$. We recall also that the radius of the two circular distributions is defined by the phase strength thanks to the equation 113:

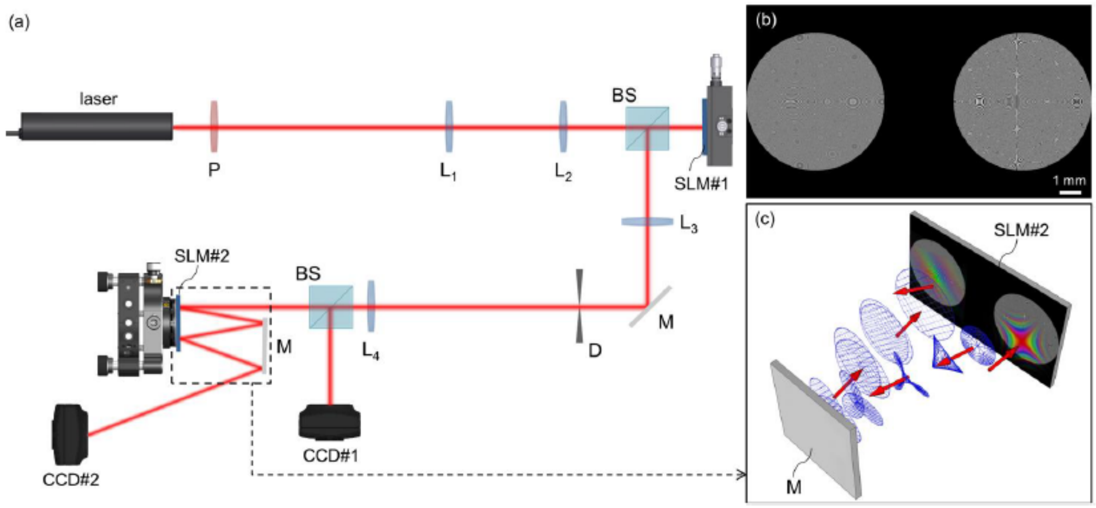

Figure 72: The whole experimental setup (a), a representation of the SLM#2 with the two phase plates used in the circular-sector transformation (b), and the propagation of the electromagnetic field between the two phase plates (c). The focal lengths used are: $f_1 = 2.54\,\mathrm{cm}$, $f_2 = 15.0\,\mathrm{cm}$, $f_3 = 20.0\,\mathrm{cm}$, $f_4 = 25.0\,\mathrm{cm}$.

$$R = f_L \frac{\lambda}{2\pi} \frac{\alpha b^m}{a} = \begin{cases} 0.23 & \text{mm for the external circle} \\ 0.12 & \text{mm for the internal circle} \end{cases} \tag{195}$$

where, in this case, we have assumed the following design parameters. For the circular-sector transformation we have: $a = 2\,\mathrm{mm}$, $b = 0.85\,\mathrm{mm}$ and $f_{CS} = 250\,\mathrm{mm}$, while the spot focusing is performed thanks to a lens of focal length $f_L = 400\,\mathrm{mm}$. Notice, as anticipated, the high value of f_{CS} (with respect to the one used in the chapter 7), due to the experimental limitations that we will see in the following section 9.2. In order to compensate this increment, and the use of an initial light beam with a waist in the scale of millimetres, the two parameters, a and b, are also increased. This set of values, however, produces the irregularities that can be seen in figure 71, in particular, for the external spots distribution.

9.2 Propagation of the light beam

Once defined the final desired spot configuration, we have to simulate the propagation of the electromagnetic field along the demultiplexing chain of our experimental setup, reported in figure 72. A detailed description of the apparatus can be found in the paper [6], where multipole-phase beams with phase order $m = 2$ have been already experimental studied by our research group. Here we can limit us to say that a laser source is propagated into a first spatial light modulator which provides the phase term necessary to generate a multipole-phase beam. The beam is then propagated into a second SLM, which is divided into two parts, as it can be seen in the (b)-frame of the figure. The first part invested by the beam provides the phase term necessary to the circular-sector transformation of the multipole-phase beam into a linear phase gradient. Thanks to the mirror M, the beam is so bounced back into the second half part of the SLM, which provides the phase correction of this linear gradient and, also, adds the Fourier phase term necessary for the generation of the final light spot. It is important to notice that the presence of the mirror M dictated the focusing term, of the circular-sector transformation, to have a value of the focal length f_{CS} in the order of the decimetres. Otherwise, if the mirror is place too closely to the SLM, the input beam could be interrupted by the mirror itself. This limitation, as anticipated, forces the values of the parameters of the circular-sector transformation, to be in a range that can produce phase distortions.

Now, from a simulation point of view, we can idealize the experimental setup in a more simply configuration, as described in figure 73. The generation of the initial light beam, its conversion to a multipole-phase beam and the circular-sector transformation (CS), can be performed in the same position, for instance, set as the origin of the

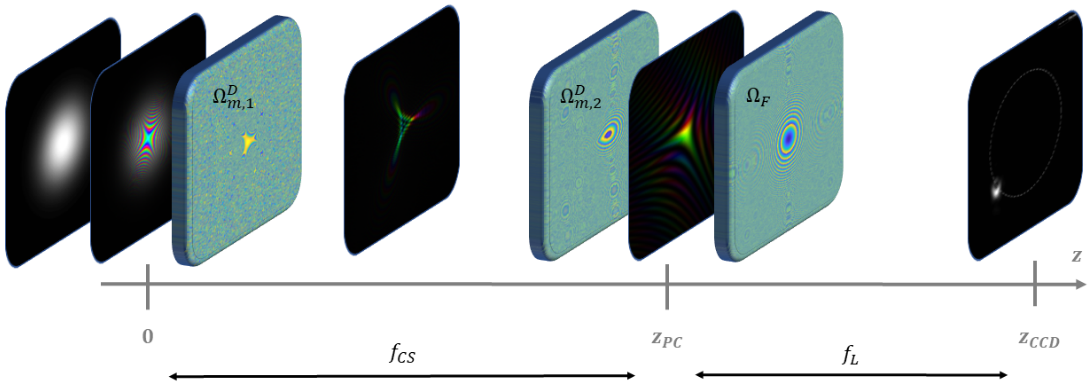

Figure 73: Demultiplexing simulation setup. From the left, the initial Gaussian beam is transformed into a multipole-phase beam, to which it is applied the phase term $\Omega^D_{m,1}$ (equation 199) in order to perform the circular-sector transformation. Then, after the phase correction thanks to the phase plate $\Omega^D_{m,2}$ (equation 200), we get the linear phase gradient, whose phase period and orientation is related to the phase strength and orientation of the initial multipole-phase beam. Finally, at the same position, the phase pattern Ω_F (equation 203) is applied in order to get the final light spot at the distance f_L, where, from an experimental point of view, is placed the sensor CCD#2.

propagation axis (the z-axis in our notation). Then, the simulated beam can be free space propagated between the two half parts of the SLM#2. After that, we have the phase correction (PC) and the application of the phase Fourier term Ω_F (characterized by a focal length f_L). Finally, after a further free space propagation for the distance f_L, we get the final light spot related to the initial multipole-phase beam. The detailed descriptions of these simulation steps, which are, actually, the same as seen in the chapter 4 for the demultiplexing of a generic set of multipole-phase beams, are reported in the following.

9.2.1 Definition of the observation plane

The first step is the usual spatial discretization of the x and y-axis,

$$x \to \left[-\frac{L}{2} : \Delta_x : \frac{L}{2} - \Delta_x\right] \tag{196}$$

in order to sample the observation plane with a mesh of coordinates (X,Y), where we remember that L is the linear size of the observation plane and M is the number of samples along each axis. The MatLab code is still the following

Listing 9.2.1: space discretization

```
    dx          = L/M;                      % sample interval
    x           = -L/2 : dx : L/2-dx;       % x coords
    y           = x;                        % y coords
    [X,Y]       = meshgrid(x,y);            % cartesian coords
    [theta, r]  = cart2pol(X,Y);            % polar coords
```

9.2.2 The initial set of multipole-phase beams

Once specified the observation plane, the initial laser beam can be defined. Our laser, of wavelength $\lambda = 632.8\,\mathrm{nm}$ and waist size $w_0 = 240\,\mu\mathrm{m}$, is expanded, thanks to the lenses, L_1 and L_2, in order to get a Gaussian beam, u_0, of waist size $w_0 = 2.5\,\mathrm{mm}$ (the starter point of our current simulation).

$$u_0(r,\theta) = \exp\left\{-\left(\frac{r}{w_0}\right)^2\right\} \tag{197}$$

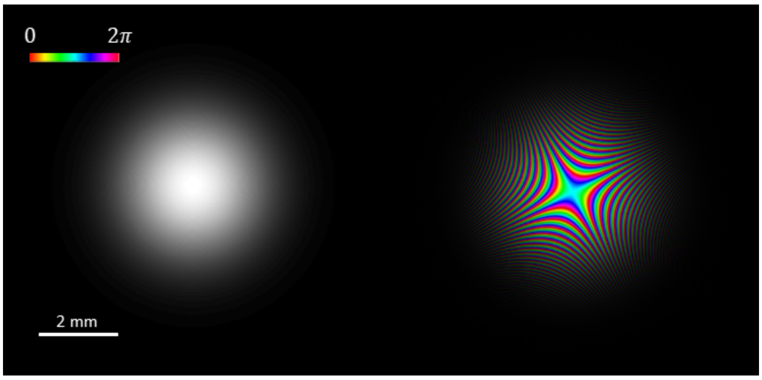

Figure 74: On the left, the simulated Gaussian beam of wavelength $\lambda = 632.8\,\mathrm{nm}$ and waist $w_0 = 2.5\,\mathrm{mm}$. On the right, the relative multipole-phase beam for $\alpha^{(1)} = 16\,\mathrm{mm}^{-2}$ and $\theta_0 = 72°$ (fifth spot of the figure 71). Brightness and colours refer to intensity and phase, respectively.

The expansion of the laser beam is necessary to have a good resolution on the first SLM, which creates the multipole-phase beam. The simulated wavefront, of the initial beam, is reported on the left of the figure 74, while the MatLab code of its generation is, as usual, the following:

Listing 9.2.2: initial gaussian beam

```
    u0 = exp(-(r/w0).^2);
```

Obtained the Gaussian field, each i-th multipole-phase beam, one for each (α, θ_0) of our configuration, is generated individually in order to compute, in the end, the Cross-Talk map. For example, in figure 74 it is shown the wavefront of the multipole-phase beam related to the fifth spot of the demultiplexer output reported in figure 71. Remembering the phase function, $\Omega(r, \theta)$, of a multipole-phase beam

$$\Omega(r, \theta) = \alpha r^m \cos[m(\theta - \theta_0)] \tag{198}$$

the MatLab code for the generation of the i-th multipole-phase beam, $u^{(i)}(r, \theta)$, is the following:

Listing 9.2.3: i-th multipole phase beam

```
    u1(:,:,i) = u0.*exp(1i*alpha(i)*(r.^m).*cos(m*(theta-theta0(i))));
```

9.2.3 Circular-sector transformation

The multipole-phase beam, u_1, generated by the SLM#1, is then propagated in the free space between the two SLMs. In our simulation, the Gaussian beam and its transformation into a multipole-phase beam, are generated in the same point (i.e., the origin of the z-axis) and the propagation between the two SLMs can be ignored. Arrived at the second SLM, thanks to the mirror M, the beam is bounced between the two half sections of the SLM#2 (as reported in the c-frame in figure 72) for a distance equal to the focal length, f_{CS}, of the circular-sector transformation plates. Indeed, the first half part (the transformer (CS)) produce the unwrapping of the multipole-phase beam (first line of the MatLab code reported below) and its transformation into a linear phase gradient at the distance f_{CS}. For this reason, the beam is free space propagated for this distance (second line of the code). Then, the beam arrives at the second half section of the SLM#2, the (PC)-phase plate, which produces the correction to the phase distortion introduced during the free space propagation between the two parts of the SLM#2 (third line). The MatLab code is, as usual, the following:

Listing 9.2.4: Circular-sector transformation

```
    u1(:,:,i) = u1(:,:,i).*exp(1i*Phase_1);                 % CS transform
    u1(:,:,i) = FreeSpaceProp(u1(:,:,i),L,lambda,f_CS);     % prop. CS - PC
    u1(:,:,i) = u1(:,:,i).*exp(1i*Phase_2);                 % Phase Correction
```

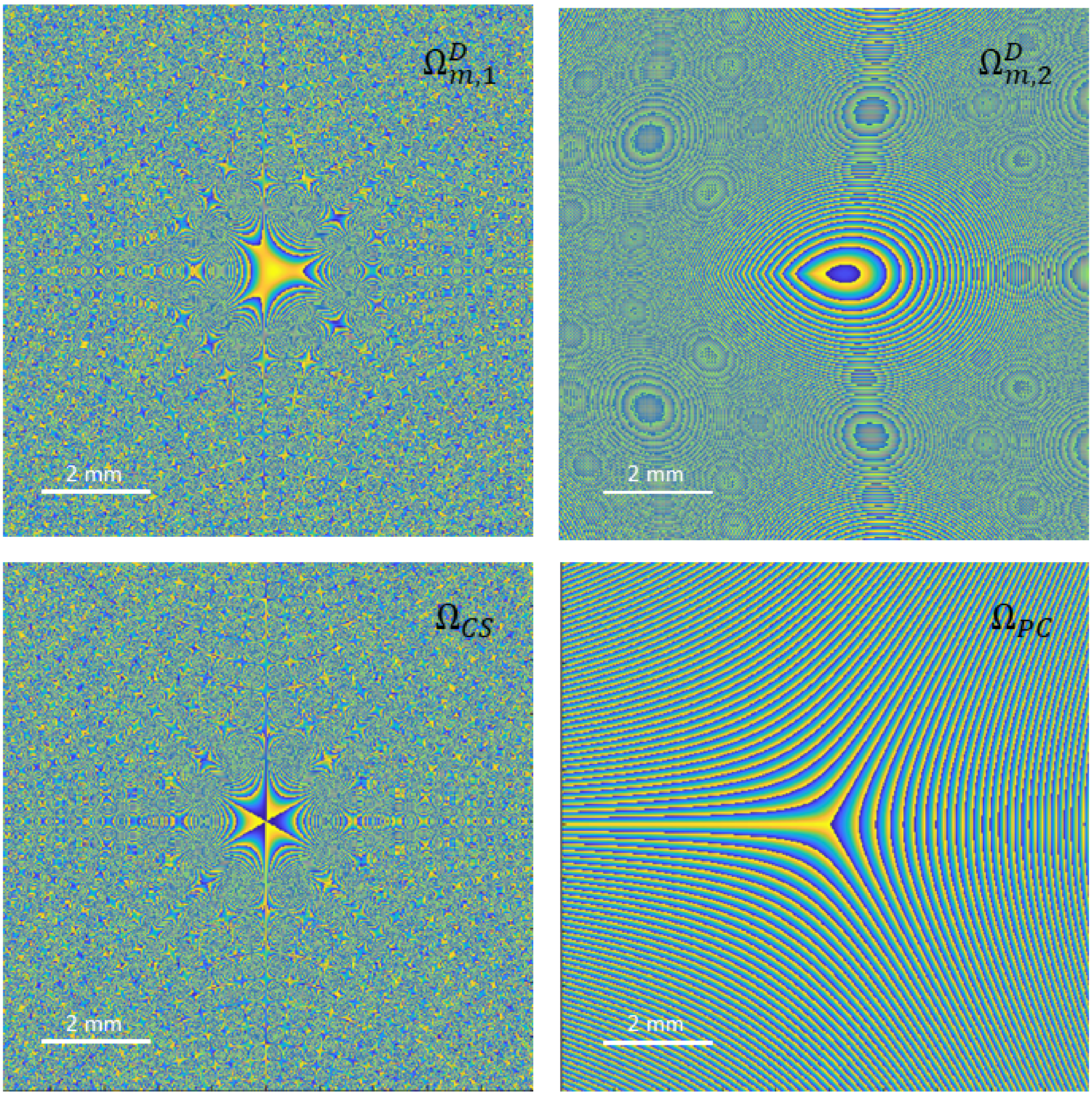

Figure 75: The phase patterns, $\left\|\frac{\Omega}{2\pi}\right\|$, of the plates performing the circular-sector transformation of the simulation analysed in this chapter. From the top left, in clockwise order: the phase pattern, $\Omega^D_{m,1}$, of the Transformer completed of the focusing term $\Omega_F = -k\frac{r^2}{2f_{CS}}$ (equation 199), the pattern of the Phase Corrector, $\Omega^D_{m,1}$, included the same focusing term (equation 200) and, finally, the same two patterns, Ω_{CS} and Ω_{PC}, without the focusing terms (equations 201 and 202, respectively). The parameters used in order to generate these patterns are: $f_{CS} = 250\,\mathrm{mm}$, $a = 2.0\,\mathrm{mm}$ and $b = 0.85\,\mathrm{mm}$.

where we remember that the two phase functions, "Phase_1" $\longleftrightarrow$ $\Omega^D_{m,1}$ and "Phase_2" $\longleftrightarrow$ $\Omega^D_{m,2}$, of the unwrapper and the phase corrector, respectively, are expressed by the equations:

$$\Omega^D_{m,1} = \Omega_{CS} - k\frac{r^2}{2f_{CS}} \tag{199}$$

$$\Omega^D_{m,2} = \Omega_{PC} - k\frac{r^2}{2f_{CS}} \tag{200}$$

where Ω_{CS} and Ω_{PC} are defined as:

$$\Omega_{CS} = k\frac{ab}{f_{CS}}\left(\frac{r}{b}\right)^{1+m}\frac{\cos[(1+m)\theta]}{1+m} \tag{201}$$

$$\Omega_{PC} = k\frac{ab}{f_{CS}}\left(\frac{r}{a}\right)^{1+\frac{1}{m}}\frac{\cos[(1+\frac{1}{m})\theta]}{1+\frac{1}{m}} \tag{202}$$

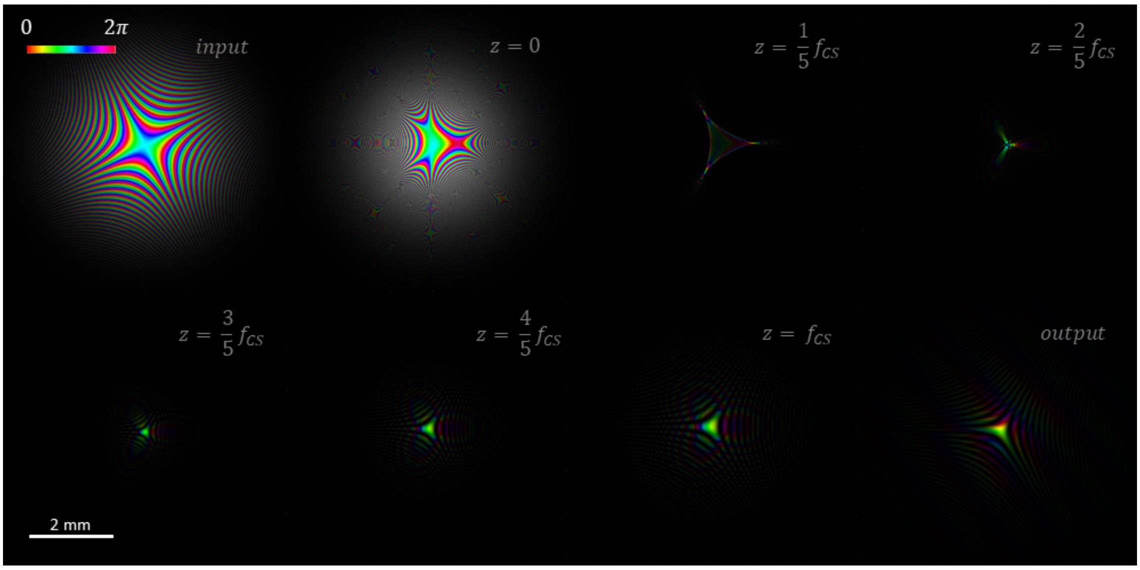

Figure 76: The circular sector transformation of the multipole phase beam with phase strength $\alpha^{(1)} = 16\,\text{mm}^{-2}$ and orientation $\theta_0 = 72°$, related to the fifth spot of the simulation output reported in figure 71. From the top left, in the first two frames, we have the multipole-phase beam at the input of the Transformer and after it. Then we have the field at five different positions between the Transformer and the Phase Corrector, in order to have an idea of the propagation of the beam between these two phase plates. Finally, the field after the Phase Corrector is shown, where you can note the stripes of the linear phase gradient. As usual, brightness and colours refer to intensity and phase, respectively.

These phase terms, Ω_{CS} and Ω_{PC}, and the same patterns with the focusing term and the Fresnel correction term, respectively, are plotted in figure 75. Instead, in figure 76, we can see the whole circular-sector transformation for the fifth multipole-phase beam reported on the right of the figure 74. In the first frame we have the beam at the input of the first half part of the SLM#2, i.e., the (CS)-phase plate, then it is reported the wavefront at various distances between the two parts of the SLM#2 and, finally, we have the field after the (PC)-phase plate, where it is possible to see the coloured stripes of the linear phase gradient.

9.2.4 Focusing of the spots

Finally, the beam is Fourier transformed (first line of the MatLab code reported in the following) and propagated in free space to the detector CCD#2, placed at the focal length f_L, where the beam spot appears (second line of the code).

Listing 9.2.5: Fourier transformation

```
    u1(:,:,i) = u1(:,:,i).*exp(1i*Phase_F);              % lens
    u2(:,:,i) = FreeSpaceProp(u1(:,:,i),L,lambda,f_L);   % final field
```

Experimentally, the Fourier transformation is performed by the same optical element as the phase correction, where the following phase term (called "Phase_F" in the previous code) is added to the second half section of the SLM#2.

$$\Omega_F(r,\theta) = -\frac{k}{2f_L}r^2 \tag{203}$$

In figure 77 it is shown the intensity pattern of the final field, u_2, for $f_L = 400\,\text{mm}$ and the final light spot of the multipole-phase beam considered in this simulation description.

9.2.5 Computation of the cross-talk

The final step of the simulation is the computation of the Cross-Talk as described in the chapter 6. However, as anticipated, due to the increment of f_{CS} and w_0, the multipole-phase beams associated to higher values of

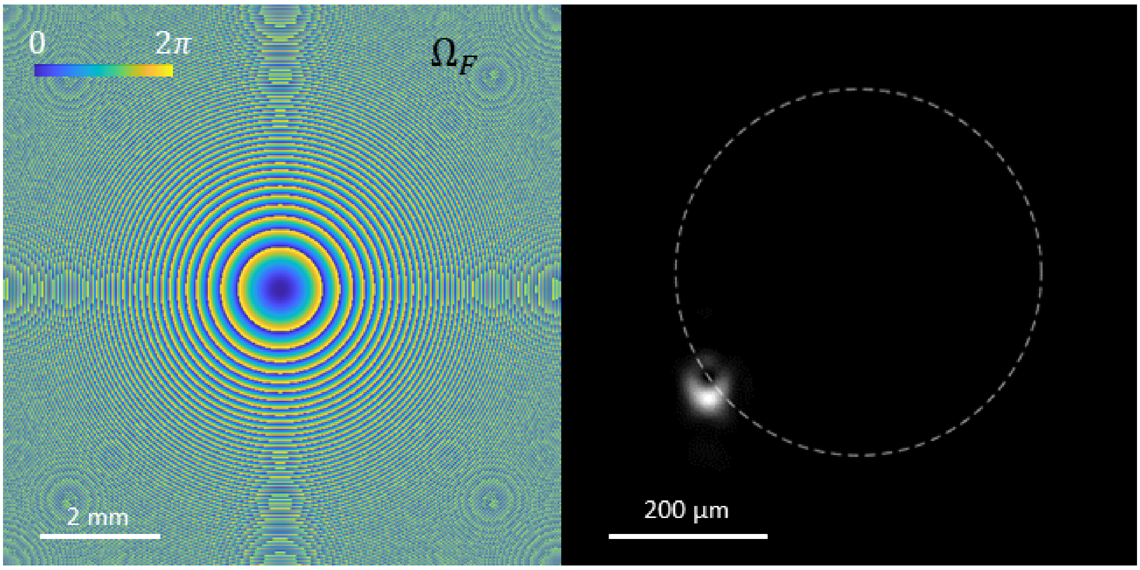

Figure 77: On the left, the Fourier transform phase term Ω_F (equation 203) used to sort the linear phase gradient, reported in the last frame of figure 76, into the final light spot shown on the right of this figure. Brightness and colours refer to intensity and phase, respectively.

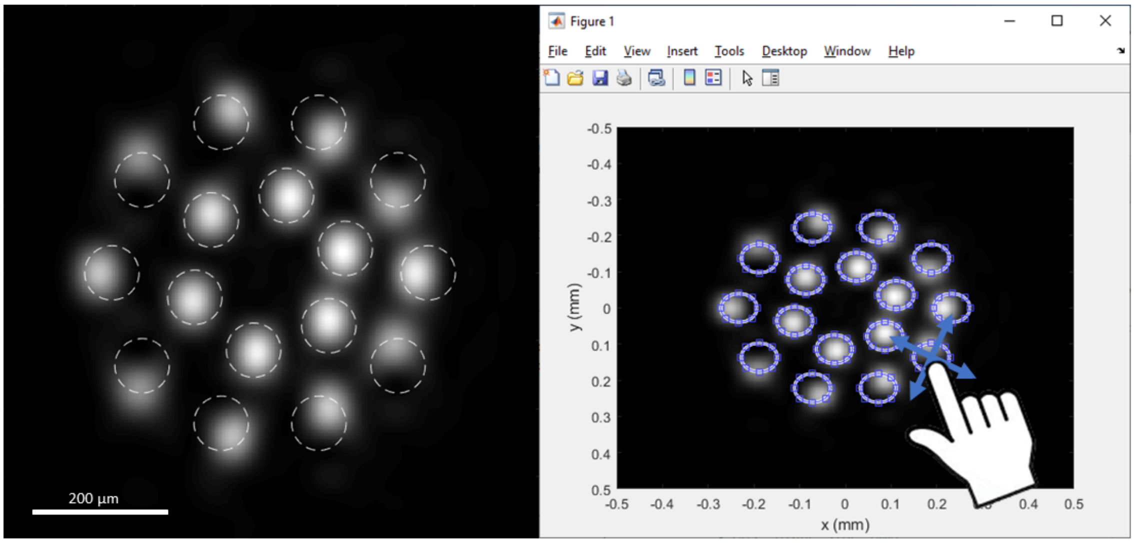

Figure 78: On the left, the misalignment of the light spots of the configuration reported in figure 71 with respect to their expected positions, represented by the detection areas plotted with a dashed line. These expected positions are defined by radial coordinates described by the equation 195 and polar coordinate given by $\theta = -m\theta_0$. On the right, the manual correction implemented in a MatLab macro.

α can produce phase distortions, are described in section 3.5. Indeed, as it can be seen from the figure 78, the detection areas of the external configuration, whose boundary are plotted on the expected positions given by the phase strength, result misaligned with respect to the light spots. Since this misalignment can produce a worsening of the Cross-Talk, a manual correction was implemented in the MatLab routine (see the code reported below), and it was performed before the Cross-Talk computation, whose results are reported in the figure 79. Notice that, despite the presence of remarkable phase distortions in the external light spots, the off-diagonal elements of the intermodal overlapping map have negligible values. This fact entails that the Cross-Talk values of the communication channels, remain below the $-10\,\mathrm{dB}$, which is an acceptable condition for our experimental apparatus.

Listing 9.2.6: manual mask positioning

```
% theoretical coords of the beam spots
radius_f = @(alpha)(f_L/k)*(alpha*b^m)/a;
[Xc,Yc]  = pol2cart(-m*theta0, arrayfun(radius_f,alpha));

% interacting plot of the total intensity to set the masks positions
h = figure();
imagesc(x,y,I_tot);
colormap('gray');
drawnow
global pos;

% for each light spot an circle-shaped mask is created (radius RI)
for i = 1 : length(alpha)
    hEllipse(i) = imellipse(gca, [Xc(i)-RI Yc(i)-RI 2*RI 2*RI]);
    pos(i,:)     = getPosition(hEllipse(i));
    addNewPositionCallback(hEllipse(i),@(p) getpos(hEllipse(i), i));
end

% the positioning remains activated until the ”p” button was pressed
while true
   pause(1);
   if strcmp(get(h,'CurrentCharacter'),'p')
        break
   end
end
```

9.3 Demultiplexer for order $m > 2$

The same experimental apparatus was design, for the first time, also for multipole-phase beams characterized by a phase order $m > 2$. The only differences, with respect to the previous case, will be the phase patterns loaded onto the two SLMs. Indeed, as seen in chapter 4.2, since the phase patterns of the Transformer and the Corrector depend on m, the parameters, a and b, of the circular-sector transformation have to be different from the case $m = 2$. For this reason, new simulations are performed for the two multipole-phase orders $m = 3$ and $m = 4$.

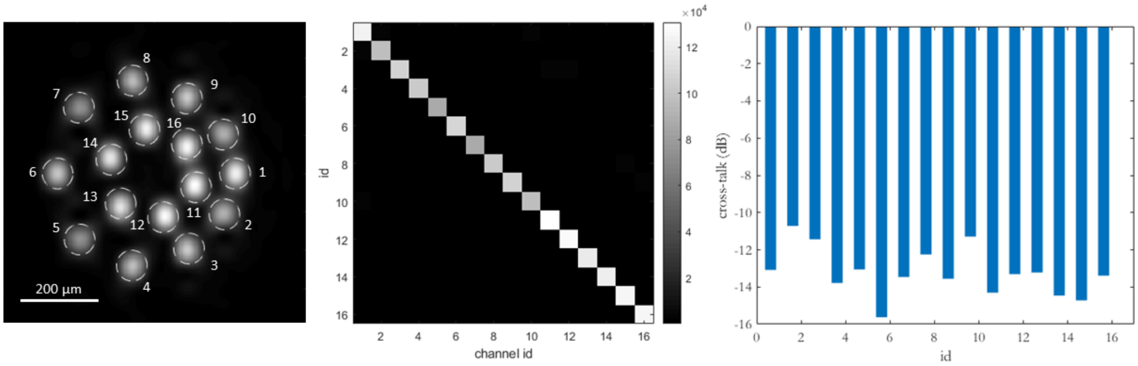

Figure 79: From the left, in the first frame, we have the demultiplexer output of the simulation for multipole-phase beams of order $m = 2$. It is worth noting how the detection areas (dashed lines) have been modified with respect to the figure 78 in order to compute the Cross-Talk correctly. In the second frame, instead, we have the intermodal overlapping map, where the indexes refer to the spots numeration reported in white in the first frame. Finally, the plot of the Cross-Talk values is shown.

9.3.1 Demultiplexer for order $m = 3$

In figure 80 it is reported the best configuration obtain for $m = 3$, which is composed by an external circular distribution of light spots related to a set of eight multipole-phase beams with a phase strength $\alpha = 120\,\mathrm{mm}^{-3}$. In additional, there are two internal spots corresponding to multipole-phase beams with $\theta_0 = 0°$ and $\alpha = 20\,\mathrm{mm}^{-3}$ and $-60\,\mathrm{mm}^{-3}$. These parameters, as the θ_0 values of the external distribution, were chosen one by one in order to compensate the phase distortion produced by the high value of α. Indeed, due to the term b^m in the equation 150 (since $b < 1$), in order to keep the spots sufficiently far from each other, α has to be larger than its value in the $m = 2$ case. However, a larger value of α implies a higher phase distortion and spots less focused. This effect is theoretically described in the section 3.5, here we want simply remember that the condition to be respected, in order to avoid excessive distortions, is expressed by the equation:

$$\alpha \ll \frac{2\pi}{\lambda} \frac{a w_0}{f_{CS} m b^m} \tag{204}$$

In our case, with $a = 4\,\mathrm{mm}$, $b = 0.45\,\mathrm{mm}$, $f_{CS} = 250\,\mathrm{mm}$, $w_0 = 2.0\,\mathrm{mm}$ and $\lambda = 632.8\,\mathrm{nm}$, we have $\alpha_{max} = 1.16 \times 10^3\ \mathrm{mm}^{-3}$, only a factor ten bigger than the $\alpha = 120\,\mathrm{mm}^{-3}$ adopted. In order to increment α_{max}, one can play with the parameters of the circular-sector transformation a, b and f_{CS}, for example, incrementing a and reducing b and f_{CS}. However, as we have seen, f_{CS} has to be equal to the distance travelled by the beam from the first half of the SLM#2 to the second one. Changing the position of the mirror, it is possible to reduce f_{CS}. However, the range is limited by the need not to hinder the incident beam with the mirror; for our experimental setup, $f_{CS} \leq 250\,\mathrm{mm}$ is prohibitive. Even a and b cannot change a lot without creating problems with the circular-sector transformation of the multipole phase beams. For all these reason, in the design of our experimental setup, the phase order m, as a degree of freedom, is less practically controlled with respect to α and θ_0 and a configuration with a high number of channels and low cross-talk values is very hard to achieve.
To better understand the phase distortions introduced by the high value of α that we have been forced to adopt, in figure 81 the spot distribution and their theoretical positions in the absence of the phase alteration (dashed line) are reported. It is easy to see that, in order to have spots equally spaced, a non-regular set of θ_0 values was adopted: $\{0°, 70°, 110°, 150°, 180°, 210°, 240°, 290°\}/m$.

9.3.2 Demultiplexer for order $m = 4$

Similarly to the previous case, it was adopted a circular configuration of 8 spots: $\alpha = 180\,\mathrm{mm}^{-4}$ and $\theta_0 = \{0°, 70°, 115°, 150°, 180°, 210°, 240°, 290°\}/m$, plus an internal spot characterized by the values $\theta_0 = 0°$ and $\alpha = -20\,\mathrm{mm}^{-4}$, while the circular-sector transformation has the parameters $a = 4\,\mathrm{mm}$ and $b = 0.5\,\mathrm{mm}$. The final computation of the Cross-Talk has produced the results reported in the figure 82.

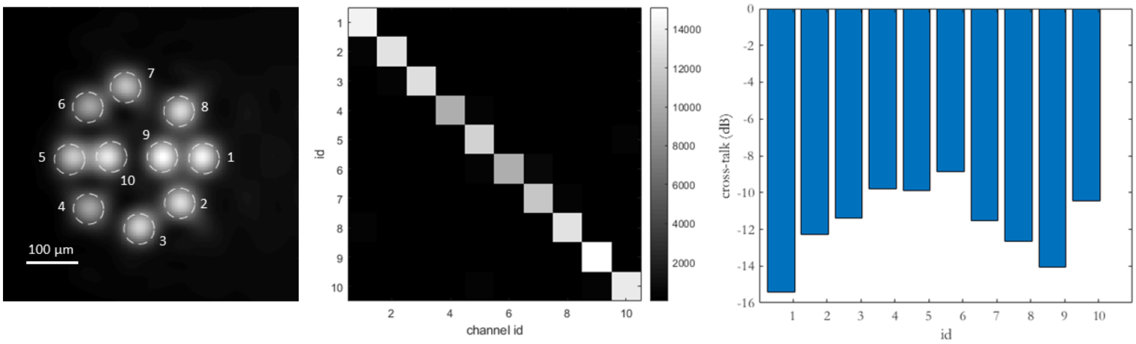

Figure 80: From the left, in the first frame, we have the demultiplexer output of the simulation for multipole-phase beams of order $m = 3$. In the second frame, we have the intermodal overlapping map, where the indexes refer to the spots numeration reported in white in the first frame. Finally, the plot of the Cross-Talk values is shown in the last frame.

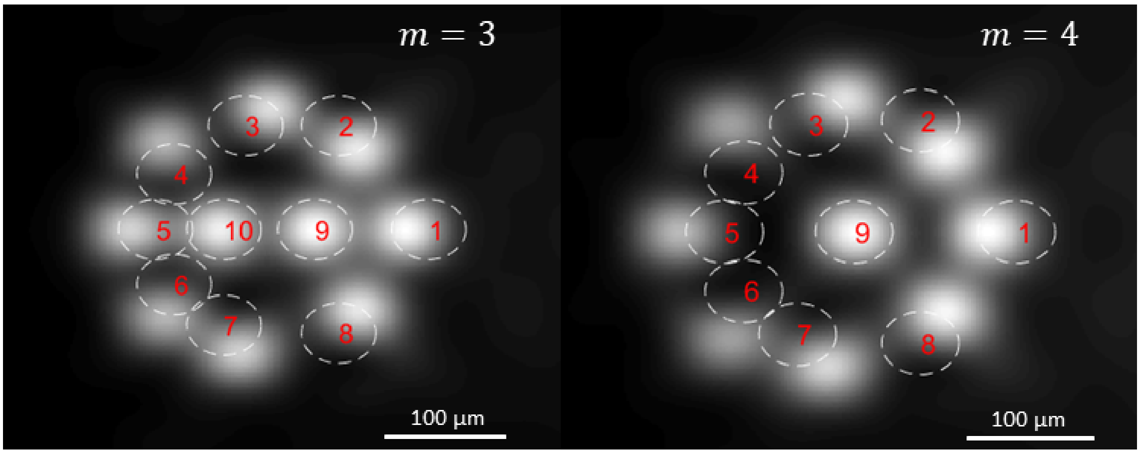

Figure 81: The misalignment of the spots with respect to their expected positions, for the case of multipole-phase beams of order $m = 3$ (on the left), and $m = 4$ (on the right).

The results of the simulation analysed in this chapter have demonstrated how the higher phase orders, with respect to the $m = 2$ case, are harder to be handled for space division multiplexing of a communication system with a high number of channels. Moreover, experimental tests on multipole-phase beams with $m > 2$, needs modifications on the experimental apparatus used by our research group for the $m = 2$ case and here illustrated. In particular, as seen, the focal length of the circular-sector transformation has a crucial role in the limitation of the channels number and a strategy in order to reduce it has to be studied. For instance, using metasurface devices instead of the SLMs. For this reason, the advantages of the metasurfaces in the framework of multipole-phase beams, will be discussed in the next chapter.

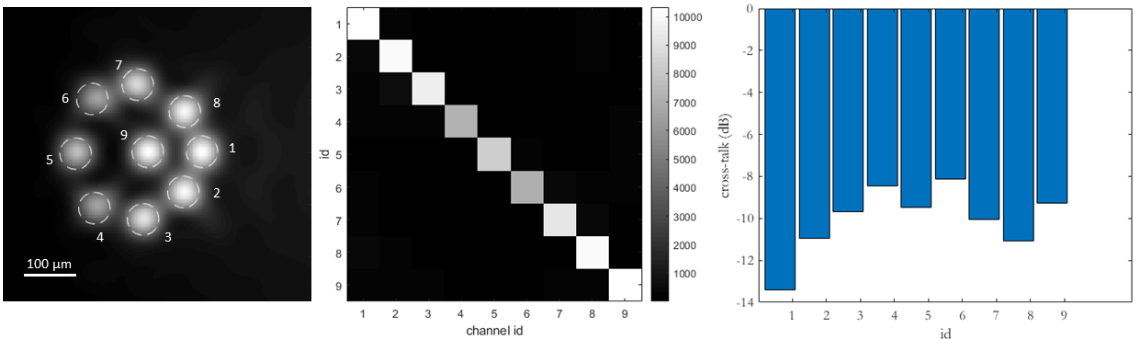

Figure 82: From the left: the demultiplexer output with the indexes of the spots and the detection areas (dashed lines), the intermodal overlapping map and the relative Cross-Talk values. Case of multipole-phase beams of order $m = 4$.

10 Manufacturing strategies for multipole-phase beams

In this chapter, it will be described a possible strategy for the manufacturing of the optical elements necessary in order to perform the generation and the sorting of a set of multipole-phase beams, which we have seen to be a new way in the framework of the spatial division multiplexing techniques. In the chapter 9, we have introduced the spatial light modulator (SLM) as possible devices able to impart, on an impinging beam, the multipole-phase structure required in order to produce multipole-phase beams or performing the circular-sector transformation used for their sorting. The SLMs, however, are designed for experimental applications and their cost, and sizes, are important obstacles in an industrial view, where cheap and miniaturized systems are requested. For this reason, in the following, the *two-dimensional multifunctional metasurfaces* (MS) will be introduced and described, reporting, moreover, a MatLab algorithm for their design. Briefly, we can say that a metasurface is a phase plate extremely thin, typically with a thickness less than one micrometer, whose structure is characterized by a bidimensional pattern designed in the nanometric scale. Controlling the geometry of this grating, we are able to impart almost any desired phase term on an electromagnetic field impinging the surface. Differently to the normal optics, moreover, a MS can transfer to a radiation a multifuctional phase term, as already seen for the spatial light modulators, for instance, in the SLM#2 of the experimental apparatus described in chapter 9, where the same element gives both the phase correction (necessary after the circular-sector transformation of the initial multipole-phase beam), and the Fourier term used for the sorting of the final light spots. However, due to resolution limitations, and bulk size of the optical elements, we were limited to use focal lengths, of the transformation in the beams' demultiplexing, bigger than 250 mm, providing an important constraint in the number of channels which can be transmitted with that apparatus. In this scenario, the very compact sizes of the metasurfaces act as a way out to go through the above-mentioned limitations. For example, in figure 83, a compact sorter for OAM beams is shown [59].

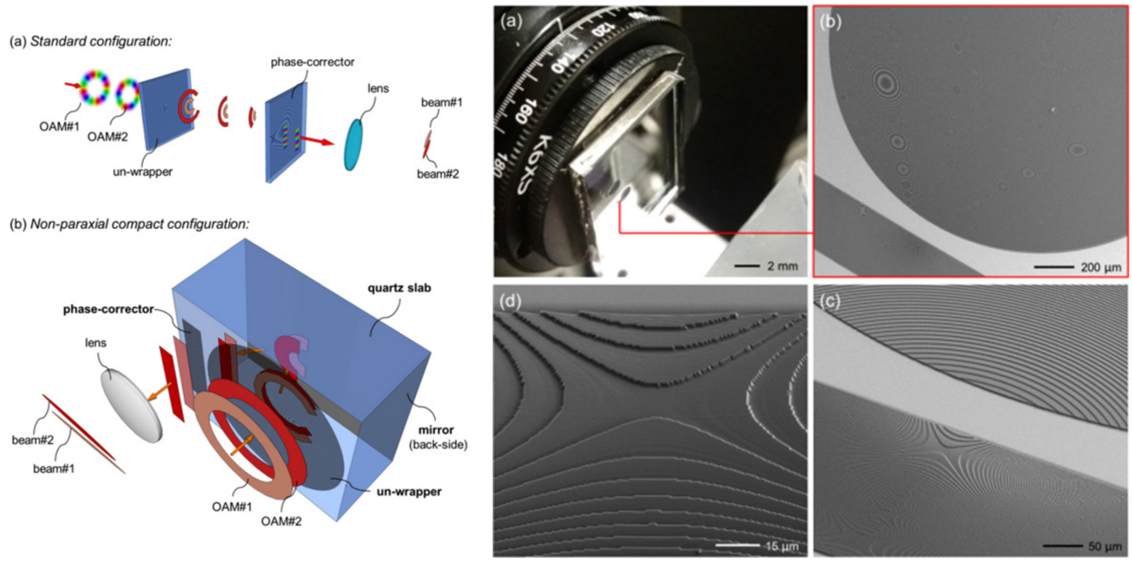

Figure 83: On the left: (a) scheme of an OAM beams' sorter, working with separated and coaxial optical elements. The azimuthal phase gradients of the initial OAM-beams are transformed into linear phase gradients and focused at different positions at the focal plane of a Fourier lens. (b) The same sorter in a non-paraxial compact configuration, where the two elements are fabricated, side-by-side, on the same facet of a quartz slab with a reflective back-side. On the right: (a) picture of the fabricated sorter mounted on the experimental setup. (b) SEM image of the zone between the Un-wrapper and the Phase Corrector. (c, d) Phase Corrector pictures at higher magnifications.

A first phase pattern, called *Un-wrapper*, transforms the azimuthal phase gradients of the input OAM-beams into linear phase gradients. Then, a second phase plate corrects the phase distortions introduced by the propagation between the two optical elements. Finally, in complete analogy with the demultiplexers seen for the multipole-phase beams, a lens produces the Fourier Transform of the linear phase gradients in order to generate the final distinct light spots associated to different values of the orbital angular moment of the input beams. This procedure, reported on the top of the figure in a coaxial configuration (a), is incorporated into a compact

Figure 84: Examples of optoelectronic devices. Notice the mismatch between the sizes of the optical and electronic parts.

device (b), where the phase patterns are realized as two metasurfaces placed on the same quartz slab. The slab has a reflective back-side, in this way, adding a tilt to the first phase plate, the unwrapping beam propagates with a non-null angle and, after a back-reflection, illuminates the second patter performing the phase correction. In this way, the focal length of the transformation is related to the thickness of the slab and can be chosen very short (4.572 mm in the sorter reported in figure), providing more efficiency demultiplexers.
It should now be clear how the fabrication of bidimensional optical elements has a crucial role in the in technology development. Today, indeed, there is an important gap between the size of the miniaturized electronic circuits and the bulk optical elements integrated with them. For instance, in figure 84, are reported some examples of optoelectronic sensors. It is quite obvious how the millimetric sizes, or even centimetric in some cases, of the optical elements it is a limitation in the manufacturing of miniaturized optoelectronic devices. Moreover, the classical bulk optics are realized in glass or plastic materials, which represent a mismatch with the silica structure of the electronic boards[60]. For all these reasons, the real fusion between the optics and the silicon photonics needs the designing of optics workable with the semiconductor manufacturing techniques [61]. In order to achieve this, in the last decade, with the improvement of the nanotechnologies, many groups of research have focused their studies on the realization of metasurfaces that could replace the current optics [62]. Moreover, we have already introduced how the potentialities of the MS do not only consist in the reduction of the sizes but permit, also, to produce new devices not realizable in the "classical" way [23, 48, 63].

In more detail, we can say that a metasurface is a material not present in nature but engineered in the nanometric scale in order to realize a two-dimensional periodical grating characterized by a period, Λ, which is much smaller than the wavelength, λ, of the electromagnetic field impinging on the MS, as reported in figure 85. Notice that, with two-dimensional MS, we mean that the metasurface is a pattern composed by three-dimensional object, called *metaelements*, of the same thickness, d. In this way, the variations in the geometry of the grating it is only in the two directions parallel to the surface. Therefore, we can image to divide the pattern in squared areas, called *MetaPixel* (MP), each of them filled with a metaelements of a particular shape. It is useful to introduce the *duty-cycle* for the two spatial direction, dc_x and dc_y, defined as the length of the filled part, of a metaelement, along that particular direction, normalized by the linear size of the MP (i.e., the period Λ of the MS). For example, in figure 86, is reported a metasurface with squared metaelements of sides a and b.

10.1 Form birefringence

The above-mentioned condition $\Lambda \ll \lambda$ is called *subwavelength regime* and, as we will see in a moment, set the upper limit to the period that can be used[5]. Indeed, in the subwavelength regime, the radiation sees the

---

[5] The lower limit, instead, is related to the resolution achievable by the fabrication process used to realize the MS.

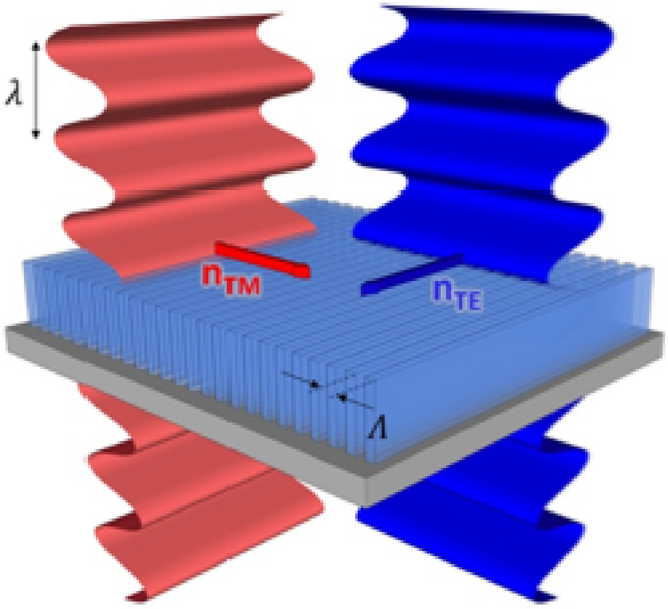

Figure 85: The two polarization, TE and TM, of an electromagnetic field, of wavelength λ, impinging a metasurface (MS), of period Λ, in the subwavelength regime [63]

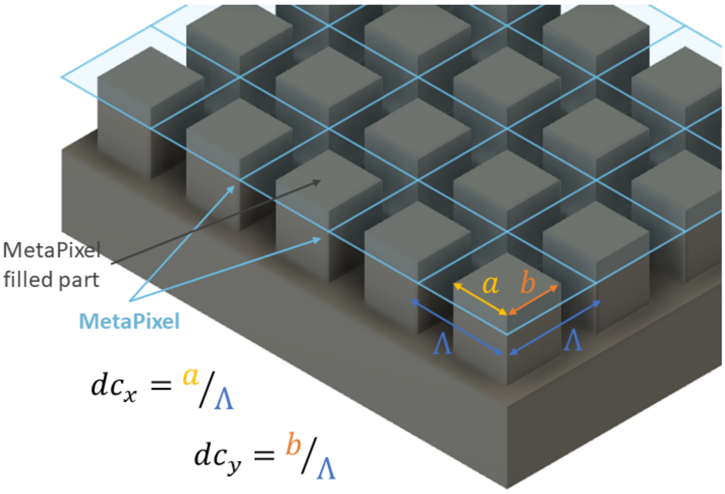

Figure 86: Example of a metasurface, characterised by a grating of period Λ, composed by squared metaelements of side length a and b. The filling fractions of each metapixel (MP) in the two axis-directions are the ratios $dc_x = \frac{a}{\Lambda}$ and $dc_y = \frac{b}{\Lambda}$, where dc_x, and dc_y, are called duty-cycles.

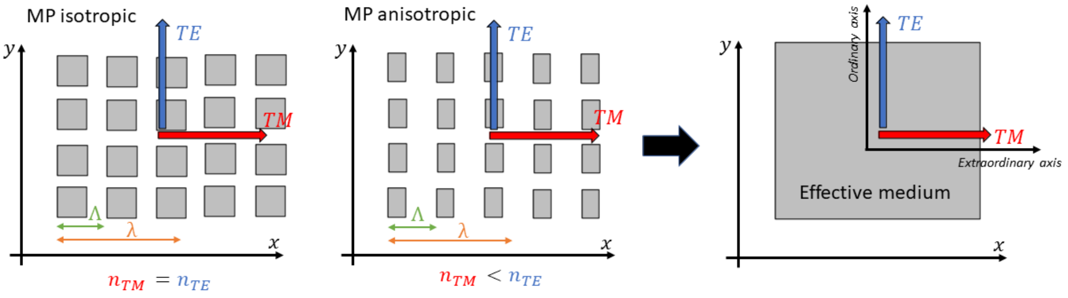

Figure 87: A metasurface in the subwavelength regime appears, to an electromagnetic radiation, as a homogeneous medium with an effective refractive index which is constant or different in the two polarization direction (TE and TM), if the grating of the MS is composed by isotropic or anisotropic metaelements, respectively.

surface as an effective medium but with an effective refractive index which depends on the geometrical pattern of the grating and varies from metapixel to metapixel. Indeed, how it easily to understand from the figure 87, choosing the metalements asymmetrical, the amount of matter that a ray of light passes through of each MP is different in the two polarization directions. The TM polarization (red in figure) has the electric field parallel to the extraordinary axis, while the TE polarization (blue in figure) has the electric field orthogonal to that axis. Therefore, we obtain an effective medium with two refractive indexes, n_{TM} and n_{TE}, that can change from metapixel to metapixel, simply orienting the metaelement differently. The different value of the refractive index in the two polarization, as we will see in a moment, produce a new phase term in the wavefunction of the radiation, which can be used in order to realize optical elements imparting a desired phase transformation on the impinging beam. This phenomenon is called *form birefringence*.

In general, the transmission matrix in the Jones formalism, τ, of a two-dimensional optical element of thickness d, is the following

$$\tau = \begin{pmatrix} e^{ikdn_{TM}} & 0 \\ 0 & e^{ikdn_{TE}} \end{pmatrix} \tag{205}$$

where $k = |\boldsymbol{k}|$ is the module of the wave-vector of the radiation impinging the metasurface. The previous equation can be rearranged as the following

$$\tau = e^{ikd\left(\frac{n_{TM}+n_{TE}}{2}\right)} \begin{pmatrix} e^{-i\frac{\delta}{2}} & 0 \\ 0 & e^{+i\frac{\delta}{2}} \end{pmatrix} \tag{206}$$

where we have introduced the phase shift, δ, between the two polarization

$$\delta := \frac{2\pi}{\lambda}\left(n_{TE} - n_{TM}\right) d \tag{207}$$

If now, we rotate the MS of a local angle, $\chi(x, y)$, as reported in figure 88, the transmissivity $T(x, y)$ of the metasurface becomes

$$T(x, y) = R(x, y)\tau(x, y)R^{-1}(x, y) \tag{208}$$

where $R(x, y)$ is the following rotation matrix

$$R(x, y) = \begin{pmatrix} \cos(\chi(x, y)) & -\sin(\chi(x, y)) \\ \sin(\chi(x, y)) & \cos(\chi(x, y)) \end{pmatrix} \tag{209}$$

Assuming δ fix, the matrix τ results spatially invariant and the unique parameter is the orientation of the optical axis χ. Therefore, substituting the matrix τ, expressed by the equation 206, in the equation 208, we get:

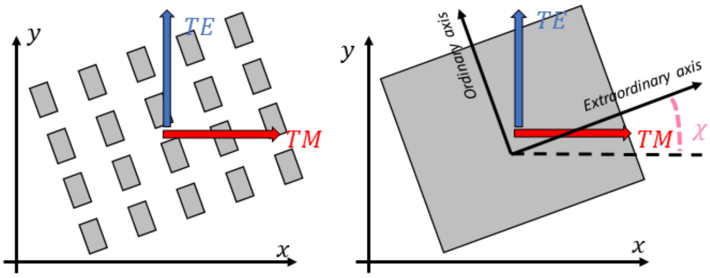

Figure 88: An anisotropic MS in the subwavelength regime with the metaelements rotated of an angle χ. In this way, the effective medium results with the two otpical axes, i.e., two directions along which the refractive index assumes constant values, which are rotated of the same angle. Therefore, the light propagation in the two polarization directions produces a phase shift depending on χ. This effect is called birefringence in form.

$$T(x,y) = \begin{pmatrix} e^{-i\frac{\delta}{2}}\cos^2(\chi(x,y)) + e^{+i\frac{\delta}{2}}\sin^2(\chi(x,y)) & -i\sin(2\chi(x,y))\sin\left(\frac{\delta}{2}\right) \\ -i\sin(2\chi(x,y))\sin\left(\frac{\delta}{2}\right) & e^{+i\frac{\delta}{2}}\cos^2(\chi(x,y)) + e^{-i\frac{\delta}{2}}\sin^2(\chi(x,y)) \end{pmatrix} \tag{210}$$

If we consider now, an impinging beam with two circular polarization components:

$$E^{(+)} = \begin{pmatrix} 1 \\ +i \end{pmatrix} \qquad E^{(-)} = \begin{pmatrix} 1 \\ -i \end{pmatrix} \tag{211}$$

the application of the transmission matrix (equation 210) to these two components, returns [64]

$$\begin{cases} T(x,y)\begin{pmatrix} 1 \\ +i \end{pmatrix} = \cos\left(\frac{\delta}{2}\right)\begin{pmatrix} 1 \\ +i \end{pmatrix} - i\sin\left(\frac{\delta}{2}\right)e^{+i2\chi(x,y)}\begin{pmatrix} 1 \\ -i \end{pmatrix} \\ T(x,y)\begin{pmatrix} 1 \\ -i \end{pmatrix} = \cos\left(\frac{\delta}{2}\right)\begin{pmatrix} 1 \\ -i \end{pmatrix} - i\sin\left(\frac{\delta}{2}\right)e^{-i2\chi(x,y)}\begin{pmatrix} 1 \\ +i \end{pmatrix} \end{cases} \tag{212}$$

Notice that for both polarization we have:

- a zero order term with the same polarization as the one of the impinging beam,
- a diffraction order polarized orthogonally to the incident beam and with a phase which is, in each point, equal to two times the orientation, χ, of the optical axis.

Therefore, we can choose the phase shift equal to $\delta = \pi$ in order to eliminate the first term, which is proportional to $\cos(\delta/2)$, and leaving only the terms with the phase factor $e^{\pm i2\chi(x,y)}$. In this way, if we want that our metasurface impart a phase function, $\Omega(x,y)$, to the impinging radiation, we only need to rotate each metaelement of an angle $\chi(x,y)$, which be half-times the phase function evaluated in correspondence to that particular metapixel. Therefore, the two conditions required for the design of our metasurface are:

$$\chi(x,y) = \frac{\Omega(x,y)}{2} \qquad \delta = \pi \tag{213}$$

With these two ansatz, the system 212, will be reduced to

$$T(x,y)\begin{pmatrix} 1 \\ \pm i \end{pmatrix} = -ie^{\pm i\Omega(x,y)}\begin{pmatrix} 1 \\ \mp i \end{pmatrix} \tag{214}$$

10.2 Design of a metasurface

With the theory of the form birefringence just introduced, we want to design a metasurface in order to transfer a multipole phase term on an impinging beam. In figure 89, for instance, is reported a rounded MS,

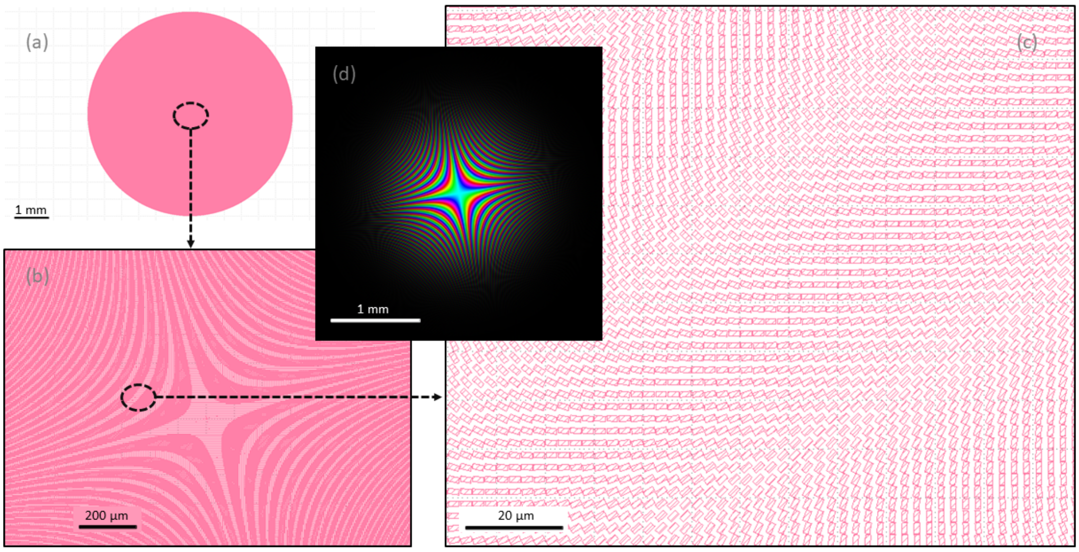

Figure 89: In the frames a, b and c, are reported, with an increasing magnification, a metasurface designed in order to transfer, to an electromagnetic field of wavelength = 1310 nm impinging the MS, a multipole-phase term (frame d) characterized by a phase order $m = 2$, a phase orientation $\theta_0 = \pi/3$, and a phase strength $\alpha = 100\,\text{mm}^{-2}$.

producing, when illuminated, a multipole-phase beam of order $m = 2$, phase orientation $\theta_0 = \pi/3$ and phase strength $\alpha = 100\,\text{mm}^{-2}$ for a wavelength of $\lambda = 1310\,\text{nm}$. The MS is supposed in silica ($n_{Si}(\lambda) = 3.503$), with a period of $\Lambda = 2.5\,\mu\text{m}$ and composed by rectangular metaelements characterized by a duty-cycle $dc_x = 0.9$. The other duty-cycle value, dc_y, is chosen in order to keep each metaelement inside its metapixel (which side is equal to Λ). Notice how the pattern of the MS (frame b) reproduces the phase structure of the multipole-phase beam (frame d), due to the proportional relation 213 between the phase, $\Omega(x, y)$, and the orientation of the optical axis.

10.2.1 Thickness of the metaelements

Before to introduce the algorithm used for the generation of the MS reported in figure 89, we remember that, in order to achieve the relation 214, we have assumed a fixed value ($\delta = \pi$) of the phase shift between the two polarization of the radiation impinging the metasurface. However, in order to keep this relation in each point of our MS, an assumption on the thickness of the metaelements has to be done. Indeed, if d is their height, when the radiation passed through the MS, for the two polarized component, TE and TM, the optical paths are $n_{TE}d$ and $n_{TM}d$, respectively. Therefore, we have the following phase shift between them:

$$\delta = \frac{2\pi}{\lambda}(n_{TE} - n_{TM})d \tag{215}$$

Substituting $\delta = \pi$, we get:

$$d = \frac{\lambda}{2(n_{TE} - n_{TM})} \tag{216}$$

which represents the metaelements thickness necessary to keep the condition $\delta = \pi$. Notice, moreover, that this relation sets a limit on the duty-cycle values, dc_x and dc_y, along the x and y-axis. Indeed, if the two sides of our rectangular metaelements have too closely values, n_{TM} and n_{TE} become similar and the thickness, d, can achieve prohibitive values for the fabrication processes. It is worth noting that, in order to obtain the refractive indexes, n_{TM} and n_{TE}, along the two optical axes of the metasurface considered, computational simulations are needed. In particular, it was used a MatLab macro, already developed by our research group, adopting the rigorous coupled-wave analysis (RCWA) method [65]. In this way, the two refractive indexes can be computed

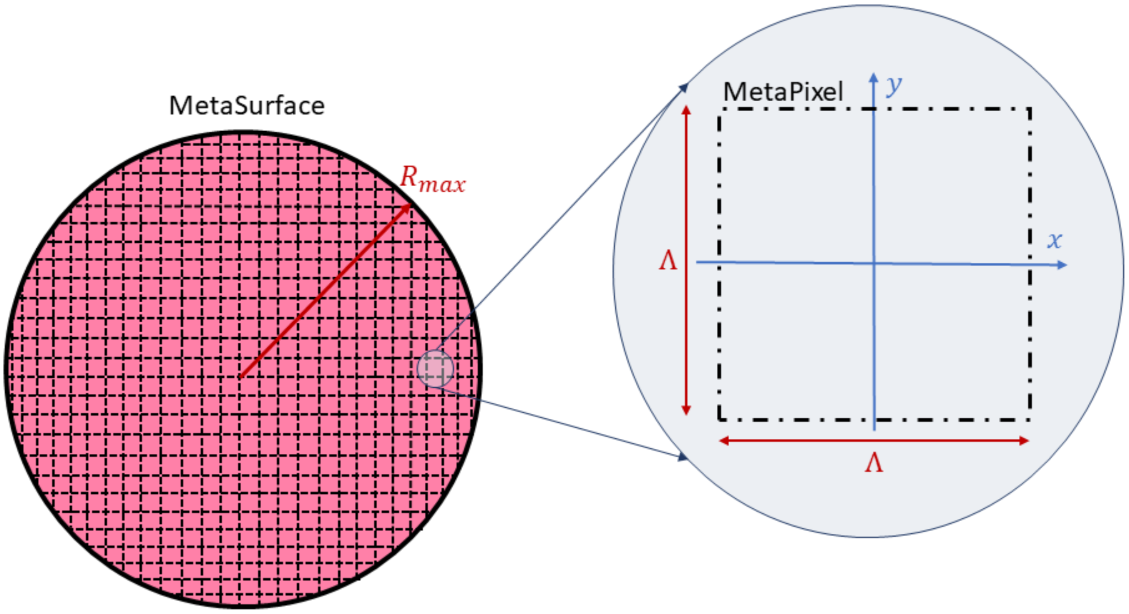

Figure 90: A representation of a circular metasurface of radius R_{max} with its grating composed of squared metapixels of side equal to the period Λ of the grating.

for a MS of a certain material and period Λ of its grating.

10.2.2 Writing of the metasurface

At this point, we can introduce the MatLab macro realized in order to write the sequence of coordinates which made up the metasurface reported in figure 89.
The first step is the definition of the mesh contains the coordinates of the MPs composing the metasurface, where the metapixels have a side equal to the period, Λ, of the MS. Therefore, if R_{max} is the size of the metasurface (assumed with a circular shape), the coordinates (xxt, yyt) of the mesh will be defined in a range of $[-R_{max}; R_{max}]$, with steps of Λ. The MatLab code used is the following, while a representation of the mesh and the metapixels is shown in figure 90.

Listing 10.2.1: defining of the mesh-grid of MPs

```
 period  = 2.5;                                 % MP side length [um]
 Rmax    = 3000;                                % MS radius [um]

 % MetaPixel mesh [um]
 xxt          = -Rmax : period : Rmax;          % MPs X absolute coords
 yyt          = -Rmax : period : Rmax;          % MPs Y absolute coords
 [X,Y]        = meshgrid(xxt,yyt);              % mesh cartesian coords
 [theta, r]   = cart2pol(X,Y);                  % mesh polar coords
```

The next step, is the definition of the metaelement of each MP, designed as a rectangle with a first side, for instance the one in the x-axis direction, of length L_x given by the product of the size of the MP and the duty-cycle value, dc_x, chosen for that axis.

$$L_x = \Lambda \cdot dc_x \tag{217}$$

Therefore, in order to keep the metaelements inside the metapixel (see figure 91), the second side of the rectangle is computed as the following:

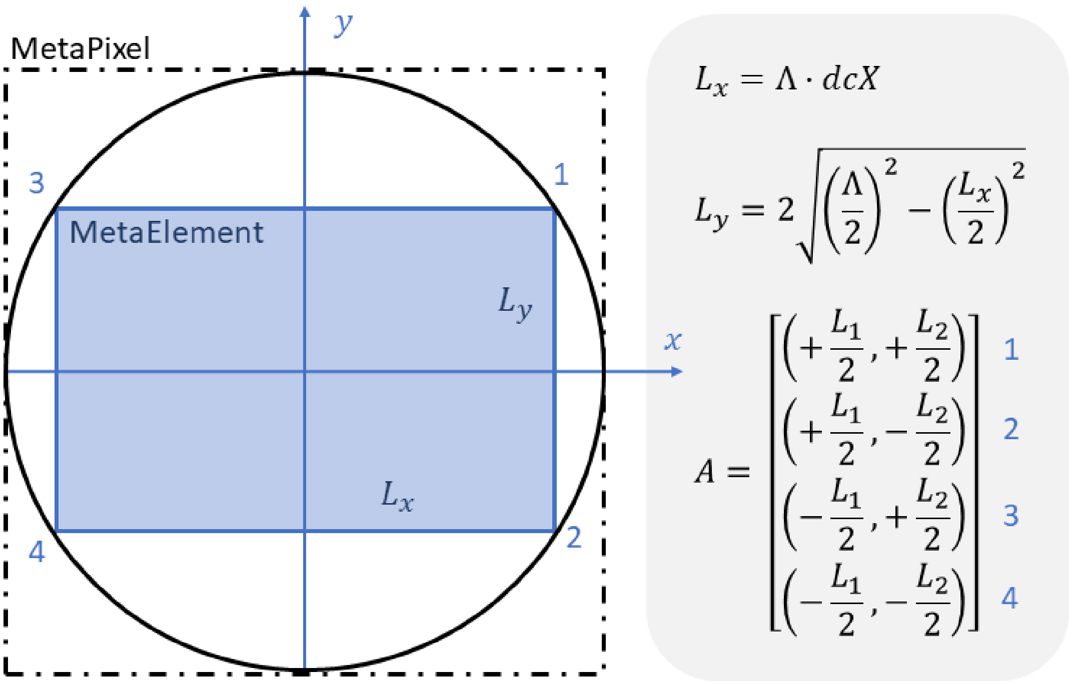

Figure 91: A representation of the rectangular shape of the metaelement that will be placed in each MP of the metasurface reported in figure 90. Notice that, in the relative MatLab code, the metaelements are generated centred in the origin. The placement of a metaelement into the MP of a particular coordinate (x_{MP}, y_{MP}) of the mesh, is performed after the computation of its rotation angle $\chi_{MP} = \frac{\Delta\Omega_{MP}}{2}$, where $\Delta\Omega_{MP}$ is the phase term that we want to transfer to the impinging beam in that coordinates (see equation 213).

$$L_y = 2\sqrt{\left(\frac{\Lambda}{2}\right)^2 - \left(\frac{L_x}{2}\right)^2} \tag{218}$$

In this way, the coordinates of the four vertices of our metelements are:

$$A = \left[\left(\frac{L_x}{2}, \frac{L_y}{2}\right); \left(\frac{L_x}{2}, -\frac{L_y}{2}\right); \left(-\frac{L_x}{2}, \frac{L_y}{2}\right); \left(-\frac{L_x}{2}, -\frac{L_y}{2}\right)\right] \tag{219}$$

and the related metaelement is reported in figure 91. The MatLab code used in this step is the following:

Listing 10.2.2: defining of metaelement coordinates

```
% duty-cycle in X-direction
dcX = 0.9;

% sides of rectangle [um]
Lx  = period*dcX;
Ly  = 2*sqrt((period/2)^2 - (Lx/2)^2);

% relative coords of the rect. vertices (before the roto-traslation) [nm]
x1 = (Lx/2)*1000;
x2 = (-Lx/2)*1000;
y1 = (Ly/2)*1000;
y2 = (-Ly/2)*1000;
A  = [x1,y1; x1,y2; x2,y2; x2,y1];
```

At this point, in order to obtain a circular metasurface, the centre (x_c, y_c) of each MP is computed and, if its distance to the origin is less than R_{max}, the phase shift $\Delta\Omega$ that we want to impart to a wavefield impinging

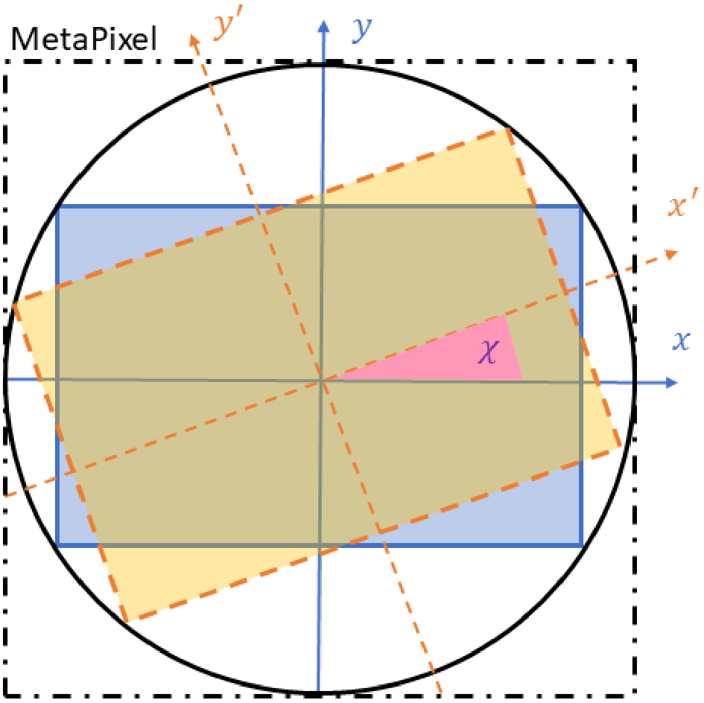

Figure 92: Rotation of the metaelements of an angle χ depending on the phase term that we want to transfer to the impinging radiation. After the rotation, the beam is translated to the position of the MP considered, as expressed by the equations 223.

the metasurface in this particular position, is computed. In this case, our intent is the generation of a multipole-phase beam of a particular phase order m, phase strength α, and phase orientation θ_0, whose phase pattern is described, in polar coordinates, by the equation 90:

$$\Omega_{MP}(r,\theta) = \alpha r^m \cos[m(\theta-\theta_0)] \tag{220}$$

The phase shift to impart to the impinging field is, therefore

$$\Delta\Omega_{MP}(r,\theta) = \left|\frac{\Omega_{MP}(r,\theta)}{2\pi}\right| \tag{221}$$

However, we have seen that, in order to transfer a generic phase $\Delta\Omega_{MP}(r,\theta)$ to a field using a metasurface, the condition to satisfy is expressed in equations 213

$$\chi(r,\theta) = \frac{\Delta\Omega_{MP}(r,\theta)}{2} \tag{222}$$

where χ is the rotation angle of the rectangular metaelement considered, as reported in figure 92.

With this rotational angle, we are finally able to compute the coordinates of the metaelement considered, whose initial values $A(x,y)$ will be transformed into the final coordinates $B(x',y')$, defined by a rotation of an angle χ and a translation of (x_c,y_x).

$$\begin{cases} x' = x_c + x\cos\left(\frac{\Delta\Omega_{MP}}{2}\right) - y\sin\left(\frac{\Delta\Omega_{MP}}{2}\right) \\ y' = y_c + x\sin\left(\frac{\Delta\Omega_{MP}}{2}\right) - y\cos\left(\frac{\Delta\Omega_{MP}}{2}\right) \end{cases} \tag{223}$$

The coordinates obtained are then saved in a text file with a GDSII format, readable by the machines used in the fabrication process. The procedure is so repeated for each MP of the mesh. The MatLab code is reported in the following:

Listing 10.2.3: defining of metaelement coordinates

```
% phase pattern
Omega = (alpha*10^-6)*(r.^m).*cos(m*(theta-theta0));
phase = mod(Omega, 2*pi);

% for each i-th MP X-value
for i = 1 : (length(xxt)-1)

    % for each j-th MP Y-value
    for j = 1 : (length(yyt)-1)

        % if the (i,j)MP is all within Rmax distance
        if(r(i,j) <= Rmax)

            % final coords of the metaelement (i,j) [nm]
            chi = phase(i,j)/2;
            xc = r(i,j)*cos(theta(i,j)) + period/2;
            yc = r(i,j)*sin(theta(i,j)) + period/2;
            B = zeros(length(A(:,1)),length(A(2,:)));
            for k = 1 : 4
                % x' = xc + [x*cos(chi) - y*sin(chi)]
                B(k,1) = (A(k,1).*cos(chi) - A(k,2).*sin(chi)) + xc*1000;
                % y' = yc + [x*sin(chi) + y*cos(chi)]
                B(k,2) = (A(k,1).*sin(chi) + A(k,2).*cos(chi)) + yc*1000;
            end

            % writing GDSII file
            fprintf(fileID,'BOUNDARY\nLAYER 1\nDATATYPE 0\nXY ');
            fprintf(fileID,'%.0f: %.0f\n',B');
            fprintf(fileID,'\nENDEL\n\n');

        end

    end

end
```

10.3 Metasurfaces for the Transformer and the Phase Corrector

In order to design a practical demultiplexer working with multipole-phase beams without the limitations of the experimental apparatus discussed in chapter 9, in particular the high value of the focal length of the circular-sector transformation due to the sizes of the two SLMs, two metasurfaces have been designed with the MatLab macro described in the previous section. It is sufficient to substitute the expression of the variable ”Omega” with the new phase term desired. The first MS designed, reported in figure 93, produces on the impinging multipole-phase beams the phase term $\Omega^{D}_{m,1}$ of the Transformer, which was given by the first half-section of the SLM#2 in the experimental setup above-mentioned. The second MS, instead, imparts on the beams the Phase Correction $\Omega^{D}_{m,2}$, which was produced by the second half-part of the SLM#2 (see figure 94). For simplicity, we remember here the expressions of the two phase terms:

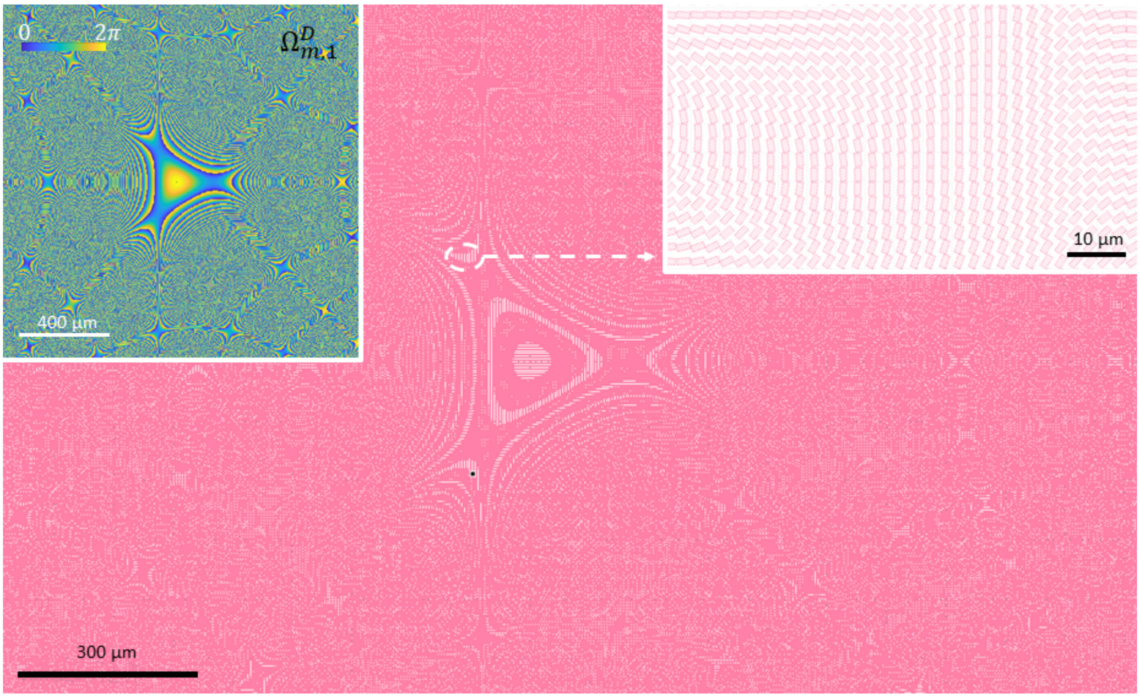

Figure 93: Metasurface designed in order to impart, on the impinging radiation, a phase term $\Omega^D_{m,1}$ as the one expressed in equation 224 and reported, in modulo 2π, in the top-left corner of the figure. The parameters of the circular-sector transformation used are: $f_{CS} = 10\,\text{mm}$, $a = 1.0\,\text{mm}$ and $b = 0.4\,\text{mm}$.

$$\Omega^D_{m,1} = \Omega_{CS} - k\frac{r^2}{2f_{CS}} \tag{224}$$

$$\Omega^D_{m,2} = \Omega_{PC} - k\frac{r^2}{2f_{CS}} \tag{225}$$

where, are usual, Ω_{CS} and Ω_{PC} are defined as:

$$\Omega_{CS} = k\frac{ab}{f_{CS}}\left(\frac{r}{b}\right)^{1+m}\frac{\cos[(1+m)\theta]}{1+m} \tag{226}$$

$$\Omega_{PC} = k\frac{ab}{f_{CS}}\left(\frac{r}{a}\right)^{1+\frac{1}{m}}\frac{\cos[(1+\frac{1}{m})\theta]}{1+\frac{1}{m}} \tag{227}$$

It is worth noting that the MS of the Phase Corrector, does not include the Fourier term $-k\frac{r^2}{2f}$ used for the final sorting of the multipole-phase beams into distinct bright spots, but it can be easily incorporated adding this term to $\Omega^D_{m,2}$ in the MatLab code. The parameters of the circular-sector transformation used for the design of the two phase plates are: $f_{CS} = 10\,\text{mm}$, $a = 1.0\,\text{mm}$ and $b = 0.4\,\text{mm}$, while the impinging multipole-phase beams are supposed of phase order $m = 2$, and wavelength $\lambda = 632.8\,\text{nm}$. These are the same parameters of the link described in chapter 8, showing the potentialities of the metasurfaces in the design of apparatus working with multipole-phase beams.

10.4 Briefly introduction to the fabrication of the MSs

We have seen that the MatLab macro, used in the design of our metasurfaces, produces an output text file with a format called GDSII. This file is, practically, a list of instructions and coordinates used by an Electron Beam Lithography (EBL) machine for the creation of a mask onto a resist layer, thanks to an energetic beam of electrons (typically in the order of 100 keV). The choice of the EBL is due to the high resolution needed to work with metasurfaces characterized by grating with a period in the order of the nanometres. Then the resist

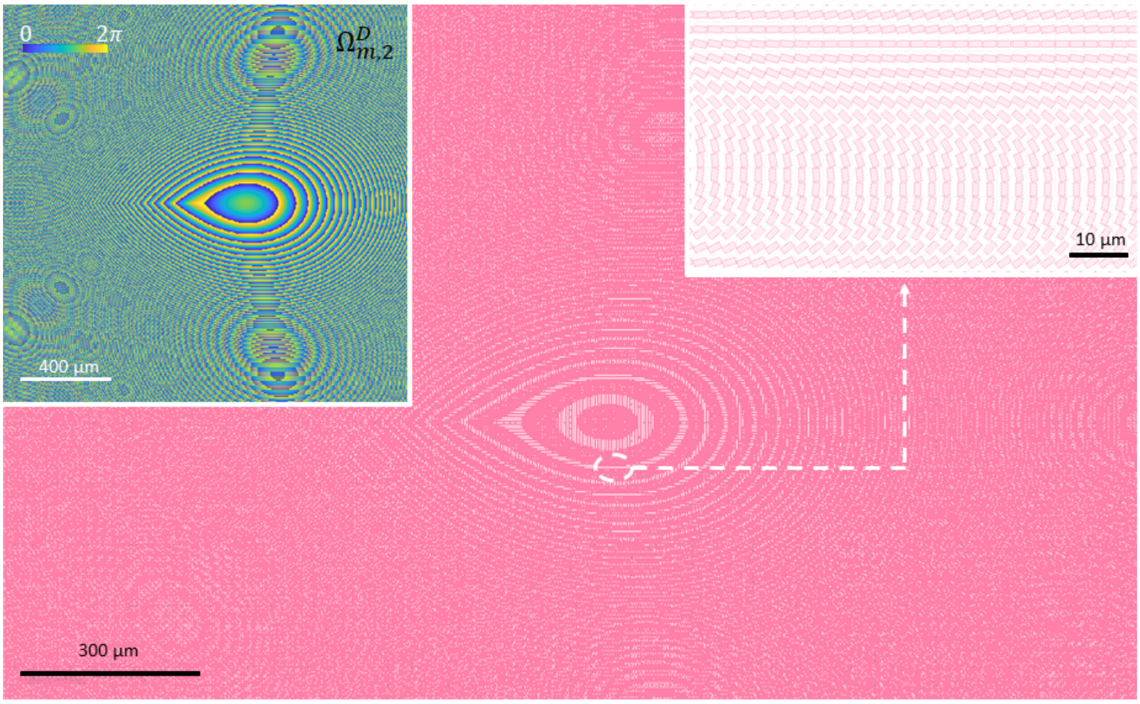

Figure 94: Metasurface designed in order to impart, on the impinging radiation, a phase term $\Omega^{D}_{m,2}$ as the one expressed in equation 225 and reported, in modulo 2π, in the top-left corner of the figure. The parameters of the circular-sector transformation used are: $f_{CS} = 10\,\text{mm}$, $a = 1.0\,\text{mm}$ and $b = 0.4\,\text{mm}$.

not impressed by the electron beam is removed and the final mask is so obtained. At this point, the material (for example TiO_2) of the final desired metaelement is deposited on the mask, for instance with an Atomic Layer Deposition (ALD) process [66]. After that, the excess material is removed with a plasma exposition, a procedure called Reactive Ion Etching (RIO), and, finally, also the remaining resist is removed, obtaining the MS.

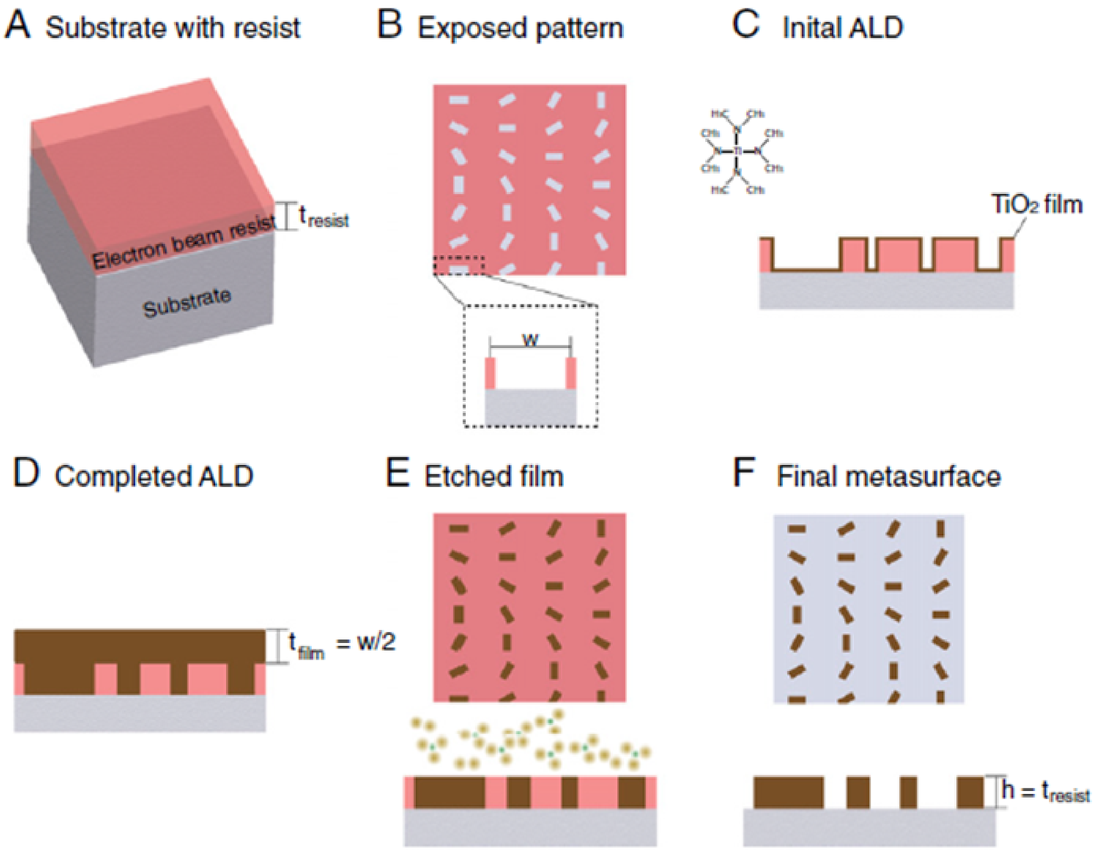

Figure 95: The main steps in the fabrication of a metasurface. A mask (B) is obtained via Electron Beam Lithography (EBL) on a photoresist layer (A). Then, (C-D) a layer of TiO_2 is deposited with Atom Layer Deposition (ALD). Finally, (E) the excess material is removed with a Reactive Ion Etching (RIO), and the remaining resist is removed with a developer (F) [62].

11 Conclusions

In the previous chapters, it was given a full immersion on a new and unique framework for the free-space communication systems, based on the transmission of light beams with a wavefront characterized by a phase with a multipole structure. We have seen that these beams arise from the general solutions of the Laplace's equation, which describes the phase structure of a generic electromagnetic field under reasonable assumptions of analyticity. In particular, it was assumed that the evolution of the phase of the beam, during a free space propagation, is described by a conformal mapping of the coordinates of the initial wavefront into the coordinates of the final one. In this way, the information contained in the phase function of the beam is preserved during the transmission and the multipole-phase beams are, therefore, a possible candidate in the free-space optical communication systems. Moreover, we have seen that these type of structured light is characterized by three parameters: the phase order, m, related to the number of poles of the phase structure, the phase strength, α, which is related to the modulus of the phase gradient, and the phase orientation θ_0, that indicates the orientation of the phase pattern of the beam. With respect to the OAM beams exploited in the last years, the multipole-phase beams present the following advantages:

- absence of phase singularities, which are detrimental for free-space transmission due to beams divergence;
- practical way to generate and measure such beams with conformal transformations;
- two dense degrees of freedom which can be practically controlled instead of only a discrete one (OAM).

We have seen, indeed, that the different values of the parameters of the multipole-phase beams define quasi-orthogonal electromagnetic fields, suggesting that the multipole-phase beams can represent a new paradigm in the spatial division multiplexing.

For this reason, the demultiplexing of these beams was investigated, showing that it can be practically implemented with two phase plates: the Transformer, which converts different multipole-phase patterns into different linear phase gradients, and the Phase Corrector, which corrects the phase distortions produced during the propagation between the two optical elements. A final Fourier lens, which can be integrated in the second phase plate, provides the generation of the final distinct light spots, corresponding to the different beams. We have seen, moreover, that illuminating this setup in the reverse direction, the constellation of a set of isolated light beams can be converted, thanks to the orthogonality above-mentioned, into a superposition of multipole-phase beams, and propagated for long distances without loss of information and any significant interference. At this point, the received beam can be demultiplexed, as already said, and an entire communication link is so established.

In particular, it was simulated the propagation, for one kilometre in free space, of thirty channels as a single beam (i.e., the superposition of the multipole-phase beams related to each light spot), showing the incredible potentialities of this new type of structured light in the communication systems. The family of multipole-phase beams used in this simulation was the one characterized by a phase order $m = 2$. Indeed, we have seen that this is the only case in which the transmitted beam conserved the phase order and, therefore, its phase structure and the information contained in it. However, the demultiplexing of multipole-phase beams of higher order was, anyway, analysed with success, unlocking the phase order itself as a possible further degree of freedom (besides α and θ_0) in the spatial division multiplexing with multipole-phase beams.

At this point, a possible demultiplexing experimental setup, already used for a low number of channels in the case of $m = 2$ [6], was considered also for the sorting of a higher number of channels and for further values of the phase order: $m = 3$, and 4 in particular. However, the sizes of the laboratory optical elements have shown the crucial role of the focal length of the circular-sector transformation used for the conversion of the multipole-phase beams into fields with a linear phase gradient, which significantly affects the compactness and number of available channels of such a such demultiplexer. Indeed, focal lengths bigger than few millimetres implies the necessity of high values of the phase strength, producing not-negligible phase distortions in the final sorted light spots. Therefore, the number of channels, that we were abled to transmits in the simulations is still remarkable, but far away from the simulations' results obtained in an ideal apparatus, for instance in the above-mentioned simulated link.

However, a way out is represented by the metasurfaces working in the sub-wavelength regime. As we have seen, the possibility of create phase plate extremely compact, which can, moreover, integrates functionalities not allowed with the common bulk optics, represents the future of the communication systems and of the structured light in general. With respect to bulk refractive optics and diffractive optical elements, metasurfaces exhibit an almost flat digital profile of subwavelength features which can be fabricated using the well-established techniques of semiconductor manufacturing. The metasurface paradigm allows achieving the real merging between optics and silicon photonics. For this reason, it was developed a MatLab algorithm in order to design a metasurface which can impart, on an impinging radiations, an arbitrary phase term. With this further know-how, the future in the free-space optical communication systems using multipole-phase beams is almost unlimited. Micro optoelectronic devices, compatible with mass-production and silicon photonics technology, can be designed and developed in order to transmit several parallel channels of information in the same electromagnetic field, improving exponentially the information capacity of more than one order of magnitude, as shown in the design of a link. This represents, moreover, a cheaper alternative in the developing countries with respect to optical fibres networks, and a sustainable solution to the worrying menace of the optical crunch with limited energy consumption and therefore reduced greenhouse emissions. For all these reason, this thesis work, paves the way to a new and unique paradigm in the communications technologies.

Bibliography

[1] Peter Winzer. “Making spatial multiplexing a reality”. In: *Nature Photonics* 8 (Apr. 2014). DOI: `10.1038/nphoton.2014.58`.

[2] Martin Lavery et al. “Tackling Africa’s digital divide”. In: *Nature Photonics* 12 (May 2018).

[3] Peter J. Winzer. “High-Spectral-Efficiency Optical Modulation Formats”. In: *Journal of Lightwave Technology* 30.24 (2012), pp. 3824–3835. DOI: `10.1109/JLT.2012.2212180`.

[4] D.J. Richardson, John Fini, and Lynn Nelson. “Space Division Multiplexing in Optical Fibres”. In: *Nature Photonics* 7 (May 2013), pp. 354–362. DOI: `10.1038/nphoton.2013.94`.

[5] Andrés Macho and Roberto Llorente. “Multi-Core Optical Fibers: Theory, Applications and Opportunities”. In: Feb. 2018. ISBN: 978-953-51-3813-6. DOI: `10.5772/intechopen.72458`.

[6] Gianluca Ruffato, Vincenzo Grillo, and Filippo Romanato. “Multipole-phase division multiplexing”. In: *Opt. Express* 29.23 (Nov. 2021), pp. 38095–38108. DOI: `10.1364/OE.438898`.

[7] Toshio Tagawa and Kewei Song. “Stability of an Axisymmetric Liquid Metal Flow Driven by a Multi-Pole Rotating Magnetic Field”. In: *Fluids* 4.2 (2019). ISSN: 2311-5521. DOI: `10.3390/fluids4020077`. URL: `https://www.mdpi.com/2311-5521/4/2/77`.

[8] L. Allen et al. “Orbital angular momentum of light and the transformation of Laguerre-Gaussian laser modes”. In: *Phys. Rev. A* 45 (11 June 1992), pp. 8185–8189. DOI: `10.1103/PhysRevA.45.8185`. URL: `https://link.aps.org/doi/10.1103/PhysRevA.45.8185`.

[9] D. McGloin and K. Dholakia. “Bessel beams: Diffraction in a new light”. In: *Contemporary Physics* 46.1 (2005), pp. 15–28. DOI: `10.1080/0010751042000275259`.

[10] Christina Alpmann, Christoph Schöler, and Cornelia Denz. “Elegant Gaussian beams for enhanced optical manipulation”. In: *Applied Physics Letters* 106.24 (2015), p. 241102. DOI: `10.1063/1.4922743`.

[11] Miles J. Padgett. “Orbital angular momentum 25 years on [Invited]”. In: *Opt. Express* 25.10 (May 2017), pp. 11265–11274. DOI: `10.1364/OE.25.011265`.

[12] Alison M. Yao and Miles J. Padgett. “Orbital angular momentum: origins, behavior and applications”. In: *Adv. Opt. Photon.* 3.2 (June 2011), pp. 161–204. DOI: `10.1364/AOP.3.000161`.

[13] Graham Gibson et al. “Free-space information transfer using light beams carrying orbital angular momentum”. In: *Opt. Express* 12.22 (Nov. 2004), pp. 5448–5456. DOI: `10.1364/OPEX.12.005448`.

[14] Jonathan Leach et al. “Measuring the Orbital Angular Momentum of a Single Photon”. In: *Phys. Rev. Lett.* 88 (25 June 2002), p. 257901. DOI: `10.1103/PhysRevLett.88.257901`.

[15] Guillaume Labroille et al. “Efficient and mode selective spatial mode multiplexer based on multi-plane light conversion”. In: *Opt. Express* 22.13 (June 2014), pp. 15599–15607. DOI: `10.1364/OE.22.015599`.

[16] Nicolas K. Fontaine et al. “Design of High Order Mode-Multiplexers using Multiplane Light Conversion”. In: *2017 European Conference on Optical Communication (ECOC)*. 2017, pp. 1–3. DOI: `10.1109/ECOC.2017.8346129`.

[17] Tiehui Su et al. “Demonstration of free space coherent optical communication using integrated silicon photonic orbital angular momentum devices”. In: *Opt. Express* 20.9 (Apr. 2012), pp. 9396–9402. DOI: `10.1364/OE.20.009396`.

[18] Gregorius C. G. Berkhout et al. “Efficient Sorting of Orbital Angular Momentum States of Light”. In: *Phys. Rev. Lett.* 105 (15 Oct. 2010), p. 153601. DOI: `10.1103/PhysRevLett.105.153601`.

[19] Martin Lavery et al. “Efficient measurement of an optical orbital-angular-momentum spectrum comprising more than 50 states”. In: *New Journal of Physics* 15 (Jan. 2013), p. 013024. DOI: `10.1088/1367-2630/15/1/013024`.

[20] Yuanhui Wen et al. "Spiral Transformation for High-Resolution and Efficient Sorting of Optical Vortex Modes". In: *Phys. Rev. Lett.* 120 (19 May 2018), p. 193904. DOI: `10.1103/PhysRevLett.120.193904`.

[21] Gianluca Ruffato et al. "A compact diffractive sorter for high-resolution demultiplexing of orbital angular momentum beams". In: *Scientific Reports* 8 (July 2018). DOI: `10.1038/s41598-018-28447-1`.

[22] Robert Fickler et al. "Interface between path and orbital angular momentum entanglement for high-dimensional photonic quantum information". In: *Nature communications* 5 (July 2014), p. 4502. DOI: `10.1038/ncomms5502`.

[23] Gianluca Ruffato et al. "Test of mode-division multiplexing and demultiplexing in free-space with diffractive transformation optics". In: *Opt. Express* 25.7 (Apr. 2017), pp. 7859–7868. DOI: `10.1364/OE.25.007859`.

[24] Wenzhe Li et al. "Rapidly tunable orbital angular momentum (OAM) system for higher order Bessel beams integrated in time (HOBBIT)". In: *Optics Express* 27 (Feb. 2019), p. 3920. DOI: `10.1364/OE.27.003920`.

[25] Satoru Takashima, Hirokazu Kobayashi, and Katsushi Iwashita. "Integer multiplier for the orbital angular momentum of light using a circular-sector transformation". In: *Phys. Rev. A* 100 (6 Dec. 2019), p. 063822. DOI: `10.1103/PhysRevA.100.063822`.

[26] Gianluca Ruffato, Michele Massari, and Filippo Romanato. *Multiplication and division of the orbital angular momentum of light with diffractive transformation optics.* Apr. 2019.

[27] Yuanhui Wen et al. "Arbitrary Multiplication and Division of the Orbital Angular Momentum of Light". In: *Phys. Rev. Lett.* 124 (21 May 2020), p. 213901. DOI: `10.1103/PhysRevLett.124.213901`.

[28] Yongxiong Ren et al. "Adaptive optics compensation of multiple orbital angular momentum beams propagating through emulated atmospheric turbulence". In: *Opt. Lett.* 39.10 (May 2014), pp. 2845–2848. DOI: `10.1364/OL.39.002845`.

[29] Charles Brunet and Leslie Rusch. "Invited Paper: Optical fibers for the transmission of orbital angular momentum modes". In: *Optical Fiber Technology* 31 (Sept. 2016), pp. 172–177. DOI: `10.1016/j.yofte.2016.08.003`.

[30] Alan E. Willner et al. "Recent advances in high-capacity free-space optical and radio-frequency communications using orbital angular momentum multiplexing". In: *Philosophical Transactions of the Royal Society A: Mathematical, Physical and Engineering Sciences* 375.2087 (2017), p. 20150439. DOI: `10.1098/rsta.2015.0439`.

[31] A. Willner et al. "Optical communications using orbital angular momentum beams". In: *Advances in Optics and Photonics* 7 (Mar. 2015). DOI: `10.1364/AOP.7.000066`.

[32] Erik Agrell et al. "Roadmap of optical communications". In: *Journal of Optics* 18.6 (May 2016), p. 063002. DOI: `10.1088/2040-8978/18/6/063002`.

[33] P.J. Winzer and R.-J. Essiambre. "Advanced Optical Modulation Formats". In: *Proceedings of the IEEE* 94.5 (2006), pp. 952–985. DOI: `10.1109/JPROC.2006.873438`.

[34] B. Mukherjee. "WDM optical communication networks: progress and challenges". In: *IEEE Journal on Selected Areas in Communications* 18.10 (2000), pp. 1810–1824. DOI: `10.1109/49.887904`.

[35] P. J. Winzer, D. T. Neilson, and A. R. Chraplyvy. "Fiber-optic transmission and networking: the previous 20 and the next 20 years [Invited]". In: *Opt. Express* 26.18 (2018), pp. 24190–24239. DOI: `10.1364/OE.26.024190`.

[36] Peter J. Winzer and David T. Neilson. "From Scaling Disparities to Integrated Parallelism: A Decathlon for a Decade". In: *Journal of Lightwave Technology* 35.5 (2017), pp. 1099–1115. DOI: `10.1109/JLT.2017.2662082`.

[37] David J. Richardson. "Filling the Light Pipe". In: *Science* 330.6002 (2010), pp. 327–328. DOI: `10.1126/science.1191708`.

[38] Manuel Erhard et al. “Twisted Photons: New Quantum Perspectives in High Dimensions”. In: *Light: Science Applications* 7 (Aug. 2017). DOI: `10.1038/lsa.2017.146`.

[39] Alicia Sit et al. “High-dimensional intracity quantum cryptography with structured photons”. In: *Optica* 4.9 (Sept. 2017), pp. 1006–1010. DOI: `10.1364/OPTICA.4.001006`.

[40] Michael de Oliveira et al. “Experimental high-dimensional quantum secret sharing with spin-orbit-structured photons”. In: *Phys. Rev. A* 101 (4 Apr. 2020), p. 042303. DOI: `10.1103/PhysRevA.101.042303`.

[41] K Dholakia and Tomáš Čižmár. “Shaping the future of manipulation”. In: *Nature Photonics* 5 (June 2011), pp. 335–342. DOI: `10.1038/nphoton.2011.80`.

[42] Mike Woerdemann et al. “Advanced optical trapping by complex beam shaping”. In: *Laser Photonics Reviews* 7 (Nov. 2013). DOI: `10.1002/lpor.201200058`.

[43] Katrin Willig et al. “STED microscopy with continuous wave beams”. In: *Nature methods* 4 (Dec. 2007), pp. 915–8. DOI: `10.1038/nmeth1108`.

[44] Florian Fahrbach et al. “Self-reconstructing sectioned Bessel beams offer submicron optical sectioning for large fields of view in light-sheet microscopy”. In: 305 (May 2013), pp. 1007–1009.

[45] Shu Jia, Joshua C. Vaughan, and Xiaowei Zhuang. “Isotropic 3D Super-resolution Imaging with a Self-bending Point Spread Function”. In: *CLEO: 2013 Postdeadline.* Optical Society of America, 2013, CTh5D.10. DOI: `10.1364/CLEO_SI.2013.CTh5D.10`.

[46] Guifang Li et al. “Space-division multiplexing: The next frontier in optical communication”. In: *Advances in Optics and Photonics* 6 (Dec. 2014). DOI: `10.1364/AOP.6.000413`.

[47] J. W. Goodman. *Introduction to Fourier Optics.* Mc Graw-Hill, 1996.

[48] Gianluca Ruffato and Filippo Romanato. “Design of continuously variant metasurfaces for conformal transformation optics”. In: *Opt. Express* 28.23 (Nov. 2020), pp. 34201–34218. DOI: `10.1364/OE.400627`.

[49] Alan Willner et al. “Design challenges and guidelines for free-space optical communication links using orbital-angular-momentum multiplexing of multiple beams”. In: *Journal of Optics* 18 (July 2016), p. 074014. DOI: `10.1088/2040-8978/18/7/074014`.

[50] Guodong Xie et al. “Performance metrics and design considerations for a free-space optical orbital-angular-momentum–multiplexed communication link”. In: *Optica* 2.4 (Apr. 2015), pp. 357–365. DOI: `10.1364/OPTICA.2.000357`.

[51] Rui Chen et al. “Orbital Angular Momentum Waves: Generation, Detection, and Emerging Applications”. In: *IEEE Communications Surveys Tutorials* 22.2 (2020), pp. 840–868. DOI: `10.1109/COMST.2019.2952453`.

[52] Feng Zheng et al. “Research status and prospects of orbital angular momentum technology in wireless communication”. In: *Progress In Electromagnetics Research* 168 (Jan. 2020), pp. 113–132. DOI: `10.2528/PIER20091104`.

[53] M. Born and E. Wolf. “Principles of Optics”. In: (1980).

[54] David Voelz and Michael Roggemann. “Digital simulation of scalar optical diffraction: Revisiting chirp function sampling criteria and consequences”. In: *Applied optics* 48 (Nov. 2009), pp. 6132–42. DOI: `10.1364/AO.48.006132`.

[55] David Voelz. *Computational Fourier Optics: A MATLAB Tutorial.* SPIE Press, 2011, p. 14. ISBN: 9780819482051. DOI: `10.1117/3.858456`.

[56] W.J. Hossack, A. M. Darling, and A. Dahdouh. “Coordinate Transformations with Multiple Computer-generated Optical Elements”. In: *Journal of Modern Optics* 34.9 (1987), pp. 1235–1250. DOI: `10.1080/09500348714551121`.

[57] Elad Greenfield et al. “Accelerating Light Beams along Arbitrary Convex Trajectories”. In: *Phys. Rev. Lett.* 106 (21 May 2011), p. 213902. DOI: `10.1103/PhysRevLett.106.213902`.

[58] G. Ruffato et al. “Arbitrary Conformal Transformations of Wave Functions”. In: *Phys. Rev. Applied* 15 (5 May 2021), p. 054028. DOI: `10.1103/PhysRevApplied.15.054028`. URL: `https://link.aps.org/doi/10.1103/PhysRevApplied.15.054028`.

[59] G. Ruffato et al. “Non-paraxial design and fabrication of a compact OAM sorter in the telecom infrared”. In: *Opt. Express* 27.17 (Aug. 2019), pp. 24123–24134. DOI: `10.1364/OE.27.024123`.

[60] Patrice Genevet et al. “Recent advances in planar optics: from plasmonic to dielectric metasurfaces”. In: *Optica* 4.1 (Jan. 2017), pp. 139–152. DOI: `10.1364/OPTICA.4.000139`.

[61] Federico Capasso. “The future and promise of flat optics: a personal perspective”. In: *Nanophotonics* 7.6 (2018), pp. 953–957. DOI: `doi:10.1515/nanoph-2018-0004`. URL: `https://doi.org/10.1515/nanoph-2018-0004`.

[62] Robert Devlin et al. “Broadband high-efficiency dielectric metasurfaces for the visible spectrum”. In: *Proceedings of the National Academy of Sciences of the United States of America* 113 (Sept. 2016). DOI: `10.1073/pnas.1611740113`.

[63] Pietro Capaldo et al. “Nano-fabrication and characterization of silicon meta-surfaces provided with Pancharatnam-Berry effect”. In: *Opt. Mater. Express* 9.3 (Mar. 2019), pp. 1015–1032. DOI: `10.1364/OME.9.001015`.

[64] Boris Desiatov et al. “Polarization selective beam shaping using nanoscale dielectric metasurfaces”. In: *Opt. Express* 23.17 (Aug. 2015), pp. 22611–22618. DOI: `10.1364/OE.23.022611`.

[65] M. G. Moharam et al. “Stable implementation of the rigorous coupled-wave analysis for surface-relief gratings: enhanced transmittance matrix approach”. In: *J. Opt. Soc. Am. A* 12.5 (May 1995), pp. 1077–1086. DOI: `10.1364/JOSAA.12.001077`.

[66] Xie Qi et al. “Atomic layer deposition of TiO2 from tetrakis-dimethyl-amido titanium or Ti isopropoxide precursors and H2O”. In: *Journal of Applied Physics* 102 (Oct. 2007). DOI: `10.1063/1.2798384`.